

AD-A105 888

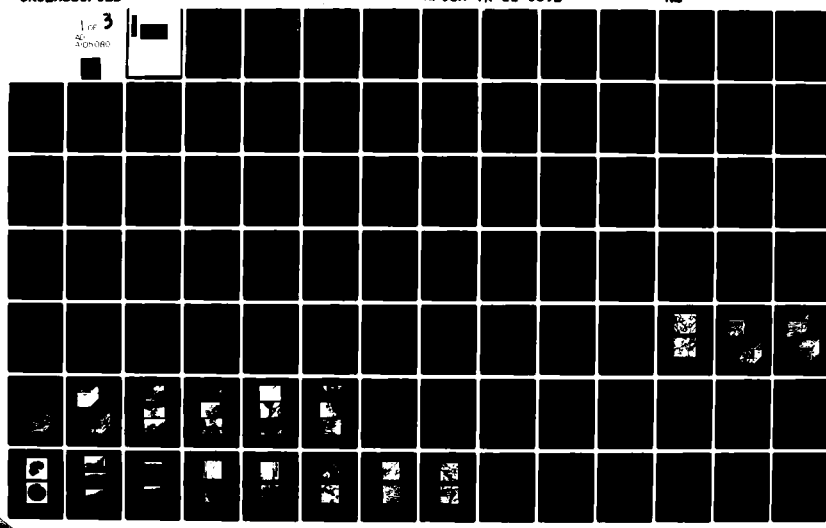
DREXEL UNIV PHILADELPHIA PA DEPT OF MATERIALS ENGINEERING F/6 11/6
A FUNDAMENTAL STUDY OF FATIGUE IN POWDER METALLURGY ALUMINUM AL--ETC(U)
AUG 81 A LAWLEY, M J KOCZAK AFOSR-77-3247

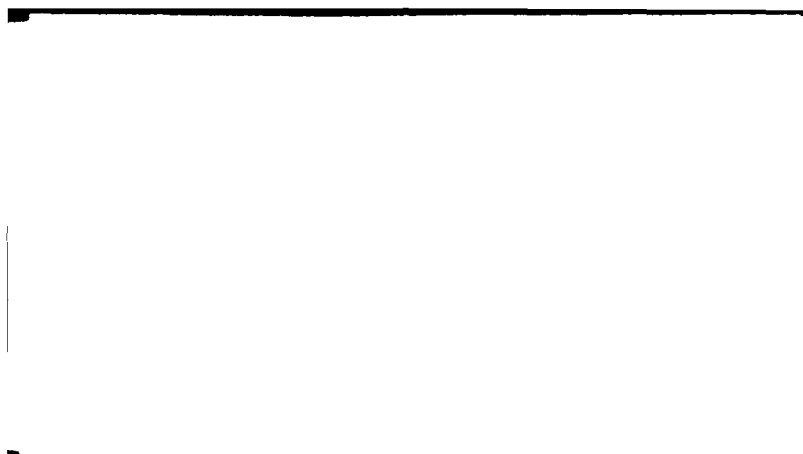
UNCLASSIFIED

AFOSR-TR-81-0692

NL

1 of 3
AFOSR-TR-81-0692





IClassified

CLASSIFICATION OF THIS PAGE (When Data Entered)

READ INSTRUCTIONS
BEFORE COMPLETING FORM

REPORT DOCUMENTATION PAGE		
1. REPORT NUMBER AFOSR-TR- 81 -0692	2. GOVT ACCESSION NO. AD-A105 080	3. RECIPIENT'S CATALOG NUMBER
4. TITLE (and Subtitle) A Fundamental Study of Fatigue in Powder Metallurgy Aluminum Alloys.		5. TYPE OF REPORT & PERIOD COVERED Final Technical Report March 1977 to Feb. 1981
7. AUTHOR(s) A. Lawley and M. J. Koczak		6. PERFORMING ORG. REPORT NUMBER AFOSR-77-3247
9. PERFORMING ORGANIZATION NAME AND ADDRESS Drexel University Department of Materials Engineering Philadelphia, Pa. 19104		10. PROGRAM ELEMENT, PROJECT, TASK AREA & WORK UNIT NUMBERS 61102F 2306/A1
11. CONTROLLING OFFICE NAME AND ADDRESS Air Force Office of Scientific Research Building 410 Bolling Air Force Base, Washington, D.C. 20332		12. REPORT DATE August 1981
14. MONITORING AGENCY NAME & ADDRESS(if different from Controlling Office)		13. NUMBER OF PAGES 96
		15. SECURITY CLASS. (of this report) Unclassified.
		15a. DECLASSIFICATION/DOWNGRADING SCHEDULE
16. DISTRIBUTION STATEMENT (of this Report) Approved for public release; distribution unlimited.		
17. DISTRIBUTION STATEMENT (of the abstract entered in Block 20, if different from Report)		
18. SUPPLEMENTARY NOTES		
19. KEY WORDS (Continue on reverse side if necessary and identify by block number) P/M forging; high-strength Al powder alloys; stress and strain-controlled fatigue; fatigue crack propagation; microstructure; fractography.		
20. ABSTRACT (Continue on reverse side if necessary and identify by block number) Processing-microstructure-fatigue relationships have been examined in high-strength powder metallurgy aluminum alloys (Al-Cu, Mg, Zn, Co) in air and salt fog. Three phases were included: (i) The combined effects of cobalt level and processing mode on fatigue life and resistance to crack propagation; (ii) The role of plane-strain forging on fatigue life and crack propagation response; (iii) The combined effects of cobalt level and processing mode on strain-controlled low-cycle fatigue. While the interplay between processing history, alloy composition and orientation		

~~SECURITY~~ Unclassified

~~SECURITY~~ CLASSIFICATION OF THIS PAGE(When Data Entered)

is complex, a basic understanding of the role of microstructure on the crack initiation and propagation stages of fatigue has been obtained. Direct comparisons of the corresponding fatigue response of counterpart ingot metallurgy alloys were included. In general, the P/M processed material exhibits superior resistance to fatigue crack initiation compared to the I/M form. However the relative crack growth rates in the P/M and I/M materials depend on orientation and the level of ΔK .

Unclassified

~~SECURITY~~ CLASSIFICATION OF THIS PAGE(When Data Entered)

AIR FORCE OFFICE OF SCIENTIFIC RESEARCH (AFSC)
NOTICE OF TRANSMITTAL TO DTIC
Printed technical report has been reviewed and is
appropriate for public release IAW AFN 190-12.
Distribution is unlimited.
MATTHEW J. KENFER
Chief, Technical Information Division

6
A FUNDAMENTAL STUDY OF FATIGUE
IN POWDER METALLURGY ALUMINUM ALLOYS

10
A. Lawley and M. J. Koczak

11
August 1981

9 Final Technical Report.

10
11-4-81
Grant AFOSR 77-3247

12 OCT 5 1981

D
A

for

13
14 Air Force Office of Scientific Research
Building 410
Bolling Air Force Base
Washington, D.C. 20332

15 by

16
17 Department of Materials Engineering
Drexel University
Philadelphia, PA 19104

18
19 11-20-81

20
21

TABLE OF CONTENTS

	<u>PAGE</u>
SUMMARY	
INTRODUCTION	1
1. Background	1
2. Ingot Metallurgy Alloys and Processing	2
3. Powder Metallurgy Alloys and Processing	3
4. The Present Study	7
PART I: Fatigue of High-Strength Powder Alloys; The Roles of Cobalt Level and Processing Mode	9
SUMMARY	9
INTRODUCTION	10
EXPERIMENTAL PROCEDURE	11
1. Material	11
a) Powder Alloys	11
b) Compaction, Forging and Heat Treatment	11
2. Specimen Preparation and Material Testing	12
a) Tensile Testing	12
b) Axial Fatigue Testing	13
c) Fatigue Crack Growth Measurements	14
3. Structural Evaluation	16
a) Optical Metallography	16
b) Scanning Electron Microscopy	17
c) Transmission Electron Microscopy	18
RESULTS AND OBSERVATIONS	18
1. Structure of Powders	18
2. Structure of Compacts and forgings	18
3. Tensile Properties	21
4. Axial Fatigue	21
a) Response to Cyclic Loading in Air	21
b) Response to Cyclic Loading in Salt Fog	22
c) Fatigue Fracture Behavior in Air	23
d) Fatigue Fracture Behavior in Salt Fog	25
5. Fatigue Crack Propagation	26
a) Response in Air	26
b) Response in Salt Fog	28
c) Fracture Morphology - Crack Propagation in Air	29
d) Fracture Morphology - Crack Propagation in Salt Fog	30

	<u>PAGE</u>
DISCUSSION	30
1) Aging Response	30
2) Tensile Properties	31
3) Fatigue Properties	33
a) Axial Fatigue in Air	33
b) Fatigue Crack Propagation in Air	35
c) Axial Fatigue in Salt Fog	38
d) Fatigue Crack Propagation in Salt Fog	39
CONCLUSIONS	39
TABLES AND FIGURES	
PART II: Fatigue of a High-Strength Powder Alloy; The Role of Deformation Processing	43
SUMMARY	43
INTRODUCTION	44
EXPERIMENTAL PROCEDURE	47
1) Material and Consolidation	47
2) Plane Strain Forging and Heat Treatment	47
3) Specimens and Location	49
4) Specimen Preparation and Testing	50
a) Tensile Testing	50
b) Axial Fatigue Testing	50
c) Fatigue Crack Growth Measurements	51
5) Metallography	51
RESULTS	51
1) Tensile Properties	51
2) Axial Fatigue	52
3) Fatigue Crack Growth	53
4) Microstructure	54
a) After Hot-Compaction	54
b) After Plane Strain Forging	55
5) Fractography	56
a) Axial Fatigue	56
b) Crack Growth Specimens	59
DISCUSSION	59
1) Tensile Properties	59
2) Fatigue Behavior	60
a) Crack Initiation and Propagation in Aluminum Alloys	60
b) Axial Fatigue in Air	63
c) Axial Fatigue in Salt Fog	65
d) Crack Growth in Air	65
e) Crack Growth in Salt Fog	66

	<u>PAGE</u>
CONCLUSIONS	66
TABLES AND FIGURES	
PART III: Low Cycle Fatigue of High-Strength Powder Alloys	69
SUMMARY	69
INTRODUCTION	69
EXPERIMENTAL PROCEDURE	70
1) Material and Processing	70
2) Specimens and Fatigue Testing	71
3) Strain-Life Curves	72
4) Metallography	73
RESULTS AND DISCUSSION	73
1) Low-Cycle Fatigue Response	73
2) Fractography	74
3) Microstructure	75
CONCLUSIONS	75
TABLES AND FIGURES	
REFERENCES	77
PUBLICATIONS AND DISSERTATIONS	81
PERSONNEL	83
COUPLING ACTIVITIES	83

A

SUMMARY

Processing-microstructure-fatigue relationships have been examined in high-strength powder metallurgy aluminum alloys (Al-Cu, Mg, Zn, Co) in air and salt fog. Three phases were included: (i) The combined effects of cobalt level and processing mode on fatigue life and resistance to crack propagation; (ii) The role of plane-strain forging on fatigue life and crack propagation response; (iii) The combined effects of cobalt level and processing mode on strain-controlled low-cycle fatigue. While the interplay between processing history, alloy composition and orientation is complex, a basic understanding of the role of microstructure on the crack initiation and propagation stages of fatigue has been obtained. Direct comparisons of the corresponding fatigue response of counterpart ingot metallurgy alloys were included. In general, the P/M processed material exhibits superior resistance to fatigue crack initiation compared to the I/M form. However the relative crack growth rates in the P/M and I/M materials depend on orientation, the level of ΔK and processing mode.

INTRODUCTION

1. Background

Because of their high strength-to-density ratio, aluminum alloys have traditionally been used in aircraft structures. Here, possibly more so than in any other area of application, increased performance requirements have led to the development of new alloys. Originally, strength and stress corrosion resistance in both the longitudinal and long transverse orientations, were the only properties specified for aircraft alloys. While adequate for thin gage materials, the use of thicker gage sections and new design concepts based on dynamic properties has resulted in property level requirements not attainable in existing aluminum alloys.

High tensile strength and fracture toughness coupled with good corrosion and fatigue resistance are essential in aluminum alloys for the aerospace industry. The age hardenable Al-Zn, Mg, Cu (7XXX) alloys exhibit high strength levels (\sim 520 MPa (75 ksi)) and reasonable ductility (~ 8 to 18% RA). However, extensive use of this series of alloys has been limited because of inadequate secondary properties such as toughness, stress corrosion resistance and fatigue resistance, particularly in the short transverse direction.

The 7XXX series alloys develop their strength via a combination of natural and artificial aging but the condition of maximum strength (T6 temper) does not correspond to optimum resistance to fatigue crack growth. Further, the material is susceptible to stress corrosion cracking, particularly in the short transverse direction. Resistance to fatigue crack propagation increases as the extent of precipitation increases,

particularly in a high humidity environment; microstructurally, coherent η' changes to incoherent $\eta(\text{MgZn}_2)$ (1).

Iron and silicon are common impurities in commercial high-strength 7XXX alloys. These elements are in solution in the liquid but they separate out from the melt during solidification and form coarse constituent particles (1), e.g., $\text{Al}_7\text{Cu}_2\text{Fe}$, and Mg_2Si ; Al_2CuMg may also be present. Constituent particles do not dissolve during homogenization of the cast ingot and are carried over to the wrought form during mechanical fibering of the insoluble second phase constituent particles. Unlike the small hardening precipitates, the coarse constituent particles do not contribute to strength. They are brittle and fracture easily, separate from the matrix and create preferential crack paths (2,3).

Most of the high-strength aluminum alloys also contain dispersoids which are intermetallic particles and arise from the use of Cr, Mn, Zr or Co as grain refiners and in the control of recrystallization (1). These elements are retained in supersaturated solid solution in rapidly cooled ingots but during subsequent heat treatment, they precipitate out as $\text{Al}_{12}\text{Mg}_2\text{Cr}$, $\text{Al}_{20}\text{Mn}_3\text{Cu}_2$, ZrAl_3 or CoAl_9 . Once formed, these dispersoids cannot be completely dissolved in the solid state but their size, distribution and volume fraction can be modified by thermal treatments (1).

2. Ingot Metallurgy Alloys and Processing

Ingot metallurgy research involving small changes in alloy chemistry, different grain refining elements, and/or lower levels of Fe and Si, coupled with more effective homogenization heat-treatment has resulted in the development of alloys with improved strength, ductility, fracture

toughness and stress corrosion resistance (4-7). However, significant increases in fatigue resistance were not achieved.

Attention has also been directed to secondary property improvements via new thermal-mechanical ingot metallurgy processing procedures. Conventional processing of 7XXX alloys results in a highly elongated grain structure with a low fracture toughness in the short transverse direction. Intermediate thermomechanical treatments (ITMT) involving specialized ingot processing techniques prior to the final working operation, result in a relatively high degree of strain hardening and promote recrystallization to a fine equiaxed grain structure (5,6,8,9). ITMT of 7075 has resulted in improved elongation, toughness and short transverse stress corrosion resistance. 7050 showed improved resistance to fatigue crack initiation as a result of ITMT but there was an accompanying decrease in resistance to fatigue crack growth (6).

Final thermomechanical treatments (FTMT) are applied to the wrought material and involve artificial preaging prior to mechanical working and a second artificial aging treatment following mechanical working (6,8). This results in a stabilized dense network of dislocations (10). FTMT has led to significant increases in the strength of 7XXX alloys with no appreciable loss in ductility. It has not been conclusively established that FTMT is beneficial to fatigue response (8,10,11); marginal improvements in fatigue crack growth resistance and fracture toughness have been reported (6).

3. Powder Metallurgy Alloys and Processing

Over the past twenty years, several heat-treatable high-strength powder metallurgy (P/M) alloys have been developed. P/M processing

offers several distinct advantages over conventional ingot metallurgy (I/M) practice. High solidification rates are achieved in the powder process so that metallurgically, each powder particle exhibits an extremely fine cast microstructure with small secondary dendrite arm spacings. Alloying flexibility is gained since large amounts of alloying elements and dispersed phases can be added without macro-segregation. The powder particles are also characterized by low concentrations of insoluble constituents. After consolidation, powder processed materials exhibit a high degree of microstructural and chemical homogeneity coupled with a fine grain size (13). Near net shapes are possible via P/M processing with a high attendant materials utilization factor (12).

Since the original work of Roberts (14), Towner (15) and Haarr (16), many different alloy compositions of high-strength aluminum powders have been investigated (13, 17-29). Early work (13) showed that the Al-Zn-Mg-Cu system was the most promising for developing high strength at room temperature. It was also found that phases containing Co or Fe and Ni were more resistant to coarsening during fabrication than phases containing Cr, Ti, V, Zr, Mo and W. The cobalt introduces a fine dispersion of Co_2Al_9 , which acts as a strengthener and inhibits grain growth. Both these effects appear to give a better combination of strength and stress-corrosion resistance (13, 28, 29) than in the cobalt-free alloys. It has been found that improved combinations of strength and stress-corrosion resistance can be achieved in high strength aluminum alloy extrusions and forgings made via P/M processing than in those made by conventional I/M practice (29).

One of the most promising P/M alloys is CT91*. The major difference

*Formerly MA87 and recently designated X-7091 by Alcoa.

between CT91 and 7075 is that CT91 contains 0.4% Co while 7075 contains ~0.2% Cr. The chromium serves as a grain refiner in the ingot metallurgy alloy. Lyle and Cebulak (13) found that this alloy has a superior combination of strength and stress-corrosion cracking resistance compared to I/M 7075 and 7050 alloys. The fracture toughness of the P/M alloy was equal to that of 7075 but somewhat lower than that of 7050. The improvement in stress-corrosion resistance was attributed to a favorable grain morphology and to the presence of Co_2Al_9 particles; the latter are formed preferentially on grain boundaries and may serve to stop or delay SCC attack. Similarly, Otto (28) obtained a small strength increment, similar ductility but substantially higher toughness in CT91, compared to 7070.

In terms of fatigue behavior, Lyle et al. (17) and Cebulak et al. (19,21) have shown that in axial loading, the S-N response of smooth or notched specimens prepared from P/M extrusions of the 7000 series alloys met or exceeded that of the corresponding I/M material. Sanders and Otto (27) and Voss (25) have achieved significant increases in notched fatigue S-N response ($K_t = 3$; 10^7 cycles) for forged or extruded P/M alloys over 7XXX I/M material. Improvements in the S-N response in the P/M product were attributed to an increase in resistance to crack initiation resulting from the smaller maximum constituent particle sizes and a smaller grain size.

Voss (25) and Ramakrishnan (30) have reported stress-controlled fatigue data for extrusions and forgings prepared from compositions equivalent to the 2000 series of I/M processed alloys. For example, the P/M processing of the 2024 alloy produces a fine grain, recrystallization resistant extrusion

product (25). The notch S-N fatigue resistance ($K_t = 3; 10^7$ cycles) of the P/M 2024-T3510 material is 11% higher (at a 50% probability of failure) than the I/M counterpart for identical yield strength levels. Contributing microstructural features to the improvement are a lower level of coarse constituent particles, smaller maximum constituent particle sizes, and a smaller grain size.

Buchovecky and Rearick (20) have confirmed the beneficial effect of material flow during densification; endurance limits in rotating bend on P/M processed compositions equivalent to 2014 and 6061 were comparable to those of corresponding I/M material. Property advantages of the P/M material are attributed in part to the fine grain size and microstructure resulting from the rapid solidification of powder particles during formation by air atomization. No attempt was made to systematically relate the S-N fatigue behavior to processing conditions or microstructure (20).

Fatigue crack propagation response in high-strength P/M processed 7XXX aluminum alloys has been studied by Otto et al. (27, 28, 31, 32), Voss (25), Santner (33) and Holloway (34). In his first study Otto (28) varied composition and processing history and reported crack propagation rates in P/M forged material that were 15-1000% lower than those reported in the literature for the corresponding I/M condition - in air or saline environments. Subsequently Otto et al. (27, 32) reported that fatigue crack growth rates in P/M extrusions were slightly higher than those in I/M 7050-T76511 control material at ΔK levels $< 4 \text{ MPa} \sqrt{\text{m}}$. In the range $4-10 \text{ MPa} \sqrt{\text{m}}$, fatigue crack growth rates were similar in both the P/M extrusions and the I/M control material. It was found that overaging was beneficial to

fatigue crack growth resistance in the P/M extrusions. Scatter in crack propagation data for P/M material processed by hand forging prevented definite conclusions from being drawn. The study did show that compressive residual stresses can markedly affect fatigue crack growth rates by altering the effective ΔK level at the crack tip.

Similarly, Voss (25) has reported higher fatigue crack propagation rates in extruded P/M 7075-T6510 compared to the I/M counterpart at ΔK values $< 9 \text{ MPa} \sqrt{\text{m}}$. Crack morphology, slip reversibility, intermediate particle distribution and dislocation density are the primary microstructural related factors which control fatigue crack growth rates. Since grain size is common to three of the above factors, it is an effective metallurgical variable for the control of crack propagation rates.

Holloway (34) monitored the threshold stress intensity (ΔK_{TH}) in I/M 7175-T651 and P/M processed (triple upset and rolled) CT-91. While the data are limited, ΔK_{TH} appears to be lower in the P/M material. Corbly (35) studied crack growth retardation in CT-91 due to overloading. Plastic zone size was measured and crack propagation response analyzed in terms of an effective stress-intensity concept.

4. The Present Study

A relative dearth of quantitative processing-microstructure-fatigue relationships in powder-processed high-strength aluminum alloys prompted the present study. The overall goal of the program has been to develop a basic understanding of the interaction of alloy composition, processing history and environment on microstructure and fatigue response. In

particular, stress and strain-controlled fatigue and resistance to fatigue crack propagation have been examined in a high strength Al-Zn, Mg, Cu powder metallurgy alloy, with and without Co additions. The alloy is comparable in composition to I/M 7075 and 7475. Fatigue response was determined in air and in a salt fog environment.

PART I

FATIGUE OF HIGH-STRENGTH POWDER ALLOYS;
THE ROLE OF COBALT LEVEL AND PROCESSING MODE

SUMMARY

Load-controlled fatigue life ($S-N$) and crack growth rates (da/dN) have been determined in powder-processed aluminum alloys in air and salt fog. Attention was directed to the interplay of cobalt level (0 to 0.8%) and processing mode (single upset and forge (A) or triple upset and forge (ABC)) on microstructure and fatigue response. Comparisons were made with ingot metallurgy (I/M) 7075 and 7475.

In air, fatigue life was dependent on orientation, processing mode and cobalt level; largest fatigue life was achieved in the longitudinal orientation with 0.8% Co and ABC-processing. The fatigue life of the P/M material was superior to that of the I/M material; enhanced resistance to crack initiation in the former is attributed to a fine-scale microstructure. Fatigue crack growth rates were anisotropic. Superiority of the P/M over the I/M material was restricted to the longitudinal orientation at high ΔK levels. This is explained in terms of the relative sizes of microstructural features and the plastic zone size.

The fatigue life of both the P/M and I/M materials was severely reduced in salt fog and life was controlled by crack propagation rather than initiation. Fatigue crack growth rates of the P/M material were lower than in the I/M material at low ΔK in the longitudinal orientation but the

effect was reversed at high ΔK . The I/M exhibited superior crack growth resistance to the P/M material at all ΔK levels for the short transverse orientation. These differences are explained in terms of the relative sizes of the plastic zone, the microstructural features, and the propensity for secondary cracking and intergranular crack propagation in salt fog.

INTRODUCTION

Recent studies on aluminum alloys have shown that lateral flow during consolidation, aimed at eliminating porosity and the fragmentation of surface oxide on powder particles, promotes a beneficial effect on the fatigue properties of the P/M material. Property levels can equal or exceed those achieved by I/M practice (13,17-25,29,30).

A new and promising P/M alloy, CT-91* developed by Alcoa, is comparable in composition to 7075 and 7475 but contains Co in addition to Zn, Mg and Cu. Attention has been directed to the tensile, stress corrosion and fatigue response of this alloy. However, very little work has been reported on the relationships between processing, microstructure, environment and fatigue response. It has been the intent of the present study to develop fundamental processing-microstructure-property relations in powder-processed high-strength aluminum CT-91 and similar alloy compositions. Attention has been directed to the effect of cobalt level, processing mode, orientation and environment on stress-controlled fatigue and resistance to crack propagation.

* Formerly MA87 and more recently designated X-7091.

EXPERIMENTAL PROCEDURE

1. Materiala. Powder Alloys

The P/M alloys used in this study were provided by Alcoa. Alloy powder was air atomized to give an average particle diameter (APD) of $\approx 13\mu\text{m}$. The nominal composition of the three powders examined is given in Table I; actual melt analyses are given in Table II. Nominal I/M compositions for 7075 and 7475 are also included in Table I. The size distribution of the three alloy powders is shown in Table III. Coulter Counter size distribution measurements and APD Fisher Sub-Sieve analyses are shown in Table IV. Auger analysis (28) of the surface of the CT-91 powder, and the estimated particle surface oxide composition, are given in Tables V and VI.

b. Compaction, Forging and Heat Treatment

Powders were cold isostatically pressed into compacts approximately 187.5mm (7.375 in) diameter and 1092.2mm (43 in) long at $\sim 70\%$ theoretical density. The compacts were then machined and encapsulated in welded 3003 aluminum cans. The canned compacts were preheated to 521°C (970°F) under a vacuum of $35\mu\text{m Hg}$, sealed and hot compacted to $\geq 99.9\%$ theoretical density. The hot compacted billets were scalped to remove the can and cut into two 184.2mm (7.25 in) diameter x 304.8mm (12 in) long cylinders for further fabrication.

The cylinders were then open die forged to a 101.6mm (4 in) x 152.4mm (6 in) x 508mm (20 in) slab configuration, by two different modes of upsetting. These were designated A and ABC and are illustrated schematically in Figure 1. In the A mode, a single upset preceded the forging step; in

the ABC mode, the compact billet was given a triple upset in three mutually perpendicular directions prior to final forging. The orientation directions L (longitudinal), LT (long transverse) and ST (short transverse), are superimposed in Figure 1. For both forging operations, the temperature of the billets was 371°C (700°F) and the die temperature was 287°C (550°F). The material used in this investigation consisted of slices 50.8mm (2 in) thick removed from each forging.

Slices cut from the forgings were solution treated at a temperature of 488°C (910°F) for two hours and water quenched. The alloy was then triple-aged* to a strength level in the range 515 to 565 MPa, i.e., 4.32×10^5 s (five days) at room temperature 21°C (70°F) plus 8.644×10^4 s (twenty-four hours) at 121°C (250°F) plus 1.44×10^4 s (four hours) at 163°C (325°F). After heat treatment, the hardness of each ingot was determined.

2. Specimen Preparation and Material Testing

a. Tensile Testing

Longitudinal and long transverse tensile properties were determined for the six conditions shown in Table VII. The tensile specimens (ASTM E8) were machined to a smooth finish and polished with 600 grit abrasive paper. Specimen orientations are illustrated in Figure 2.

Testing was done in a standard Instron machine at a cross-head speed of 0.5mm/min (0.02 in/min). A strain gage extensometer was used and load-deformation curves were obtained directly from the machine. Yield strength (YS 0.2% off-set), ultimate tensile strength (UTS) and percent elongation

*T6 temper + overage

(with a 12.7mm (0.5 in) gage) were determined. The reduction in area (% RA) was measured with a toolmaker's microscope.

b. Axial Fatigue Testing

Hourglass-shaped fatigue specimens (Figure 3) were machined from the A and ABC processed material in each of the three orientations L, LT and ST and for the three cobalt levels. The reduced section on each specimen was polished on a lathe with successively finer grades of abrasive paper up to 600 grit, followed by a final polish with Linde B (Al_2O_3). The mechanically polished specimens were then electropolished (in a solution containing 7 parts by volume of glacial acetic acid and 2 parts perchloric acid) to remove all scratches. The minimum diameter of each specimen was determined by means of a toolmaker's microscope.

Tension-tension axial fatigue tests in air and in salt fog (3.5% NaCl solution) were made on a Satec Universal Fatigue Testing machine, model SF-1-4 (Sontag). In order to insure that no stress relaxation due to deformation of the specimen occurred during fatigue testing, the machine was equipped with an automatic device for maintaining constant preload. The maximum stresses for fatigue testing were 448, 379 and 310 MPa (65, 55 and 45 ksi) at a fatigue ratio R of +0.1 ($R = \sigma_{\min}/\sigma_{\max}$), and a load frequency of 30 Hz. The same conditions were used for testing in air and in salt fog. Three to five specimens were tested at each stress level and S-N curves were plotted for σ_{\max} vs N (cycles to failure). In this study, the fatigue strength (endurance limit) was not evaluated.

For fatigue testing in salt fog, a plexiglass fogging nozzle was used in conformity with ASTM B117. A rubber chamber was clamped over each grip

and the incoming air filtered to avoid contamination. The fog was emitted into the specimen chamber 3 to 5 seconds before application of the cyclic load, and was maintained throughout the fatigue test. Fracture surfaces were flushed with water, dried with an air blast and the specimen stored in a desiccator.

For purposes of comparison, identical stress-controlled axial fatigue tests were run on I/M 7075 and 7475 alloys in air and salt fog.

c. Fatigue Crack Growth Measurements

Compact type (CT) specimens were machined from the A and ABC processed material, in each of the three orientations L, LT and ST and at the three cobalt levels. Figure 4 shows the dimensions of the compact type (CT) specimen; these comply with ASTM E24 for measurement of constant load-amplitude fatigue crack growth rates above 10^{-8} m/cycle. The specimens were designated L, LT or ST in such a way that the crack grew normal to the designated orientation as shown in Figure 5. Specimens were hand polished with successively finer grades of abrasive paper (250, 325, 400 and 600 grit).

An MTS closed loop system with a load amplitude controller was used for the crack propagation studies. The load was applied as a sine wave at a frequency of 30 Hz (the same frequency as that used in axial fatigue testing) and with a fatigue ratio R of +0.1. Two traveling microscopes mounted on micrometer traveling stages were used for monitoring crack growth. An accuracy of 0.03mm (0.001 in) in measurement of the position of the crack tip was achieved with the reticle eye piece and micrometer traveling stages.

FCG (da/dN) vs ΔK curves were obtained by means of the finite difference

method. The stress intensity range, ΔK , was determined with the aid of the polynomial expression:

$$\Delta K = \frac{\Delta P}{B\sqrt{W}} \frac{(2 + \alpha)}{(1 - \alpha)^{3/2}} (0.886 + 4.64\alpha - 13.32\alpha^2 + 14.72\alpha^3 - 5.60\alpha^4) \quad (1)$$

where

$$\alpha = a/W$$

W = specimen width

B = specimen thickness

a = crack length

ΔP = load range

The crack length used to calculate ΔK was the mean crack length a_m , where:

$$a_m = \left(a_{\text{initial}} + \frac{1}{2} \Delta a_{\text{growth}} \right) = \frac{1}{2} (a_{\text{final}} + a_{\text{initial}}) \quad (2)$$

The crack was initiated by overloading (i.e. by using a value of ΔK greater than $\sim 8.8 \text{ MN m}^{-3/2}$ [8 ksi $\sqrt{\text{in}}$]), and then decreasing ΔK in increments no larger than 10% of the previous maximum load. Transient effects were avoided after ΔK was decreased by propagating the crack an increment greater than three times the monotonic plastic zone size as given by the expression (25):

$$\Delta a > \frac{3}{\pi} \left(\frac{K_{\max}}{0.2\% \text{ YS}} \right)^2 \quad (3)$$

where

Δa = required incremental crack length

K_{\max} = the maximum value of the stress intensity factor based on the previous maximum load.

YS = yield strength

After the required precrack length was obtained, testing was initiated. The cycle increment was adjusted so that the incremental crack growth Δa was not greater than 0.71mm (0.028 in), as required by ASTM E24 for the geometry of the specimen. This was carried out until the crack length reached a value of $a = 21.3\text{mm}$ (0.84 in). Subsequently, Δa increments were limited to 0.355mm (0.014 in).

The same procedure was followed for the crack growth rate tests in the salt fog environment (3.5% NaCl in distilled water). A plexiglas chamber was used for the salt fog environment test. Specimens were precracked in air and the actual test then conducted in the salt fog environment. The fogging nozzle was similar to the one used for the axial fatigue tests.

Fatigue crack propagation tests were performed on specimens in the A and ABC processed condition and in the three orientations (L, LT and ST) and for the three levels of Co (0.0, 0.4 and 0.8% Co). Duplicate tests were run to assure reproducibility. In addition, and for purposes of comparison, FCG tests were run on I/M 7475 alloy in the T6510* condition in air and salt fog. Specimen size, geometry and test conditions were identical to those used for the P/M material.

3. Structural Evaluation

a. Optical Metallography

Powder was mounted in Bakelite, hand polished through 600 grit abrasive paper, followed by a final polishing using a suspension of cerium oxide in distilled water; Keller's etch was used as an etchant.

* T6 plus 1 1/2% stretch for stress relief; material supplied by Alcoa.

Sections of the as-upset and forged material were prepared perpendicular to each of the directions L, LT and ST for optical metallography. The sections were mounted in Bakelite and hand polished on successively finer grades of abrasive paper down to 600 grit. Specimens were then lapped with lum diamond paste and given a final polish with a suspension of cerium oxide in distilled water. Keller's etch and 50% HNO₃ in distilled water were used to delineate grains and subgrains, respectively.

After fatigue testing, sections were prepared perpendicular to the fracture surface of tension-tension specimens (parallel to the specimen axis), for optical metallography. The gage section was mounted in Bakelite reinforced with alumina and polished the same was as described previously. Crack paths were observed as a function of processing mode, chemistry, orientation and environment. Fatigue fracture surfaces were also examined directly at low magnification in the optical microscope.

b. SEM (Scanning Electron Microscopy)

Powders were characterized by SEM at different magnifications. The effects of processing mode, level of cobalt, orientation and environment (air or salt fog) were studied with respect to the fracture surface morphologies of the forged tension-tension axial fatigue specimens. SEM studies were also performed on the fatigue fracture surface of the forged CT specimens. The effects of ΔK , processing mode, composition, orientation and environment were included in this study.

Specimens tested in salt-fog were cleaned ultrasonically for one to two minutes in a solution of 35 ml of 85% phosphoric acid, 20 gr of chromic acid (chromium trioxide) in one liter of distilled water. This treatment

was necessary to remove the corrosion products (i.e., "mud-cracks") that were present on the fracture surfaces.

c. TEM (Transmission Electron Microscopy)

Thin film transmission electron microscopy studies were carried out on the P/M material in the A and ABC processed mode, and 0, 0.4 and 0.8% Co levels in both the L orientation and the ST orientation. Electron transparent foils were prepared by standard jet polishing in a Fischione unit using a 20% HNO_3 - 80% methanol solution at -40°C .

RESULTS AND OBSERVATIONS

1. Structure of Powders

The powders are irregular in shape with rough surfaces, Figure 6. Optical metallography confirms the presence of gross porosity inside some of the particles. From the secondary dendrite arm spacings ($\sim 0.05\mu\text{m}$) the particle cooling rates are estimated to be $\sim 10^5$ - 10^6°C/s (36). Formation of Al_2O_3 on the particle surface counteracts the effect of surface tension and leads to an irregular particle shape.

2. Structure of Compacts and forgings

Optical micrographs of the grain structure of a hot compacted billet before and after heat treatment are shown in Figure 7. Before heat treatment the original individual powder particles can be seen forming an equiaxed grain structure. The dark constituents at the grain boundaries are oxides, and partially soluble "S" phase particles (Al_2CuMg) (37); it is also possible that small amounts of insoluble phases of Fe and Si (e.g. $\text{Al}_7\text{Cu}_2\text{Fe}$ and Mg_2Si) are present. The fine precipitates (0.002 to $0.01\mu\text{m}$ in diameter) within the grains are mainly $\eta(\text{MgZn}_2)$ together with

dispersoids of Co_2Al_9 , internal oxides and porosity (37).

Grain morphology after hot compaction and heat treatment (Figure 7b) is similar to that observed before heat treatment. In both conditions, there is no evidence of grain deformation or elongation as a result of axial compression during hot compaction. The second phases along the grain boundaries are probably oxides and the equilibrium phase η ($\text{Mg}(\text{Zn}_2\text{Al}_2\text{Cu})$) resulting from the heat treatment. Subgrain boundaries are also observed within the grains.

Optical micrographs illustrating the grain and subgrain structure after hot compaction, upsetting and forging of CT-91 are given in Figures 8 and 9, respectively. No systematic differences were detected in grain size and morphology as a result of differences in cobalt level and/or processing mode. In general the grains are equiaxed in the L-LT plane. Anisotropy of the grain structure is evident with grain elongation parallel to the forging (draw) direction L as expected. Grain size is extremely inhomogeneous, varying from ~ 2 to $\sim 20\mu\text{m}$. Occasionally original powder particles ($\sim 13\mu\text{m}$ diameter) can be seen within the grain structure. Second phases are present at the grain boundaries. These are similar to those described in the hot-compacted material, Figure 7b. The degree of recrystallization diminishes with increasing levels of cobalt; this effect is more obvious for the case of A processing than for ABC processing.

Figures 10a and 10b show three dimensional photomicrographs of I/M 7075 and 7475 rolled plate which has been solution treated and aged. The grain size of the I/M material is much larger than the grain size in the P/M material. The massive black phases shown in Figure 10a are probably

$\text{Al}_7\text{Cu}_2\text{Fe}$ and Mg_2Si , since the Fe and Si content of the 7075 alloy is relatively high. When compared to 7475 alloy which has a much lower level of Fe and Si, the amount of these phases is much smaller. These phases are essentially absent in the powder forged material, because of the lower content of Fe and Si.

Representative micrographs (TEM) of the ST-LT and L-ST planes in each of the six conditions are shown in Figures 11 through 14. There are no major differences in dispersoid size or distribution between the ST-LT planes and L-ST planes. For a given processing mode the subgrain size decreases with increasing cobalt content; this is clearly seen at lower magnifications. The Co_2Al_9 dispersoids are essentially spherical having a random distribution within the grains and a wide size range (0.05-0.5 μm). These particles do not appear to be deformed or fractured by the upset forging process.

The oxides and η' precipitates are distributed primarily at grain and subgrain boundaries. Comparing the A and ABC processing modes, it is seen that the oxide particle distribution throughout the subgrain structure is more uniform for the ABC processing than for A processing. Thus, the amount of oxides at subgrain and grain boundaries is smaller for the ABC process than the A process; this facilitates precipitation of η' at grain boundaries in the ABC processed material.

Due to the higher density of η' precipitates at the grain boundaries after ABC processing, growth of the η' precipitates is restricted. In the case of A processing, the η' precipitates at the boundaries are more widely spaced; in consequence the η' precipitate transforms more readily to the equilibrium η phase on aging (38). With the exception of these

differences, ABC processing does not introduce any dramatic structural modifications compared to A processing.

3. Tensile Properties

Tensile tests were conducted in the six conditions listed in Table VII, in both the L and LT orientations. Average tensile properties, together with average hardness readings, are given in Table VIII. Yield strength (YS 0.2% offset) and ultimate strength (UTS) are plotted as a function of cobalt content in Figures 15 and 16. The alloy exhibited a good combination of high strength and reasonable ductility. There does not appear to be any clear correlation between ductility (represented by % E and RA %) and strength.

In general, YS and UTS increase from the Co-free condition to the 0.4% Co level and then decrease at 0.8% Co. For A processing, strength in the longitudinal direction is higher than in the long transverse direction. For ABC processing, strength in the longitudinal direction is lower or equal to that in the long transverse direction with the exception of the 0.4% Co level in which case the longitudinal direction has a higher strength than in the long transverse direction.

4. Tension-Tension Axial Fatigue

a. Response to Cyclic Loading in Air

Load-controlled axial fatigue data for the eighteen variables studied are summarized in Table IX. Fatigue life is plotted as a function of maximum stress in Figures 17, 18 and 19. The S-N curves are arranged in pairs in order to compare the effect of processing mode for each of the three levels of cobalt. The effect of specimen orientation can also be seen in these figures. Similarly, the data were plotted in S-N form to

assess the effects of cobalt level and processing mode at a fixed orientation, and to assess the effects of processing mode and specimen orientation at a fixed cobalt level.

Anisotropy in fatigue response is observed in each of the six combinations of cobalt level and processing mode. For a given cobalt level and processing mode, fatigue life increases in the order LT to ST to L. For A processing, the degree of anisotropy between the L, LT and ST orientations is independent of cobalt level (Figures 17, 18, 19). For ABC processing, the degree of anisotropy increases with increasing cobalt content.

In the cobalt-free alloy there is little effect of processing mode on S-N behavior (Figures 17a and 17b). At the higher cobalt levels (0.4% and 0.8% Co), the processing mode does affect fatigue response; ABC processing gives superior S-N performance compared to A processing. The best S-N response in air is achieved with a combination of cobalt additions and ABC processing. The ABC processed alloy containing 0.8% Co gives the best S-N response in each orientation; this combination of cobalt content and processing mode also maximizes anisotropy. It is important to note that in the P/M forgings, the increase in performance in the longitudinal orientation is not achieved at the expense of a decrease in transverse properties such as normally occurs in I/M materials.

Small shifts between the S-N curves were obtained by normalizing the fatigue data in terms of tensile strength (i.e., σ_{max}/UTS). However, the generalizations, trends and differences outlined above still hold.

b. Response to Cyclic Loading in Salt Fog

Load-controlled axial fatigue data for the twelve variables studied are

summarized in Table X. Fatigue life is plotted as a function of maximum stress in Figures 20, 21 and 22. For a given cobalt level in the L orientation, processing mode has no significant effect on S-N response in salt fog, and no systematic trends can be identified (Figure 23). Fatigue life is essentially independent of cobalt level in the L orientation (Figure 23). This figure also includes the corresponding data for fatigue in air. It is seen that fatigue life is reduced significantly in the salt fog environment, compared to air.

Similarly, in the LT orientation, fatigue life is reduced in salt fog relative to air but the difference is smaller than for the L orientation. This is due primarily to the lower fatigue life of the material in air in the LT orientation as compared to the L orientation.

c. Fatigue Fracture Behavior in Air

In characterizing and comparing the fracture surfaces of the load controlled tension-tension fatigue specimens, it was convenient to define a high and low regime of fatigue stress. The high regime ($\sigma_{max} = 448$ MPa (65 ksi)) was associated with fatigue lives $\sim 6 \times 10^3$ to 3×10^4 cycles and the low regime ($\sigma_{max} = 379$ MPa (55 ksi)) with a range $\sim 3 \times 10^4$ to 3×10^6 cycles.

Low magnification optical metallography of fatigue fracture surfaces in each of the eighteen material conditions* permits a differentiation in fatigue response between the low and high stress levels. Irrespective of cobalt level, processing mode and orientation, the high stress fatigue fractures are characterized by multiple crack initiation sites; an example is given in Figure 24. Ratchet marks are also frequently visible at the

* Two processing modes, three orientations, and three levels of cobalt.

edges of the fracture surfaces following fatigue at the high stress level. The fatigue fracture mode accounts for between 14% and 39% of the total fracture surface area; the fraction of total cross-section consumed by fatigue increases as tensile strength increases, independent of cobalt level, orientation and cyclic stress level. There is no clear correlation between the fraction of total fatigue fracture cross-section and processing mode or specimen orientation.

The overall orientation and profile of the fracture surfaces, relative to the stress axis, is influenced by the specimen orientation. For each processing mode, orientation, and independent of cobalt level, the fatigue crack component propagates normal to the stress axis. In the L orientation, the overload fracture surfaces are at an angle to the stress axis, Figure 25. For the majority of the specimens fatigued in the LT or ST orientations, the overload fracture surfaces are normal to the stress axis, Figure 24.

In the L orientation, the fracture mode is transgranular, independent of processing mode and cobalt level, Figure 25. In the LT orientation and for both A and ABC processing modes, increasing the cobalt level changes the fatigue fracture mode from transgranular to intergranular, or at least to a mixed mode. In the ST orientation, grain structures at fatigue fracture surfaces reflect a predominantly intergranular mode of failure, Figure 26. For each of the three orientations, no effect of processing mode on fracture path could be established.

SEM studies of fracture surfaces were performed in the fatigue crack initiation and fatigue crack propagation regions. These are delineated as stages I and II in Figure 25. All specimens exhibited a similar

appearance in the stage I region. Differences in processing mode, cobalt content and orientation did not change fracture morphology; representative SEM fractographs of stage I are shown in Figure 27.

d. Fatigue Fracture Behavior in Salt Fog

All specimens tested in salt fog exhibited multiple initiation sites, and the SEM studies revealed that at each of the multiple initiation points there was evidence of corrosion products. Figure 30 shows the initiation site and stage I region of two representative specimens. Pitting can be observed on the outer surface of the specimen in Figure 30b. Such surface attack is absent in specimens fatigued in air.

Examples of SEM fractographs in stage II for specimens tested in salt fog are shown in Figure 31. Intergranular fracture appears to be the primary mode of fatigue fracture. The different material conditions do not appear to influence the fracture mode of these specimens tested in salt fog.

In salt fog the striations exhibit a jagged appearance whereas in air, ductile-type striations predominate, cf. Figures 28, 29 and 31. Fewer striations occur in fatigue in salt fog than in air. It is also evident that a greater number of secondary cracks are present after fatigue in salt fog than in air. Examples of these secondary cracks are seen in Figure 31.

Representative SEM fractographs in the stage II region of specimens fatigued in air are shown in Figures 28 and 29. The fractographs are from the central region of fracture. In the L orientation, the fracture mode is transgranular, independent of processing mode and cobalt level. Increasing the level of cobalt changes the fracture mode from transgranular to a mixed mode in the LT orientation. The mode of fracture is

primarily intergranular in the ST orientation, Figure 29. This is true for both the A and ABC processing modes and at each level of cobalt.

SEM of fracture surfaces following fatigue in air shows that irrespective of cobalt level or processing mode, there are ridges oriented in the general direction of crack propagation. Flat featureless plateaus characterize the regions between the ridges. Ductile striations, characteristic of stage II fatigue are visible in all the specimens fatigued in air. Differences in striation spacing and orientation relative to the direction of overall crack propagation are the result of local changes in the direction of crack propagation.

5. Fatigue Crack Propagation

a. Response in Air

Fatigue crack propagation rates (da/dN) were determined in air as a function of the stress intensity range (ΔK) for each of the eighteen material conditions. Excellent reproducibility was obtained with duplicate specimens.

The effect of orientation on FCG rates as a function of ΔK in air for a fixed cobalt level (0.4%) and processing mode (A or ABC) is illustrated in Figures 32 and 33. Corresponding data for the two other cobalt levels showed similar trends with respect to the effect of orientation and processing mode on FCG rates. In all eighteen conditions, data fit the Paris-Erdogan relation (39,40) over the range $\Delta K \sim 9 \text{ MN m}^{-3/2}$ (8.2 ksi $\sqrt{\text{in}}$) to $\sim 20 \text{ MN m}^{-3/2}$ (18.2 ksi $\sqrt{\text{in}}$), i.e.:

$$da/dN = A\Delta K^m \quad (4)$$

where

da/dN = FCG rate

ΔK = stress intensity factor range ($\Delta K = K_{\max} - K_{\min}$)

A and m = function of stress-ratio, frequency, temperature, environment and materials variables.

Values of A and m in air, in the eighteen conditions are given in Table XI.

FCG rates as a function of cobalt content and processing mode, but with a fixed (L) orientation are given in Figures 34 and 35. Corresponding relationships in the ST orientation are presented in Figures 36 and 37. In the LT orientation, FCG response is similar to that in the ST orientation.

A comparison of P/M and I/M 7475 FCG rates in air as a function of cobalt level and processing mode, for each of the three orientations, is given in Figures 38-40. In the L orientation, the lowest FCG rates in the P/M material are achieved with a combination of ABC processing and 0.8% Co. The I/M 7475 material exhibits lower FCP rates up to ΔK of $\sim 13.2 \text{ MN m}^{-3/2}$ (12 ksi $\sqrt{\text{in}}$), Figure 38. For the other orientations (LT and ST), in the P/M material the highest resistance to crack propagation is achieved with a combination of 0.8% Co and A processing. In the LT orientation this is true only up to intermediate levels of ΔK ($\sim 13.2 \text{ MN m}^{-3/2}$ (12 ksi $\sqrt{\text{in}}$)). At higher ΔK levels the ABC processing mode and 0.8% Co again exhibit the best crack propagation resistance. For the corresponding LT and ST orientations in the I/M 7475 material, FCG rates are significantly lower than in the P/M material at all levels of ΔK , Figures 39 and 40.

In the P/M material, for all the conditions tested, the ST orientation exhibited the highest crack propagation rate at all levels of ΔK . At low

ΔK , the LT orientation offers the lowest FCG rates whereas at high ΔK , it is the L orientation that provides the lowest FCG rates. The ΔK level at which the change occurs in the L orientation is between $\Delta K \approx 11 \text{ MN m}^{-3/2}$ (10 ksi $\sqrt{\text{in}}$) and $K \approx 14 \text{ MN m}^{-3/2}$ (12.7 ksi $\sqrt{\text{in}}$).

b. Response in Salt Fog

The effect of orientation on FCG rates as a function of ΔK in salt fog for a fixed cobalt level (0.8%) and processing mode (A or ABC) is illustrated in Figures 41 and 42. Similar trends were observed with respect to the effect of orientation and processing mode on FCG rates for the other two cobalt levels. As in air, excellent reproducibility existed with duplicate specimens.

FCG rates as a function of cobalt content and processing mode, but at a fixed orientation (L), are given in Figures 43 and 44. For a given processing mode and orientation, no systematic trend exists re the effect of cobalt content on FCG rates in salt fog. For a given cobalt content and processing mode, the highest FCG rates occur in the short-transverse orientation. In general, the L orientation material has better resistance to FCG at high and intermediate ΔK levels ($\geq 11 \text{ MN m}^{-3/2}$ (10 ksi $\sqrt{\text{in}}$)) than does the LT orientation material. A complete set of da/dN vs. ΔK plots for all the material conditions examined is contained in reference (41).

A comparison with the da/dN vs. ΔK plots in air shows that in all the eighteen material conditions examined, FCG rates are higher in salt fog than in air when compared at a fixed level of ΔK . Values of A and m from the Paris-Erdogan equation are given in Table XI; the constants were obtained by fitting the best straight line through the data points by linear regression analysis.

A comparison of P/M and I/M 7475 FCG rates in salt fog as a function of cobalt level and processing mode, for each of the three orientations, is given in Figures 45-47. At ΔK levels $< 13.2 \text{ MN m}^{-3/2}$ (12 ksi $\sqrt{\text{in}}$) the P/M material has a better resistance to crack propagation than the I/M 7475 in the L orientation, Figure 45. A similar situation exists in the LT orientation, but, depending on the P/M condition (processing mode and cobalt content), the cross-over point varies over a range from $\sim 11 \text{ MN m}^{-3/2}$ (10 ksi $\sqrt{\text{in}}$) to $16.5 \text{ MN m}^{-3/2}$ (15 ksi $\sqrt{\text{in}}$), Figure 46. For the ST orientation the 7475 I/M material has superior crack propagation resistance over the entire range of ΔK studied, Figure 47.

Values of A and m, from the Paris-Erdogan relation, are compared in the P/M and I/M materials for FCG rates in air and salt fog in Table XI.

c. Fracture Morphology - Crack Propagation in Air

Macroscopically, for each processing mode, and independent of cobalt level, the fatigue crack propagates normal to the stress axis. However, in the L orientation, when the stress intensity range ΔK increases to a value of $\sim 11 \text{ MN m}^{-3/2}$ (10 ksi $\sqrt{\text{in}}$) the direction of crack propagation changes to one that is parallel to the stress axis.

Independent of orientation and processing mode, at low ΔK cleavage-like facets are common whereas at intermediate ΔK levels, fatigue striations predominate. Microvoid coalescence occurs at high ΔK levels. Examples of these features are seen in Figures 48, 49 and 50. In the L orientation, the fatigue striations are also seen at high ΔK , Figure 50. The width of the striation increases with increasing ΔK . For all the conditions examined, the material in the L orientation exhibited the highest density of secondary cracks at high ΔK . These secondary cracks

are evident on the primary fracture surface in Figure 50.

d. Fracture Morphology - Crack Propagation in Salt Fog

The CT specimens tested in salt fog show similar macroscopic features to those of specimens fatigued in air. The main fatigue crack propagates normal to the stress axis for all cobalt levels and processing modes. However, in the L orientation, the crack changes direction at high ΔK levels to become parallel to the stress axis. Corrosion products ("mud cracks") were removed from the fracture surface prior to SEM examination.

Other things being equal, fracture morphologies are independent of processing mode. At low ΔK levels, cleavage is the predominant feature for all material conditions evaluated. Microvoid coalescence is a characteristic feature on fracture surfaces at high ΔK levels and in the L orientation, a high density of secondary cracks is visible. In the ST orientation, brittle striations were found for both processing modes in the cobalt-free alloy; the incidence of fatigue striations decreased with increasing cobalt level. Representative micrographs illustrating these features are shown in Figures 51 and 52.

DISCUSSION

1. Aging Response

The aging response of the CT-91 P/M alloy and the cobalt-free version have been studied via differential scanning calorimetry (DSC) and TEM by Skinner et al. (38). A comparison of the DSC curves of two P/M alloys (0% Co and 0.4% Co), both in the ABC-processed condition, showed that during aging, cobalt increases the amount of precipitation of GP zones. This effect is similar to that of chromium in commercial 7475

and 7075 I/M alloys. With artificial aging, the GP zones grow and transform to the semi-coherent n' precipitate; the final result is a mixture of fine precipitates of GP zones and n' with some n' precipitating on grain boundaries. In the fully heat treated material the hardening precipitates in the P/M alloys considered in this investigation, consist of a mixture of approximately 10% GP zones and 90% n' phase (38).

In the present investigation a detailed and quantitative assessment of the various microstructural features was made. These included grain and subgrain sizes, % recrystallization, the volume fraction, average diameter and mean free path of dispersoids, and the grain boundary area per unit volume. Data were obtained with the aid of the various quantitative metallographic techniques discussed by Underwood and Starke (42) and are summarized in Table XII.

Although cobalt content did not have any appreciable effect on grain size for a given processing mode, the degree of recrystallization and subgrain size were modified, as shown in Table XII. With increasing cobalt content, the volume fraction of the Co_2Al_9 increases. These dispersoids act as barriers to subgrain growth and assist in suppressing recrystallization.

2. Tensile Properties

In the longitudinal orientation yield and tensile strength are higher in the P/M forgings than in the I/M 7475 and 7075 rolled plate, Table VIII. These results agree with previously published studies in which the yield strength and UTS of 7XXX I/M alloys in the T6 condition were measured and compared with the tensile properties of P/M forgings (17,19,21,25,29).

The grain size of the P/M material is smaller than that of the I/M material by a factor $\sqrt[4]{4}$, Table XII. However, for the range of grain sizes studied, yield strength (Table VIII) shows only a small dependence on grain size. A similar response has been reported in the 7XXX series alloys (43) and has been attributed to the reduced slip distances that the combined effects of dispersoids and η' precipitates produce within each grain. As the grain size approaches the magnitude of the dispersoid spacing, a more significant role of the grain boundaries on strength can be expected.

The superior tensile fracture properties (UTS) of the P/M alloy forgings in comparison to the commercial I/M material can be attributed to the smaller grain size and the lower amount of constituent second phase particles in the P/M material. A smaller grain size has the effect of reducing the slip length and homogenizing the deformation. This reduces stress concentrations at grain boundaries and delays crack nucleation and together with the relative absence of constituent particles in the P/M alloys, results in a higher UTS as shown in Table VIII.

The 0.4% Co P/M alloy (CT-91) contains a larger amount of hardening precipitates (GP zones and η'), compared to the cobalt-free P/M alloy (38). In addition, CT-91 has a smaller grain size and has undergone less recrystallization than the cobalt-free P/M alloy. In combination, these microstructural differences account for the higher UTS of CT-91. The difference is seen in Table VIII and Figures 15 and 16. In contrast, increasing the cobalt level of the P/M alloy from 0.4% to 0.8% results in a decrease in UTS. The increase in the volume fraction and decrease of

spacing of Co_2Al_9 dispersoids at the higher cobalt level, should reflect in a further increase in tensile strength. However, these dispersoids reduce the energy necessary to propagate monotonically loaded cracks. The latter are initiated by microvoids at matrix-dispersoid interfaces and coalesce into void sheets (32).

3. Fatigue Properties

a. Axial Fatigue in Air

Specimens tested in the longitudinal orientation, in which the crack propagates in the LT-ST plane (Figure 2), exhibit a higher fatigue resistance compared to the LT and ST orientations. This pattern is observed at each cobalt level and for each processing mode and is expected due to the anisotropy present in the microstructure. The smaller cross-sections of the elongated grains in the LT-ST plane (L orientation), give rise to a higher resistance to fatigue crack initiation than the grains in the L-LT and L-ST planes. A smaller grain dimension reduces the slip length and therefore the stress concentration at grain boundaries, and delays crack nucleation by homogenizing slip, i.e. distributing slip more uniformly in the material.

The superior performance of the 0.8% Co P/M forgings compared to the 0.4% Co and the cobalt-free forgings, for the same processing mode and in the same orientation, is the result of a combination of microstructural features. These are a small subgrain size, a small amount of recrystallized material and a large volume fraction of non-shearable Co_2Al_9 dispersoids. These features promote a homogeneous mode of deformation by reducing the influence of slip concentrations. In consequence the resistance of the material to crack nucleation increases.

Consideration is now given to the effect of processing mode on microstructure. The single upset and forged material (A processing) contains precipitate free zones (PFZ) of longer length along the grain and subgrain boundaries than the triple upset and forged material (ABC processing). This difference increases with increasing levels of cobalt. The PFZ are weaker than the matrix and can therefore act as sites for preferential deformation during cyclic loading. The deleterious effect of the PFZ is diminished at small grain or subgrain sizes. At each cobalt level, and in particular in the 0.8% Co alloy, ABC processing gives superior S-N performance compared to the A processed material.

The axial fatigue properties of the P/M material were compared with those of I/M 7075-T6 and 7475-T6 rolled plate. Data for the I/M material were obtained by Buzolits and Lawley (44) using identical test procedures, specimen size/geometry as in the present study. Overall superiority in fatigue response of the P/M material in both the longitudinal and transverse orientations compared to I/M 7475-T6 and 7075-T6 is shown in Figure 53. From a comparison of the microstructures of the I/M 7475, 7075 and P/M materials, it is concluded that improved fatigue performance is the result of a higher resistance to crack initiation. This is attributed to a smaller grain size and the relative absence of brittle constituent particles ($\text{Al}_7\text{Cu}_2\text{Fe}$ and Mg_2Si) in the matrix. These constituent particles in the I/M material fracture easily and separate from the matrix, creating preferential crack paths. The absence of constituent particles in the P/M material is a result of the high solidification rate that exists during atomization; this suppresses constituent particle formation. In contrast, the relatively slow solidification rates characteristic of

ingot casting promote formation of the constituent particles.

b. Fatigue Crack Propagation in Air

The influence that microstructural features exert on FCG rate depends on the relative size of these features and the size of the plastic zone developed at the crack tip during cyclic loading. When the plastic zone size is significantly smaller than any microstructural features, the material will behave as a continuum and the relationships of linear elastic fracture mechanics will apply. Under conditions in which the plastic zone is significantly larger than the microstructural features, the effect of microstructure on FCG rate will be maximized.

The size of the plastic zone developed at the crack tip during fatigue crack propagation, and which experiences alternating tensile and compressive yielding, may be estimated by means of the Paris and Erdogan (40) equation:

$$d_{pz} = \frac{1}{8\pi} \left(\frac{\Delta K}{\sigma_{YS}} \right)^2 \quad (5)$$

where

d_{pz} = plastic zone diameter

Calculated values of d_{pz} , using equation (5), are summarized in Table XIII. At all levels of ΔK , the plastic zone size in the P/M material is significantly larger than the recrystallized grain size or the sub-grain size in unrecrystallized material. Thus, fatigue response will be affected by the several microstructural features in the P/M forgings. In particular, slip reversibility will be limited with an associated increase in FCG rates.

Anisotropy in fatigue crack response was observed in all the P/M alloys. Specimens tested in the ST orientation (Figure 5) gave higher FCG rates than in the L and LT orientations at all ΔK levels. This behavior can be explained by localized plastic flow in the soft precipitate-free zones (PFZ) in the ST orientation. The PFZ provide preferential crack paths in the L-LT plane. If the stress axis is parallel or perpendicular to the long grain dimension, there will be no shear stress parallel to the grain boundary. Consequently, deformation within the PFZ will be restricted.

The grain and subgrain dimensions in the LT-ST and L-ST planes are similar, Table XII. However, the dispersoid spacing for the 0.4% and 0.8% Co alloys is not distributed uniformly. On the principal crack plane ST-LT the particle spacing is smaller than on the principal crack plane L-ST. The distribution of oxides follows a similar pattern and is a consequence of the final forging operation which aligns oxides and dispersoid particles of Co_2Al_9 . This is similar to the phenomenon of mechanical fibering in I/M materials but to a much smaller degree. A smaller dispersoid spacing will lead to a more homogeneous distribution of strain which will reduce the extent of slip reversibility and increase the FCG rate.

When a crack intersects a weak interface it will show a strong tendency to propagate along the interface. The amount that this secondary crack grows will depend on the stress distribution in the vicinity of the crack tip. The weak PFZ surrounding the elongated grains normal to the main crack path of the specimens tested in the L orientation will tend to nucleate secondary cracks. In turn, secondary cracks will consume part

of the energy normally available for propagation of the principal crack, effectively lowering ΔK at the crack tip. Hence, FCG rate is lowered.

At high ΔK levels, FCG rates in the L orientation are lower than in the LT orientation. This is attributed to the presence of a high density of secondary cracks in the L orientation material at high ΔK . These cracks consume energy and therefore lower the propagation rate of the principal crack. It was observed that the highest density of secondary cracks occurred in the 0.8% Co alloy processed in the ABC mode. This represented the optimum microstructural condition for resistance to crack propagation.

Comparing FCG rates in the I/M and P/M material in the LT and ST orientations, it is seen that at all levels of ΔK , FCG rates are lower in the I/M material, Figures 39 and 40. In the L orientation, FCG rates in the I/M are lower than in the P/M material at low ΔK , Figure 38. For the I/M LT and ST orientations the plastic zone size is smaller than the grain size at all levels of ΔK . Thus, there is a high degree of slip reversibility and FCG rates are lower than in the P/M material. In the latter, plastic zone size is larger than the grain size so that grain boundaries restrict slip reversibility and increase FCG rates.

In the L orientation, the cross-over of the FCG rates in I/M and P/M materials occurs at $\sim 12 \text{ MN m}^{-3/2}$, Figure 38. This corresponds to the condition where the grain size in the I/M material is slightly smaller than the plastic zone size. At higher ΔK values, the grain boundaries limit slip reversibility. This effect, together with the high density of secondary cracks in the P/M material at high ΔK results in a lower FCG rate in the P/M material.

c. Axial Fatigue in Salt Fog

The fatigue life of the P/M materials tested in salt fog under load controlled conditions suffered serious degradation with respect to the response in air. Low magnification examination of the external surfaces of the axial fatigue specimens after testing in salt fog, revealed a high density of corrosion pits produced by the aggressive environment. Fracture surface observations revealed that for all the specimens tested in salt fog, the common pattern was the presence of multiple crack initiation sites. SEM observations at these initiation sites showed the presence of corrosion products. Due to a high stress concentration developed at the corrosion pits, the fatigue process changes from one governed by resistance to crack initiation to one governed by resistance to crack propagation.

Grain boundary attack by the aggressive environment is manifest in the SEM fractographs in stage II. The primary mode of failure appears to be by intergranular secondary cracking, independent of cobalt level, processing mode or orientation.

Anisotropy in the S-N response is maintained and is similar to that observed in laboratory air. No effect of processing mode or cobalt level was observed in S-N response for tests performed in salt fog.

A comparison of S-N response of the P/M and I/M 7475 and 7075 in salt fog is given in Figure 54 for the L and ST orientations. In the L orientation the P/M material and the I/M material exhibit a similar S-N response. In the ST orientation, a small advantage in fatigue life exists in the P/M material at higher stress levels.

d. Fatigue Crack Propagation in Salt Fog

FCG rates increase significantly in salt fog compared to those measured in laboratory air for all the P/M and I/M materials. The dependence of anisotropy in FCG rate with orientation is similar in laboratory air and salt fog. Processing mode and cobalt level do not show a definite affect on FCP rates in salt fog.

Fractographic SEM examination of the P/M material shows that in the ABC mode and the L orientation, and at all ΔK levels studied, the predominant feature is the presence of secondary intergranular cracks. These secondary cracks are also present in the I/M material but only at high ΔK .

In the L orientation, the P/M material exhibits a lower FCG rate than the I/M material at low ΔK , Figure 45. However, the situation is reversed at high ΔK . In the high ΔK regime, the presence of secondary cracks coupled with the larger grain size in the I/M material account for the lower FCG rate in the I/M material. In the I/M material at a low level of ΔK there is a high degree of slip reversibility and hence a high level of resistance to FCG. However, under the same conditions (low ΔK), extensive crack branching occurs in the P/M material, which increases FCG resistance to a level higher than that existing in the I/M material.

CONCLUSIONS

The grain structure of the P/M forgings is anisotropic with grain elongation parallel to the forging direction. Grain size is inhomogeneous with dimensions in the range ~ 2 to $20 \mu\text{m}$. Dispersoids of Co_2Al_9 are spherical, in the size range $\sim 0.05 \mu\text{m} - 0.5 \mu\text{m}$ and randomly distributed

within the grains. In contrast, oxide and n' precipitates are distributed at grain and subgrain boundaries. Cobalt level did not influence grain size. After A and ABC-processing, oxide and dispersoid spacing is smaller in the LT-ST plane than in the L-ST plane. The oxide distribution is more uniform after ABC processing than after A processing. Grain and subgrain size in the P/M material are smaller than those in the I/M 7075 and 7475 material. The volume fraction of constituent particles is lower in the P/M material than in the I/M 7475 material.

In air, anisotropy in fatigue life is observed for each condition of cobalt level and processing mode; fatigue life is longer in the longitudinal orientation than in the transverse orientations. The degree of anisotropy is relatively independent of cobalt content for the A processing mode. In the ABC processing mode, the degree of anisotropy increases with increasing cobalt content. At a fixed cobalt level, ABC processing gives a higher degree of anisotropy in terms of S-N response than does the A processing mode. The longest fatigue life is achieved in the longitudinal orientation with 0.8% Co after ABC-processing.

Anisotropy in fatigue crack growth rates in air exist for the three P/M alloys studied. The specimens oriented with the crack propagation plane normal to the ST direction show the highest crack propagation rates at all cobalt levels and for each processing mode. At high ΔK , the lowest fatigue crack growth rates are found with the L direction perpendicular to the crack propagation plane, independent of cobalt level or processing mode. At low ΔK levels, the lowest crack growth rates are found with the LT direction perpendicular to the crack propagation plane, independent of cobalt level or processing mode.

The fatigue life of the P/M alloys in air is superior to that of the I/M 7075 and 7475 alloys in both the longitudinal and transverse orientations. This is attributed to the higher resistance to crack initiation of the P/M alloys in comparison to the I/M material and is the result of a finer microstructure in the former.

The fatigue crack growth rates of the I/M 7475 in the LT and ST orientations are lower than those in the P/M material at all the ΔK levels examined. At high ΔK levels in the L orientation, the crack growth rates in the P/M material are lower than the correspondent crack growth rates in the I/M material. At low ΔK levels in the L orientation, the crack growth rates in the I/M material are lower than those in the P/M material.

Fatigue life of the P/M and I/M alloys suffers serious degradation when tested in salt fog. Anisotropy in S-N response for the P/M alloys is maintained and is similar to that observed in air. There is no systematic trend in S-N fatigue response in the P/M material as a function of processing mode and cobalt level. In the L orientation, fatigue lives of the P/M alloys and I/M 7475 are similar; this is true for all combinations of cobalt level and processing mode studied. At high stress levels and in the ST orientation, the P/M alloys show a higher fatigue life than the I/M alloy. In salt fog, fatigue life is controlled by the crack propagation resistance of the material.

The fatigue crack growth rates for the I/M and P/M alloys increase significantly in salt fog compared to the corresponding rates measured in air. Processing mode and cobalt level do not have a definite effect on crack growth rates in salt fog. At high ΔK and in the L orientation, the crack growth rates of the P/M alloys are higher than those of the I/M alloy. This response is reversed at low ΔK levels in this orientation.

In air, crack initiation and propagation response can be explained in terms of the scale of the microstructure and the relative sizes of microstructural features and the plastic zone size at the crack tip, respectively. In salt fog fatigue response is explained similarly but with the added effects of secondary cracking and intergranular crack propagation taken into account.

Table I: Nominal Composition of Atomized Powders and I/M Alloys, Wt %.

<u>Alloy</u>	<u>Si</u>	<u>Fe</u>	<u>Cu</u>	<u>Mn</u>	<u>Mg</u>	<u>Cr</u>	<u>Zn</u>	<u>Ti</u>	<u>Co</u>	<u>Al</u>
7075 (I/M)	.40	.50	1.2/2.0	.30	2.1/2.9	.18/.35	5.1/6.1	.20	-	Balance
7475 (I/M)	.10	.12	1.2/1.9	.06	1.9/2.6	.18/.25	5.2/6.2	.06	-	Balance
P/M	.05	.09	1.5	-	2.5	-	6.5	-	-	Balance
CT-91 P/M	.05	.09	1.5	-	2.5	-	6.5	-	0.4	Balance
P/M	.05	.09	1.5	-	2.5	-	6.5	-	0.8	Balance

Table II: Actual Composition of CT91 and the 0% Co and 0.8% Co Versions, Wt % (28).

<u>Sl</u>	<u>Re</u>	<u>Cu</u>	<u>Mg</u>	<u>Zn</u>	<u>Co</u>	<u>Al</u>
0.05	0.07	1.44	2.33	6.62	0	Balance
0.05	0.09	1.53	2.44	6.38	0.33	Balance*
0.06	0.05	1.42	2.40	6.73	0.79	Balance

* Alcoa designation CT-91; new designation is X-7091.

Table III: Aluminum Powder Size Distribution; (U.S. Standard Screen Analysis),
Wt % (28).

<u>% Co of Alloy</u>	<u>APD*</u>	<u>+30</u>	<u>-30</u>	<u>-50</u>	<u>-100</u>	<u>-200</u>	<u>-325</u>
0% Co	13.10	0	0	0.6	3.8	8.2	87.2
0.4% Co	12.93	0	0	0.4	3.4	9.2	87
0.8% Co	13.10	0	0	0.6	4.0	9.2	86.2
Average	13	0	0	0.5	4	9	86.5

Table IV: Coulter Counter Size Distribution and APD by Fisher Sub-Sieve Analysis of Aluminum Alloy Powders (% < Diameter in μm) (28).

<u>% Co of Alloy</u>	<u>Diam. μm</u>	<u>75</u>	<u>60</u>	<u>50</u>	<u>40</u>	<u>30</u>	<u>20</u>	<u>15</u>	<u>10</u>	<u>8</u>	<u>5.5</u>	<u>APD*</u>
0% Co	90.2	84.6	80.5	77.4	64.6	41.3	27.9	14.9	10.0	3.6	13.1	
0.4% Co	95.0	93.8	91.2	84.2	70.1	45.5	31.0	17.2	11.7	4.2	12.1	
0.8% Co	94.0	92.9	91.9	88.2	73.6	46.7	30.5	16.5	10.8	3.8	13.1	

*Average particle diameter.

Table V: Auger Analysis of the Surface of CT-91 Powders
(atomic %) (28).

Al	Mg	Zn	Cu	Co	Fe	O
12.83	10.38	6.83	2.24	2.01	2.32	45.92
N	Ca	C	Cl	S	Si	K
2.17	1.16	9.66	0.99	0.41	1.11	1.95

Table VI: Estimated Particle Surface Oxide Composition of Air Atomized CT-91 Powders (28).

Oxide	MgO	Al ₂ O ₃	ZnO	CuO
Mole %	26.6	50.0	17.6	5.8

Table VII: Experimental Alloys and Processing Modes

Base Alloy (wt %)	Co Addition (wt %)	Process Condition*
6.5Zn-2.5Mg-1.5Cu	0	A
6.5Zn-2.5Mg-1.5Cu	0	ABC
6.5Zn-2.5Mg-1.5Cu	0.4	A
6.5Zn-2.5Mg-1.5Cu	0.4	ABC
6.5Zn-2.5Mg-1.5Cu	0.8	A
6.5Zn-2.5Mg-1.5Cu	0.8	ABC

* A - Single Upset and Forged.

ABC - Triple Upset and Forged.

Table VIII: Average Tensile Properties of P/M Aluminum Forgings
and I/M 7475 and 7075 Rolled Plate

Process	%Co	Orien-tation	Hard Rb	YS (0.2%) MPa Ksi	UTS MPa Ksi	ZE 13mm gage	%Ra
A	0	L	84	505 73.3	524 76.1	9.5	-
A	0	LT	83	478 69.4	523 75.9	8.4	-
A	0.4	L	90	508 73.8	561 81.3	14.2	30.5
A	0.4	LT	88	460 66.7	529 76.7	7.4	26.2
A	0.8	L	87	496 71.9	558 81.0	12.6	33.4
A	0.8	LT	89	497 72.1	548 79.5	9.6	32.2
ABC	0	L	83	467 67.8	515 74.7	8.7	36.0
ABC	0	LT	83	482 69.9	539 78.3	9.8	37.8
ABC	0.4	L	87	507 73.6	566 82.2	11.8	30.5
ABC	0.4	LT	87	482 69.9	538 78.1	8.1	25.6
ABC	0.8	L	88	464 67.4	527 76.4	9.4	29.5
ABC	0.8	LT	89	471 68.3	527 76.4	9.3	31
7475	-	L	76	421 61.2	480 69.7	11.7	-
	-	ST	75	417 60.5	476 69.1	8.9	-
7075	-	L	85	464 67.3	523 75.9	6.9	-
	-	ST	84	458 66.5	492 71.3	7.8	-

Table IX: Load Controlled Axial Fatigue Data (S-N); Laboratory Air,
 $R = \sigma_{\min} / \sigma_{\max} = 0.1$, 30 Hz.

a) A Processing

χ	G_0	Orien-	Cycles to Failure $\times 10^3$			
		tion	448 MPa (65 ksi)	379 MPa (55 ksi)	364 MPa (50 ksi)	310 MPa (45 ksi)
0	L	13, 23, 20, 24	131, 50, 148, 70	-	-	556, (5042)*
0	LT	13, 16, 14, 17	33, 27, 22, 14	-	-	68, 227
0	ST	12, 17, 14, 18	34, 28, 26, 47, 44	-	-	-
0.4	L	20, 29, 31, 33	40, 46, 67, 168	-	-	223, 3076
0.4	LT	10, 10, 8, 6	21, 15, 15, 18	-	-	37, 32
0.4	ST	23, 14, 15, 17	25, 29, 46, 26, 20	-	-	-
0.8	L	22, 21, 26, 36	315, 33, 35, 57	-	-	-
0.8	LT	8, 6, 9, 11	12, 21, 35, 17	-	-	33 (7092)
0.8	ST	23, 14, 16, 19	24, 30, 27, 50, 43	-	-	-

b) ABC Processing

0	L	12, 33, 36	198, 73, 31, 52	-	-
0	LT	12, 4, 5, 24, 11	18, 19, 14, 15	-	-
0	ST	10, 19, 14, 21	25, 39, 23, 25, 45	-	-
0.4	L	37, 19, 23, 26	39, 146, 80, 512	-	-
0.4	LT	12, 17, 20, 15	25, 22, 21, 23	-	45, 32 (3150)
0.4	ST	18, 16, 24, 20	-	30, 30, 85, 77	-
0.8	L	32, 37, 94	85, 76, 92, 450	-	-
0.8	LT	18, 18, 15, 16	-	-	87, 77, 141, 42
0.8	ST	12, 24, 20, 18	19, 68, 18	130, 30, 888, 196 (3080)(2125)	-

* Values in brackets (run out)

Table X: Load Controlled Axial Fatigue Data (S-N) 3.5% NaCl
 Solution Salt Fog, $R = \sigma_{\min}/\sigma_{\max} = 0.1$, 30 Hz.

Process	% Co	Orientation	Cycles to Failure $\times 10^3$	
			448 MPa (65 ksi)	379 MPa (55 ksi)
A	0	L	5,5,5,5	7,8,9,8,8
A	0	LT	3,6,2,5	12,8,5,2,1,11
A	0.4	L	6,5,7,8	12,11,10,10,10
A	0.4	LT	3,3,3,3.5	4,4,3,4,4
A	0.8	L	6,4,6,6	8,9,10,7.5,10
A	0.8	LT	5.5,5,3,3	9,3.5,4.5,7.4
ABC	0	L	4,6,6,7	7,10,9,13,6
ABC	0	LT	4.5,7.4,3	4,10,15,10,16
ABC	0.4	L	5,5,4,6	11,9,9,12,10
ABC	0.4	LT	3,4,3,3	4,5,5,4,6
ABC	0.8	L	6,5,4,4	10,6.5,7,16,10
ABC	0.8	LT	8,9,8,8	10,11,14,11,14

Table XI: Values of A and m for $da/dN = A \Delta K^m$

% Co	Processing	Orien-	Laboratory Air				Salt Fog			
			tation	m	$A \times 10^{-10}$	r^*	m	$A \times 10^{-10}$	r^*	
0	A	L	2.23	5.04	.98	1.92	136		.93	
0	A	LT	3.68	9.6	.99	-	-			
0	A	ST	3.71	24.4	.98	2.98	243		.98	
0.4	A	L	1.86	110	.99	2.48	357		.97	
0.4	A	LT	3.9	8.7	.99	4.24	5.73		.99	
0.4	A	ST	4.66	4.08	.97	-	-			
0.8	A	L	1.98	911	.99	2.75	203		.97	
0.8	A	LT	4.31	1.85	.99	4.43	3.85		.99	
0.8	A	ST	3.94	11.8	.99	2.95	367		.94	
0	ABC	L	2.06	619	.98	1.72	221		.95	
0	ABC	LT	3.8	9.42	.99	4.14	8.79		.98	
0	ABC	ST	3.96	11.91	.99	2.88	390		.99	
0.4	ABC	L	2.23	549	.98	1.8	2130		.95	
0.4	ABC	LT	4.22	2.84	.95	4.14	4.83		.98	
0.4	ABC	ST	2.9	207	.98	3.48	137		.97	
0.8	ABC	L	2.07	609	.99	2.51	270		.96	
0.3	ABC	LT	4.03	4.2	.99	5.02	.89		.99	
0.8	ABC	ST	3.63	35	.97	3.18	229		.96	
<hr/>										
7475	I/M	L	3.65	11.3	.98	1.64	3100		.97	
7475	I/M	LT	4.29	1.3	.99	2.10	1230		.98	
7475	I/M	ST				2.63	350		.98	

* r = correlation coefficient

Table XII: Quantitative Microstructural Data

χ_{Co}	0	0	0.4	0.4	0.4	0.8	0.8	0.8	0	0	0	0.4	0.4	0.4
Processing	A	A	A	A	A	A	A	A	ABC	ABC	ABC	ABC	ABC	ABC
Orientation	L	LT	ST	L	LT	ST	L	LT	ST	L	LT	L	LT	ST
$\bar{L}_g \mu\text{m}$	6.8	6.8	8.8	6.7	6.9	10.5	6.7	6.9	9.8	6.7	6.8	8.7	6.8	6.9
$\bar{L}_{sg} \mu\text{m}$	2.8	2.5	2.4	2.3			1.78	1.76		3.15	3.4		2.3	2.5
χ_{UR}	19		30.5		41		33		38					
f_D			0.096	0.086		.317	.329					.145	.111	
$D_D \mu\text{m}$.21	.20		.22	.20				.20	.18	
$\lambda_D \mu\text{m}$					2.3	2.7		.55	.60			1.6	1.9	
$S_v \mu\text{m}^{-1}$.29	.22	.32	.29	.19	.28	.21	.22	.23	.18	.25	.22
														.20

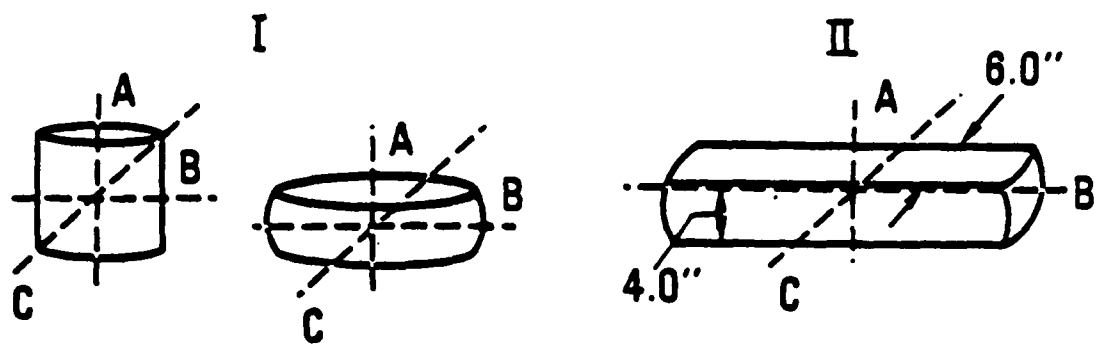
- L - longitudinal orientation; crack propagates in plane ST/LT
- LT - long transverse orientation; crack propagates in plane L/ST
- ST - long transverse orientation; crack propagates in plane LT/L
- \bar{L}_g - grain size mean intercept length
- \bar{L}_{sg} - subgrain size mean intercept length
- χ_{UR} - percent of unrecrystallized structure
- f_D - volume fraction of dispersoids
- λ_D - mean free path of dispersoids
- D_D - average dispersoid diameter
- S_v - grain boundary area per unit volume

Table XIII: (Continued)

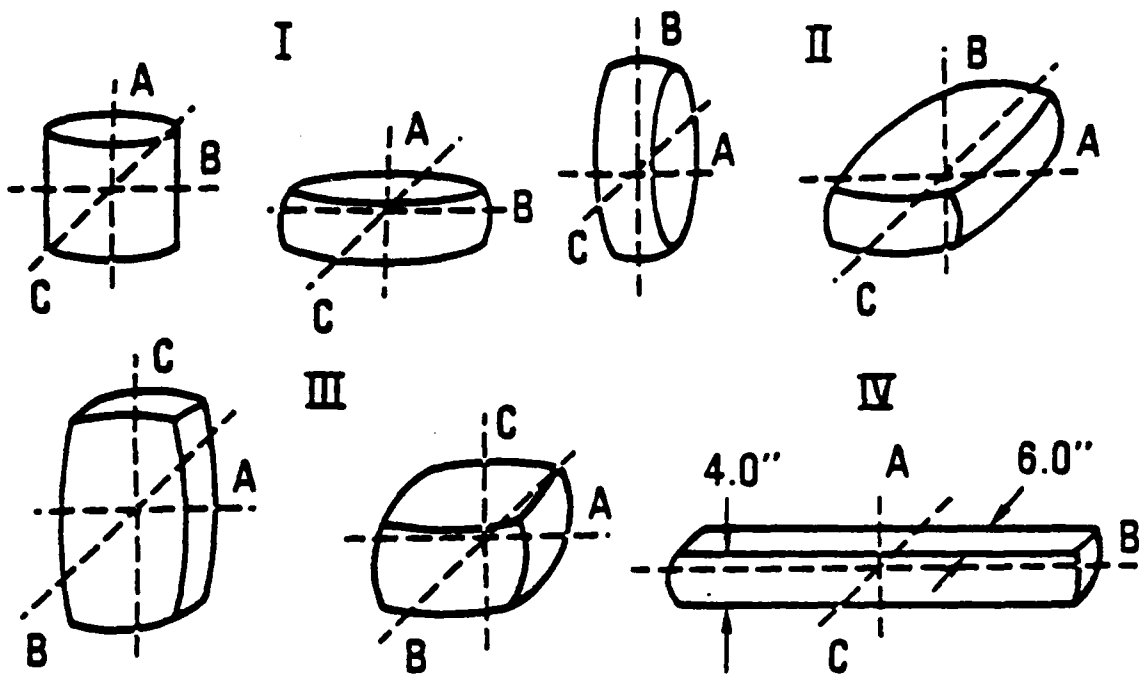
χ_{Co}	0.8	0.8	0.8	7475	7475	7475	7075	7075	7075
Processing	ABC	ABC	ABC	I/M	I/M	I/M	I/M	I/M	I/M
Orientation	L	LT	ST	L	LT	ST	L	LT	ST
$\bar{L}_g \mu m$	6.6	6.7	9.7	26.6	48	46	22	44	43
$\bar{L}_{sg} \mu m$	1.9	1.8	6.7						
χ_{UR}	44								
f_D		.44	.33						
$D_D \mu m$.21	.21						
$\lambda_D \mu m$.38	.48						
$S_v \mu m^{-1}$.22	.24	.27					

Table XIII: Cyclic Plastic Zone Size at Different ΔK for P/M and I/M Materials

Alloy	Processing	Oriental-tion	YS (MPa)	ΔK $8.8 \text{ MNm}^{-3/2}$	ΔK $11 \text{ MNm}^{-3/2}$	ΔK $16.5 \text{ MNm}^{-3/2}$
P/M 0% Co	A	L	505	12 μm	18 μm	42 μm
P/M 0% Co	A	LT	478	13.5 μm	21 μm	47.6 μm
P/M 0.4% Co	A	L	508	12 μm	18.7 μm	42.2 μm
P/M 0.4% Co	A	LT	460	14.6 μm	22.8 μm	51.4 μm
P/M 0.8% Co	A	L	496	12.6 μm	19.6 μm	44.2 μm
P/M 0.8% Co	A	LT	497	12.6 μm	19.6 μm	44.2 μm
P/M 0% Co	ABC	L	467	14.2 μm	22.2 μm	49.9 μm
P/M 0% Co	ABC	LT	482	13.3 μm	20.1 μm	46.8 μm
P/M 0.4% Co	ABC	L	507	12.0 μm	18.8 μm	42.3 μm
P/M 0.4% Co	ABC	LT	482	13.3 μm	20.8 μm	46.8 μm
P/M 0.8% Co	ABC	L	464	14.3 μm	22.4 μm	50.5 μm
P/M 0.8% Co	ABC	LT	471	13.9 μm	21.8 μm	49.09 μm
I/M 7475	Rolled Plate	L	421	17.4 μm	27.3 μm	61.4 μm
I/M 7475	Rolled Plate	ST	417	17.8 μm	27.8 μm	62.6 μm



Upset and Forge - A Process



Upset and Forge -
ABC Process

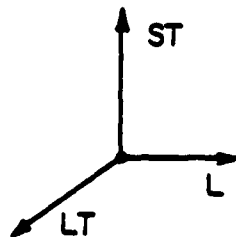


Figure 1. Schematic of the two upset and forge (draw) modes of deformation (28).

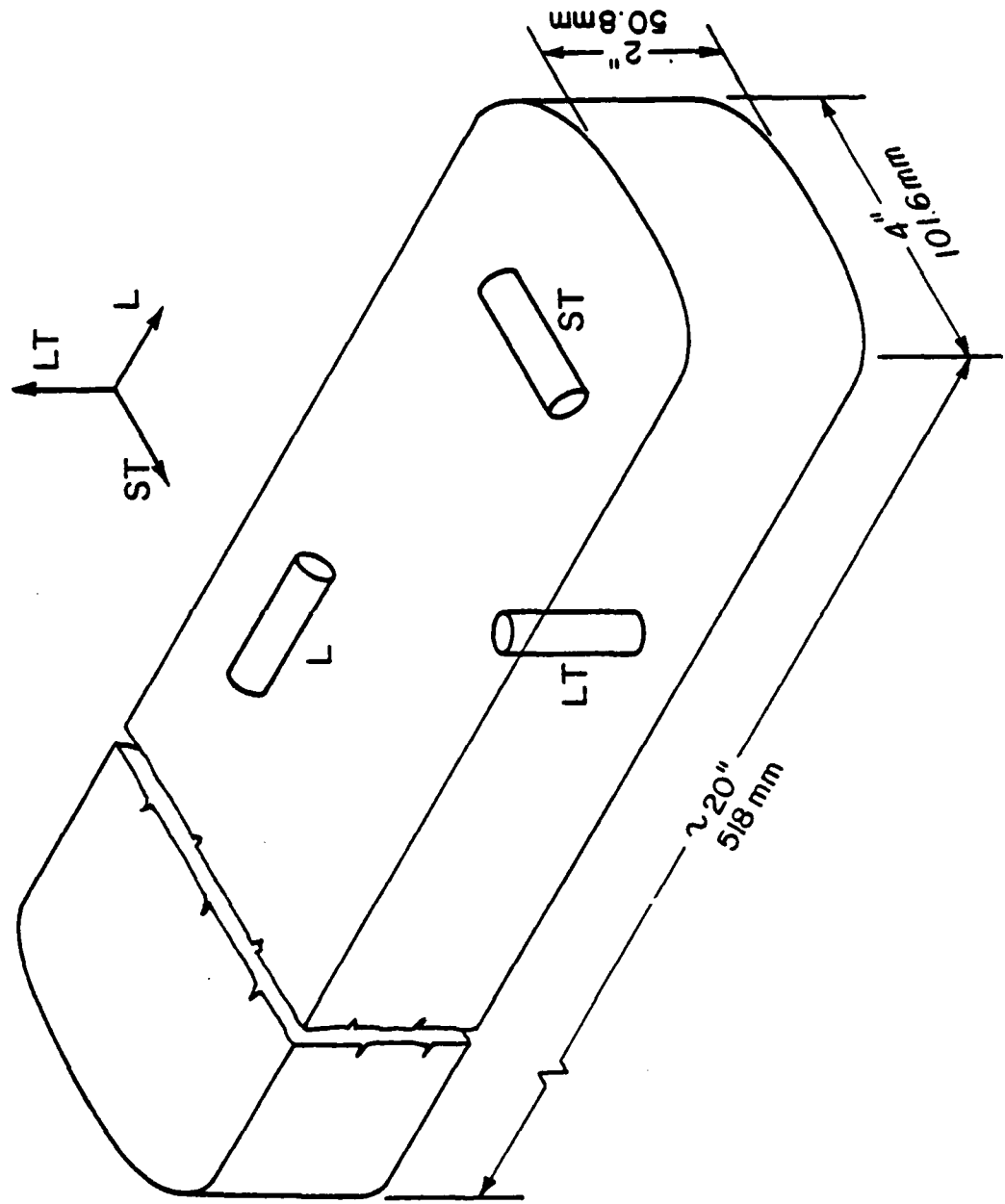


Figure 2. Specimen orientation for tensile and fatigue (S-N) tests.

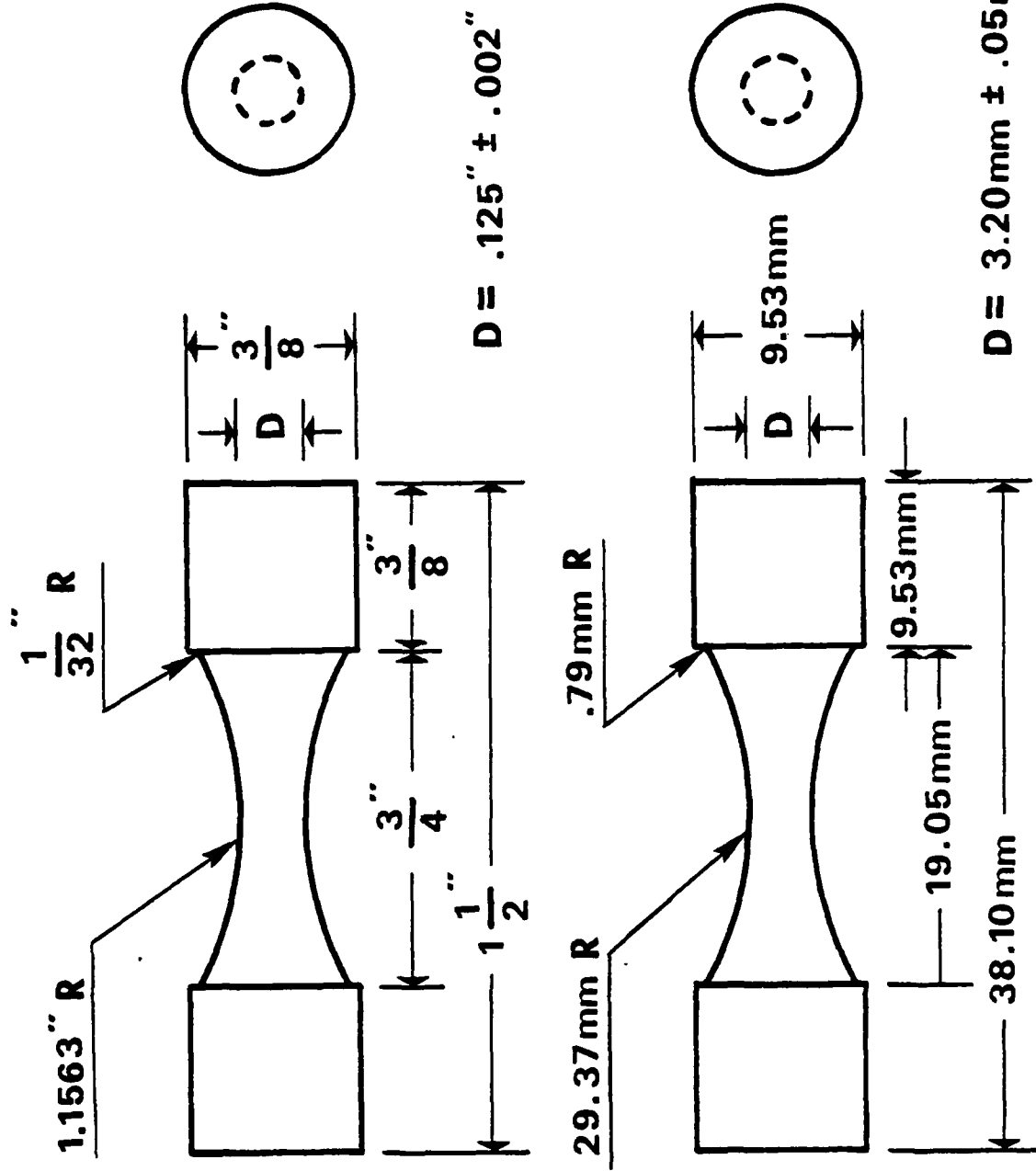


Figure 3. Dimensions of axial fatigue test specimens (S-N).

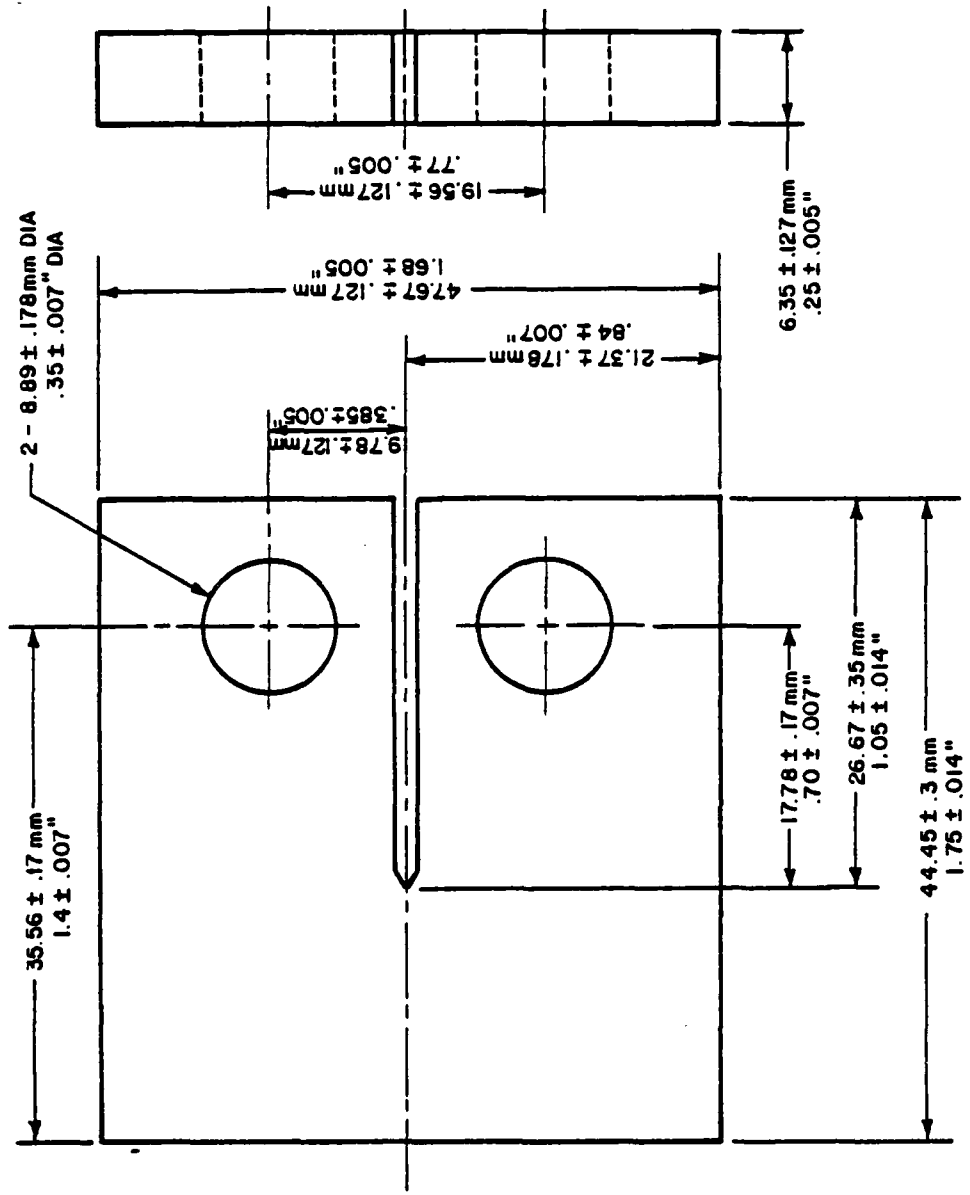


Figure 4. Dimensions of CT specimens for crack propagation tests.

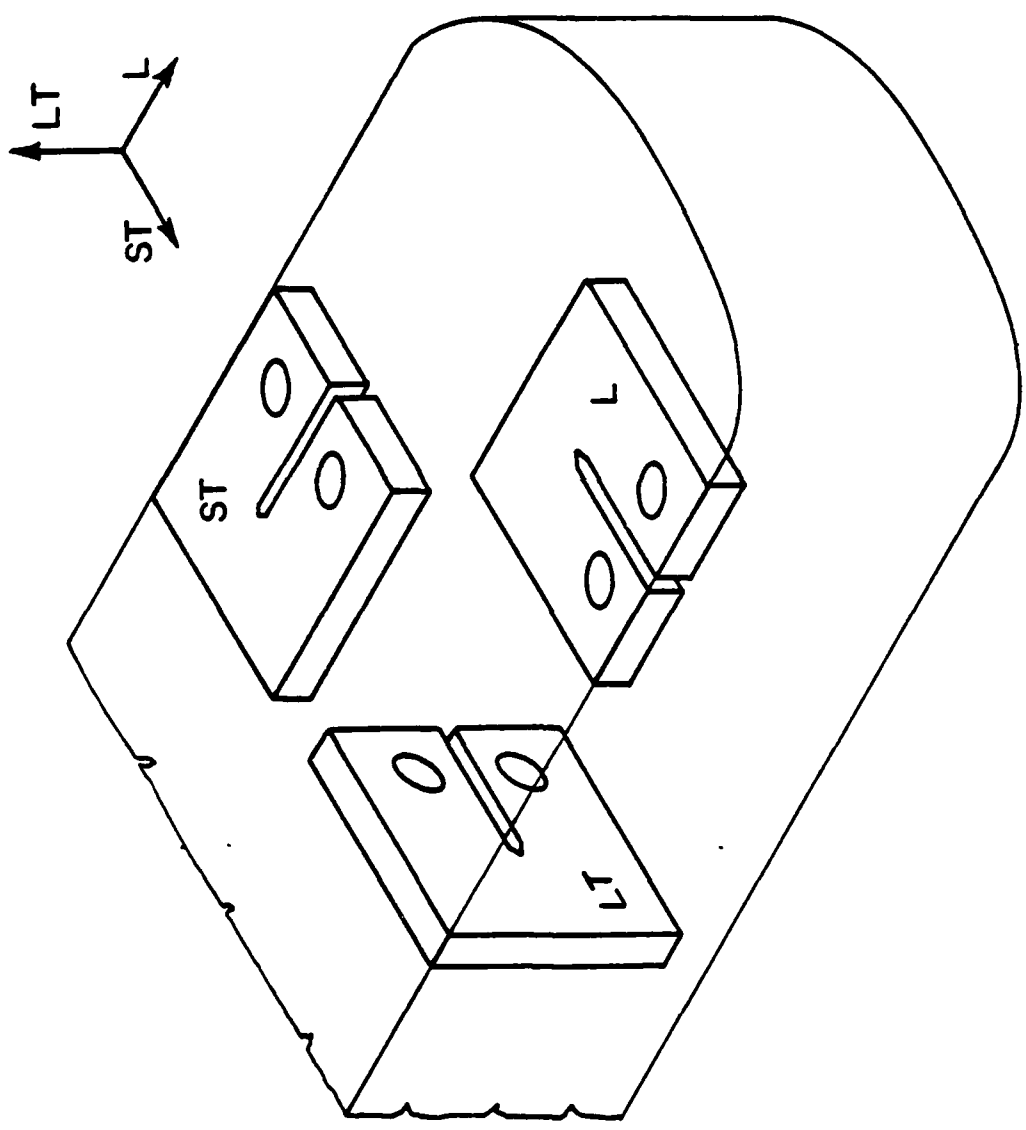
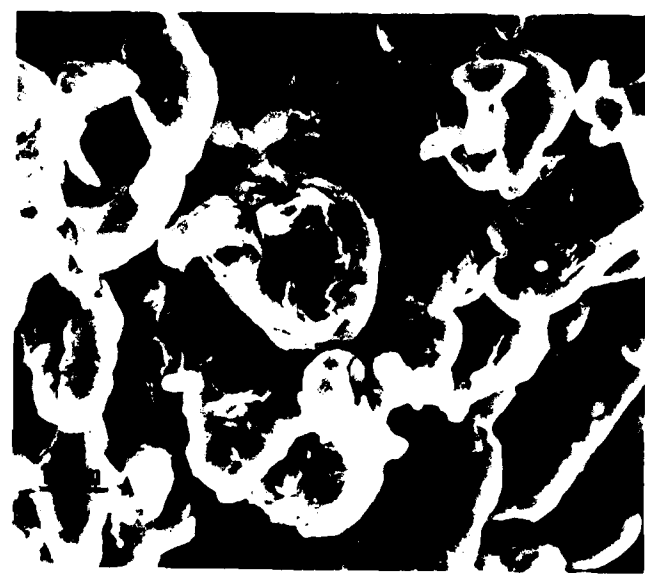


Figure 5. Specimen localization for crack propagation studies.



a



b

Figure 6. SEM of air atomized CT-91 aluminum powders.
a) 1000X, b) 500X.

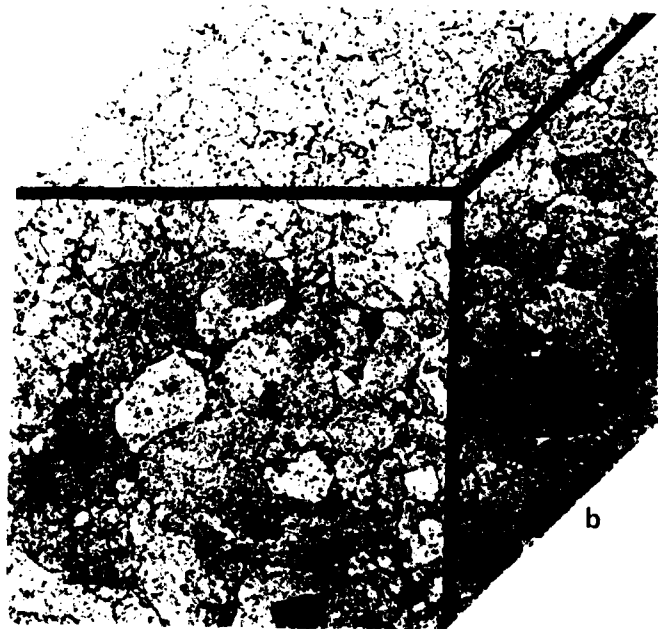
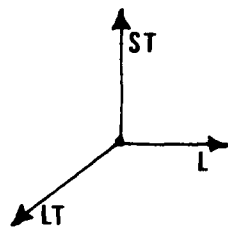
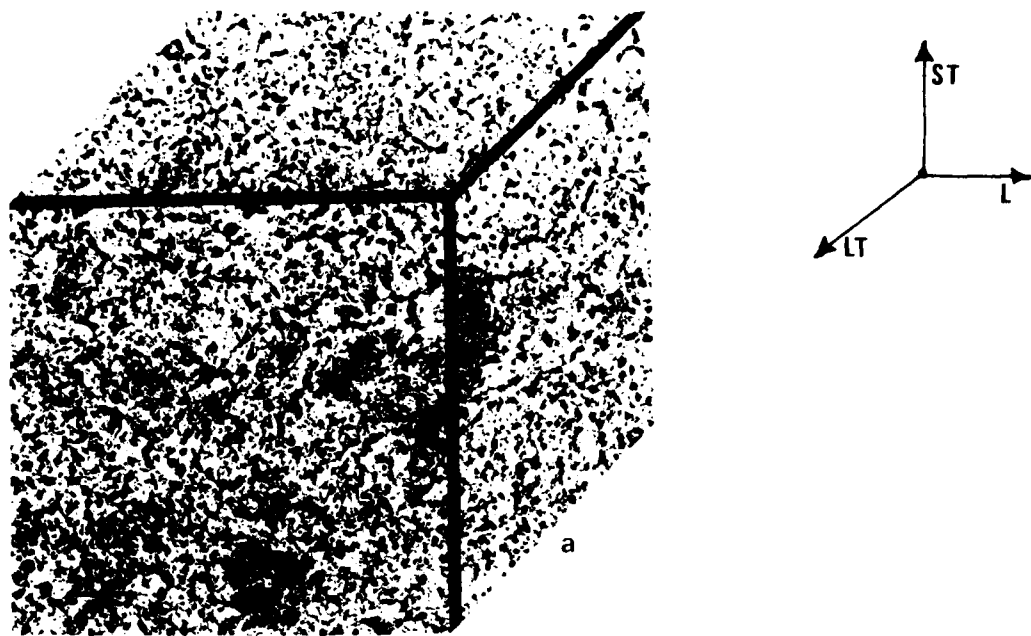


Figure 7. Optical micrographs of hot compacted billet. a) Before heat treatment, b) after heat treatment, Keller's etch.

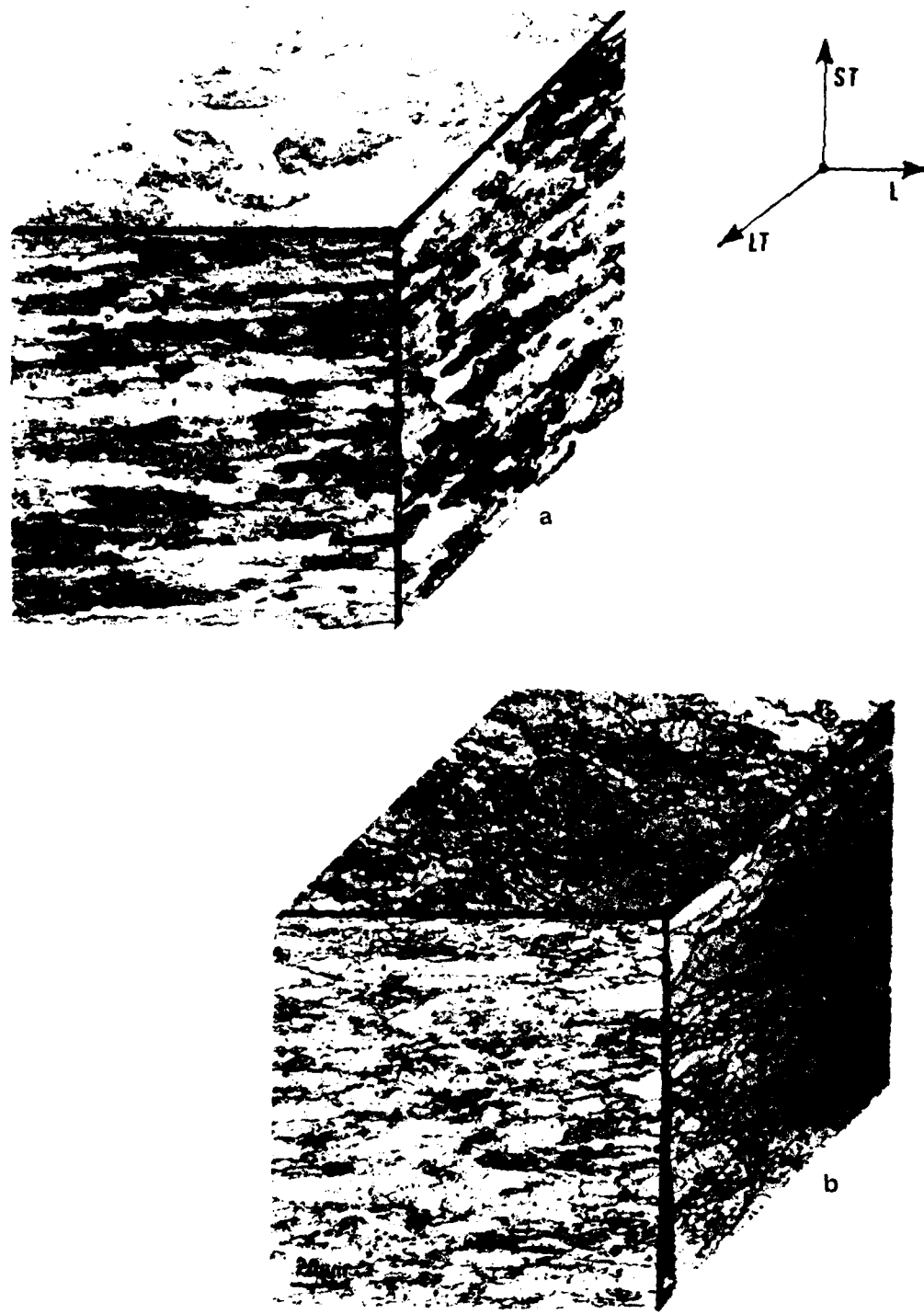


Figure 8. Optical micrographs of upset and forged billets, 0.4% Co, Keller's etch. a) A process, b) ABC process.

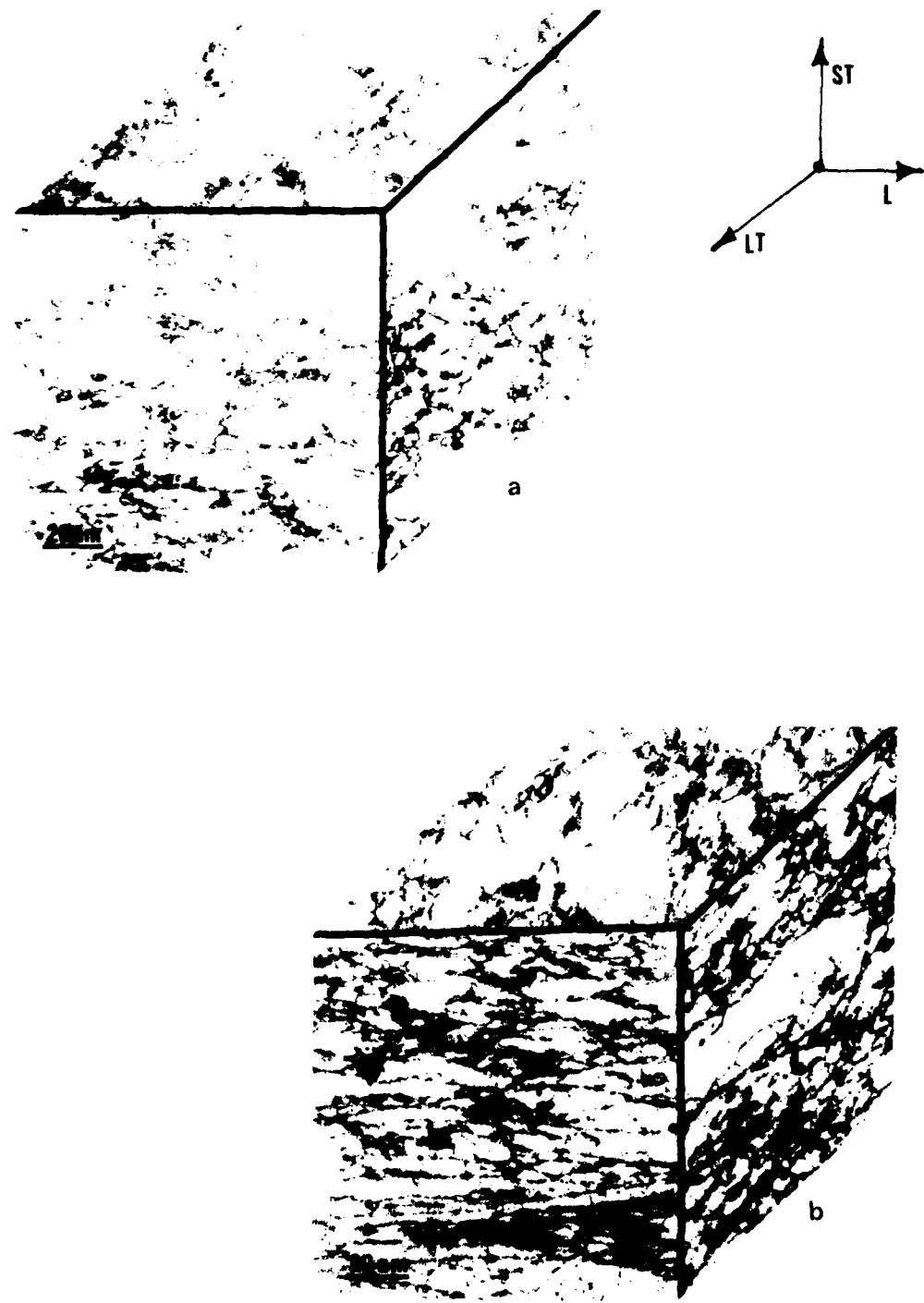


Figure 9. Optical micrographs of upset and forged billets; 0.4% Co, HNO₃ etch. a) A process, b) ABC process.

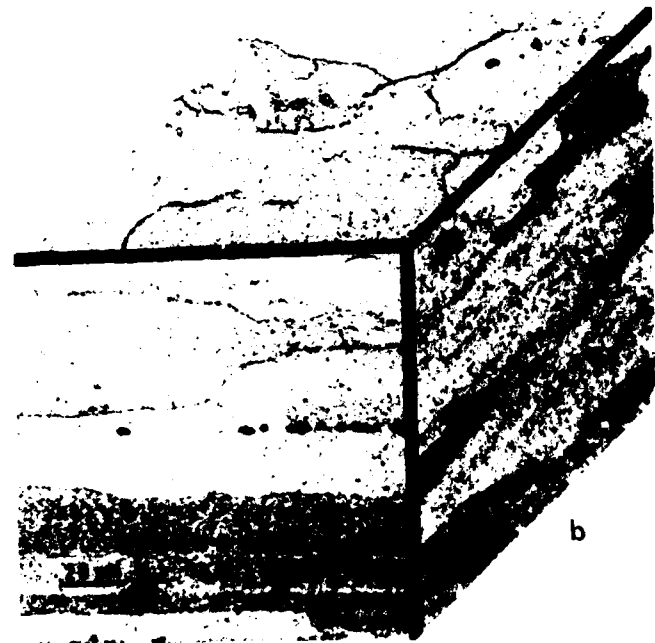
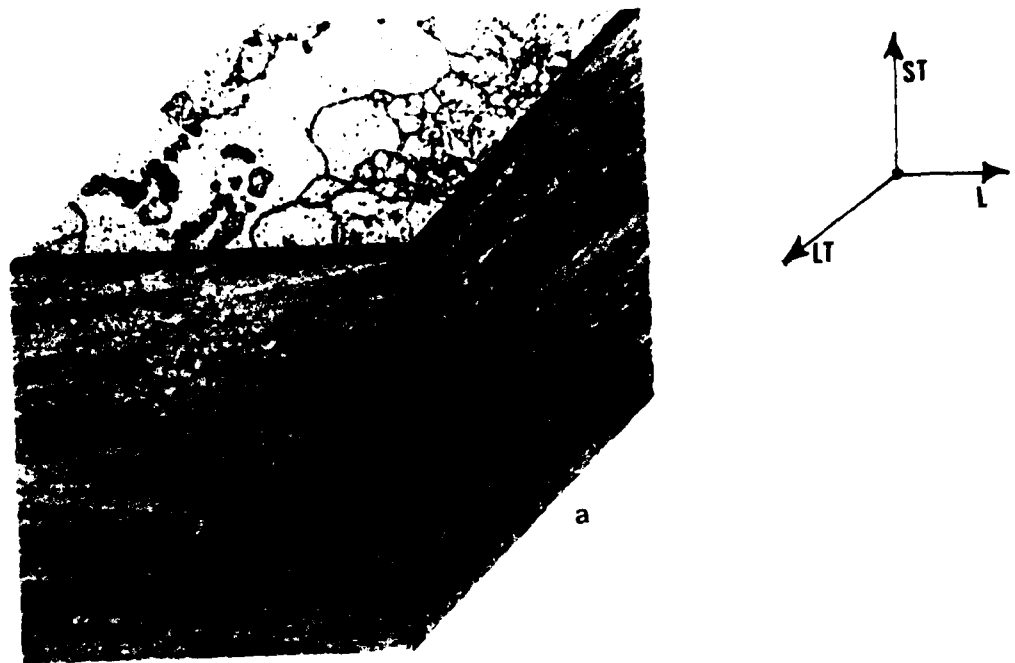
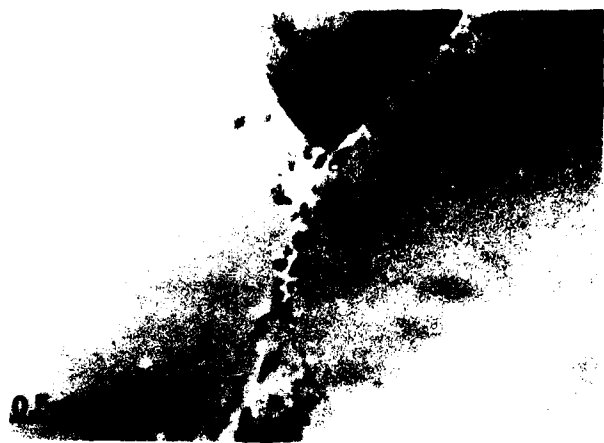


Figure 10. Optical micrographs of commercial rolled plate solution treated and aged, HNO_3 etch. a) 7075 aluminum alloy, b) 7475 aluminum alloy.



a



b



c

Figure 11. TEM of ABC processed P/M material; L orientation. a) 0% Cobalt, b) 0.4% Cobalt, c) 0.8% Cobalt, 20000X.



a



b



c

Figure 12. TEM of A processed P/M material; L orientation. a) 0% Cobalt, b) 0.4% Cobalt, c) 0.8% Cobalt, 20000X.



a



b



c

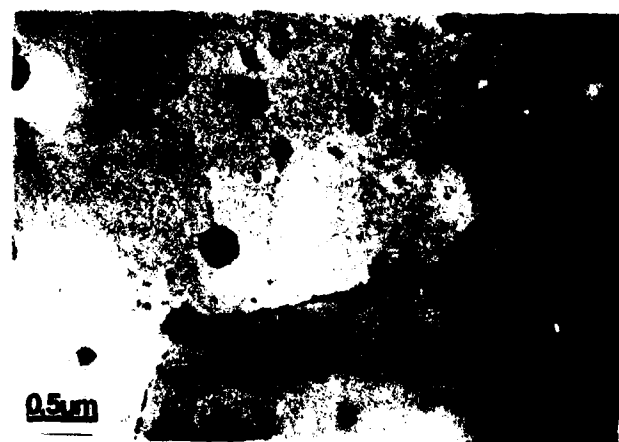
Figure 13. TEM of ABC processed P/M material; LT orientation.
a) 0% Cobalt, b) 0.4% Cobalt, c) 0.8% Cobalt, 20000X.



a



b



c

Figure 14. TEM of A processed P/M material; LT orientation. a) 0% Cobalt, b) 0.4% Cobalt, c) 0.8% Cobalt, 20000X.

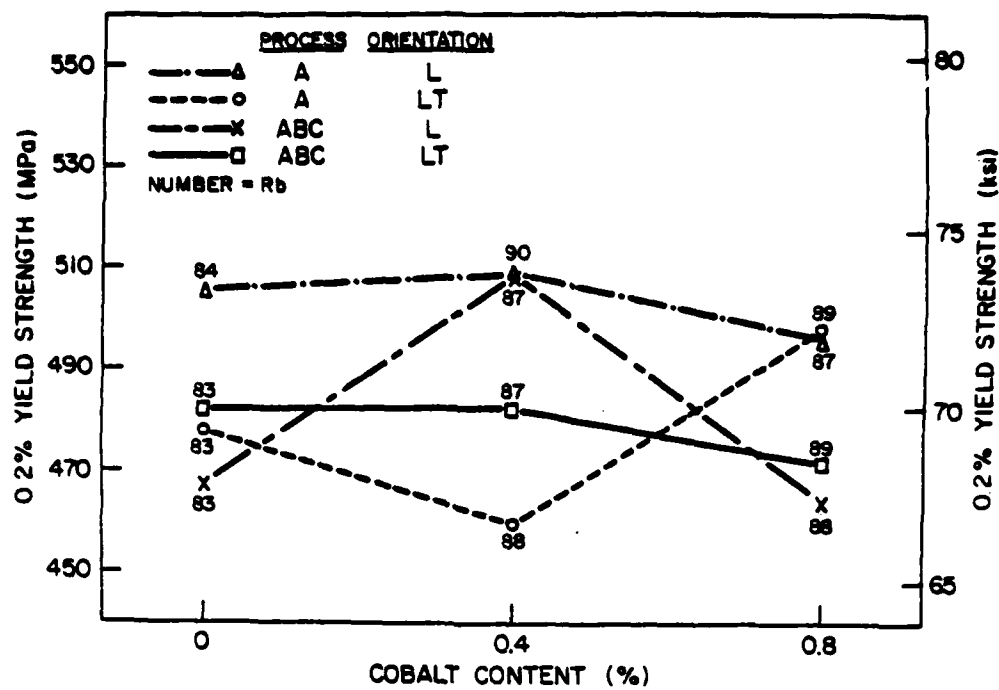


Figure 15. Yield strength (0.2% offset) vs. cobalt content for P/M forged material.

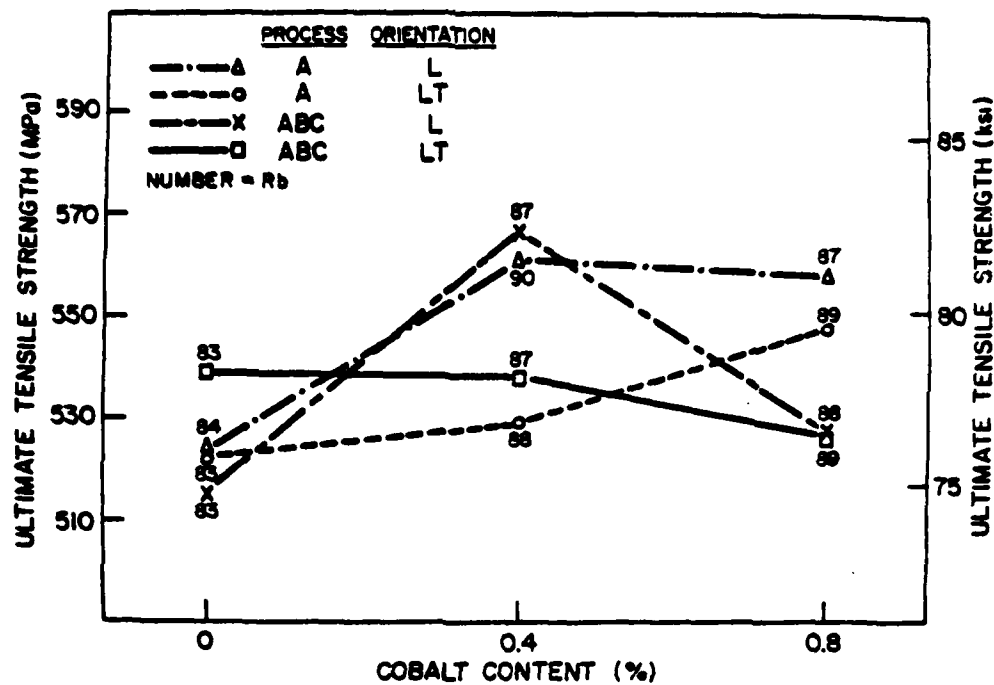
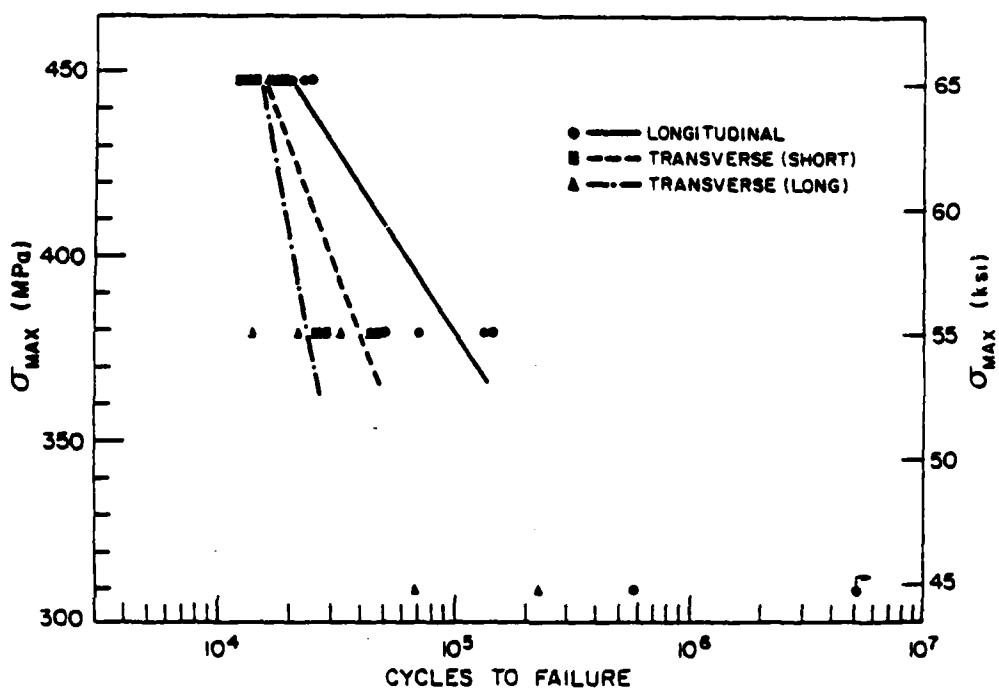
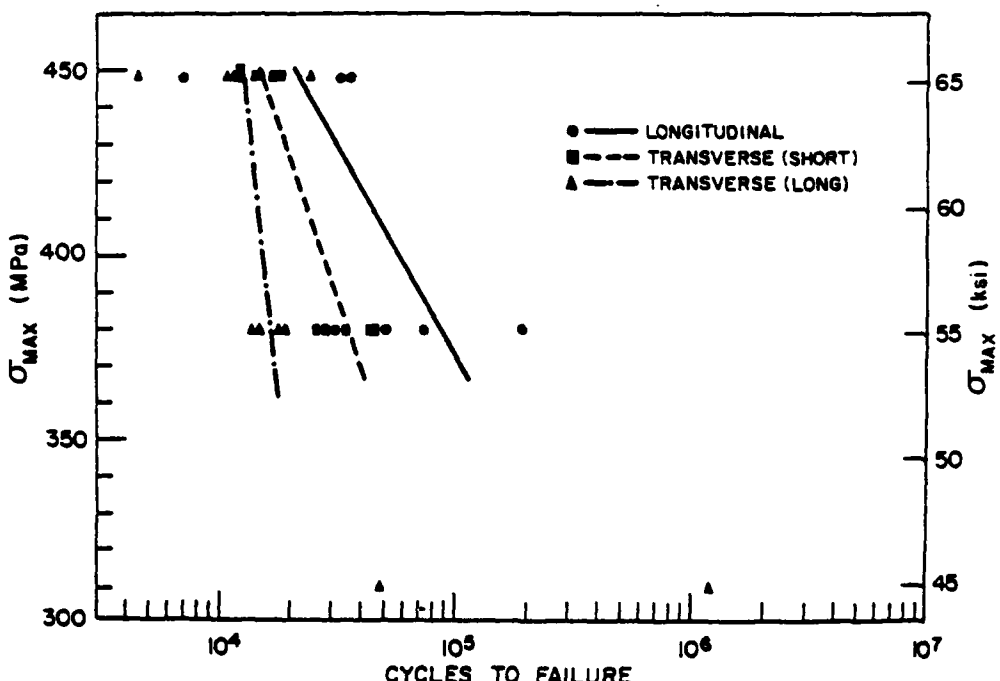


Figure 16. Ultimate tensile strength (UTS) vs. cobalt content for P/M forged material.

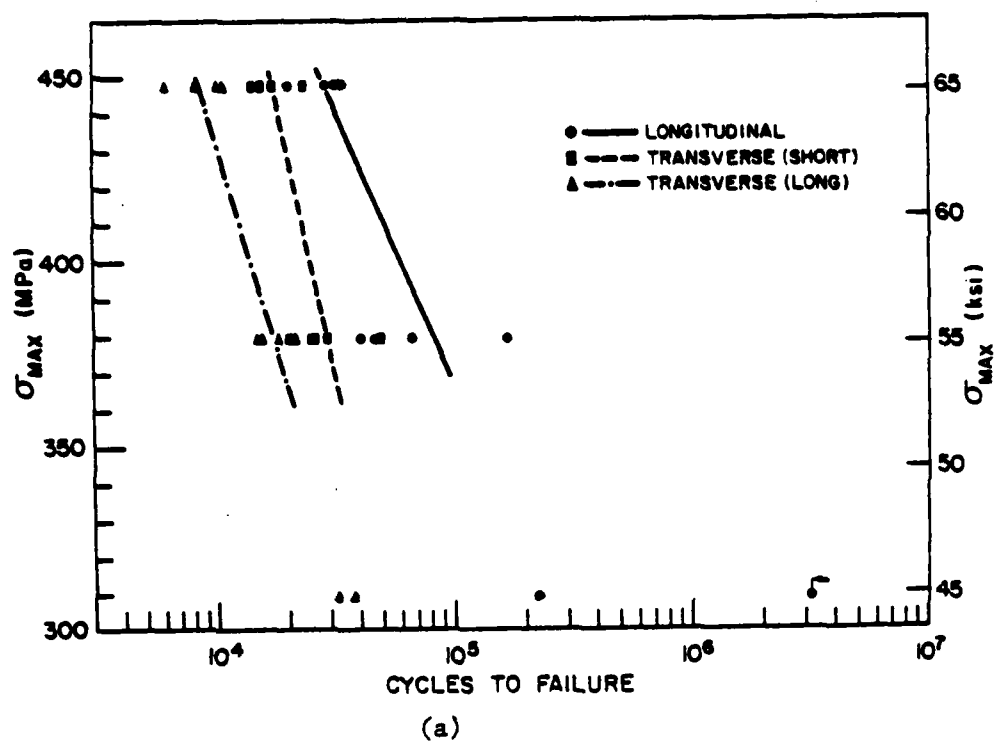


(a)

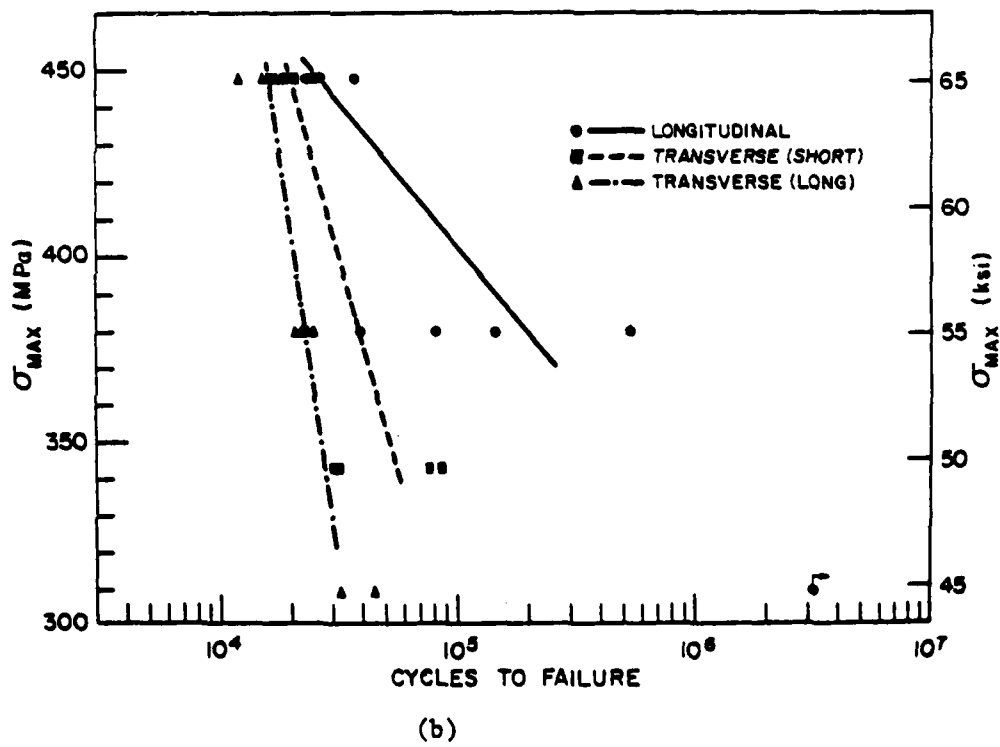


(b)

Figure 17. S-N curves for 0% Co P/M forged material tested in laboratory air. a) A processing, b) ABC processing.

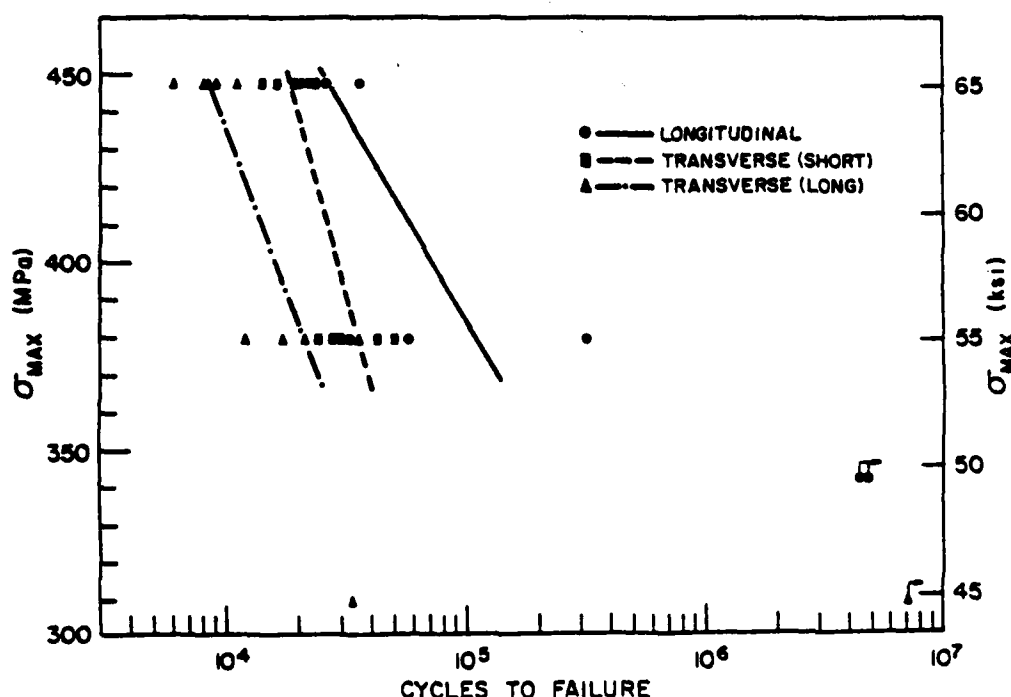


(a)

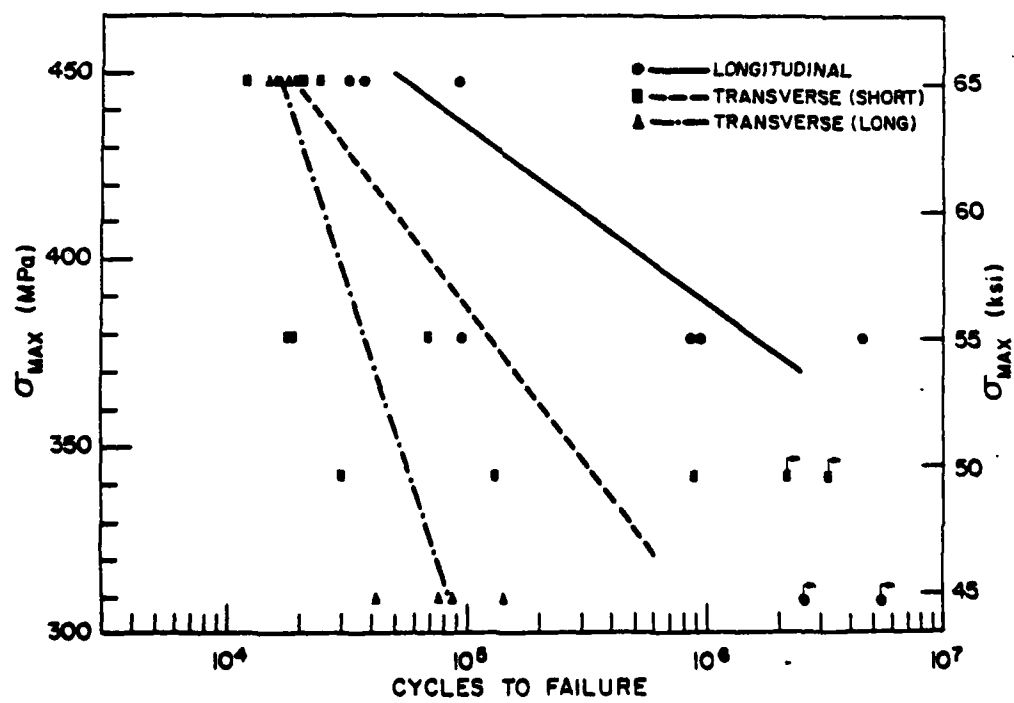


(b)

Figure 18. S-N curves for 0.4% Co P/M forged material tested in laboratory air. a) A processing, b) ABC processing.

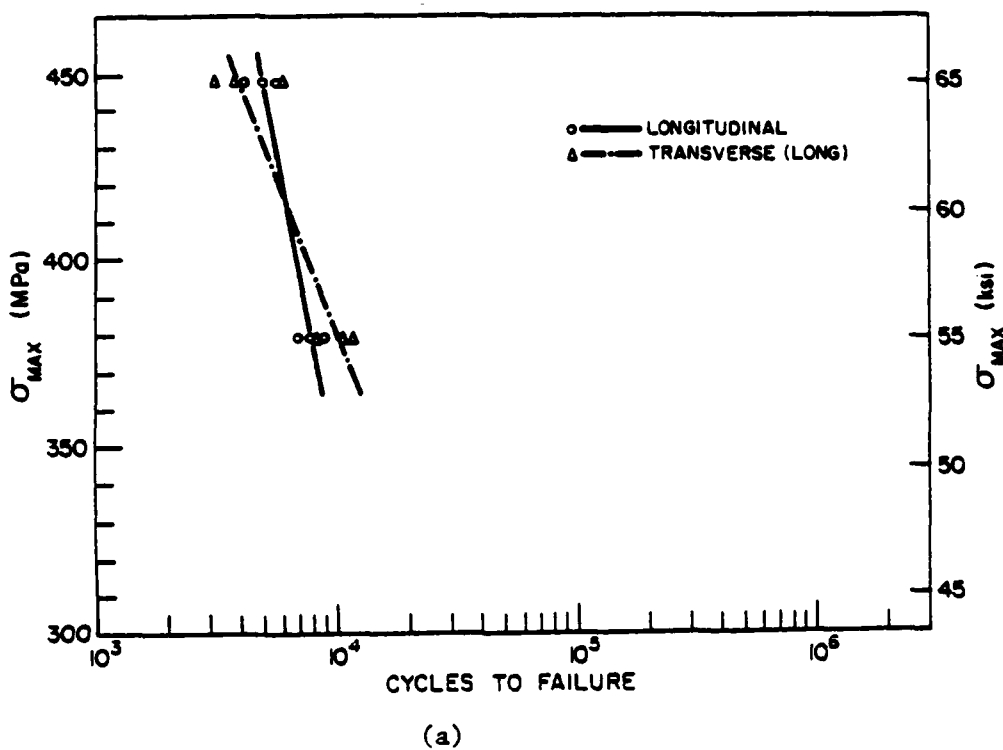


(a)

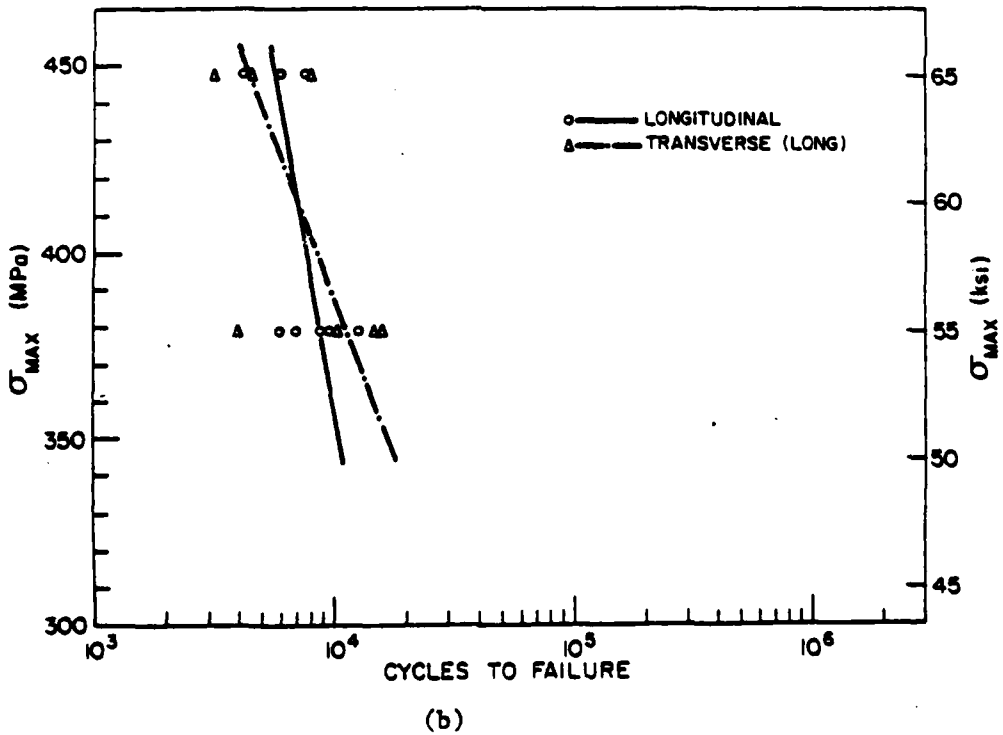


(b)

Figure 19. S-N curves for 0.8% Co P/M forged material tested in laboratory air. a) A processing, b) ABC processing.

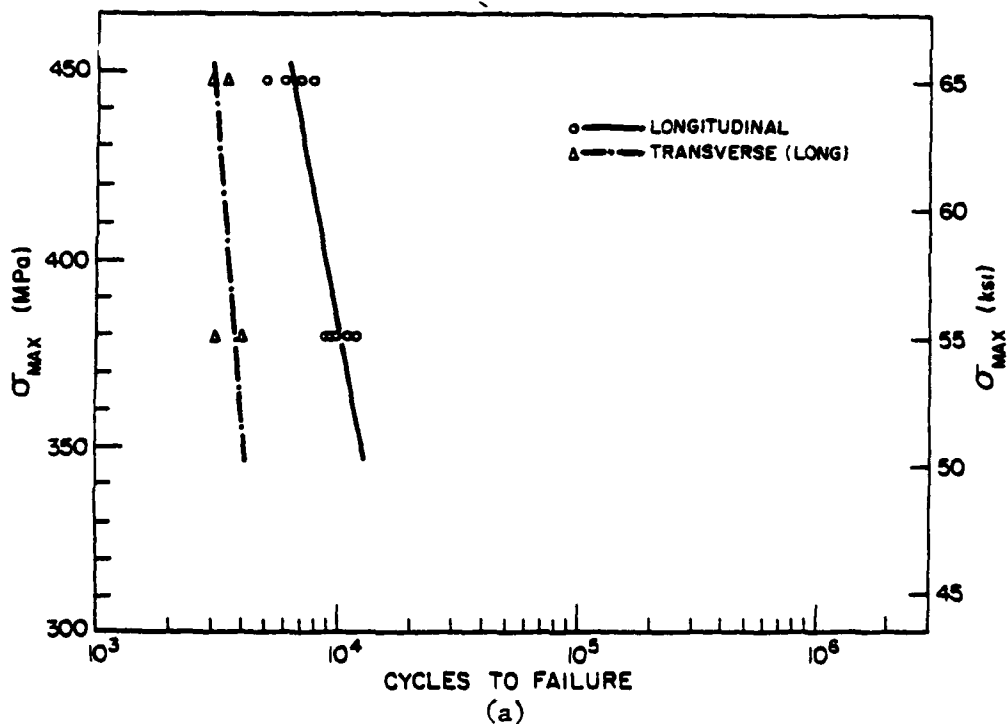


(a)

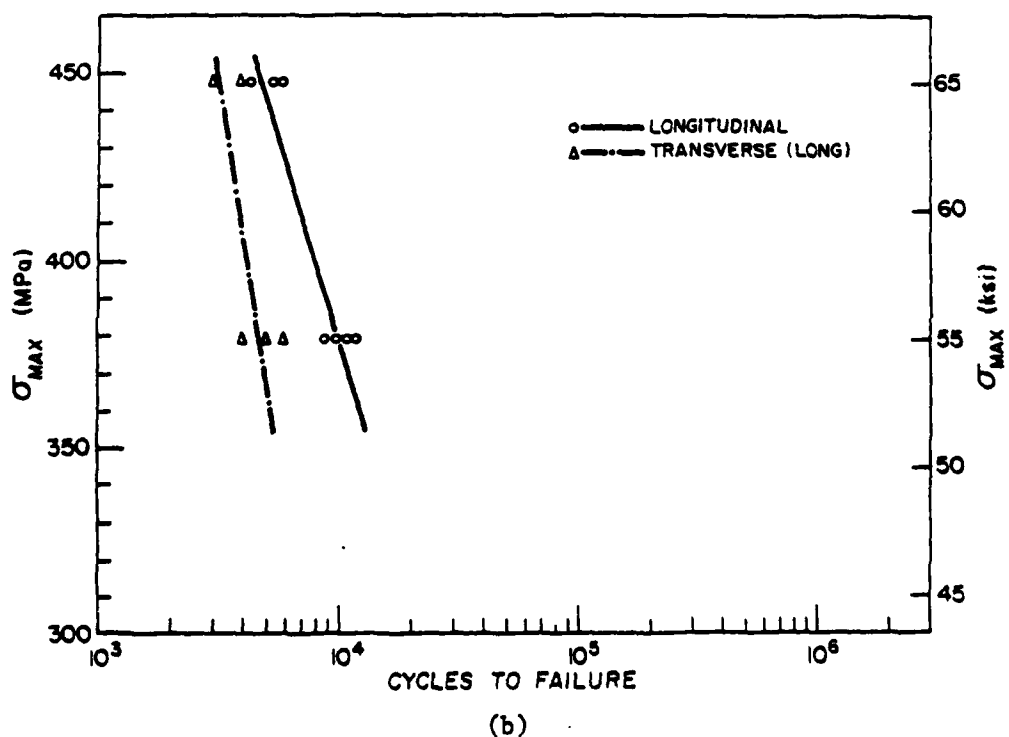


(b)

Figure 20. S-N curves for 0% Co P/M forged material tested in 3.5% NaCl solution salt fog. a) A processing, b) ABC processing.

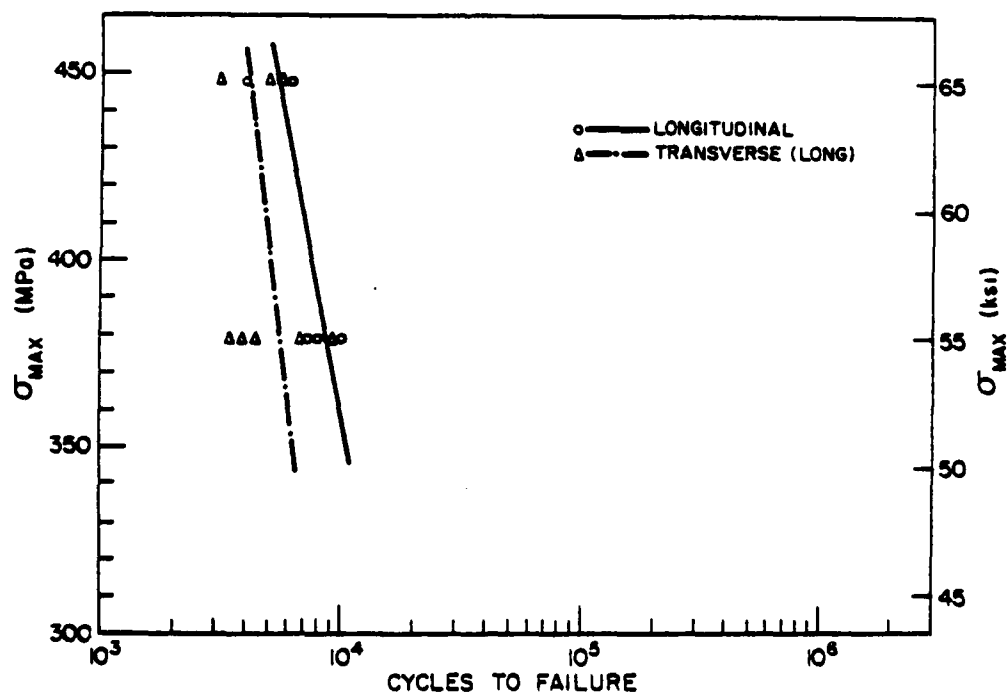


(a)

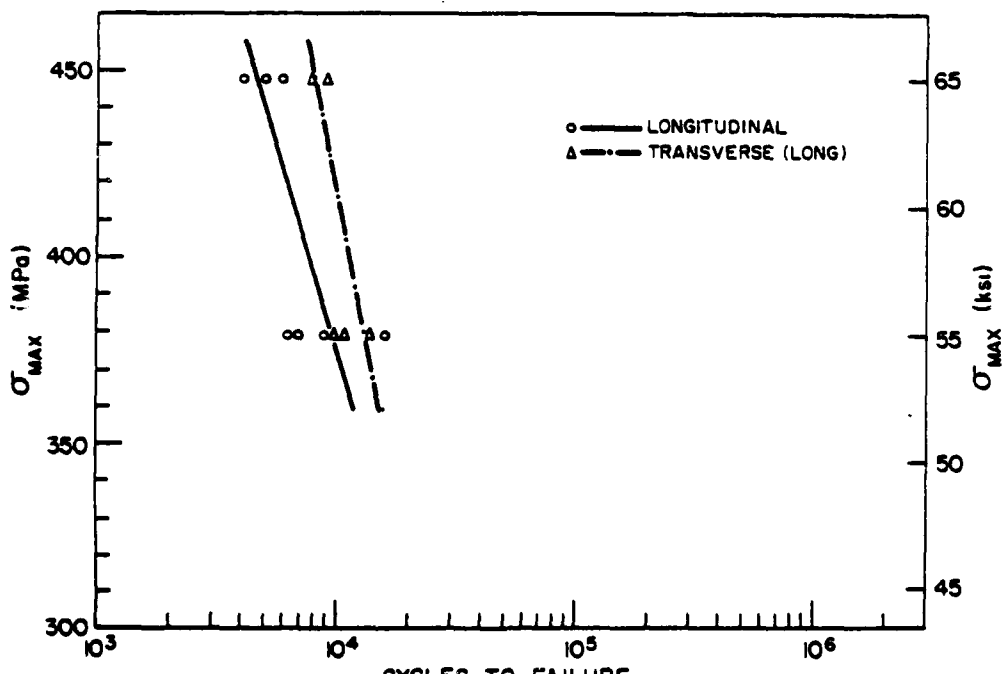


(b)

Figure 21. S-N curves for 0.4% Co P/M forged material tested in 3.5% NaCl solution salt-fog. a) A processing, b) ABC processing.

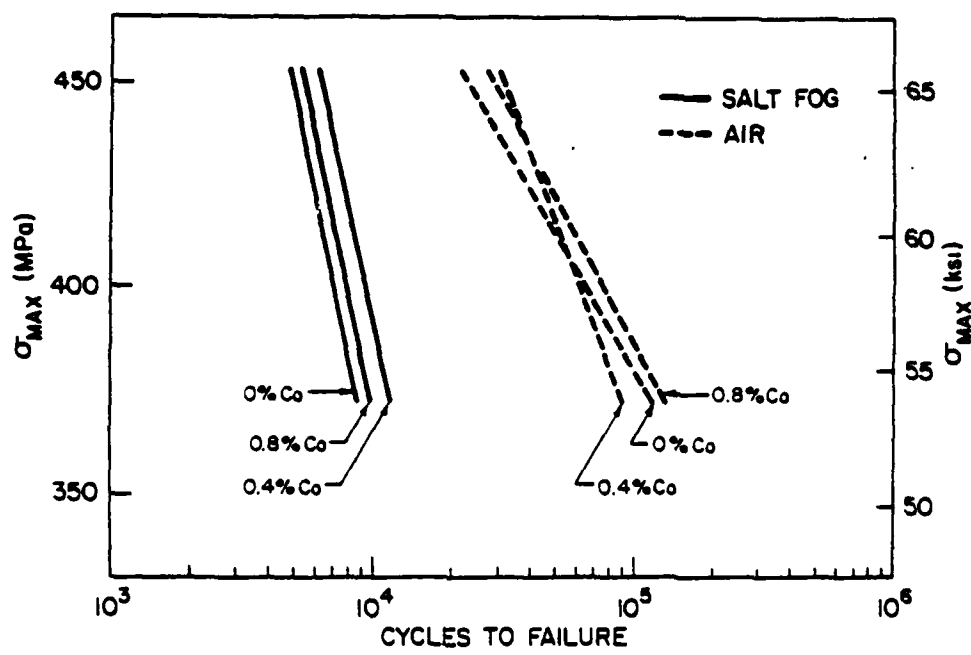


(a)

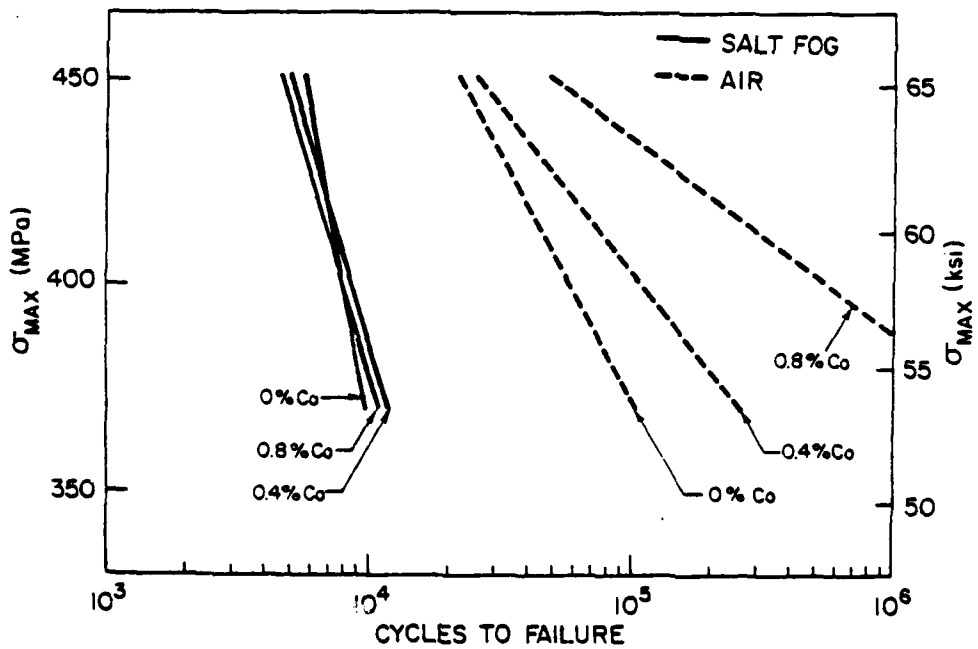


(b)

Figure 22. S-N curves for 0.8% Co P/M forged material tested in 3.5% NaCl solution salt-fog. a) A processing, b) ABC processing.

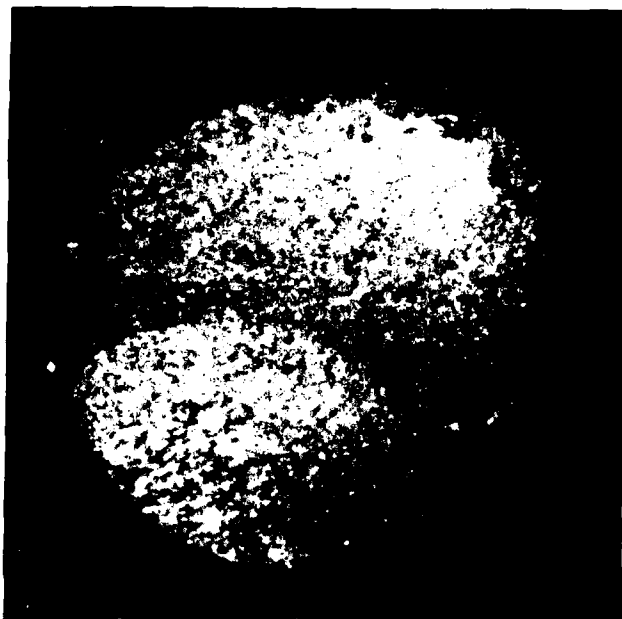


(a)



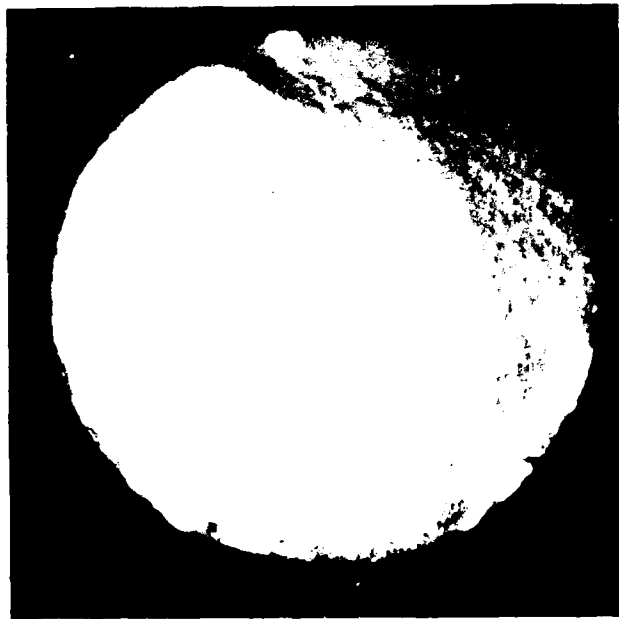
(b)

Figure 23. S-N behavior of P/M forged material tested in laboratory air and salt fog; L orientation. a) A processing, b) ABC processing.



0.5mm

a



0.5 mm

b

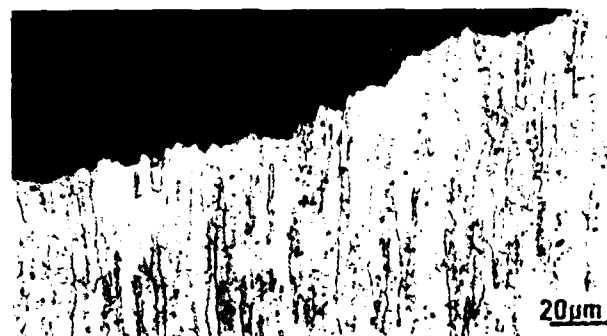
Figure 24. Optical micrographs of fatigue fracture surfaces tested in laboratory air; ABC processing, ST orientation, 0.4% Co. a) Low stress, b) high stress fatigue.



a

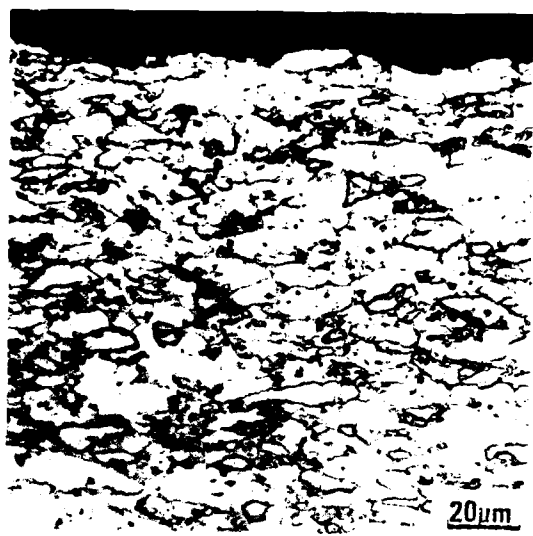


b



c

Figure 25. a) Profile of fracture surface showing stage I fatigue, stage II fatigue and overload regions; A processing, L orientation, 0.4% Co, low stress grain structure in b) fatigue, c) overload regions.

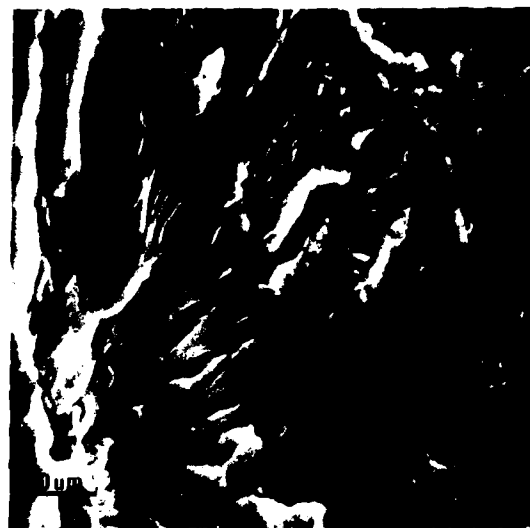


a



b

Figure 26. Grain structure at fatigue fracture surface, ST orientation and ABC processing. a) 0% Co, b) 0.8% Co. Keller's etch.



a

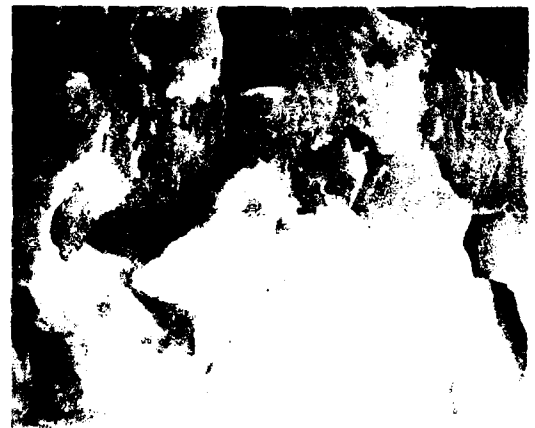


b

Figure 27. SEM, origin of fatigue fracture surface, S-N specimens tested in laboratory air. a) ABC processing, 0% Co, LT orientation, high stress, b) ABC processing, 0.4% Co, ST orientation, low stress. Crack propagates from left to right.



a



1.6um

b

Figure 28. SEM, fracture surface, Stage II, S-N specimens tested in laboratory air. a) L orientation, ABC processing, 0.4% Co, b) L orientation, ABC processing, 0.8% Co. Low stress. Crack propagates from left to right.



a



b

Figure 29. SEM, fracture surface, Stage II, S-N specimens tested in laboratory air. a) ST orientation, A processing, 0% Co, low stress, b) ST orientation, ABC processing, 0.8% Co, low stress. Crack propagates from left to right.



a

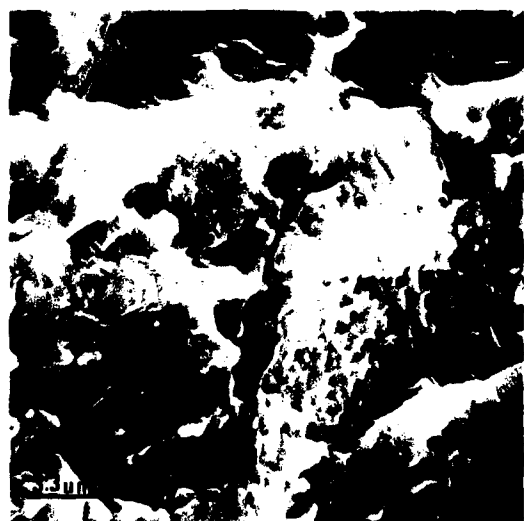


b

Figure 30. SEM, origin of fatigue fracture surface, S-N specimens tested in 3.5% NaCl solution salt-fog. a) A processing, 0.8% Co, L orientation, b) ABC processing, 0.8% Co, L orientation. Crack propagates from left to right.



a



b

Figure 31. SEM, fracture surface, Stage II, S-N specimens tested in 3.5% NaCl solution salt-fog, a) ABC processing, 0.4% Co, LT orientation, b) ABC processing, 0% Co, L orientation. Crack propagates from left to right.

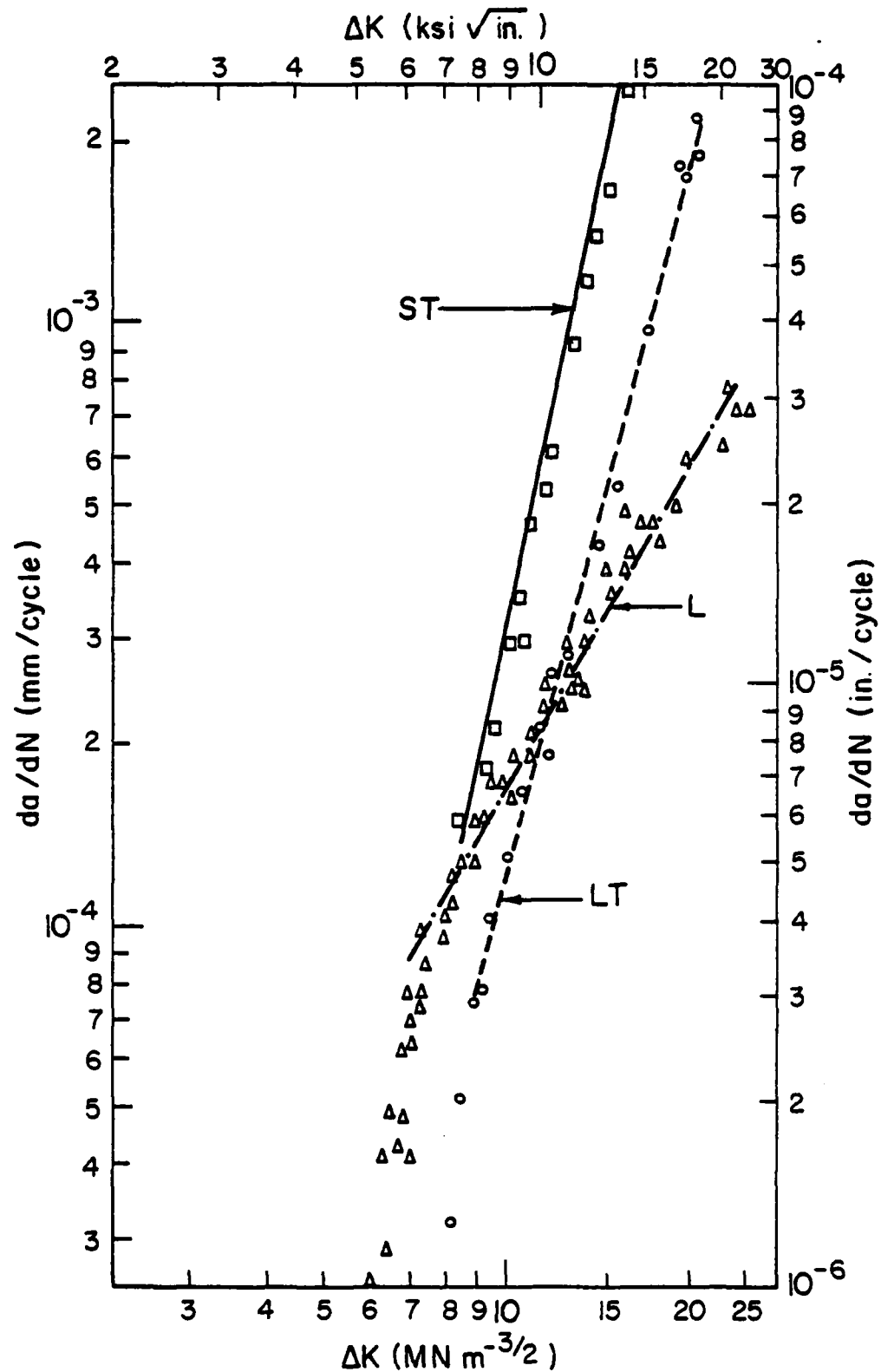


Figure 32. Crack propagation rate as a function of ΔK in laboratory air for L, LT and ST orientations; 0.4% Cobalt, A processing.

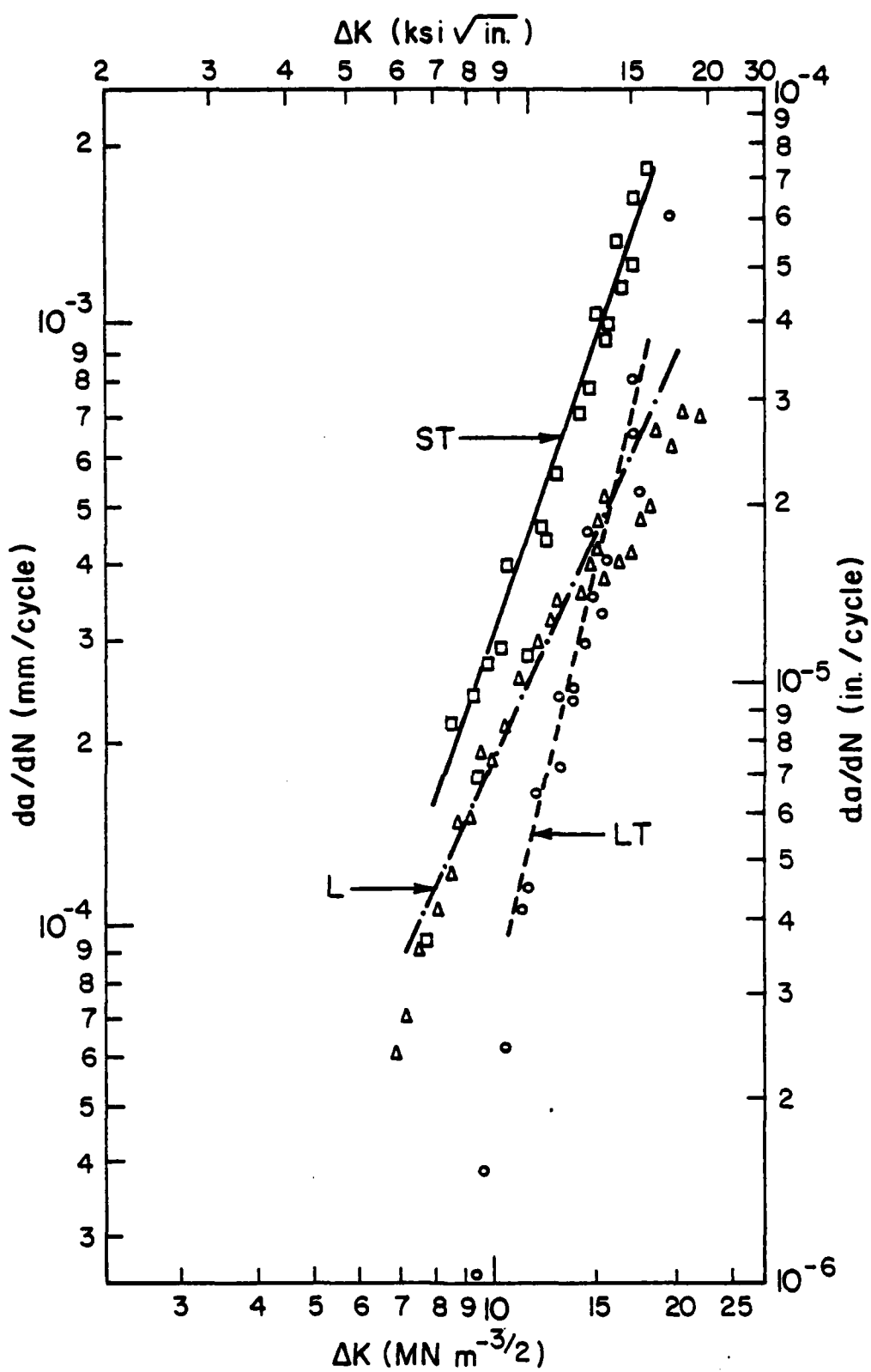


Figure 33. Crack propagation rate as a function of ΔK in laboratory air for L, LT and ST orientations; 0.4% Cobalt, ABC processing.

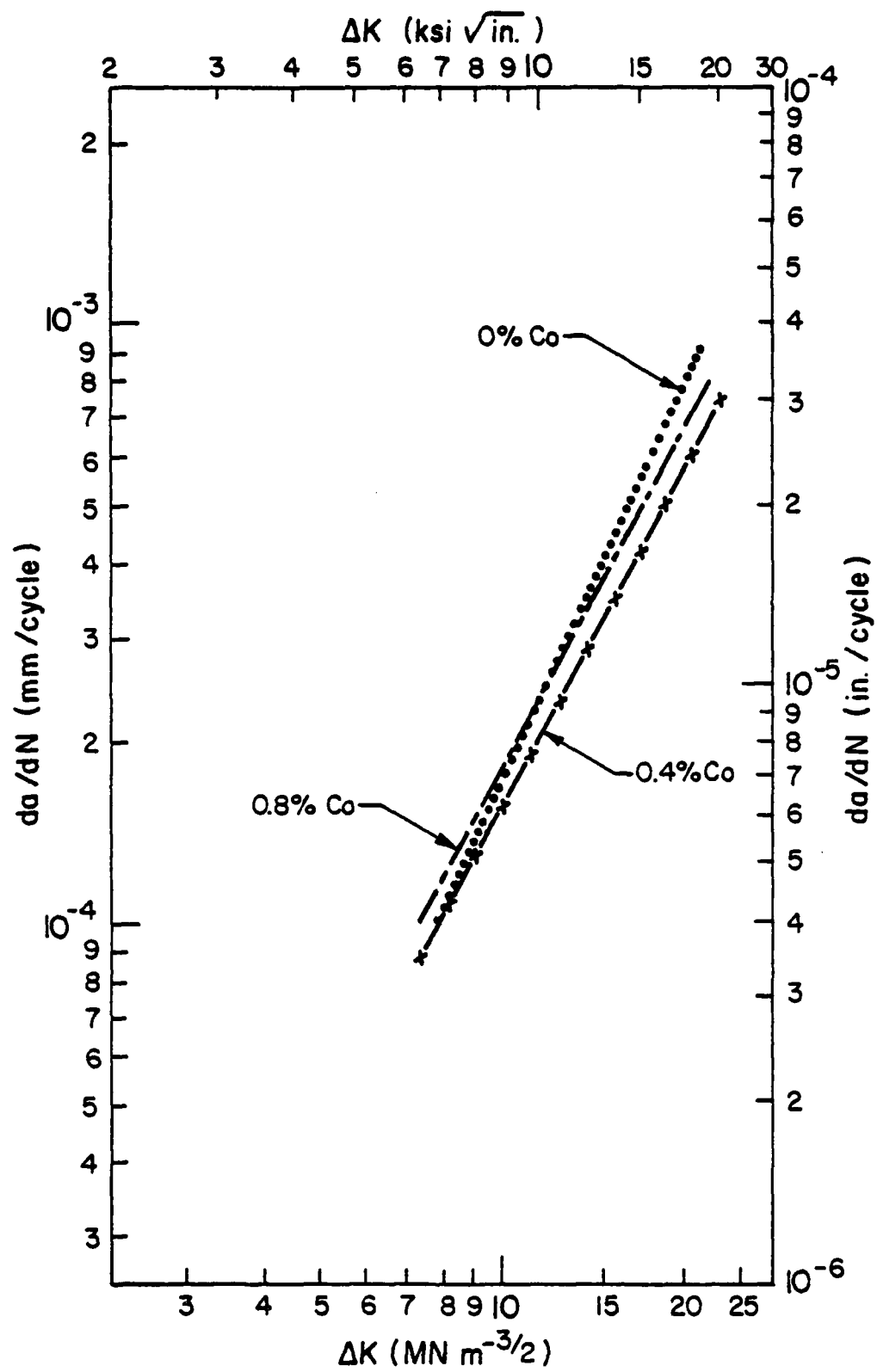


Figure 34. Crack propagation rate as a function of ΔK in laboratory air for 0% Co, 0.4% Co and 0.8% Co; L orientation, A processing.

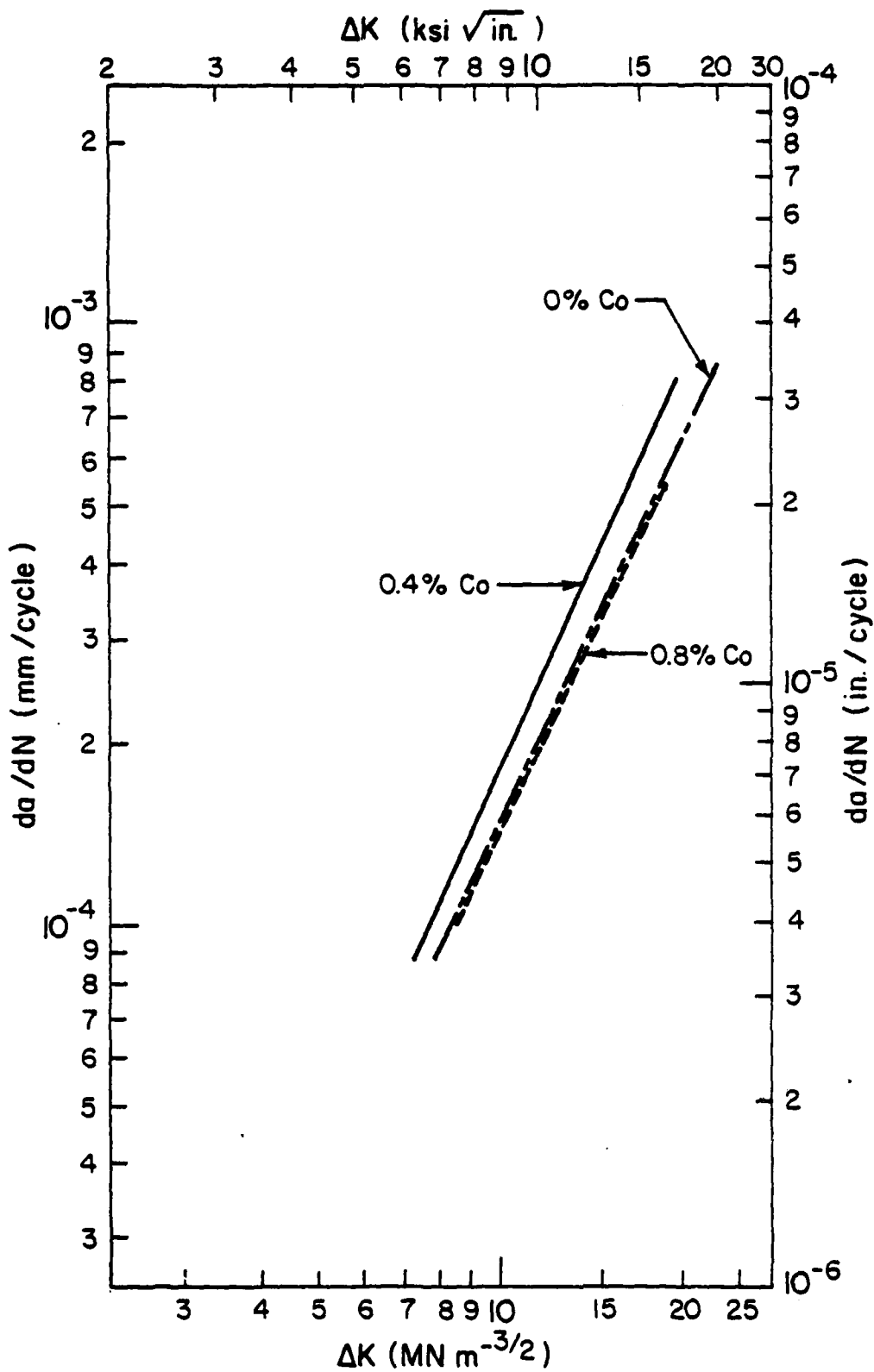


Figure 35. Crack propagation rate as a function of ΔK in laboratory air for 0% Co, 0.4% Co and 0.8% Co; L orientation, ABC processing.

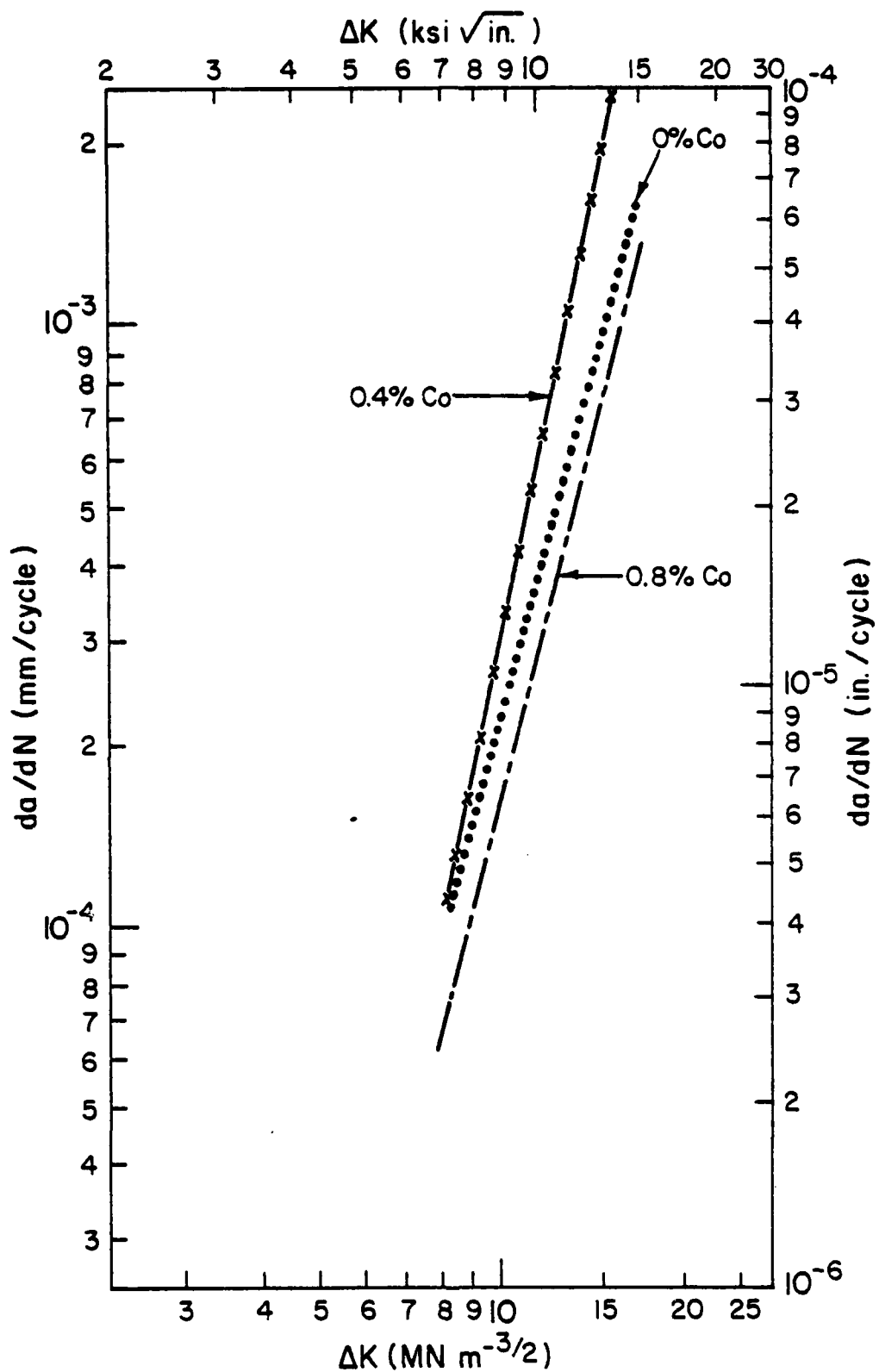


Figure 36. Crack propagation rate as a function of ΔK in laboratory air for 0% Co, 0.4% Co and 0.8% Co; ST orientation, A processing.

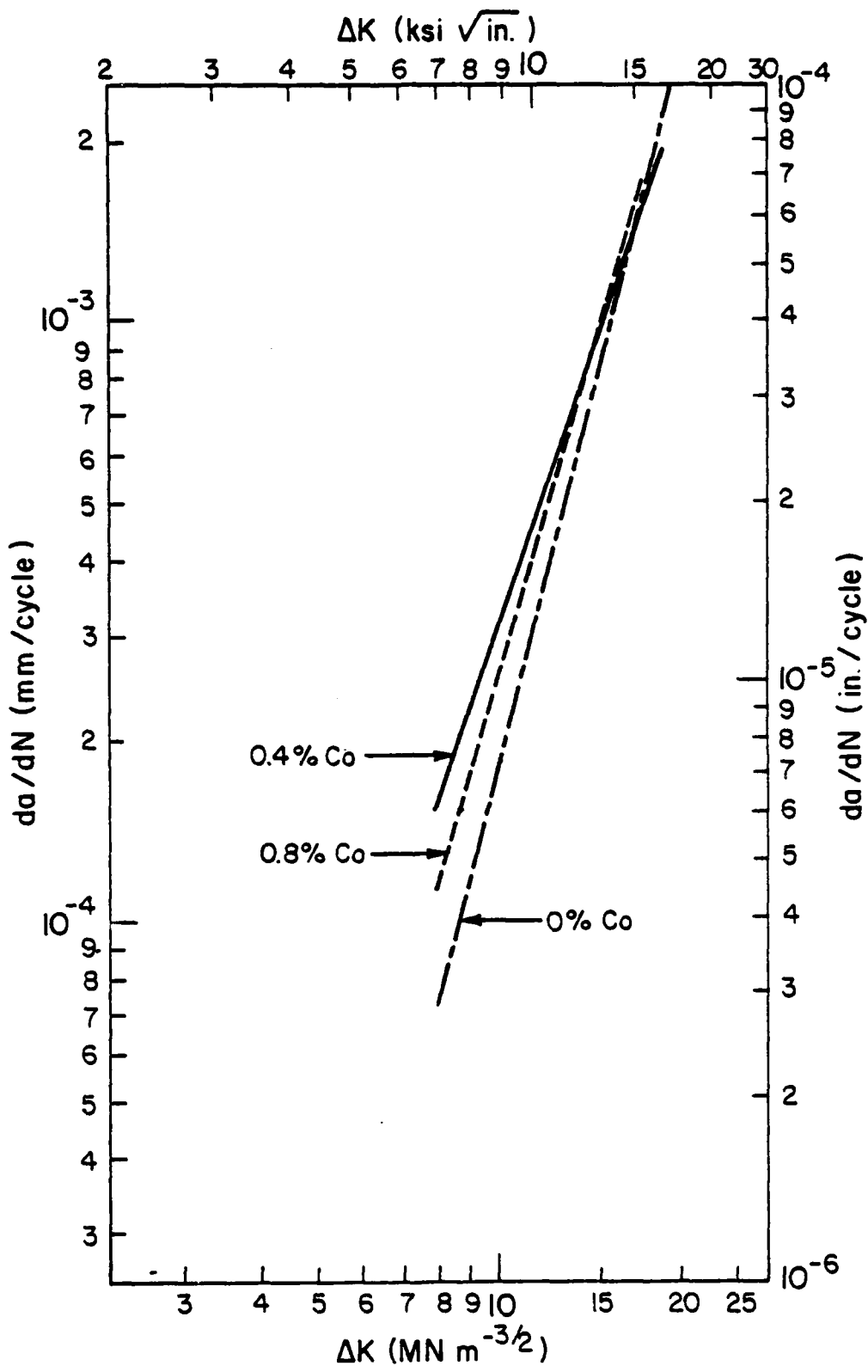


Figure 37. Crack propagation rate as a function of ΔK in laboratory air for 0% Co, 0.4% Co and 0.8% Co; ST orientation, ABC processing.

AD-A105 080

DREXEL UNIV PHILADELPHIA PA DEPT OF MATERIALS ENGINEERING F/8 11/6
A FUNDAMENTAL STUDY OF FATIGUE IN POWDER METALLURGY ALUMINUM AL-ETC(U)
AUG 81 A LAWLEY, M J KOCZAK AFOSR-77-3247

UNCLASSIFIED

2-3

AFOSR-TR-81-0692

SR-77-3247

247

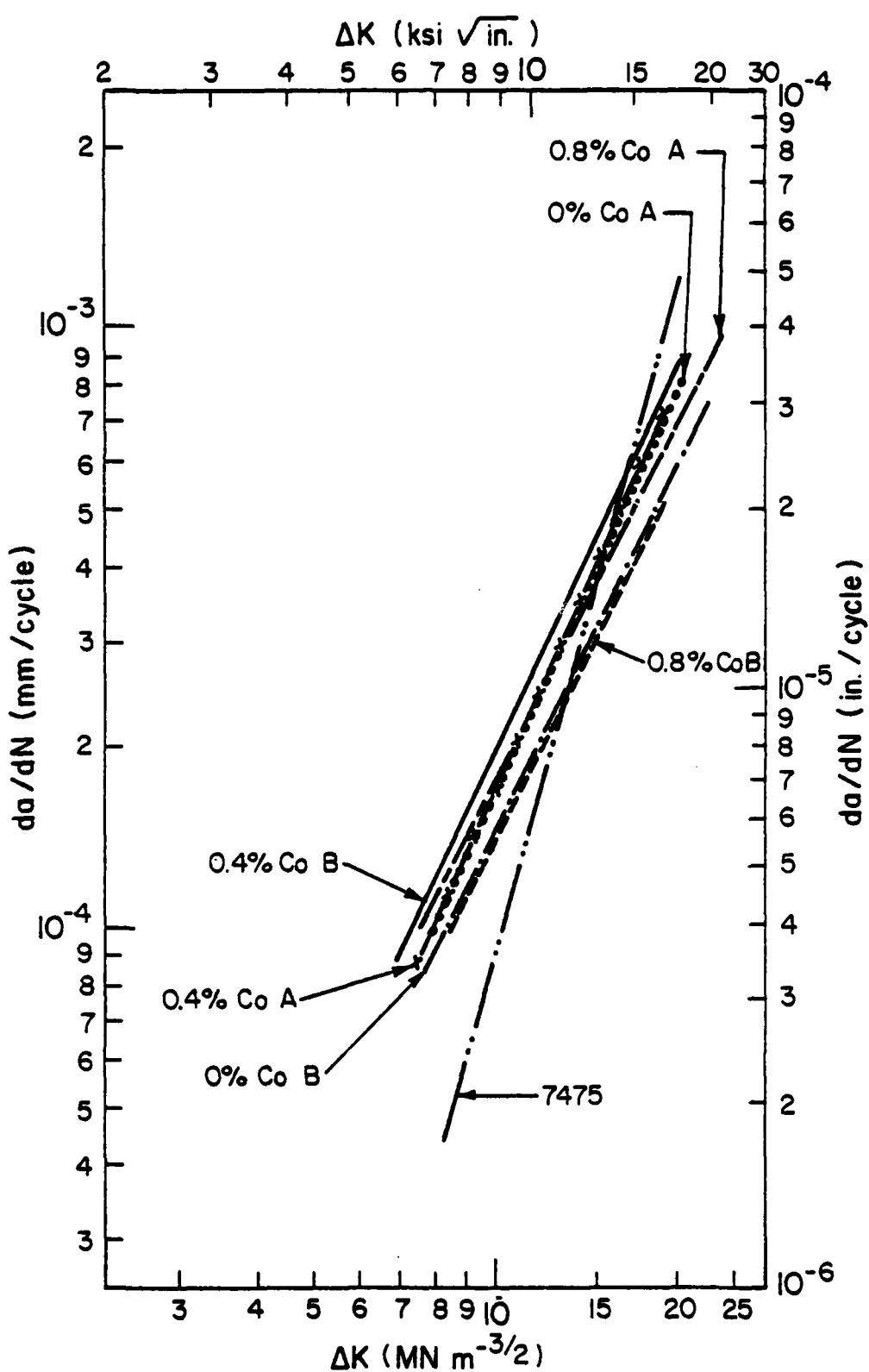


Figure 38. Crack propagation rate as a function of ΔK in laboratory air for the L orientation; 7475 I/M, A = P/M(A processing), B = P/M(ABC processing).

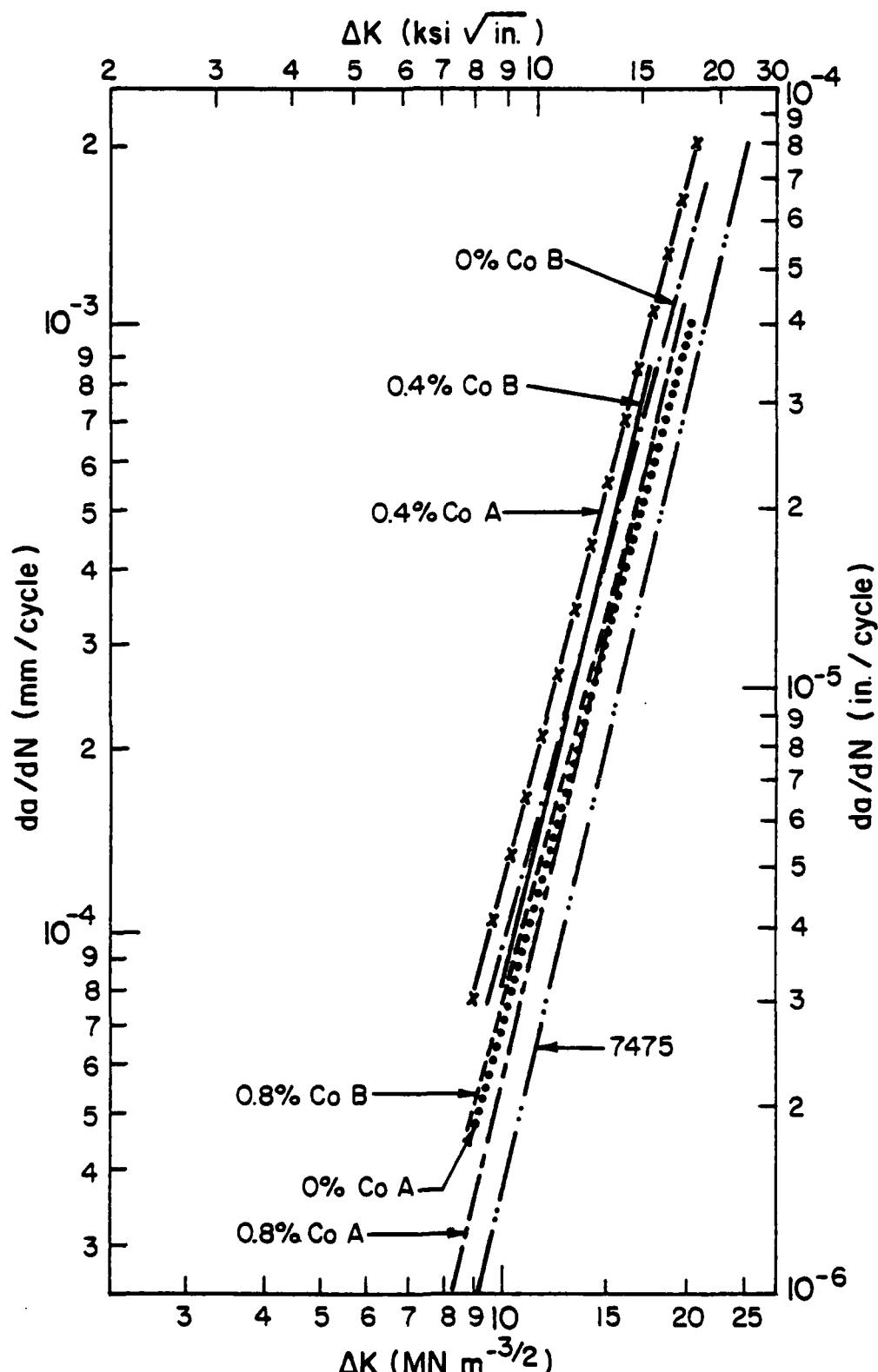


Figure 39. Crack propagation rate as a function of ΔK in laboratory air for the LT orientation; 7475 I/M: A = P/M (A processing), B = P/M (ABC processing).

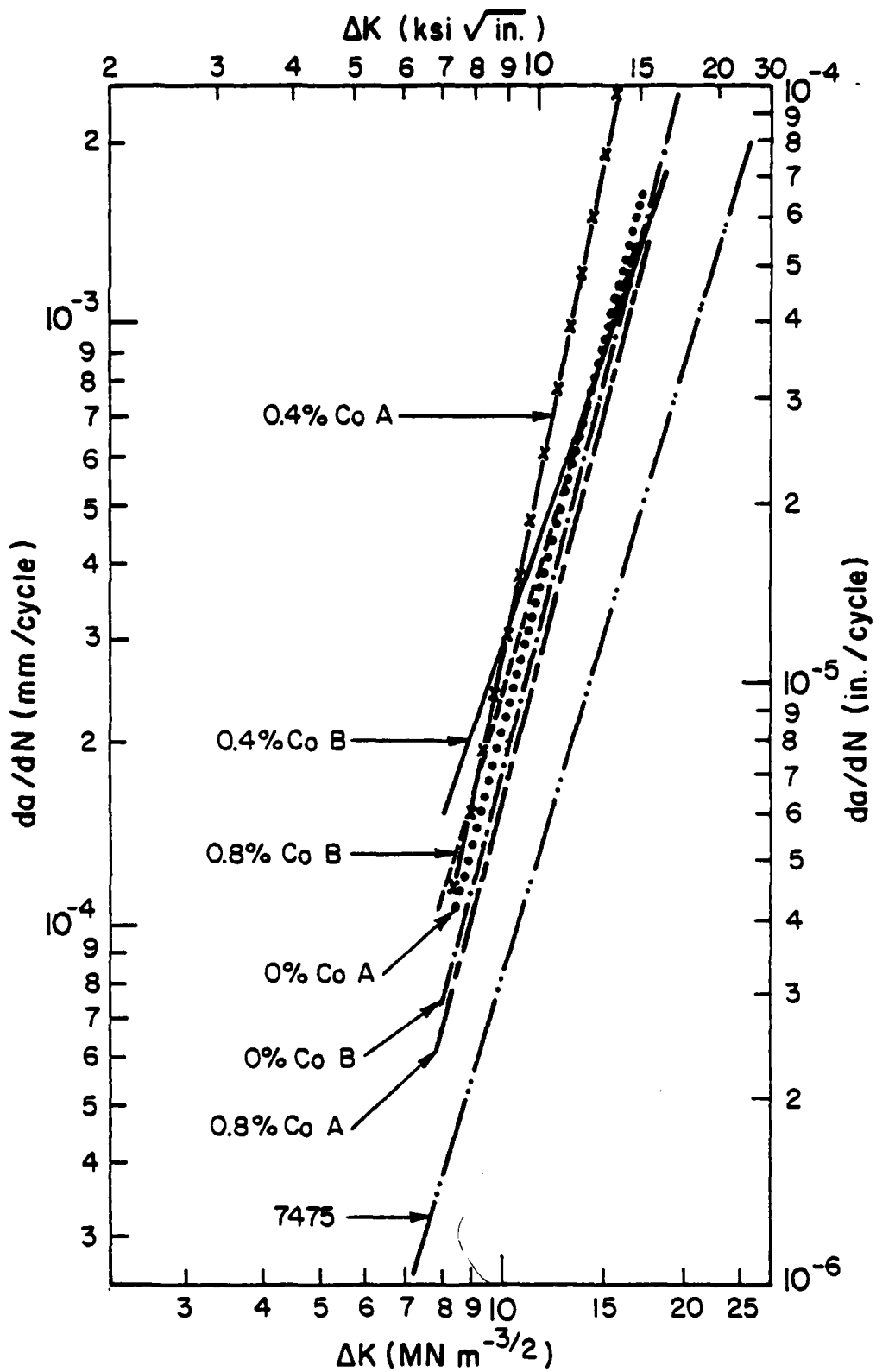


Figure 40. Crack propagation rate as a function of ΔK in laboratory air for the ST orientation; 7475 I/M, A = P/M (A processing), B = P/M (ABC processing).

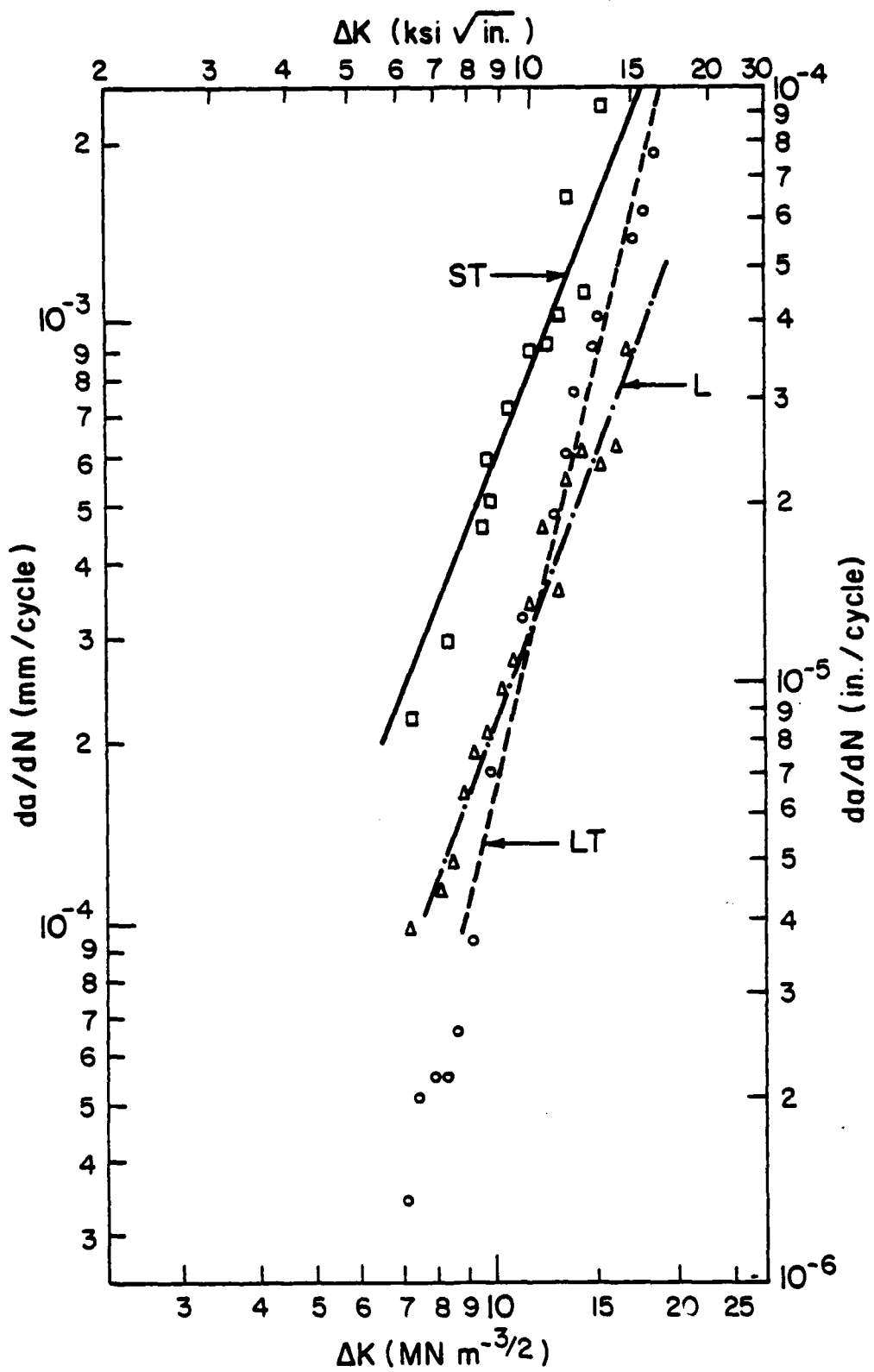


Figure 41. Crack propagation rate as a function of ΔK in 3.5% NaCl solution salt-fog for L, LT and ST orientations; 0.8% Cobalt, A processing.

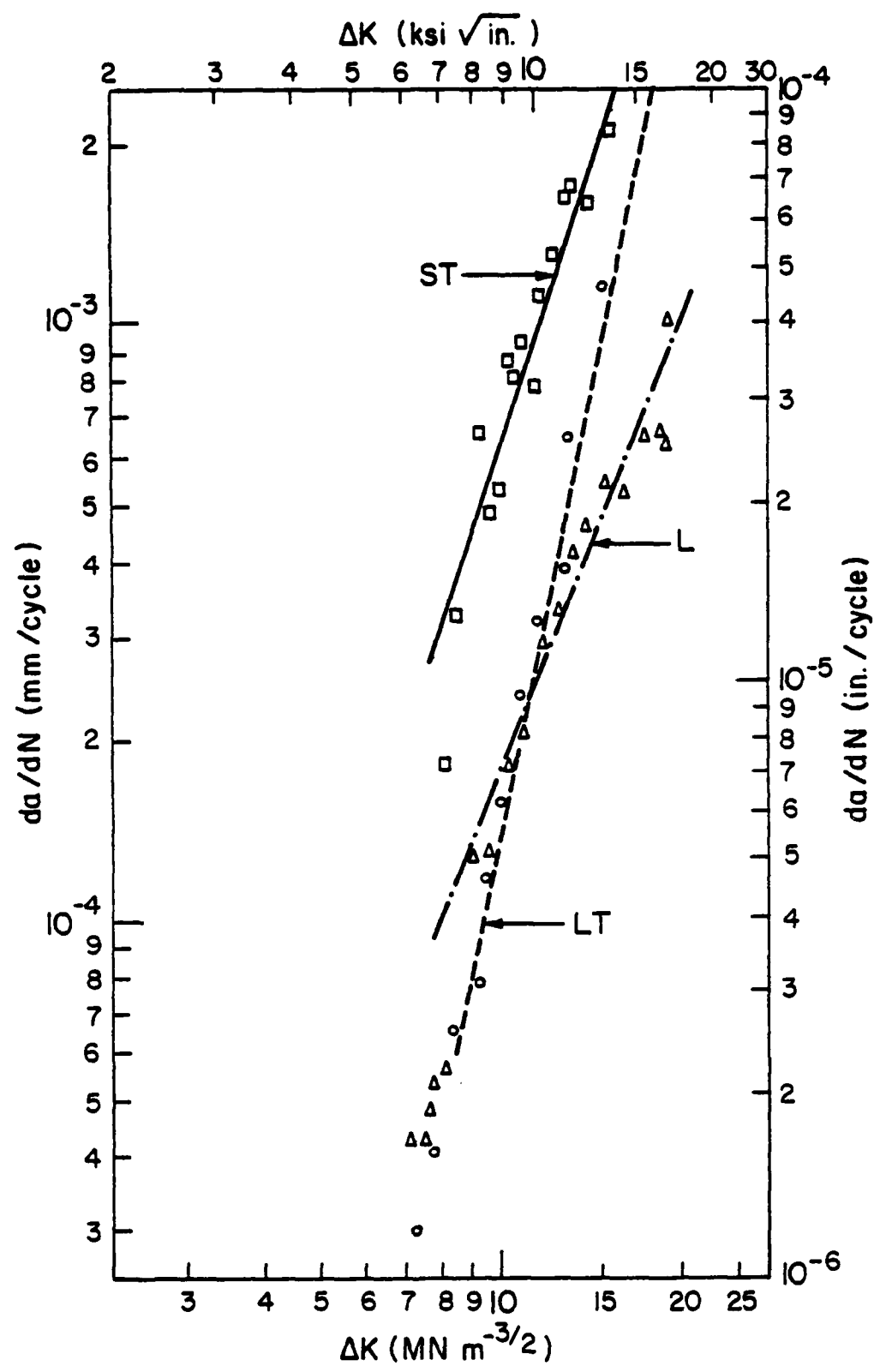


Figure 42. Crack propagation rate as a function of ΔK in 3.5% NaCl solution salt-fog for L, LT and ST orientations; 0.8% Cobalt, ABC processing.

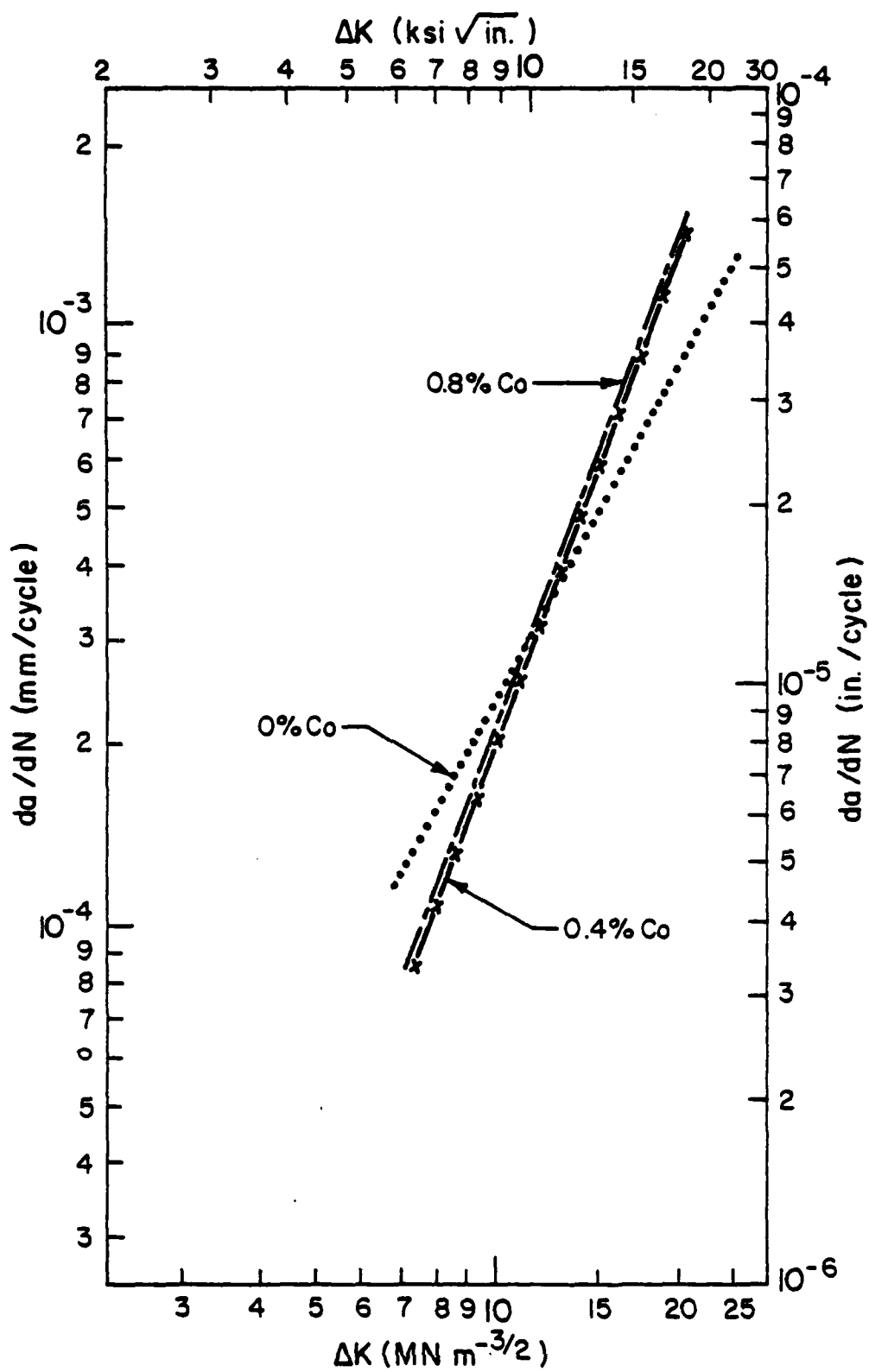


Figure 43. Crack propagation rate as a function of ΔK in 3.5% NaCl solution salt-fog for 0%, 0.4% and 0.8% Cobalt; L orientations, A processing.

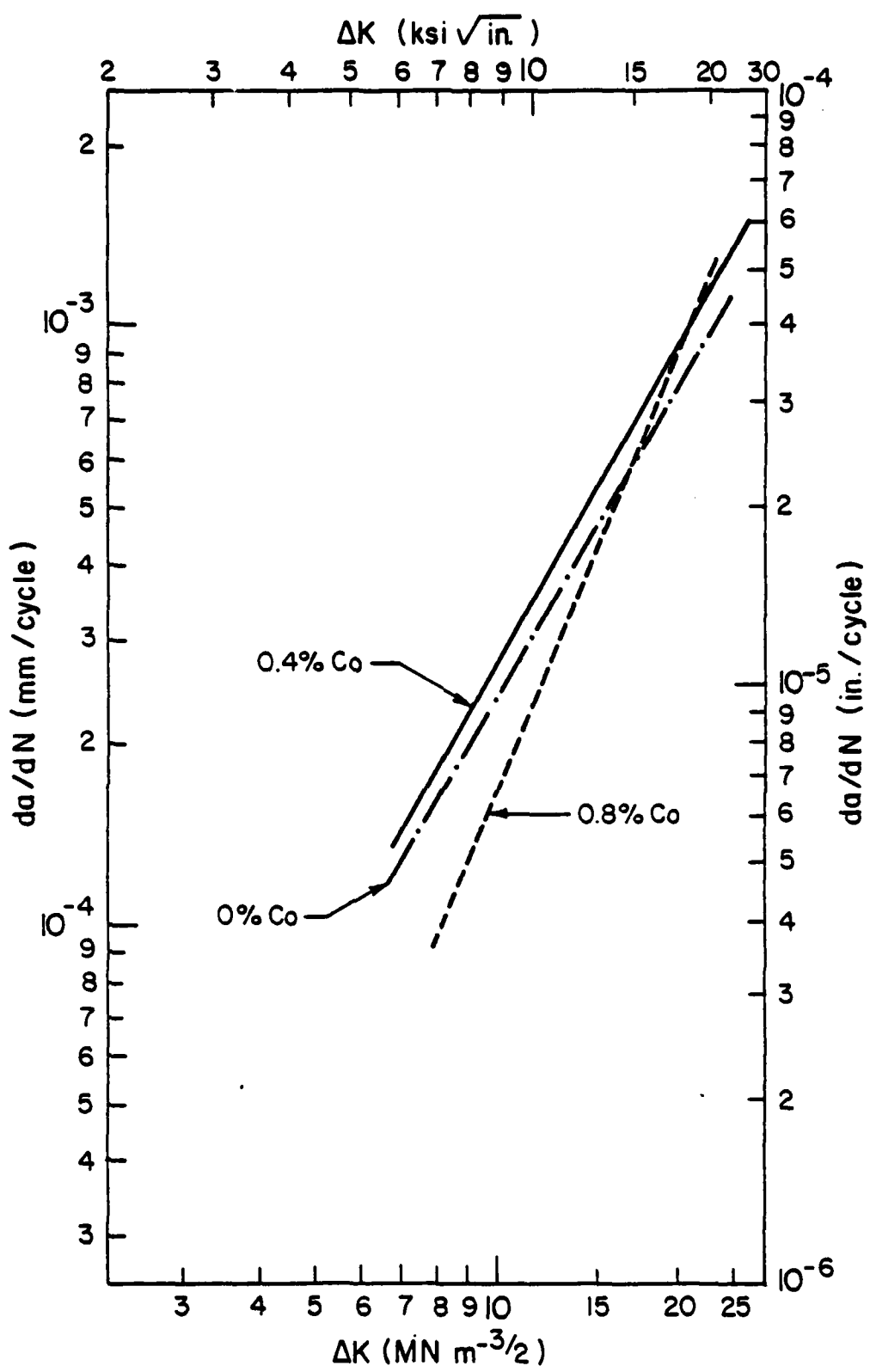


Figure 44. Crack propagation rate as a function of ΔK in 3.5% NaCl solution salt-fog for 0%, 0.4% and 0.8% Cobalt; L orientation, ABC processing.

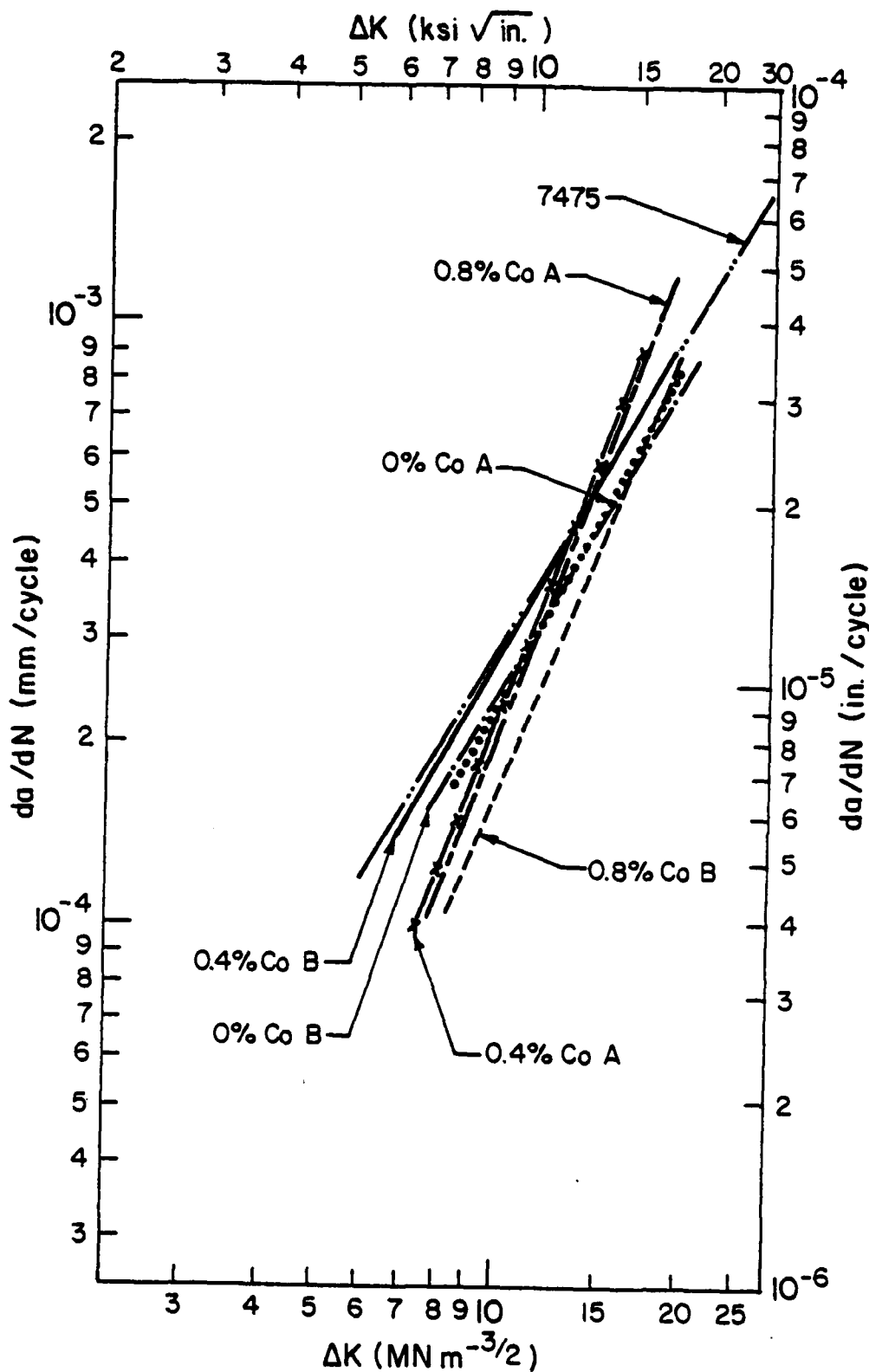


Figure 45. Crack propagation rate as a function of ΔK in 3.5% NaCl solution salt-fog for the L orientation; 7475 I/M, A = P/M (A processing), B = P/M (ABC processing).

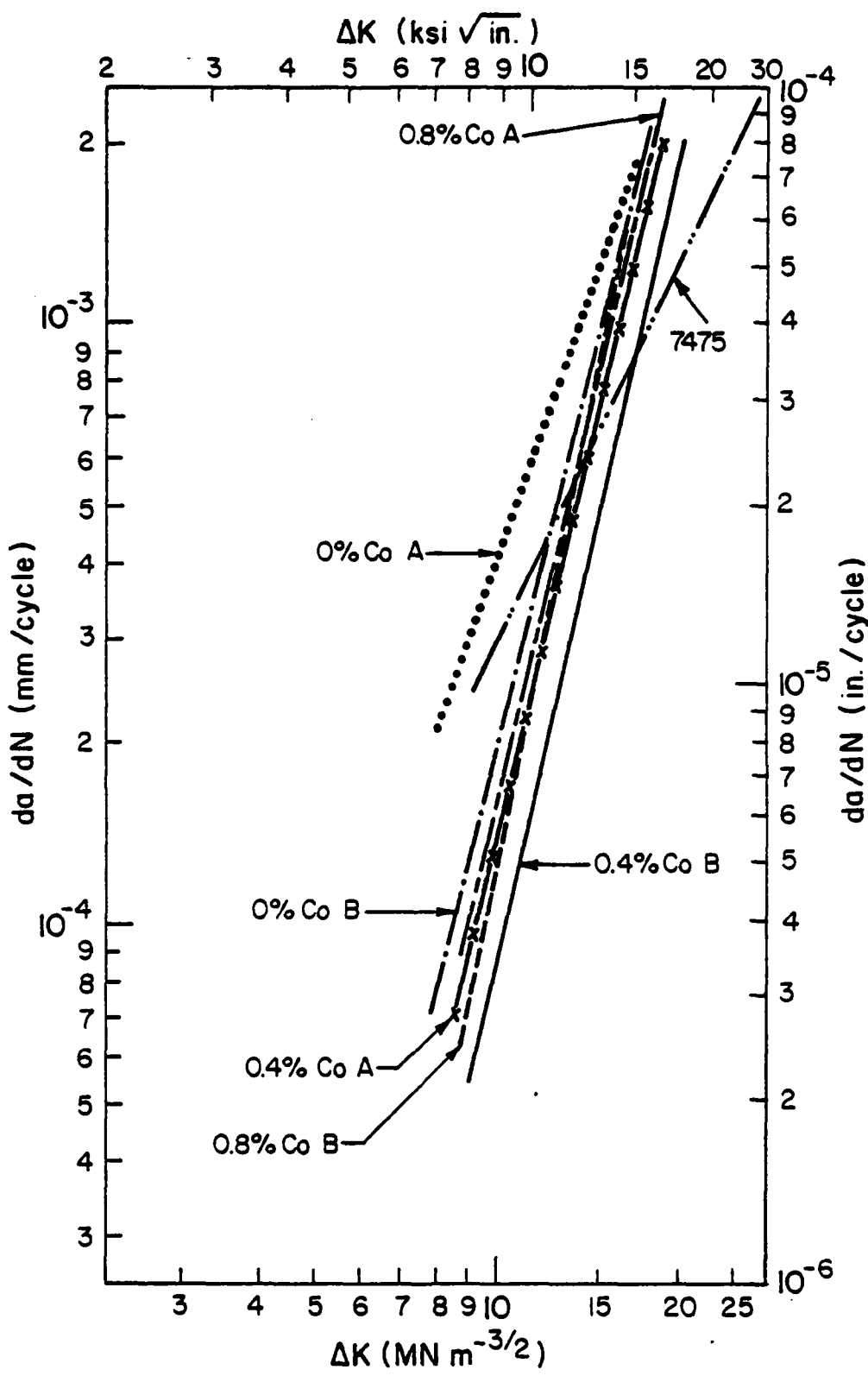


Figure 46. Crack propagation rate as a function of ΔK in a 3.5% NaCl solution salt-fog for the LT orientation; 7475 I/M, A = P/M (A processing), B = P/M (ABC processing).

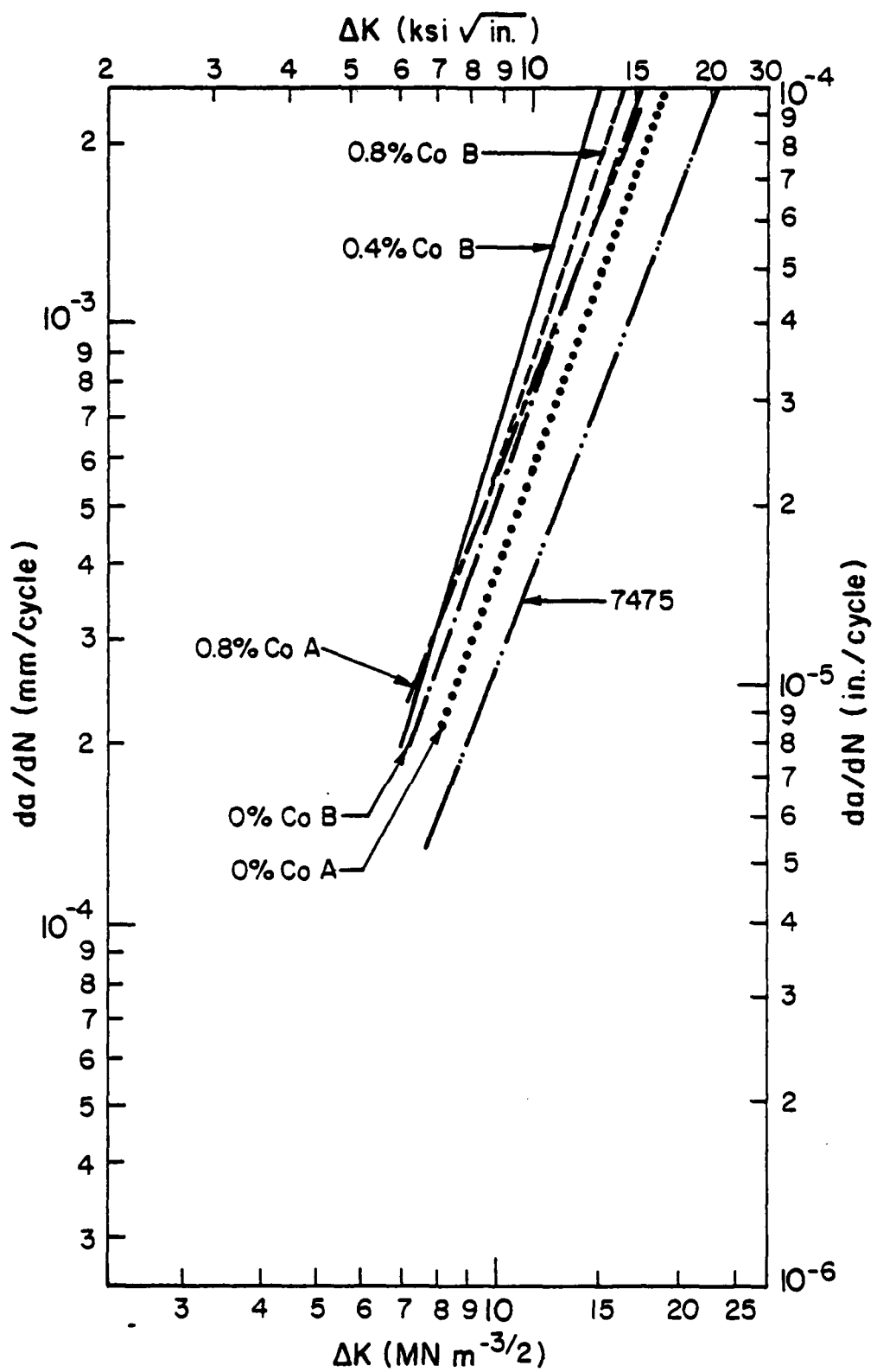


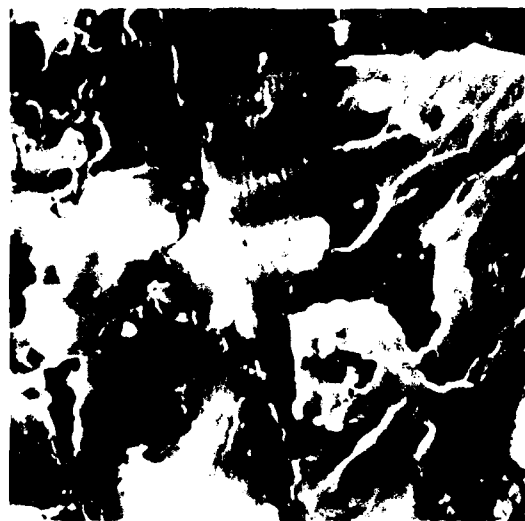
Figure 47. Crack propagation rate as a function of ΔK in 3.5% NaCl solution salt-fog for the ST orientation; 7475 I/M, A = P/M (A processing), B = P/M (ABC processing).



a



Figure 48. SEM, fracture surfaces of specimens tested in laboratory air at $\Delta K = 8.8 \text{ MN m}^{-3/2}$ (8 ksi $\sqrt{\text{In.}}$). a) 0.8% Cobalt, A processing, L orientation, b) 0% Cobalt, ABC processing, L orientation. Crack growth from left to right.



a



Figure 49. SEM, fracture surface of specimens tested in laboratory air at $\Delta K = 11 \text{ MN m}^{-3/2}$ (10 ksi $\sqrt{\text{in.}}$). a) 0.8% Cobalt, A processing, L orientation, b) 0% Cobalt, ABC processing, L orientation. Crack growth from left to right.



a

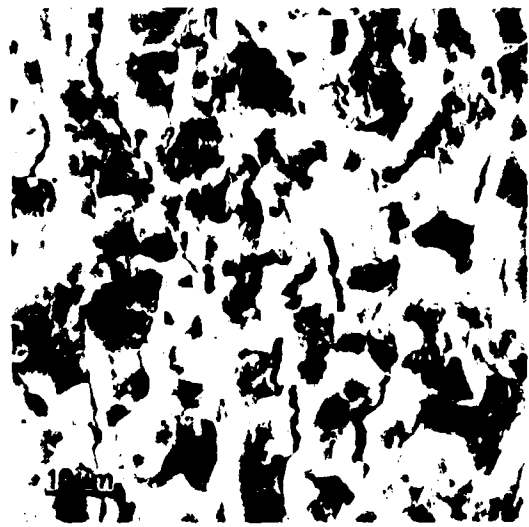
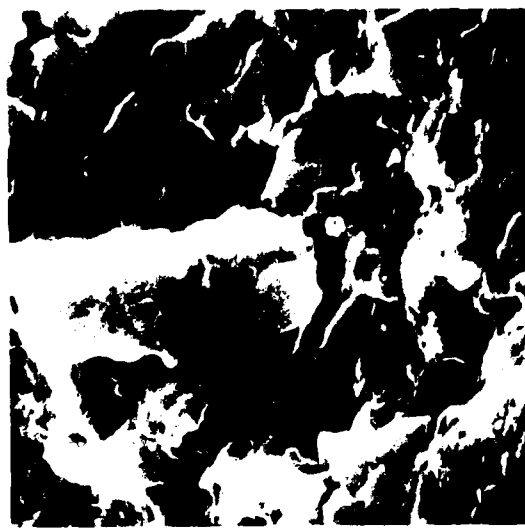


Figure 50. SEM, fracture surface of specimen tested in laboratory air; $\Delta K = 16.5 \text{ MN m}^{-3/2}$ (15 ksi $\sqrt{\text{in.}}$), 0.4% Cobalt, ABC processing, L orientation. a) 5000X, b) 1000X. Crack growth from left to right.



a

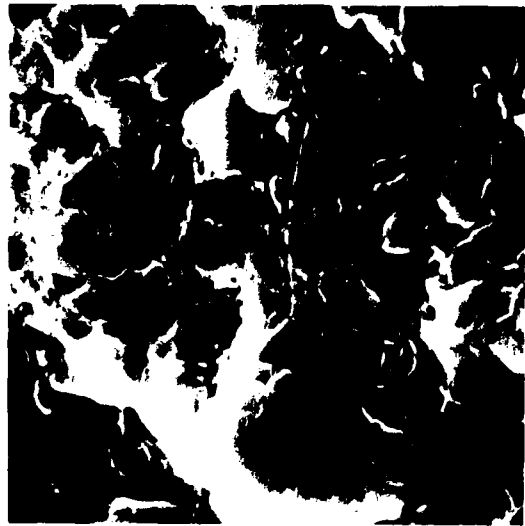
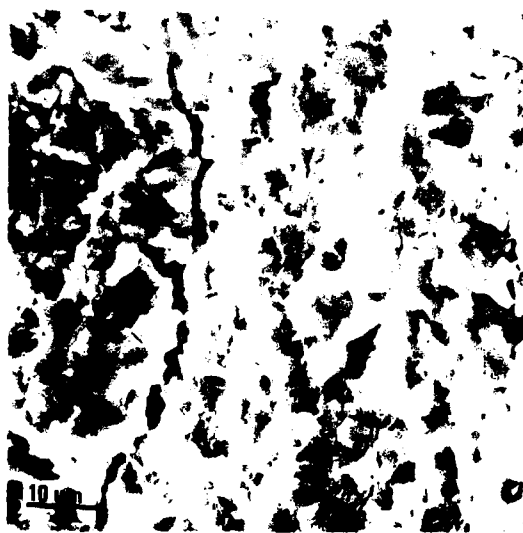


Figure 51. SEM, fracture surfaces of specimens tested in 3.5% NaCl solution salt-fog at $\Delta K = 8.8 \text{ MN m}^{-3/2}$ (8 ksi $\sqrt{\text{in.}}$).
a) 0.8% Cobalt, ABC processing, L orientation,
b) 0.8% Cobalt, A processing, L orientation. Crack growth from left to right.

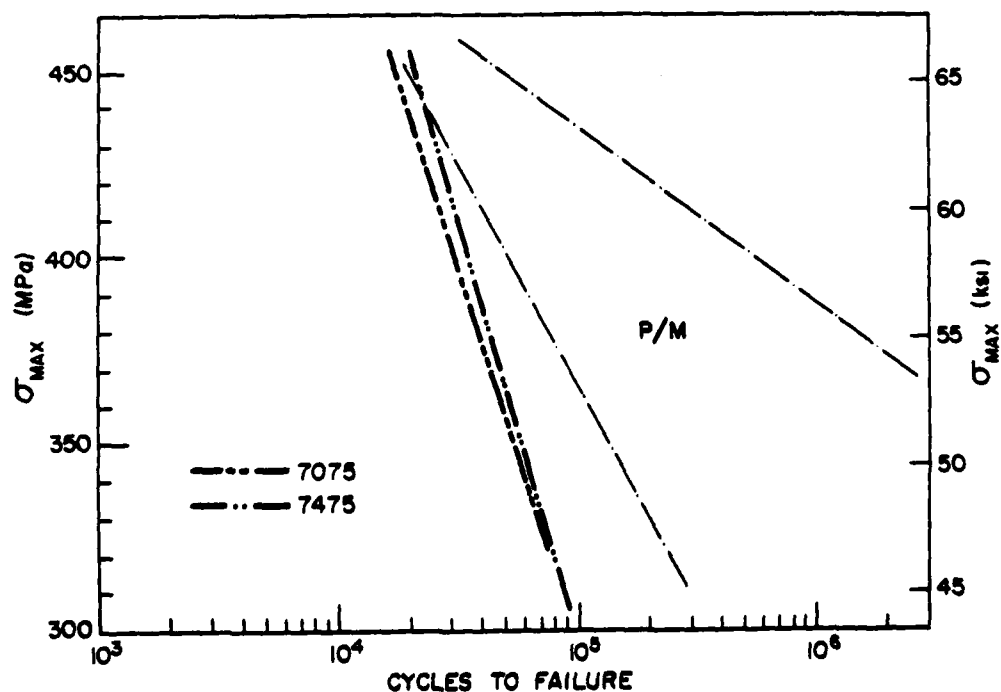


a

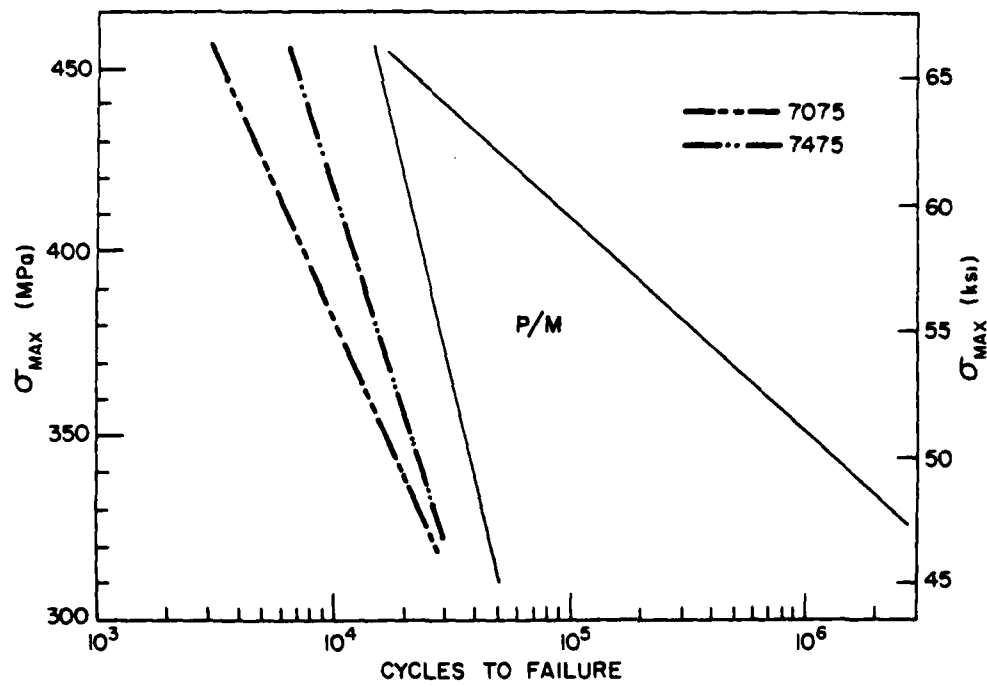


b

Figure 52. SEM, fracture surfaces of specimens tested in 3.5% NaCl solution salt-fog at $\Delta K = 16.5 \text{ MN m}^{-3/2}$ (15 ksi $\sqrt{\text{in.}}$).
a) 0.4% Cobalt, A processing, L orientation, b) 0% Cobalt, ABC processing, L orientation. Crack growth from left to right.

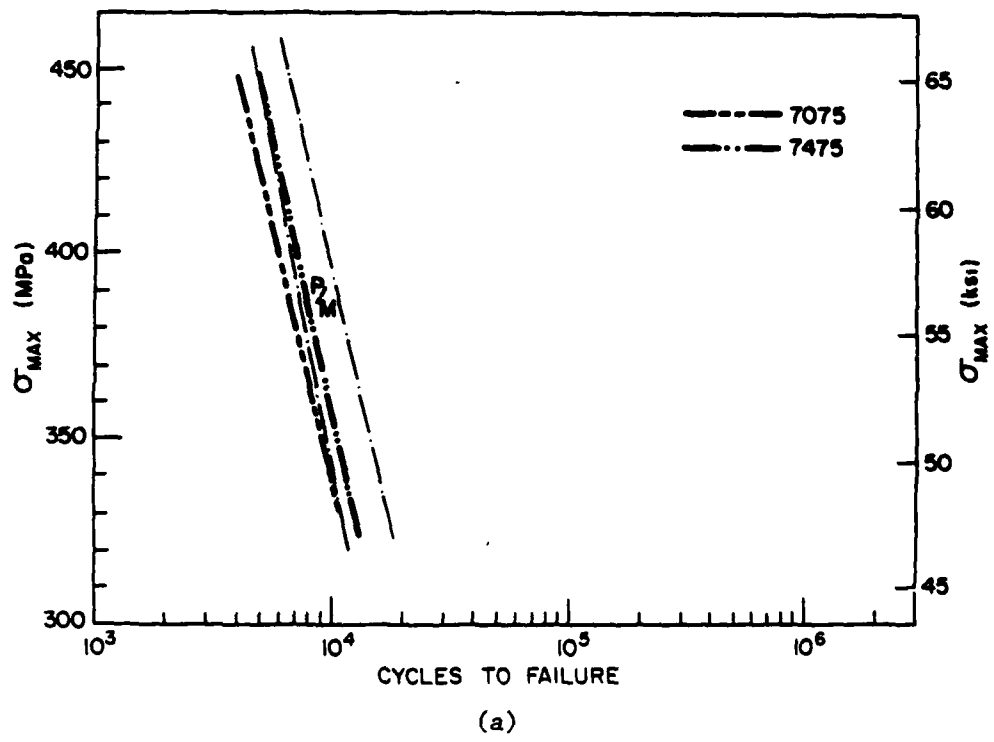


(a)

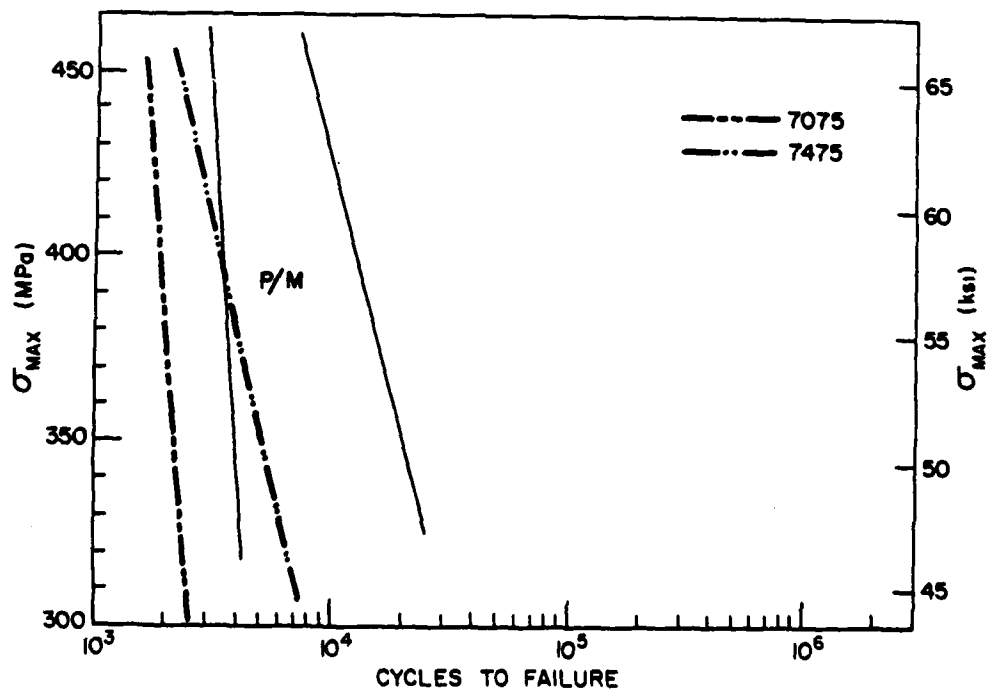


(b)

Figure 53. Comparison of S-N curves of I/M 7475 and I/M 7075 with P/M materials, tested in laboratory air. a) L orientation, b) ST orientation.



(a)



(b)

Figure 54. Comparison of S-N curves of I/M 7475 and I/M 7075 with P/M materials, tested in 3.5% NaCl solution salt-fog.
a) L orientation, b) ST orientation.

PART II

FATIGUE OF A HIGH-STRENGTH POWDER ALLOY;
THE ROLE OF DEFORMATION PROCESSING

SUMMARY

The effect of local deformation on fatigue life and fatigue crack growth rates was determined in powder metallurgy preforms that had been warm forged in plane strain. Atomized aluminum alloy powder (CT-91) was isostatically compacted, sintered, hot-repressed and warm-forged in plane strain to provide full density material. Visioplasticity was used to establish the exact local deformation at various locations in the forging. After heat treatment, longitudinal and short transverse fatigue specimens were excised from regions of the forging at true local strains (ϵ) of 0, 0.3, 0.6 and 0.7. Similarly, compact fatigue crack growth specimens were excised from forgings for the longitudinal and short transverse orientations at true local strains of $\epsilon = 0.0, 0.5$ and 0.7. Tension-tension axial fatigue tests ($R = +0.1$) were run in air and salt-fog to determine the portion of the S-N curves between 60 ksi (414 MPa) and 70 ksi (483 MPa). Weibull analysis of the data was used to establish the median life S-N curves. Fatigue crack growth rate tests were run in air and salt fog at $R = +0.1$ on compact tension specimens.

Increasing the amount of flow increases fatigue life in air in the longitudinal orientation but has little effect in the short transverse orientation. Fatigue life in salt fog is much lower than in air in each orientation. In salt fog, short transverse fatigue life is decreased slightly but there is no significant change in longitudinal fatigue life.

Fatigue crack growth rates in air in both the longitudinal and short transverse orientations increase as the level of local deformation increases; the magnitude of the increase is highest at low ΔK levels. In salt fog, fatigue crack growth rates are higher than in air. At low ΔK , increasing deformation first increases fatigue crack growth rates but at higher strain levels the rate decreases; however, the rate is always higher than in the zero flow condition. At high ΔK levels, local flow decreases fatigue crack growth rates in salt fog.

Optical metallography, TEM and SEM were used to characterize microstructure and fracture morphology. The fatigue life and crack growth response are explained in terms of the form and scale of the microstructure, the relative sizes of the plastic zone at the crack tip and microstructural features. Of primary importance are the grain and sub-grain size, the precipitate, dispersoid and oxide size and distribution, and the extent of secondary cracking.

INTRODUCTION

Over the past several years there has been significant interest and numerous research activities in the area of fabricating and evaluating wrought forms that start from a metal powder compact, rather than a cast ingot. It has been well established that the amount and mode of deformation has a significant effect on the properties of ferrous powder formed materials (12). This is especially true for the dynamic properties such as impact and fatigue. It has been found that lateral

flow or shearing, is important in facilitating complete elimination of porosity and in achieving the highest mechanical property integrity.

Properties and performance of ferrous powder metal (P/M) hot formed components have exceeded those of counterparts made from conventional ingot metallurgy (I/M) processes (12). The superior performance of P/M formed components has been attributed to the greater degree of homogeneity achievable with powder products. This greater homogeneity contributes to more efficient utilization of alloying elements. However, the superior properties are achieved only when there is sufficient lateral flow to eliminate porosity, fragment powder particle surface oxides, and generate adequate nascent surfaces to develop high integrity metallurgical bonds.

Atomized powders have extremely fine cast structures that homogenize readily, thus eliminating the segregation problem. The inclusions in powders are finer than in large cast ingots and at worst can be no larger than the size of the powder particle. Furthermore, most of the oxides are on the surface of the powder particles. In the case of ferrous materials, these oxides can be reduced during the sintering process. These factors contribute to greater microstructural and chemical homogeneity and less mechanical fibering.

Aluminum alloy powders present a somewhat different problem in that the thermodynamics are such that surface oxides cannot be reduced during sintering. However, recent work on high strength

powder processed aluminum alloys has shown a similar potential to that realized with ferrous powder materials (21,28,31,35). It has been found that lateral flow has a beneficial effect on the fatigue properties of P/M formed aluminum alloys of equivalent composition to I/M 2014 and 6061 (13).

Similar results were found for P/M formed aluminum alloys that were equivalent to the high strength I/M 7075 alloy. When comparisons were made in notched axial fatigue testing an enhancement of endurance limit of up to 40% was realized for the P/M formed material (17,21). It was found that powder alloy composition and processing history affected the crack propagation behavior. Proper selection of these variables can provide material with properties superior to those of corresponding I/M material (28,31).

In the work on aluminum powder alloys cited above, no attempt was made to correlate the effects of precise amounts of deformation with microstructure and material properties. Therefore, it was the purpose of this study to determine the effect of microscopic lateral flow on the structure and the resulting axial fatigue life and crack propagation resistance of a hot formed high strength aluminum alloy powder material in air and a salt-fog environment.

EXPERIMENTAL PROCEDURE

1. Material and Consolidation

The aluminum alloy powder used in this study was CT-91. Powder composition and size distribution data are summarized in Tables I through III. Billet fabrication procedures involving cold isostatic pressing and hot pressing were similar to those described in Part I of this report.

2. Plane Strain Forging and Heat Treatment

Preforms were cut from the hot-compacted billet to provide upset ratios of 0, 1.5:1 and 2:1 after plane strain forging, Figure 1. Upset ratios provide average macroscopic true strains (ϵ) of 0, 0.4 and 0.7, where $\epsilon = -\ln[h_f/h_o]$; h is the height dimension, parallel to Z in Figure 1. The dimensions after forging were 51mm x 127mm x 76mm high (2 in. x 5 in. x 3 in. high). The preform sizes and upset ratios are given in Table IV. In order to make the preforms, the hot compacted billet was cut into 76mm, 114mm and 152mm high cylinders (3 in., 4 1/2 in., and 6 in. high). The height dimension of all preforms was parallel to the axis of symmetry of the powder billet, which was also the direction of hot axial compaction. All six preform surfaces were milled to provide perpendicular faces with dimensions accurate to within 0.13mm (0.005 in.).

All metal working operations involve friction and therefore inhomogeneous deformation. Local strains were calculated by the visioplasticity method in which grid markings are used on sectioned billets. Laminated preforms of 7075 aluminum plate were built-up of two 1.2 in. (1.27 cm) thick slabs and one 1 in. (2.54 cm) thick slab. Grids, 0.394 in. (1 cm) square, were scribed on both faces of the slab. A toolmaker's height gage with a carbide point was used to scribe the grid onto the surfaces. In-

spection with a toolmaker's microscope indicated the grids were accurate to $\pm .002$ in. ($\pm .005$ cm). In order to prevent the preform segments from welding/sticking together during forging, each face was sprayed with a graphite emulsion.

All forging was done in a 500 ton (4.45 MN) hydraulic press with a ram speed of 100 in./min. (254 cm/min.). A trap die was used with simultaneous motion of both top and bottom punches during the deformation. Die temperature was maintained at 500°F (260°C) while billets were preheated to 550°F (288°C) for the forging operation. The forging die and punches were sprayed with graphite and fine copper particles for lubrication.

Incremental deformation tests were made in order to be assured that plane strain conditions were maintained throughout the forging process, i.e. $\varepsilon_z = -\varepsilon_y$ and $\varepsilon_x = 0$ in Figure 1. The sides of all segments remained planar and parallel for all incremental upsets.

After forging, the segments were separated and the grid spacings measured at a magnification of 2.5X so that the true local strains could be calculated to an accuracy of $\varepsilon = .005$. The deformed grid patterns are shown in Figure 2. Calculated local true strains (deformations) are given in Figure 3 for the center of each 1/2 in. x 1/2 in. (1.27 cm x 1.27 cm) square area. Only one quadrant is shown for each upset since deformation was symmetrical.

Identical procedures were used for forging both the laminated 7075 I/M preforms and the CT-91 powder preforms. In addition, the die temperature, preform size, preheat temperature and lubrication conditions were the same in both cases. Therefore, it was assumed that the local strain

distribution in the powder forged material was the same as that determined for the laminated billet forgings.

Forgings were solution treated and aged as described in Part I of this report. The hardness on the y-z face was R_B 92 ± 1 , for each of the three upset ratios.

3. Specimens and Location

For tensile and axial fatigue tests, local deformation strains of $\epsilon = 0, 0.3, 0.6$ and 0.7 were selected. Specimen orientations were defined with reference to Figure 1:

Longitudinal - specimen axis parallel to y direction

Transverse - specimen axis parallel to x direction

Short Transverse - specimen axis parallel to z direction

The center of the gage length or reduced section was located in the center of the zone shown in Table V. It should be noted that a local true strain deformation of 0.6 was tested from both the 1.5:1 and the 2:1 upset material. Tensile and fatigue specimen size and geometry were identical to those used in Part I.

For crack growth studies, compact type (CT) specimens were used with dimensions conforming to E24, as described in Part I. All CT specimens were oriented so that the crack grew in the direction of constant local deformation (x direction, Figure 1). Specimens were tested in a longitudinal orientation (x-z fracture plane) and a short-transverse orientation (x-y fracture plane). These orientations are the same as those for the tension and axial fatigue specimens.

Local deformations of $\epsilon = 0, 0.5$ and 0.7 were used in the studies of crack growth rates. Specimen and forging sizes required the substitution

of $\epsilon = 0.5$ as the intermediate value. The locations of the CT specimens were the same as that shown in Table V for $\epsilon = 0$ and $\epsilon = 0.7$. The specimens with $\epsilon = 0.5$ had the crack growth regions located at the center of B-3 (see Fig. 3) of the 1.5:1 upset ratio forgings.

4. Specimen Preparation and Testing

Tensile, axial fatigue and CT crack growth specimens were prepared as described in Part I.

a. Tensile Testing

Tensile properties were measured in triplicate. Longitudinal, transverse and short-transverse properties were determined for $\epsilon = 0$ and 0.6. Longitudinal and short-transverse properties were also determined for $\epsilon = 0.3$ and $\epsilon = 0.7$. Testing was done in a standard Instron at a cross-head speed of 0.005 in./min (0.013 cm/min). A strain gage extensometer was used and load-deformation curves were plotted automatically.

Yield strength (YS, 0.2% offset), ultimate tensile strength (UTS), percent reduction in area (%RA) and percent elongation (%E 0.5 in. [1.3 cm] gage) were determined. In addition, average hardness was determined for each specimen from six readings taken on the surfaces of the grip section of the test specimen.

b. Axial Fatigue Testing

Axial fatigue tests were made at $R = +0.1$ on a Sontag constant load machine (Part I). Maximum stresses selected for testing were 60, 75 and 70 ksi (414, 448 and 483 MPa), as determined by a Goodman analysis (45). Although the bulk of the testing was done at these stress levels additional tests were made at higher and lower values of σ_{max} . Three to five specimens were tested at each stress level with the lower number of specimens being used at the highest stress. Median value fatigue life

was determined from Weibull statistics (46). All cyclic loading was at 30 Hz.

Details of the axial fatigue facility and test procedure with a salt fog environment are contained in Part I.

c. Fatigue Crack Growth Measurements

All crack growth tests were carried out at $R = +0.1$ in an MTS closed loop system; this included precracking as well as growth rate testing. Maximum and minimum loads were maintained to within 2% and load was applied as a sine wave at 30 Hz. Details of the testing apparatus, and procedures for determination of crack growth rates in air and salt fog are given in Part I and reference (47).

5. Metallography

Microstructures of the P/M forgings were characterized by a combination of optical, scanning and transmission electron microscopy.

Conventional wet hand grinding of mounted specimens was used through 600 grit paper for the preparation of metallographic specimens. Specimens were then lapped with 1 μm diamond paste followed by final polishing with a suspension of cerium oxide abrasive in distilled water. The etchants used were either Keller's or 50% $\text{HNO}_3/\text{H}_2\text{O}$. Details of specimen preparation, and cleaning following fatigue testing in salt fog, for SEM and TEM studies are given in Part I.

RESULTS

1. Tensile Properties

Average tensile properties (3 tests) are given in Table VI. Yield and ultimate strength are plotted as a function of hardness (with ϵ and

orientation indicated) in Figure 4. There is a reasonable correlation between strength and hardness with no apparent effect of local deformation (ϵ). Furthermore, longitudinal strengths are higher than short-transverse strengths at the same hardness level. The yield and ultimate strengths are plotted as a function of local deformation (true strain (ϵ)) in Figure 5. There is no strong correlation between strength and local deformation. The variations observed may be explained in terms of hardness differences rather than by the effect of local deformation.

2. Axial Fatigue

The median fatigue life in air as a function of maximum stress is plotted in Figure 6. It can be seen from this figure that for $\epsilon = 0$ there is very little difference in the curves for the longitudinal and short-transverse orientations, indicating reasonably isotropic behavior. However, as ϵ is increased the difference between the two orientations increases; thus anisotropy increases with increasing local deformation. It can be seen that there is a significant enhancement in longitudinal fatigue life with local deformation (ϵ). There is some shifting of the short transverse curve but the net change is small in comparison to the change in the longitudinal orientation.

No distinction could be made between the fatigue properties of the $\epsilon = 0.6$ specimens from the 1.5:1 and the 2:1 upsets. Importantly, therefore, properties are independent of the macroscopic deformation and depend only on the local deformation.

Median fatigue life as a function of maximum stress in salt fog is plotted in Figure 7. The fatigue life is very short in the salt-fog environment. There is very little change in the longitudinal properties as the local deformation is increased. However, there is a decrease in the

short transverse properties with increasing local deformation (ϵ), particularly at the higher stress levels. As in air, anisotropy is seen to increase with increasing local deformation. However, in salt-fog the increase in anisotropy is caused by a degradation of the short-transverse fatigue resistance. The degrading effect of the salt-fog overshadows the beneficial effect that local deformation has when tested in air.

A complete Weibull analysis of the axial fatigue data in air and salt fog is included in reference (47).

3. Fatigue Crack Growth

Fatigue crack propagation rates for the CT-91 alloy as a function of orientation, deformation level and environment are summarized in Table VII. It was found that for ΔK values in the range of 6.0 to 6.5 ksi $\sqrt{\text{in.}}$ (6.6 to 7.2 MN m $^{-3/2}$) the da/dN values were less than 2×10^{-8} in./cyc. (5×10^7 mm/cyc) for the material tested in air. Although the procedures used did not provide true threshold values of ΔK , the very low crack growth rates do indicate an expected threshold range for ΔK . The da/dN vs. ΔK data are plotted in Figures 8, 9 and 10. It can be seen that for a given local deformation and ΔK , higher crack growth rates were observed in salt-fog than in air. Furthermore, higher crack growth rates occurred for the short-transverse orientation than for the longitudinal orientation.

The effects of local deformation and ΔK on the crack growth rates are plotted in Figure 11. It can be seen from this figure that the crack growth rate increases as the local deformation increases when the material is tested in air. However, when tested in salt-fog, there is a decrease in the crack growth rate with increasing local deformation at the inter-

mediate and higher values of ΔK . At the lower value of ΔK , in salt-fog, there is an increase in crack growth rate with increasing local deformation.

The da/dN vs. ΔK plots in Figures 8-10 were used to calculate the constants A and m in the Paris-Erdogan (40) equation. These values are given in Table VIII. The value of m is related to the fracture toughness of the material; lower values of m reflect higher toughness.

4. Microstructure

a. After Hot-Compaction

The structure of the hot compacted material as revealed by optical microscopy is shown in Figure 12. There is gross precipitation owing to the slow cooling after hot compaction. Darker etching constituents at the grain boundaries are oxides and possibly some "S" phase (Al_2CuMg) and minor amounts of Al_7Cu_2Fe and Mg_2Si . Within the grains the precipitate is predominantly $\eta(MgZn_2)$ with dispersoids of Co_2Al_9 and internal oxides.

TEM in the hot compacted condition reveals an equiaxed grain structure with a grain diameter $\sim 13\mu m$ (the original powder particle size). The Co_2Al_9 dispersoids are spherical in shape and exist over the size range $0.1\mu m$ to $0.3\mu m$, Figure 13. $\eta MgZn_2$ is present in a rod-like form and nucleates preferentially around the Co_2Al_9 dispersoids, Figure 13(b).

A representative optical micrograph of the hot-compacted structure after solution treatment and aging is shown in Figure 14. This material was taken through the forging operation but with $\epsilon = 0$ prior to heat treatment. It is seen that there are subgrain boundaries within the prior powder particles. The grains are approximately equiaxed with a slight

indication of elongation or flattening as a result of the axial compression in the z direction during hot compaction. The visible second phases present are predominantly at the grain boundaries and are probably oxides, $\eta(\text{MgZn}_2\text{Al}_2\text{Cu})$, and some S (Al_2CuMg) that did not dissolve during solution treatment.

TEM in the heat-treated condition (and $\epsilon = 0$) shows little difference in grain size between longitudinal and short transverse directions. The grain and subgrain boundaries are decorated with oxide particles; Co_2Al_9 dispersoids are distributed relatively uniformly throughout the material and are similar in size to those present after hot compaction, Figure 15. STEM analysis shows that Cu and Fe are associated with the Co_2Al_9 dispersoids; the approximate dispersoid composition is $(\text{Co}_{1.5}\text{Cu}_{0.3}\text{Fe}_{0.2})\text{Al}_9$. For the heat-treatment given, the hardening precipitates are a mixture of G.P. zones (~10%) and η' (~90%), within a size range of 8 to 15nm (38).

b. After Plane Strain Forging

The microstructure after forging and heat treatment is shown in Figure 16. Deformation of the grains is evident. The inclined angle of the elongated grains is the result of shearing during forging. TEM shows no significant change in the hardening precipitates or dispersoids as a result of forging and the dispersoids do not appear to be sheared. The most pronounced effect of deformation is in terms of subgrain size; as shown in Figures 17 and 18, subgrain size decreases significantly with deformation. Since the Co_2Al_9 dispersoid distribution is not changed during forging, dispersoids are more likely to be found on subgrain boundaries and triple points as the subgrain size decreases; this effect is seen in Figure 19.

Deformation also affects the size and distribution of the oxides that were originally present on the powder particle surfaces, cf. Figures 20 and 21. For $\epsilon = 0$, the oxides are relatively large and appear at subgrain boundaries and in the interior of the subgrains, (Figure 20); the oxides act as nucleating sites for the hardening precipitates. During forging ($\epsilon > 0$), the oxides are fragmented and become more homogeneously distributed. As the subgrain size decreases with deformation, the probability of finding the smaller fragmented oxides at subgrain boundaries increases, Figure 21. In turn, precipitation is more continuous at these boundaries in the deformed material than in the undeformed material. Primary changes in microstructure as a function of deformation are summarized in Table IX.

The structure of the powder forged material is significantly finer than that of 7075 and 7475 rolled plate, cf. Figures 16 and 22, noting the lower magnification in the latter. TEM reveals a large subgrain size ($\sim 20\mu\text{m}$) in the I/M material and the presence of secondary phases, primarily $\text{Al}_7\text{Cu}_2\text{Fe}$ and Mg_2Si , Figure 23. Continuous precipitation is also seen along the subgrain boundaries in 7475, Figure 24; this mode of precipitation is much more apparent in the I/M material than in the P/M counterpart, cf. Figures 21 and 24.

5. Fractography

a. Axial Fatigue

Following fatigue testing, specimens were sectioned perpendicular to the overall fracture surface and in the approximate direction of crack growth. Detailed optical metallographic studies were made in regions corresponding to Stages I and II of fatigue crack growth. Fracture mode

in Stage II is summarized in Table X as a function of deformation and orientation. The tendency toward intergranular fracture increases in the short transverse orientation coupled with no deformation, i.e. $\epsilon = 0$. Similar modes of fracture were observed in salt fog. In addition, extensive secondary cracking occurs in salt fog for the various combinations of deformation level and orientation, except for longitudinal specimens at $\epsilon = 0.7$. Cracks initiate at grain boundaries.

SEM studies were made of the fatigue fractues at both low and high magnifications after testing in air and salt fog. In air, most fractures exhibit a single fatigue initiation site at the lower stress levels, i.e. 60 ksi (414 MPa) and 65 ksi (448 MPa). Multiple initiation sites, accompanied by "ratchet marks" between sites, are frequently visible at the higher stress level, i.e. 70 ksi (483 MPa).

In salt fog, virtually every specimen exhibits multiple initiation sites. Several specimens have initiation sites almost completely around the periphery of the fracture surface. A representative comparison between macroscopic fracture morphologies in air and salt fog is illustrated in Figure 25.

Higher magnification SEM fractographs in air near fatigue fracture initiation sites are shown in Figures 26 and 27, for $\epsilon = 0$ and $\epsilon = 0.7$, respectively. The coarse texture in the fractographs indicates that fracture progresses along several paths. Features on the fractographs are defined as narrow plateaus, smooth textured zones and tear ridges (6, 37, 48, 49). All four conditions in Figures 26 and 27 exhibit similar fracture characteristics but the relative size varies. Thus, in the longitudinal orientation with $\epsilon = 0.7$, fracture surface features are on

a finer scale than in the other conditions. This is consistent with Figure 16 where it is seen that the fracture plane x-z corresponds to a fine-scale microstructure. The extent of Stage I is found to decrease with increasing stress level and no fatigue striations are observed in the above fracture areas.

Examples of fatigue fracture surfaces near initiation sites after testing in salt fog are shown in Figures 28 and 29. At each of the multiple initiation points there is evidence of corrosion products that appear to be concentrated at grain boundaries. Compared to fatigue in air, there is no well-defined Stage I and most of the fracture surfaces are characterized by the presence of smooth plateaus.

Fractographs from Stage II after fatigue in air show crack propagation on multiple plateaus with fatigue striations on the plateaus. The plateaus are at different elevations and are joined by walls or tear ridges. Examples are shown in Figures 30 and 31. Energy-dispersive x-ray analysis of larger particles on the fracture surfaces shows that these are cobalt-enriched, probably Co_2Al_9 . Several of these dispersoids are marked "Co" in Figure 31. The smaller particles "P" in Figure 31 are too small to be amenable to x-ray analysis. The dispersoids are located at the edges of tear ridges or walls, while the smaller particles are distributed over the plateaus. These smaller particles do not affect striation spacing.

Corresponding fracture surfaces from Stage II after fatigue in salt fog are shown in Figures 32 and 33. Multiple plateaus are observed as in air. Some of the plateaus exhibit ductile striations (as when tested in air) while others are characterized by brittle striations. The appearance of the latter form of striation is the result of their forming

on crystallographic fracture planes in the aggressive salt fog environment (48).

b. Crack Growth Specimens

SEM fractographs following crack propagation in air in the longitudinal orientation are shown in Figures 34, 35, 36 and 37 as a function of ΔK . Striations were not observed at da/dN values less than $\sim 10^{-6}$ in/cycle (2.5×10^{-5} mm/cycle). It is necessary to exceed crack propagation rates $\sim 10^{-5}$ in/cycle (2.54×10^{-4} mm/cycle) in order to develop clearly defined fatigue striations.

Problems were encountered in observing fracture surfaces at the beginning of crack propagation for specimens tested in salt-fog. However, the "mud-crack" deposits could be removed by cleaning in a phosphoric acid/chromic acid solution. SEM fractographs after crack propagation in salt fog followed by cleaning and without cleaning are shown in Figures 38 and 39, respectively. After cleaning, ductile striations are observed at relatively low rates of crack propagation, e.g. 5×10^{-5} in/cycle (127×10^{-5} mm/cycle) in Figure 38. Thus, it is possible that cleaning enhances fracture surface details by light etching. Brittle striations characteristic of Stage II in corrosion fatigue are evident in Figure 39.

DISCUSSION

1. Tensile Properties

The yield and tensile data in Figure 5 show that no correlation exists between the level of local deformation and tensile properties. At a local true strain of 0.6, material given an upset ratio of 2:1 has a higher tensile strength than that given an upset ratio of 1.5:1. Thus, although

the local linear strain is the same for each upset ratio, the amount of shear strain is different. This difference in strength is probably a reflection of differences in the level of redundant work between the two upset ratios. It is clear from Figure 2 that significant rigid body rotational strains accompany forging deformation; these will differ with the upset ratio.

2. Fatigue Behavior

a. Crack Initiation and Propagation in Aluminum Alloys

The normal sequence of fracture-related events that culminate in failure under cyclic loading in metals and alloys may be classified as: 1) Crack initiation at the surface, 2) Stage I crack growth - in which the initial cracks deepen on slip planes of high shear stress, 3) Stage II crack growth - involving growth of well-defined cracks on planes normal to the maximum tensile stress, 4) Overload fracture - when the fatigue crack is sufficiently large that the remaining cross-section cannot support the applied cyclic load.

Microstructural features that provide resistance to slip, or that result in uniform (homogeneous) slip will have the strongest influence in retarding fatigue crack initiation. Conversely, microstructural features that accentuate plastic strain or non-homogeneity of slip decrease resistance to crack initiation under cyclic loading. Once a fatigue crack is initiated, the propagation process is dependent on the relative sizes of the plastic zone at the crack tip and microstructural features (grain and subgrain size, precipitate size and spacing, etc.). Material in the plastic zone experiences reverse cyclic straining as a result of alternating tensile and compressive yielding. Resistance to

subsequent slip and/or a high degree of slip reversibility are associated with low rates of crack propagation, i.e. the crack only advances a small amount per load cycle. Conversely, microstructural features that enhance irreversible slip result in high rates of crack propagation.

In the 7XXX Al alloys peak static strength, and therefore maximum resistance to slip, is achieved in the T6 condition by virtue of the coherent η' precipitates. However, when dislocations do glide they shear the small precipitates and deformation is localized on a few active slip planes where the strengthening particles have been destroyed. This localized softening and inhomogeneous distribution of plastic strain results in early crack nucleation. Similarly, stress concentrations associated with localized plastic flow in precipitate-free zones at grain boundaries lead to early crack nucleation. In the overaged (T73) condition, the incoherent η precipitate is non-shearable so that dislocations bow out between and around the precipitates. This results in a relatively homogeneous mode of deformation with increased resistance to fatigue crack initiation, but at the expense of static strength.

A small grain size or unrecrystallized structure promote homogeneous deformation by reducing slip length and stress concentrations at grain boundaries. Both enhance resistance to crack nucleation in 7XXX alloys containing shearable precipitates. Similarly, the fine grain size achieved by ITMT of 7050 eliminates slip band decohesion and improves the resistance to crack initiation (6).

Unfortunately, the microstructural features that enhance resistance to crack initiation in the high-strength 7XXX Al alloys frequently reduce resistance to fatigue crack propagation by limiting slip reversibility.

Constituent particles provide preferential crack paths since they are brittle and separate from the matrix; this lowers resistance to fatigue crack propagation. Dispersoids behave in a similar fashion but their effect in increasing FCG rate appears to be limited to high ΔK levels (2). Overaging to convert η' (coherent) to η (incoherent) results in a decrease in internal strain level. Resistance to FCG increases since the environment is now less degrading to the alloy.

The results of the present study on a P/M processed high-strength aluminum alloy show that deformation can be beneficial or detrimental to fatigue life. Increasing the amount of flow in the CT-91 increases fatigue life in air in the longitudinal orientation but has little effect in the short transverse orientation. Fatigue life in salt fog is much lower than in air. In salt fog, short transverse fatigue life is decreased slightly by deformation but there is no significant change in longitudinal fatigue life.

FCG rates in both the longitudinal and short transverse orientations increase in air as the level of prior deformation increases; the magnitude of the increase is highest at low ΔK levels. In salt fog, FCG rates are higher than in air. At low ΔK increasing deformation first increases FCG rates but at higher strain levels the rate decreases; however the rate is always higher than in the $\epsilon = 0$ condition. At high ΔK levels, prior deformation decreases FCG rates in salt fog.

These results and observations on fatigue life and fatigue crack growth rates are now considered in terms of microstructure and fracture morphology. Particular interest is vested in the role of deformation and environment on crack initiation and propagation during cyclic loading

and on differences in the response of P/M processed and I/M material.

b. Axial Fatigue In Air

In the longitudinal orientation, fatigue life in air is increased significantly as a result of the prior plane strain deformation. The results of the FCG studies also show that the prior deformation increases FCG rates in the longitudinal orientation in air, at all levels of ΔK . Thus it can be concluded that the increase in fatigue life as a result of the prior deformation is associated with an increase in the resistance of the P/M material to crack initiation. A similar conclusion can be drawn for the material in the short transverse orientation in air. Here, fatigue is not significantly changed by the prior plane strain deformation but FCG rates increase with prior deformation; hence, there must be increased resistance to fatigue crack initiation. However, since total fatigue life is not increased, the beneficial effect of prior deformation in the short transverse orientation must be much less than in the longitudinal orientation.

The above observations on axial fatigue response in air are understood in terms of the several microstructural changes accompanying the plane strain deformation. The grain structure changes from the relatively isotropic equiaxed form characteristic of the hot compacted condition to one in which there is pronounced grain elongation in the direction of the y-axis, i.e. grains assume lengths $\gtrsim 100\mu\text{m}$ with widths $< 5\mu\text{m}$. This anisotropy in grain structure enhances resistance to fatigue crack initiation since there are now fewer transverse grain boundaries, i.e. boundaries oriented in the x-z plane of fracture. In addition to grain morphology, deformation leads to a smaller limiting subgrain size ($\sim 0.7\mu\text{m}$) and a

correspondingly finer and more uniform distribution of oxides and n' precipitates. This promotes a finer and more homogeneous mode of slip than in the hot compacted condition ($\epsilon=0$) which further enhances resistance to crack initiation (3, 6, 50).

The effect of deformation on fatigue life takes on added significance when a comparison is made with I/M material tested under identical conditions. This is done in Figures 40 and 41, using the data of Buzolits and Lawley (44) for I/M 7075 and 7475. In air the longitudinal and short transverse fatigue lives of the deformed P/M material ($\epsilon=0.7$) are significantly higher than those of the I/M 7475. For example, at $\sigma_{max} = 60$ ksi (44 MPa), median fatigue life in the longitudinal orientation is more than seven times higher in the P/M than in the I/M 7475 alloy. In the hot-compacted condition ($\epsilon=0$) fatigue life in the short transverse orientation of the P/M material is as good as that of the I/M alloys in the longitudinal orientation. The overall superiority of the P/M material compared to the I/M alloys in terms of fatigue life is a result of the finer microstructural features (grain and subgrain size, n' phase and oxide distribution) in the former.

It is important to recognize the differences in the origins of anisotropy in fatigue life in the P/M and I/M materials. In the P/M material, deformation improves fatigue life in the longitudinal orientation with little effect in the short transverse orientation. In contrast, in I/M wrought plate, anisotropy is the result of degradation in short transverse fatigue life with little change in longitudinal properties.

c. Axial Fatigue in Salt Fog

The sensitivity of fatigue life to crack initiation is very much in evidence in the salt fog tests. Crack initiation occurs at the structurally weak points generated by the aggressive corrosive attack of the salt fog at grain boundaries. Cyclic stresses rupture the surface oxide allowing pitting to occur and they also dislodge corrosion products that might otherwise impede corrosion. Corrosion proceeds inwards and cracking occurs when the stress concentration at the base of the pit becomes high enough. In consequence, crack initiation in salt fog is accomplished in a relatively few number of cycles and fatigue life is drastically reduced compared to testing in air. The ease of fatigue crack initiation in salt fog completely mitigates against any benefit from refinement of the microstructure by deformation.

Fatigue life (i.e. S-N response) of the P/M and I/M 7075 and 7475 in salt fog is compared in Figure 42. The I/M material suffers the same serious degradation as the P/M material for the reasons discussed above. However, as in air, the P/M material exhibits superior life to the I/M material, with the short transverse life of the P/M material being as good as that of the I/M material in the longitudinal orientation.

d. Crack Growth in Air

In both the longitudinal and short transverse orientations, FCG rates in air increase with increasing deformation independent of ΔK . This is understood in terms of the effect of deformation on the relative sizes of the plastic zone at the crack tip and the several microstructural features that influence slip. As shown in Part I, the size of the plastic zone is similar to that of the grain and subgrain size in the P/M material. Thus, slip reversibility is limited and is expected to diminish as the

scale of the microstructure decreases with increasing deformation.

In turn this increases FCG rates.

It is also possible that the finer and more homogeneous microstructure at $\epsilon = 0.7$ provides an easier transgranular path for the fatigue crack to follow, as discussed by Voss (25). As the scale of the microstructure increases the crack must propagate via a more tortuous path. This difference is apparent in the fracture morphologies for $\epsilon = 0$ and $\epsilon = 0.7$ at constant ΔK , Figures 43 and 34.

The anisotropy in FCG rates and lower FCG rates in the longitudinal orientation, particularly at high ΔK levels, are explained in a similar manner to that given in Part I. Of primary importance are the PFZ and the differences in distribution and spacing of dispersoids and oxides as a function of specimen orientation. At high ΔK , the high density of secondary cracks in the L orientation enhances FCG resistance.

e. Crack Growth in Salt Fog

FCG rates are higher in salt fog than in air. However, the dependence of FCG rate on specimen orientation is similar in both environments at each level of deformation. It is expected that the same microstructural features will control FCG rates in both environments, but with the added detrimental effect of the corrosive medium in salt fog. The tendency toward intergranular fatigue crack propagation in the salt fog is also expected to result in higher FCG rates.

CONCLUSIONS

In air, increasing the local deformation increases fatigue life in the longitudinal orientation but has little effect on short transverse fatigue life. Anisotropy in fatigue life in air increases with increasing

local deformation and is caused by an enhancement of longitudinal properties. Local deformation increases resistance to crack initiation through the development of a fine-scale microstructure with associated homogeneous plastic deformation. The mode of fracture in Stage II is a mixture of intergranular and transgranular; increasing the level of local deformation reduces the extent of intergranular fatigue fracture. The fatigue life of the P/M material is significantly higher than that of the I/M material in air; this reflects the improved resistance to crack initiation in the P/M material by virtue of its finer microstructure (grain and subgrain size; precipitate, oxide and dispersoid size (distribution).

Fatigue life in salt fog is much lower than in air in both the longitudinal and short transverse orientations. This is the result of rapid corrosive attack at the grain boundaries which creates local weak spots that facilitate multiple crack initiation. In salt fog, short transverse fatigue life is decreased slightly by deformation but there is no significant change in longitudinal fatigue life. This results in increased anisotropy in fatigue life with increasing deformation but the extent of anisotropy is much less than in air. No Stage I region was detected in salt fog. In Stage II, the mode of fracture in salt fog is predominantly intergranular with a significant amount of secondary cracking. The fatigue life of the P/M processed material is greater than that of the I/M material in salt fog.

FCG rates in both the longitudinal and short transverse orientations increase in air as the level of deformation increases; the magnitude of the increase is highest at low ΔK levels. In salt fog, FCG rates

are higher than in air and are anisotropic with FCG rates in the short transverse direction higher than those in the longitudinal orientation. At low ΔK , increasing deformation first increases FCG rates but at higher strain levels the rate decreases; however the rate is always higher than in the $\epsilon = 0$ condition. At high ΔK levels, deformation decreases FCG rates in salt fog.

TABLE I
Chemical Compositions of Aluminum Alloys (28)

ALLOY	Si	Fe	Cu	Mn	Mg	Cr	Zn	Ti	Co	Al
7075 (IM)	.40	.50	1.2/2.0	.30	2.1/2.9	.18/.35	5.1/6.1	.20	-	Bal
7475 (IM)	.10	.12	1.2/1.9	.06	1.9/2.6	.18/.25	5.2/6.2	.06	-	Bal
CT91 Powder	.06	.05	1.4	-	2.00	-	5.6	-	.35	Bal

TABLE II
Typical U.S. Standard Screen Analysis of Aluminum
Alloy Powder (Weight Percent); (28)

APD	-30 -50 -100 -200					
	+30	+50	+100	+200	+325	-325
13	0	0	0.5	4	9	86.5

TABLE III
Typical Powder Particle Size by Coulter Counter (28)

Diameter (μm)	75	60	50	40	30	20	15	10	8	5
Percent < dia.	93	88	81	73	63	44	29	16	11	4

TABLE IV
Preform Sizes and Upset Ratios

Preform Size			Upset Size			Upset Ratio	True Height Strain $\epsilon = -\ln(h_f/h_o)$
h_o (z)	w_o (y)	d_o (x)	h_f	w_f	d_f		
3"	5"	2"	3"	5"	2"	0	0
4.5"	3.25"	2"	3"	5"	2"	1.5:1	0.4
6"	2.5"	2"	3"	5"	2"	2:1	0.7

TABLE V
Location of Center of Gage Length for Tensile and Fatigue Specimens

Upset Ratio	ϵ	Location*	
		Long.	S. Trans.
0	0	var	var
1.5:1	.3	B-2	B-2
1.5:1	.6	C-4	C-4
2:1	.6	C-3	C-3
2:1	.7	B-4	B-4

*See Figure 3 for location matrix

TABLE VI
Average Tensile Properties

True Strain (ϵ) [upset]	Orient.	Hard (R_b)	YS(0.2%) ksi (MPa)	UTS ksi (MPa)	%E (.5 in. gage) [1.3 cm]	%RA
0	L	80	76.8(530)	82.3(567)	8.1	28
0	ST	86	76.5(527)	82.1(566)	8.9	27
0	T	84	75.2(519)	80.6(556)	6.3	29
0.3	L	83	72.4(499)	79.1(545)	9.7	30
0.3	ST	83	72.6(501)	78.6(542)	7.4	24
0.6[1.5:1]	L	80	69.7(481)	77.1(532)	10.1	30
0.6 [2:1]	L	83	75.7(522)	82.2(567)	9.0	23
0.6[1.5:1]	ST	80	67.2(463)	74.7(515)	7.2	17
0.6 [2:1]	ST	81	68.2(470)	75.2(519)	5.6	12
0.6 [2:1]	T	82	70.3(485)	76.6(528)	9.7	34
0.7	L	81	71.0(490)	78.1(538)	8.8	25
0.7	ST	82	69.3(478)	76.2(525)	7.9	21

TABLE VII

Effect of Local Deformation and ΔK on Crack Growth Rate (da/dN)

ΔK ksi $\sqrt{\text{in}}$ ($\text{MNm}^{-3/2}$)	ENVIR.	ORIENT.	da/dN [in./cyc X 10^6 (mm/cyc X 10^6)]		
			Local Deformation		
			$\epsilon=0$	$\epsilon=0.5$	$\epsilon=0.7$
7(7.7)	Air	Long	.20(5.1)	.40(10.2)	.75(19.1)
7(7.7)	Air	S.Trans	.30(7.6)	.55(14.0)	.80(20.3)
7(7.7)	Salt-Fog	Long	.50(12.7)	1.3(33.0)	1.0(25.4)
7(7.7)	Salt-Fog	S.Trans	.40(10.2)	2.0(50.8)	1.3(33.0)
10(10.99)	Air	Long	1.7(41.9)	2.8(69.9)	4.3(109)
10(10.99)	Air	S.Trans	2.7(67.3)	3.9(99.1)	3.5(88.9)
10(10.99)	Salt-Fog	Long	8.6(218)	8.2(208)	7.0(178)
10(10.99)	Salt-Fog	S.Trans	5.5(140)	12.5(318)	10.0(254)
15(16.49)	Air	Long	13.5(343)	12.0(305)	21.0(533)
15(16.49)	Air	S.Trans	30.0(762)	33.0(838)	30.0(762)
15(16.49)	Salt-Fog	Long	73.0(1854)	60.0(1524)	47.0(1194)
15(16.49)	Salt-Fog	S.Trans	120 (3048)	100 (2540)	90.0(2286)

TABLE VIII

Values of A and m for $da/dN = A \Delta K^m$

ϵ	Orient.	Envir.	m	$A \times 10^{12}$
0	Long	Air	5.7	4
0	S.Trans	Air	6.0	3
.5	Long	Air	3.6	631
.5	S.Trans	Air	5.3	20
.7	Long	Air	3.9	513
.7	S.Trans	Air	5.3	16
<hr/>				
0	Long	Salt-Fog	5.3	45
0	S.Trans	Salt-Fog	7.6	0.14
.5	Long	Salt-Fog	4.9	101
.5	S.Trans	Salt-Fog	5.1	93
.7	Long	Salt-Fog	4.6	163
.7	S.Trans	Salt-Fog	5.4	38

TABLE IX

Changes in Microstructure with Deformation

Local True Strain	: Subgrain Size(μm)	: Co_2Al_9 Distribution	: Subgrain Boundary η' Precipitate
$\epsilon = 0$: 3.00 +7.00 -1.20	: size 0.1 to 0.3 μm	Precipitates found at subgrain boundaries and at most dispersoids and oxide particles within subgrains.
	:	:	:
	:	:	:
	:	:	:
$\epsilon = 0.3$: 1.10 +1.00 -0.20	: Size remains constant. Distribution becomes more homogeneous with increasing deformation.	-----
	:	:	:
	:	:	:
$\epsilon = 0.7$: 0.70 +0.10 -0.20	: With the smaller subgrain size, there is a greater probability of finding Co_2Al_9 dispersoids at subgrain boundaries and triple points.	Increasing deformation tends to confine the η' precipitates to the subgrain boundaries.
	:	:	:
	:	:	:
	:	:	:

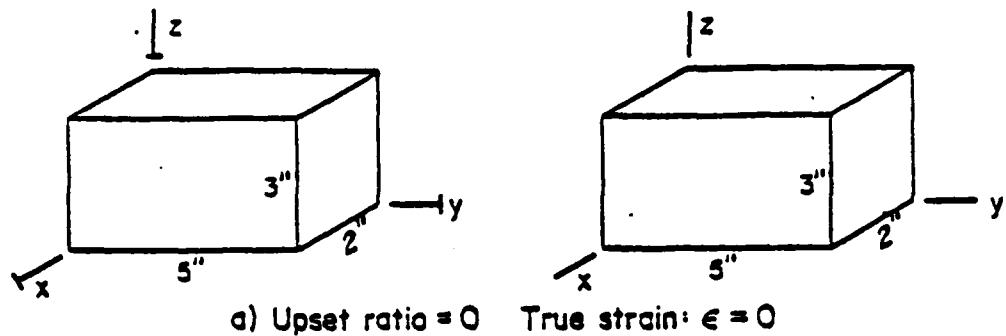
TABLE X

Effect of Orientation and Deformation on Fracture Mode in Stage II in Air; Axial Fatigue

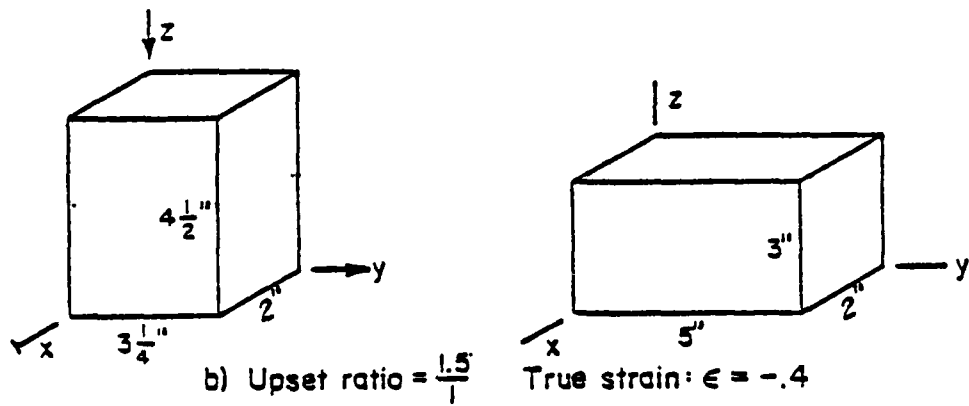
ϵ	Orientation	Fracture Mode
0	Longitudinal	Transgranular + Intergranular
	Short Transverse	Transgranular + Intergranular
0.3	Longitudinal	Transgranular
	Short Transverse	Transgranular + Intergranular
0.7	Longitudinal	Transgranular
	Short Transverse	Transgranular + Intergranular

PREFORMS

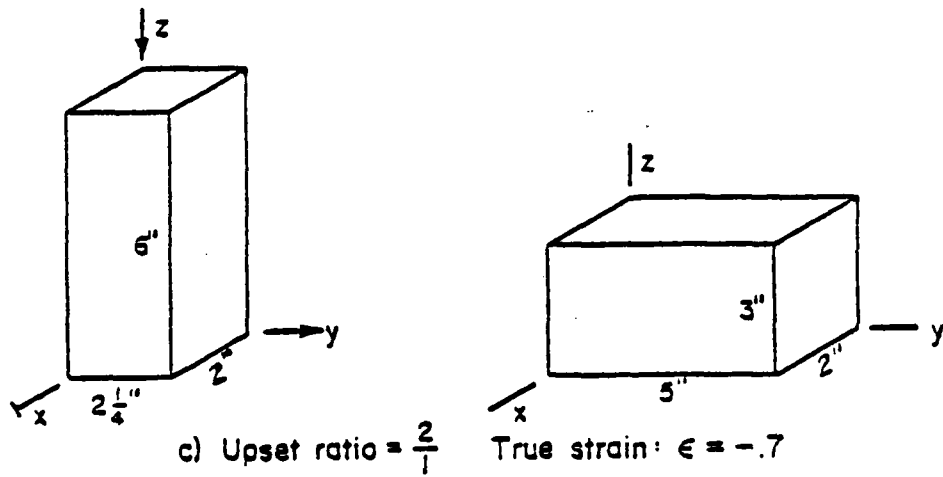
FINAL FORGING



a) Upset ratio = 0 True strain: $\epsilon = 0$

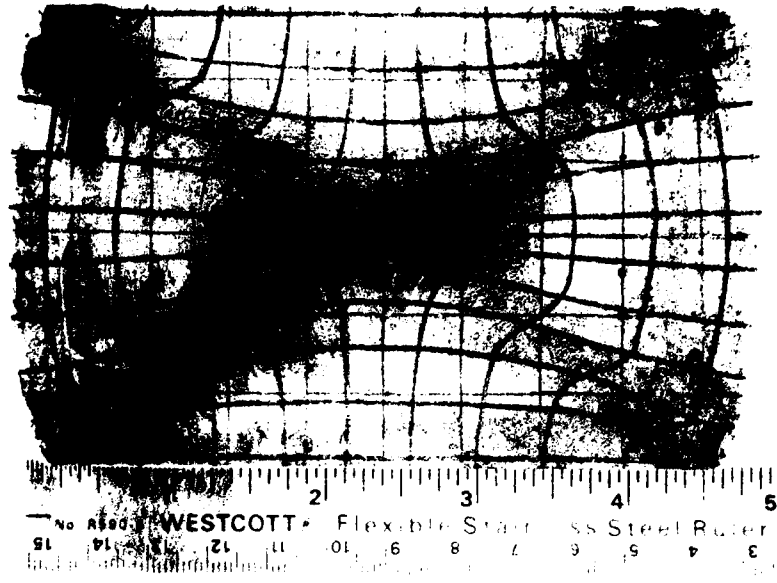


b) Upset ratio = $\frac{1.5}{1}$ True strain: $\epsilon = -.4$

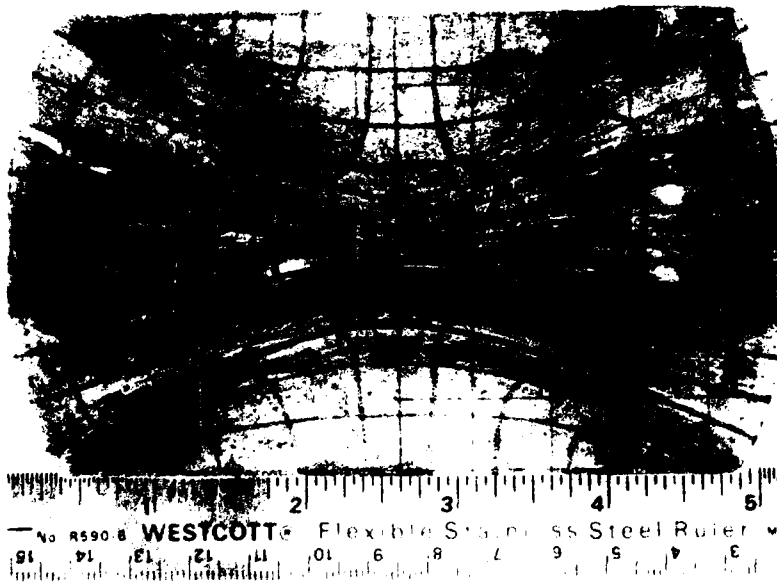


c) Upset ratio = $\frac{2}{1}$ True strain: $\epsilon = -.7$

Figure 1. Forging preform sizes and orientations for final forged size.



a



b

Figure 2. Deformation grid pattern: (a) 1.5:1 upset, (b) 2:1 upset.
Note: grids were originally 10 mm square.

1	2	3	4	5	5	4	3	2	1	
					.10	.28	.35	.69		A
					.27	.43	.51	.31		B
					.84	.60	.36	.21		C
										C
										B
										A

a

1	2	3	4	5	5	4	3	2	1	
					.11	.25	.63	.63		A
					.39	.69	.60	.36	.30	B
					1.27	1.14	.60	.36	.30	C
										C
										B
										A

b

Figure 3. Local upset true strains for the center of the area indicated:
 (a) 1.5:1 upset; (b) 2:1 upset.

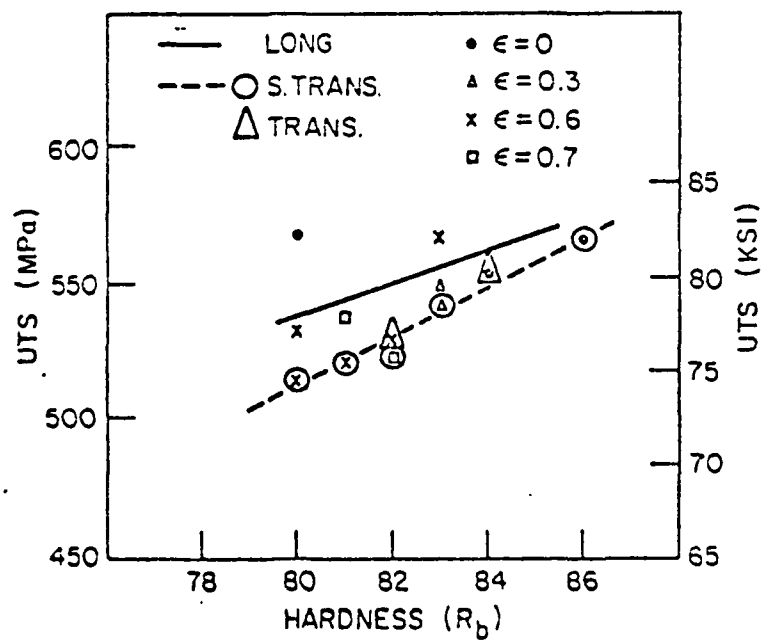
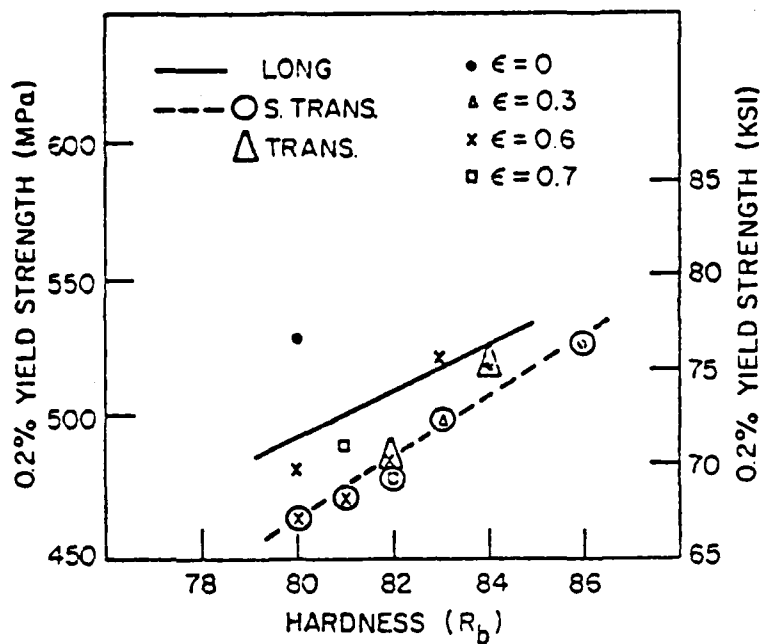


Figure 4. Yield strength (0.2% offset) and ultimate tensile strength vs. hardness for P/M forged material.

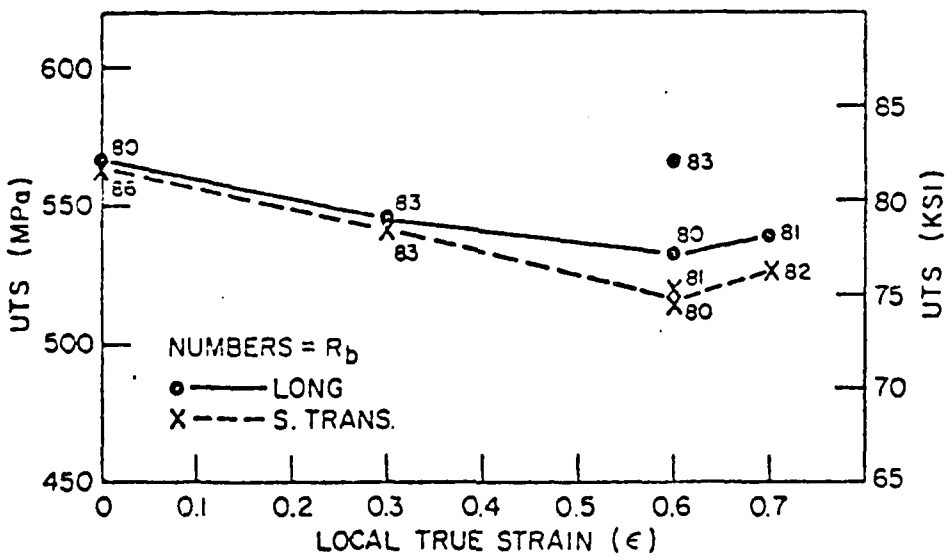
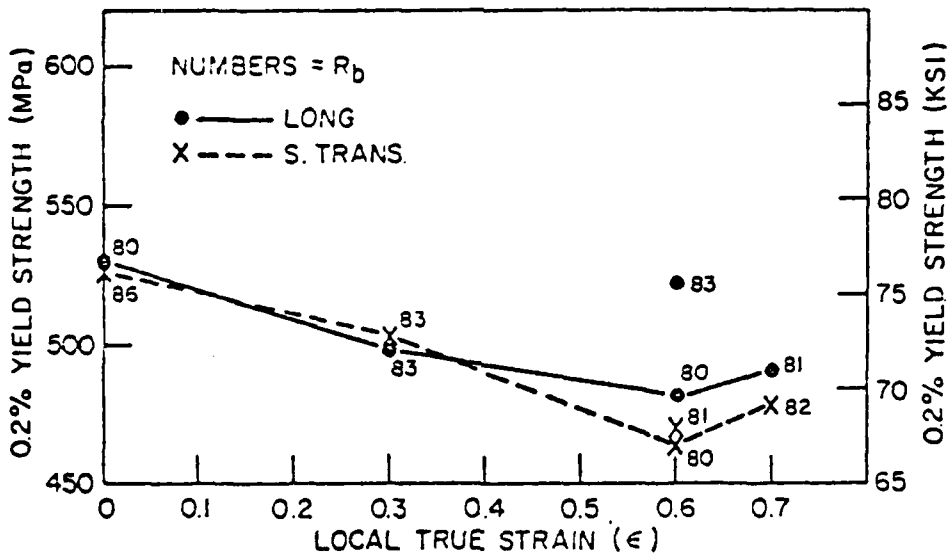


Figure 5. Yield strength (0.2% offset) and ultimate strength vs. local true strain for P/M forged material.

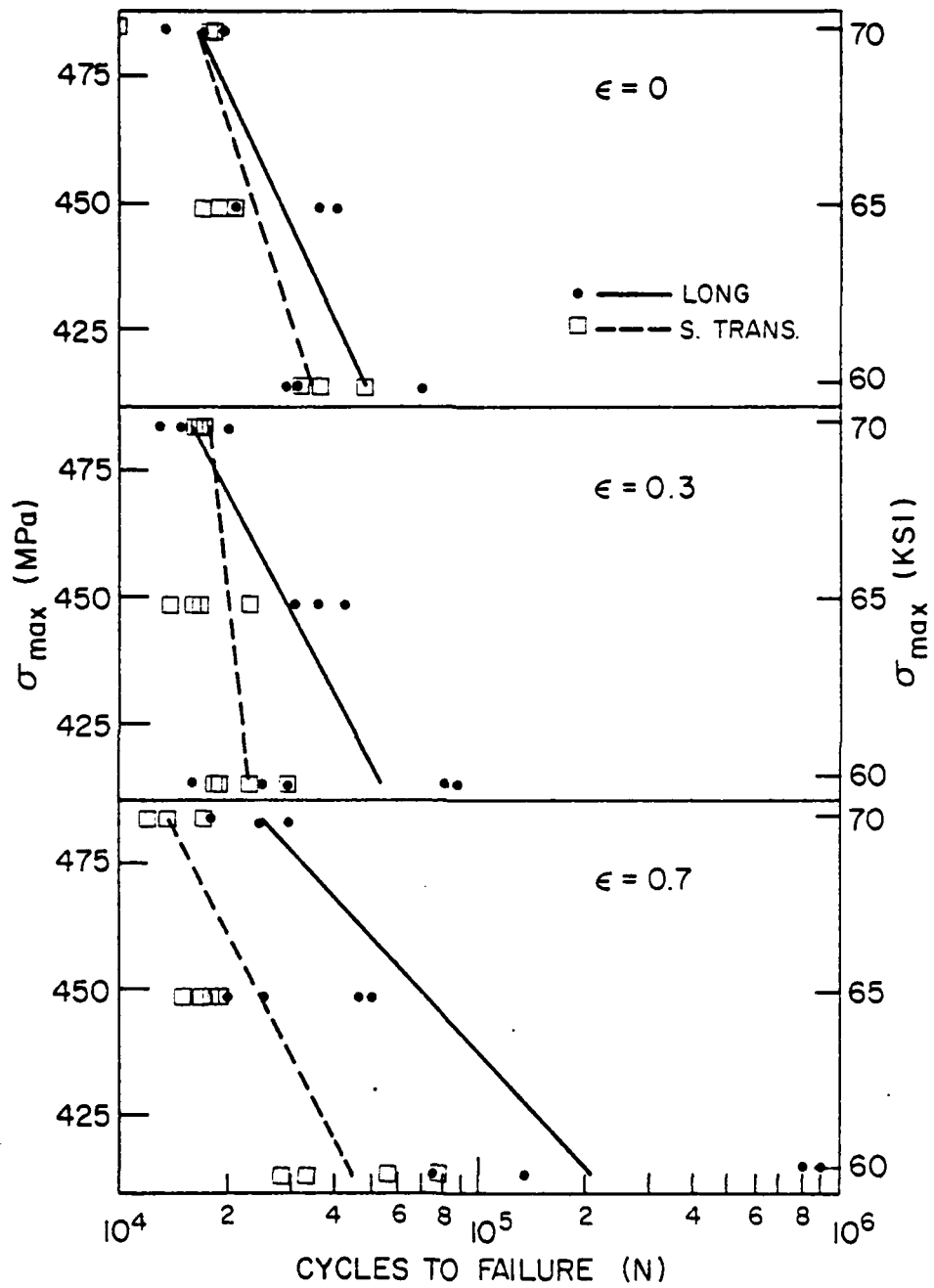


Figure 6. Median fatigue life vs. σ_{max} for P/M forged material tested in air.

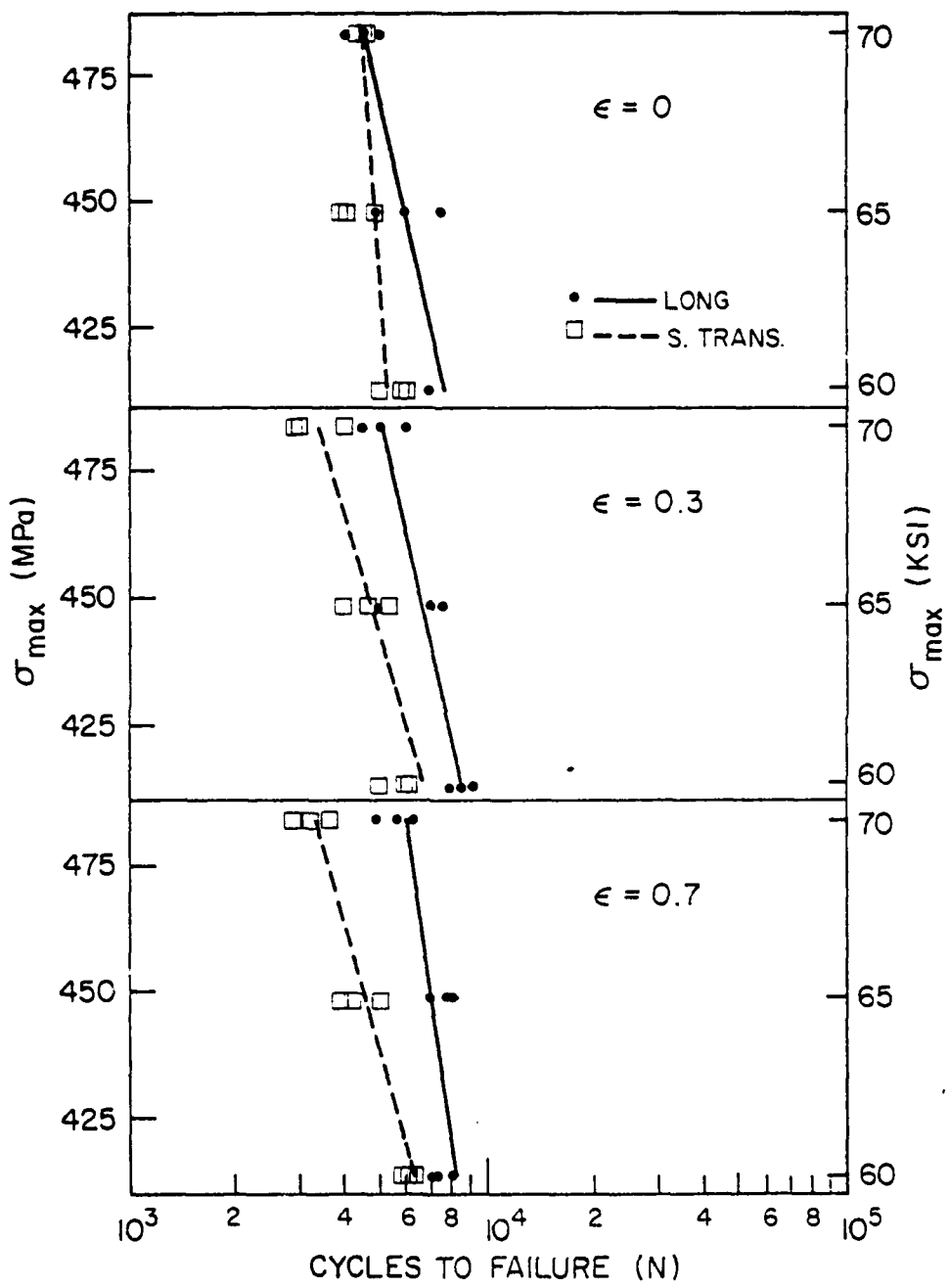


Figure 7. Median fatigue life vs. σ_{\max} for P/M forged material tested in 3 1/2% NaCl solution salt-fog.

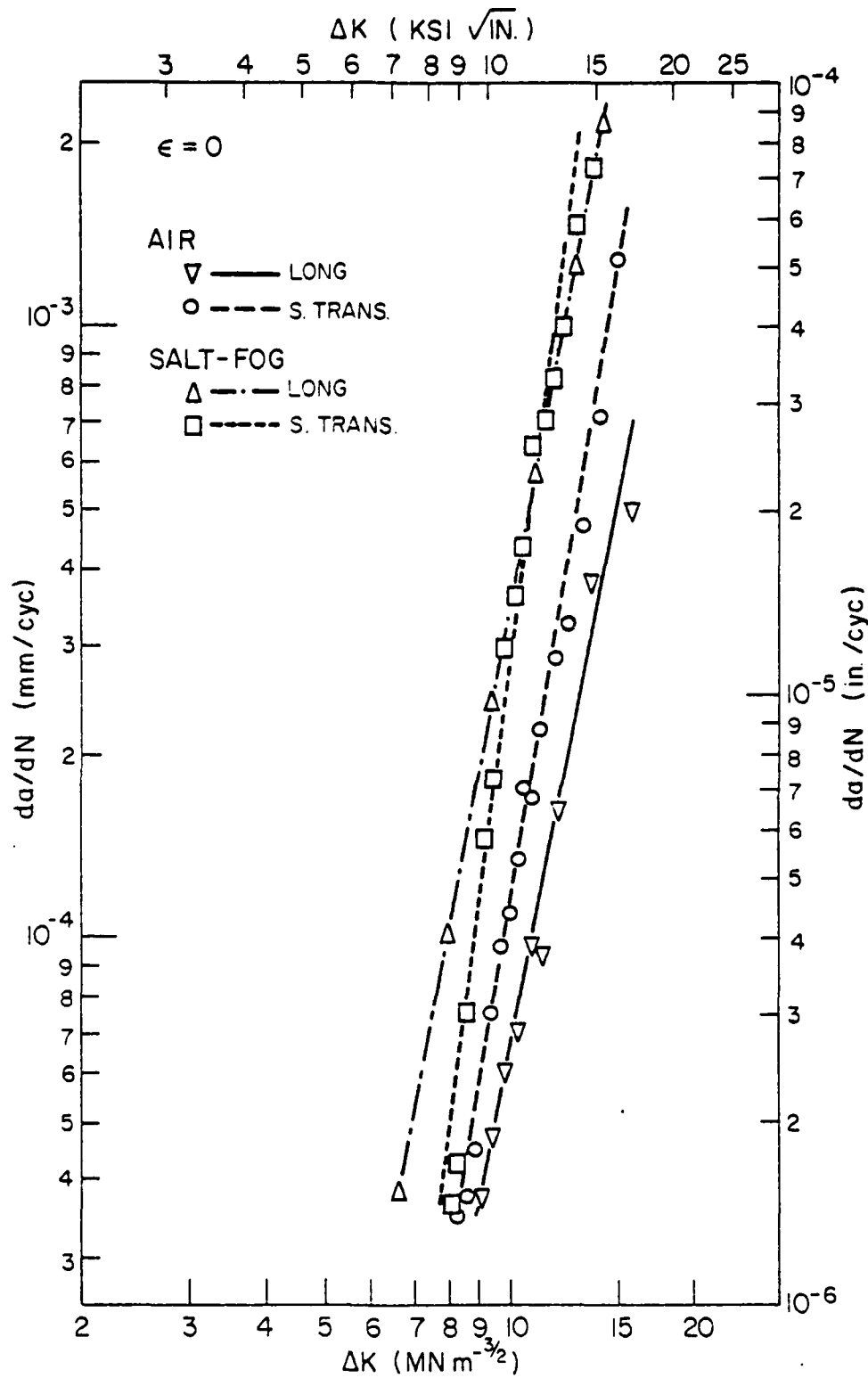


Figure 8. da/dN vs. ΔK ; local deformation: $\epsilon = 0$, for P/M forged material tested in air and 3 1/2% NaCl solution salt-fog.

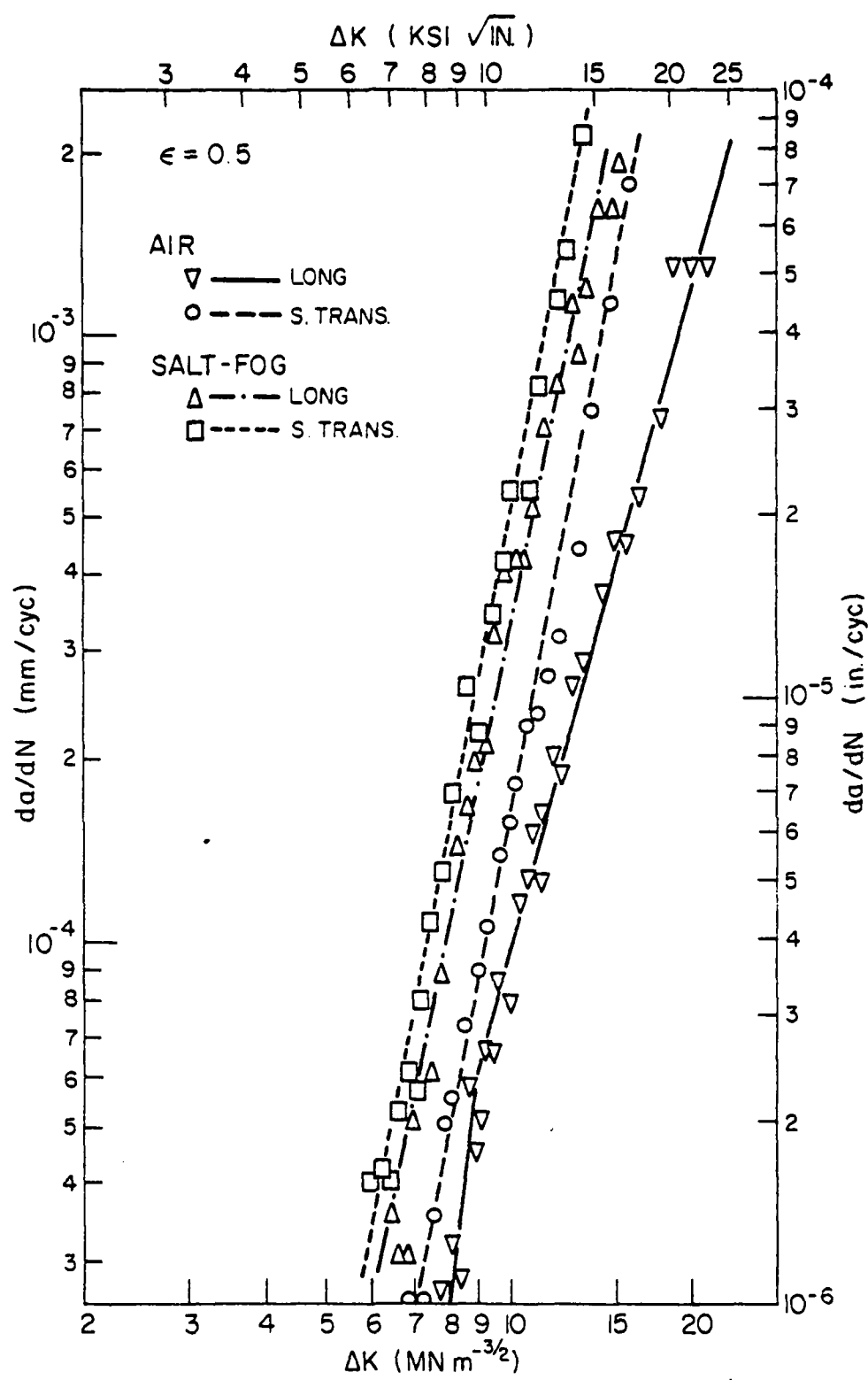


Figure 9. da/dN vs. ΔK ; local deformation: $\epsilon = 0.5$, for P/M forged material tested in air and 3 1/2% NaCl solution salt-fog.

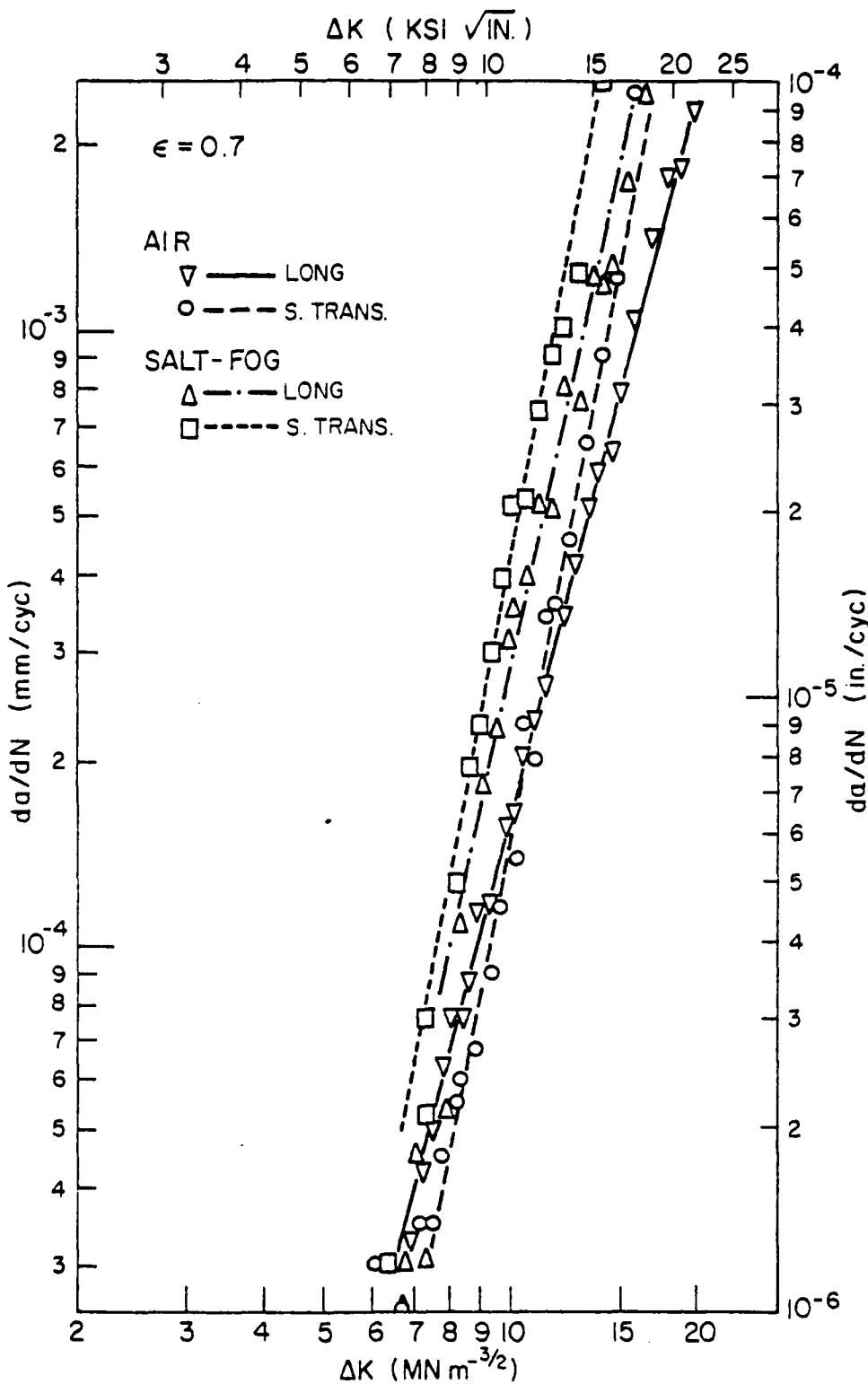


Figure 10. da/dN vs. ΔK ; local deformation: $\epsilon = 0.7$ for P/M forged material tested in air and 3 1/2% NaCl solution salt-fog.

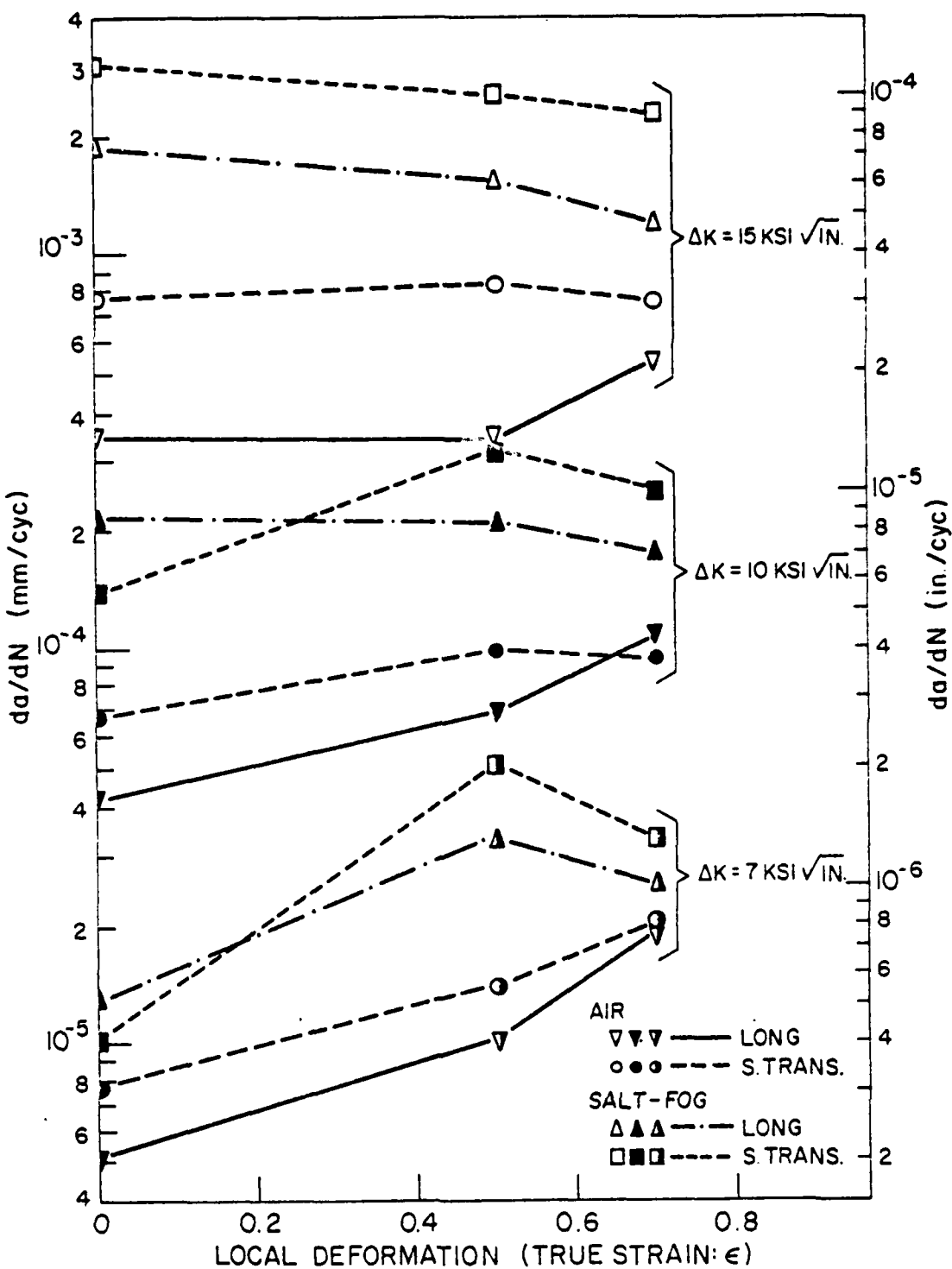


Figure 11. da/dN vs. ϵ ; three (3) values of ΔK , for P/M forged material tested in air and 3 1/2% NaCl solution salt-fog.

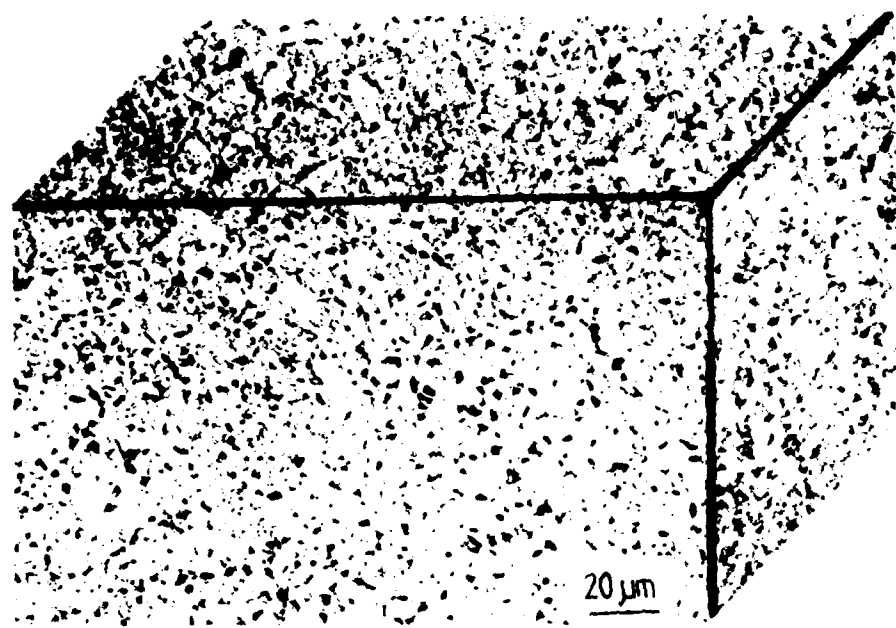


Figure 12. Optical micrograph of hot compacted P/M alloy, HNO_3 etch.

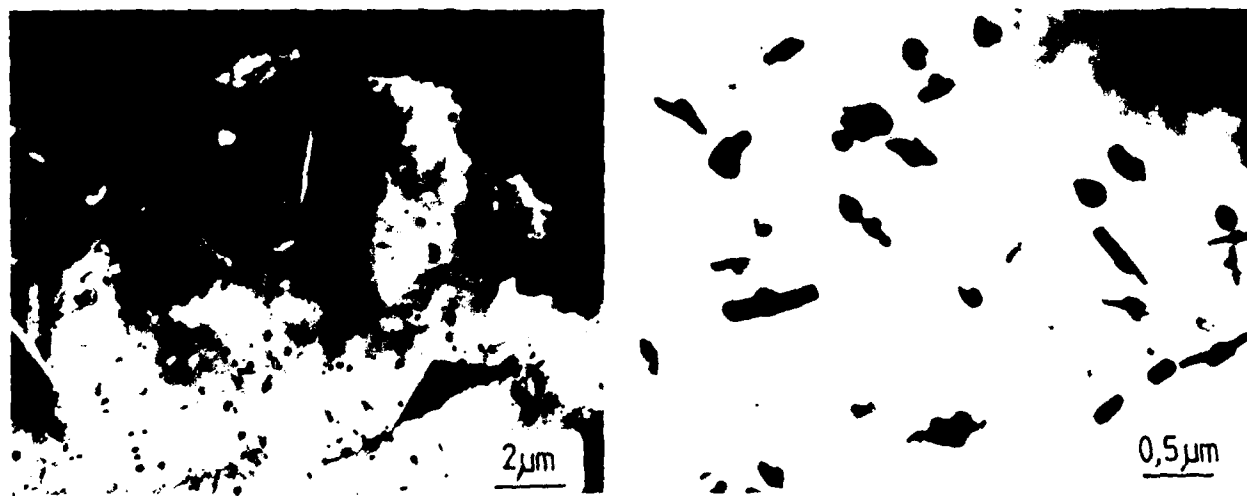


Figure 13. TEM of hot compacted P/M alloy.

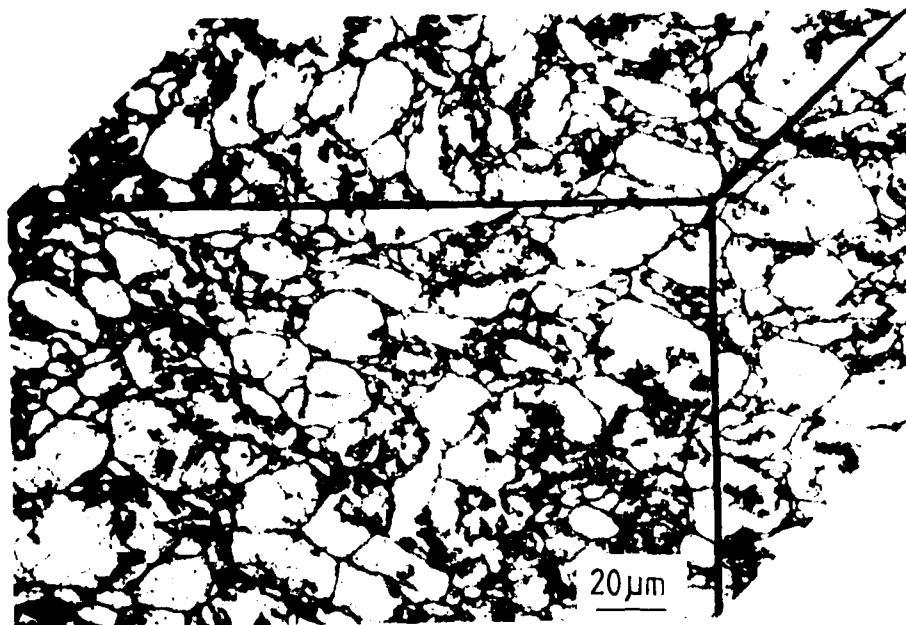


Figure 14. Optical micrograph of hot compacted and heat-treated P/M alloy for $\epsilon = 0$; HNO_3 etch.



Figure 15. TEM of hot compacted and heat-treated P/M alloy for $\epsilon = 0$; short transverse orientation.

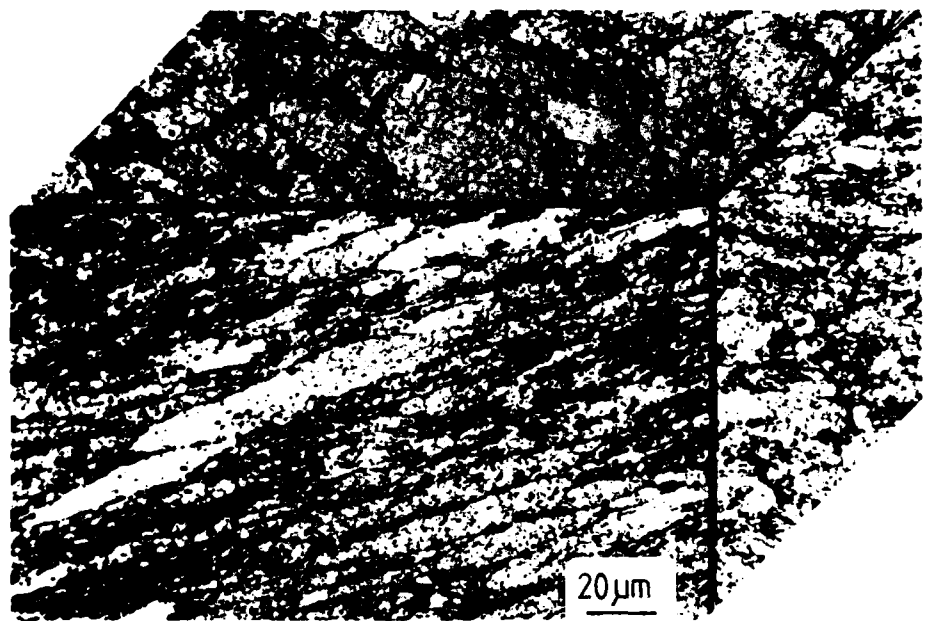


Figure 16. Optical micrograph of hot compacted, forged ($\epsilon = 0.6$) and heat-treated P/M alloy; HNO_3 etch.

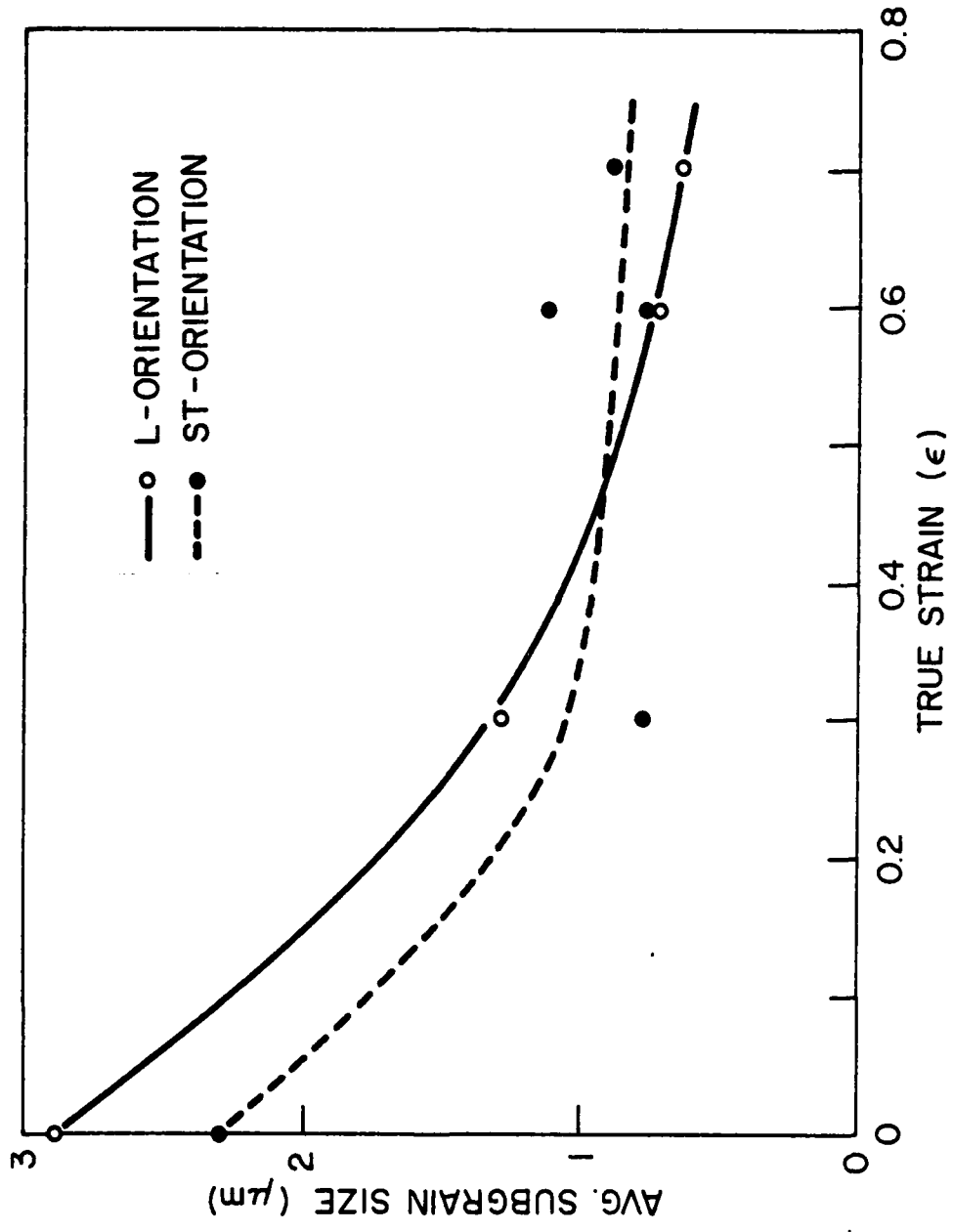
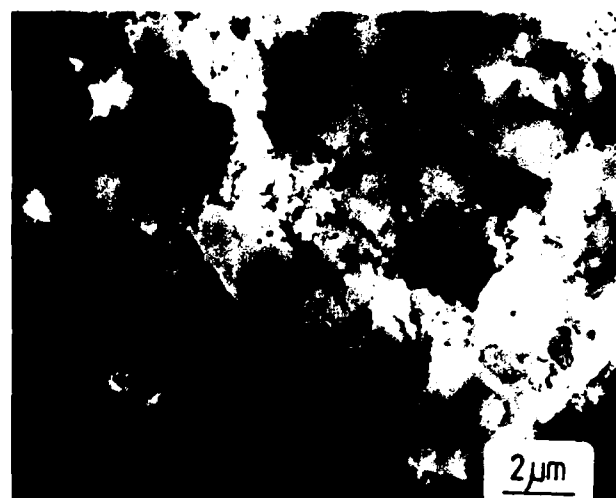


Figure 17. Effect of deformation on subgrain size in the longitudinal (L) and short transverse (ST) orientations.



(a)

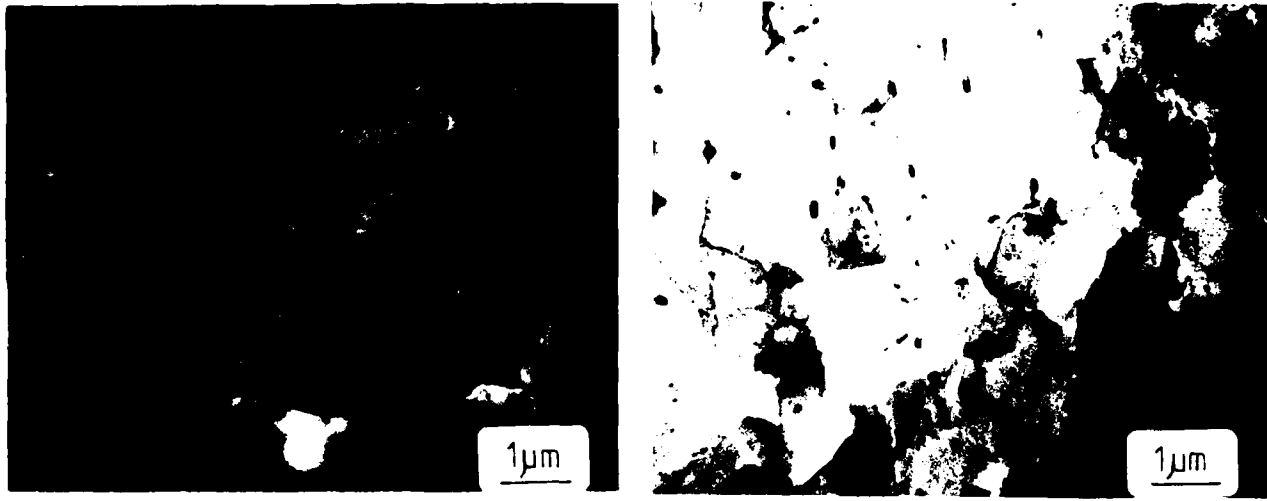


(b)



(c)

Figure 18. TEM showing subgrain size as a function of deformation in the longitudinal orientation; (a) $\epsilon = 0$; (b) $\epsilon = 0.4$; (c) $\epsilon = 0.7$.



(a)

(b)

Figure 19. TEM showing distribution of dispersoids at (a) $\epsilon = 0$ and (b) $\epsilon = 0.7$. Longitudinal orientation.

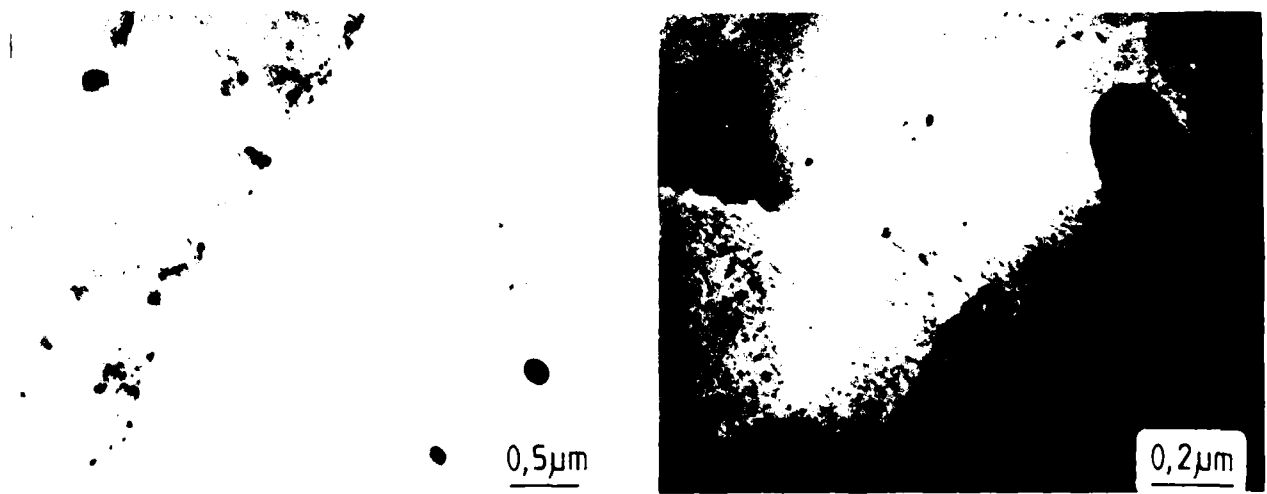


Figure 20. TEM showing non-uniform distribution of oxide particles at subgrain boundaries for $\epsilon = 0$; short transverse orientation.

Figure 21. TEM showing uniform precipitation along subgrain boundaries for $\epsilon = 0.7$; short transverse orientation.

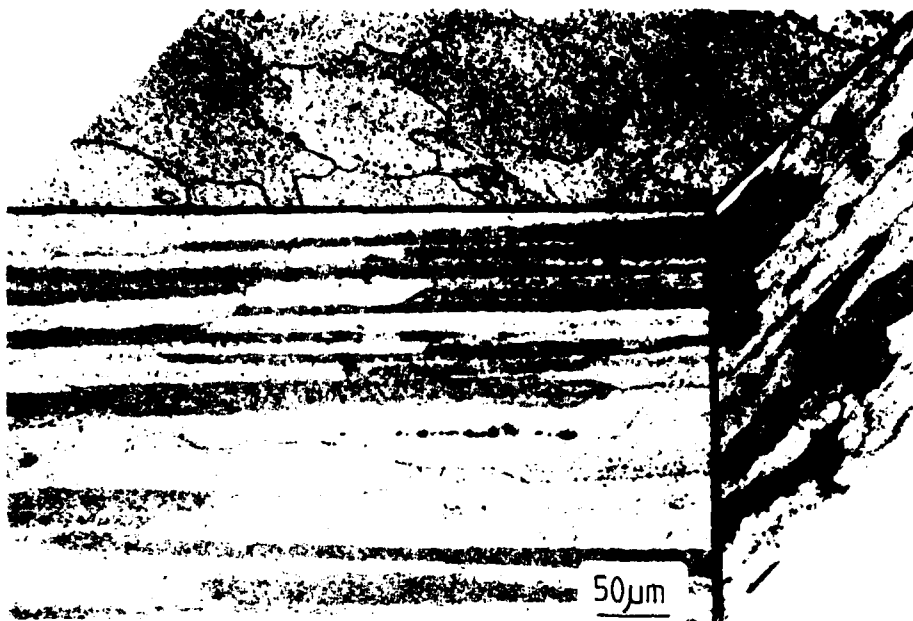


Figure 22. Optical micrograph of 7475 I/M rolled plate after heat-treatment; HNO_3 etch.

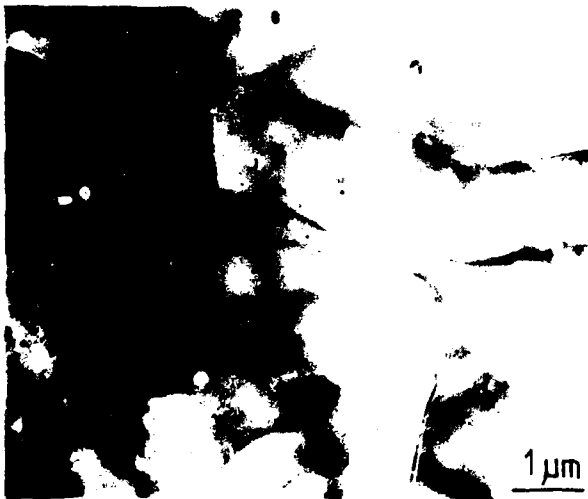


Figure 23. TEM showing large subgrain size in rolled and heat-treated 7475; longitudinal orientation.

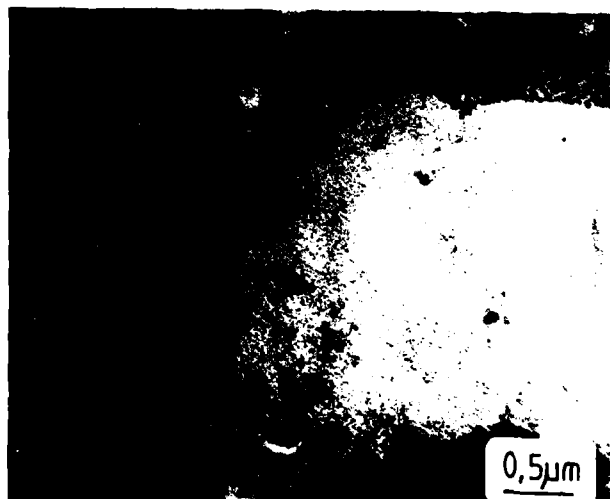
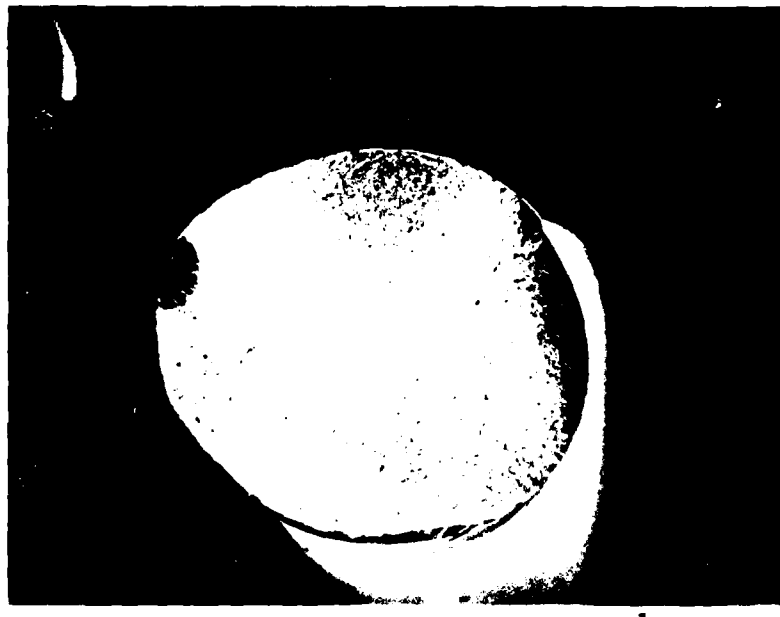


Figure 24. TEM showing precipitation at subgrain boundaries in rolled and heat-treated 7475; longitudinal orientation.



a



b

Figure 25. SEM, axial fatigue fracture surfaces, $\varepsilon = 0$, longitudinal, $\sigma_{\max} = 60$ ksi (414 MPa): (a) salt-fog, multiple initiation sites almost completely around edge of specimen, $N = 7,000$ cycles; (b) air, single initiation site, $N = 30,000$ cycles. 20X

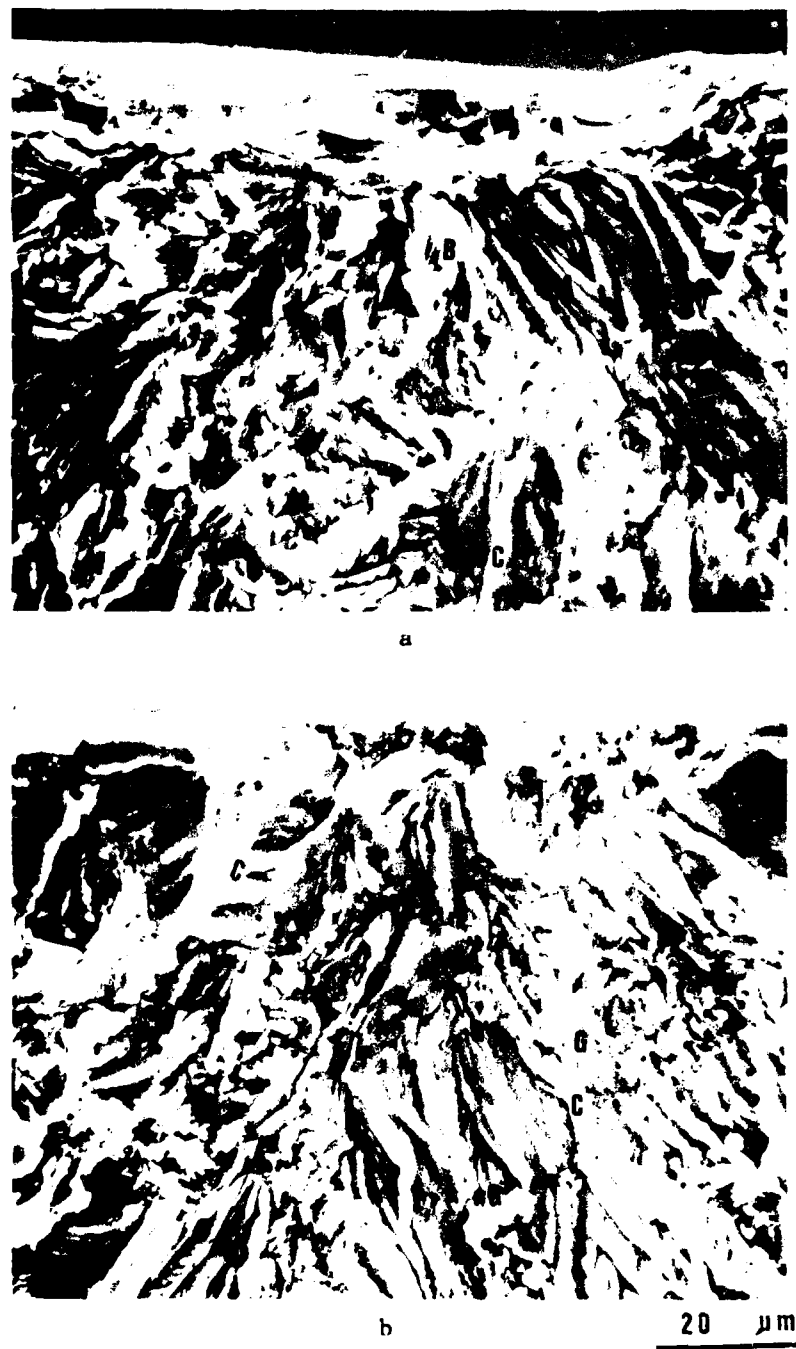


Figure 26. SEM, origin of fatigue fracture surfaces, $\epsilon = 0$, in air; $\sigma_{\text{max}} = 60$ ksi (414 MPa), A, narrow plateaus; B, smooth textured regions; C, tear ridges; G, grain boundaries; S, initiation site; (a) longitudinal, (b) short transverse. Direction of crack growth from top to bottom. 1000X



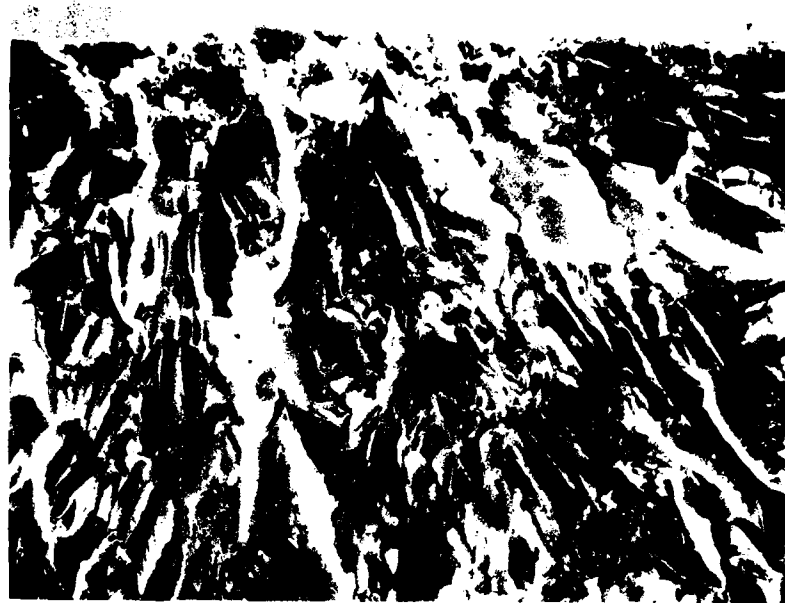
a



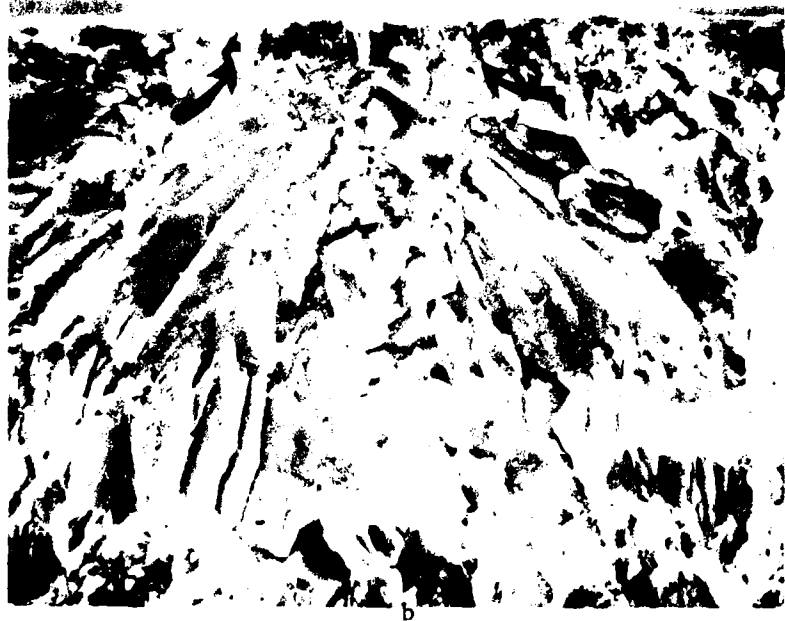
b

20 μm

Figure 27. SEM, origin of fatigue fracture surfaces, $\epsilon = 0.7$, air; $\sigma_{\text{max}} = 60 \text{ ksi}$ (414 MPa); A, narrow plateaus; B, smooth textured regions; C, tear ridges; G, grain boundaries: (a) longitudinal, (b) short transverse. Direction of crack growth from top to bottom. 1000X.

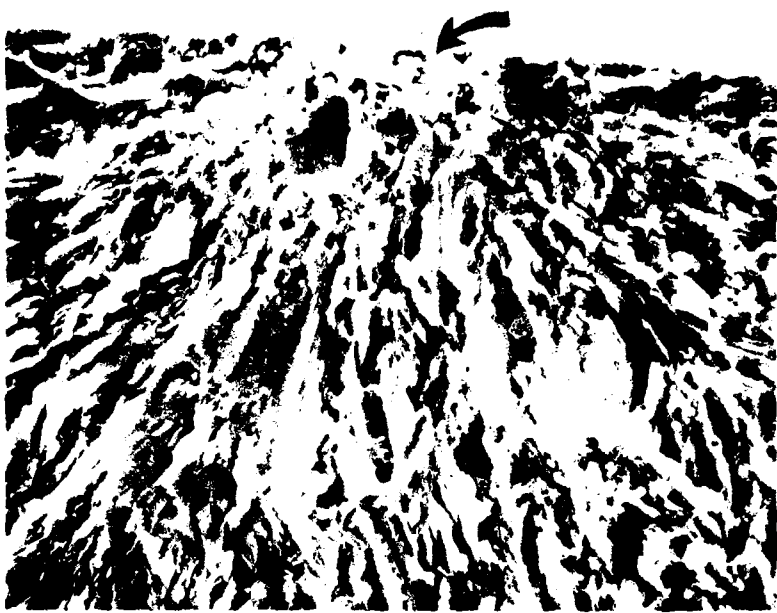


a



b

Figure 28. SEM, origin of fatigue fracture surfaces, $\epsilon = 0$, salt-fog $\sigma_{max} = 60$ ksi (414 MPa), arrows point to corrosion products at initiation sites: (a) longitudinal, (b) short transverse. Direction of crack growth from top to bottom. 1000X.



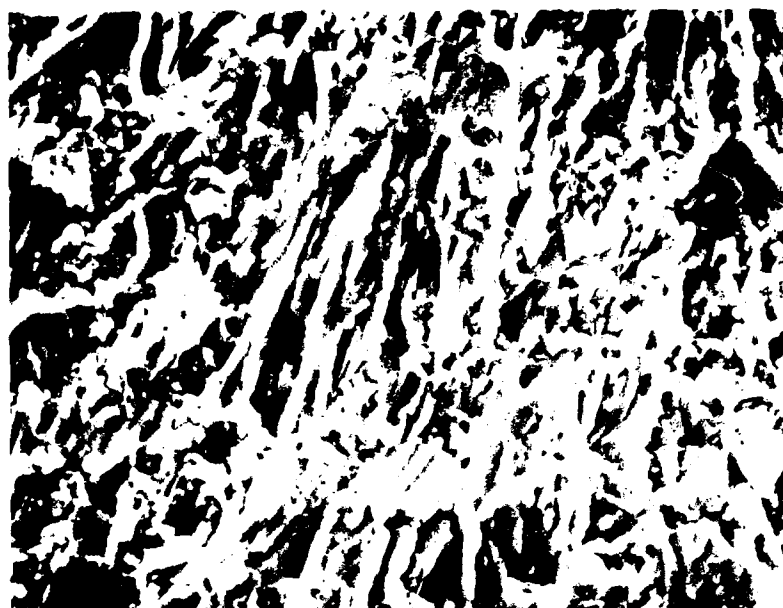
a



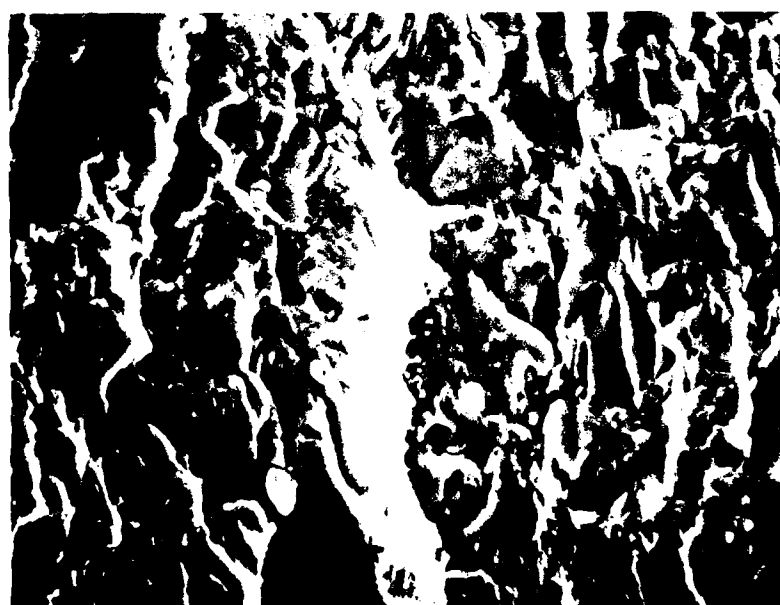
b

20 μm

Figure 29. SEM, origin of fatigue fracture surfaces, $\epsilon = 0.7$, longitudinal, salt-fog; arrows point to corrosion products at initiation sites:
(a) $\sigma_{\max} = 70 \text{ ksi (483 MPa)}$, (b) $\sigma_{\max} = 60 \text{ ksi (414 MPa)}$.
Direction of crack growth from top to bottom. 1000X.



a



b

Figure 30. SEM, center of fatigue fracture, Stage II, $\varepsilon = 0$, air,
 $\sigma_{\text{max}} = 60$ ksi (414 MPa): (a) longitudinal, (b) short
transverse. Direction of crack growth from top to
bottom. 1000X.

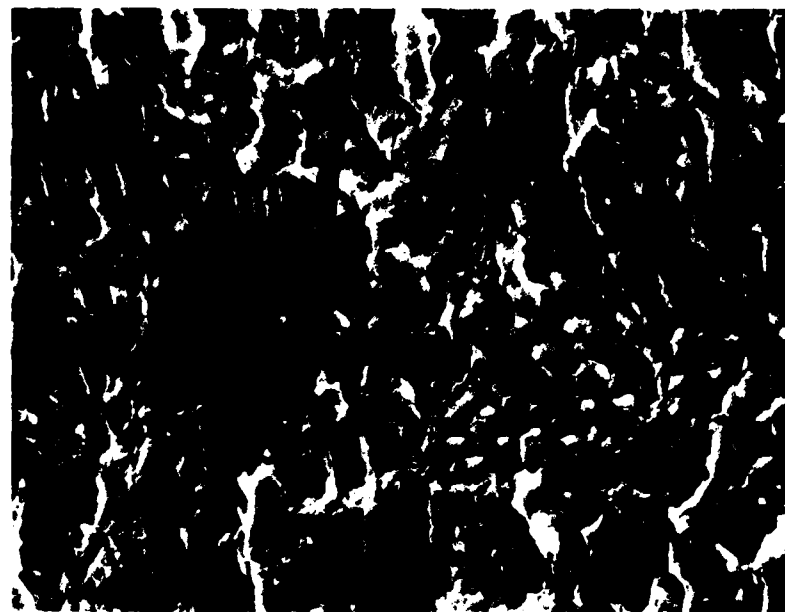


a

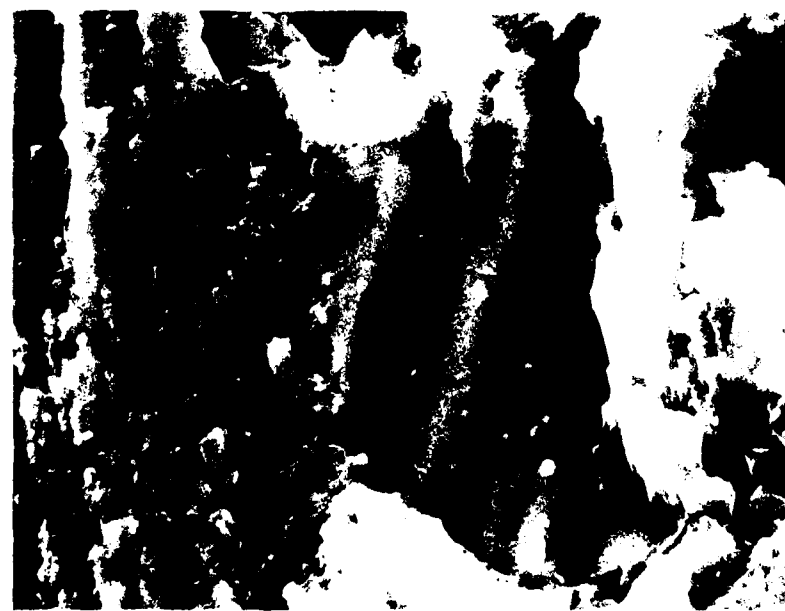


b

Figure 31. SEM, center of fatigue fracture, Stage II, $\epsilon = 0.3$, air, short transverse; Co, cobalt rich regions; P, fine particles: (a) $\sigma_{\max} = 70$ ksi (483 MPa), (b) $\sigma_{\max} = 60$ ksi (414 MPa). Direction of crack growth from top to bottom. 5000X.



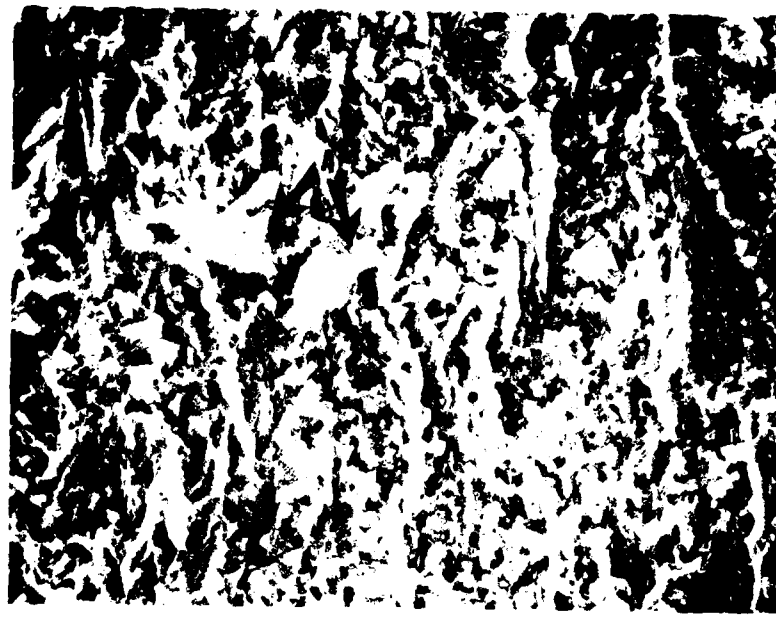
a



b

4 μm

Figure 32. SEM, center of fatigue fracture, Stage II, $\epsilon = 0$, salt-fog, longitudinal, $\sigma_{\text{max}} = 70 \text{ ksi}$ (483 MPa); A, brittle striations; B, ductile striations: (a) 1000X, (b) 5000X. Direction of crack growth from top to bottom.



a



b

Figure 33. SEM, center of fatigue fracture. Stage II, $\epsilon = 0.7$, salt-fog, longitudinal, $\sigma_{max} = 70$ ksi (483 MPa); A, plateaus of brittle striations: (a) 1000X, (b) 5000 X.



a

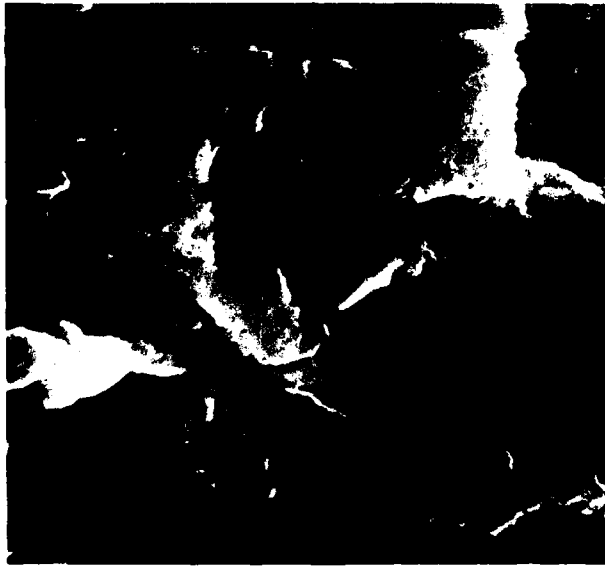


b

Figure 34. SEM, fracture surface for $\Delta K = 7 \text{ ksi} \sqrt{\text{in.}}$ ($7.7 \text{ MNm}^{-3/2}$)
 $\epsilon = 0.7$, longitudinal air, CT specimen: (a) 1000X,
(b) 5000X. Crack growth from left to right.

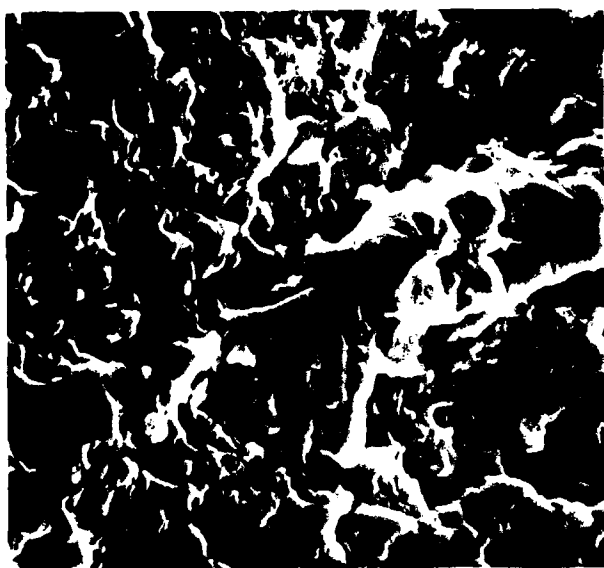


a



b

Figure 35. SEM, fracture surface for $\Delta K = 10 \text{ ksi}\sqrt{\text{in.}}$ ($11 \text{ MNm}^{-3/2}$)
 $\epsilon = 0.7$, longitudinal, air, CT specimen: (a) 1000X,
(b) 5000X. Crack growth from left to right.

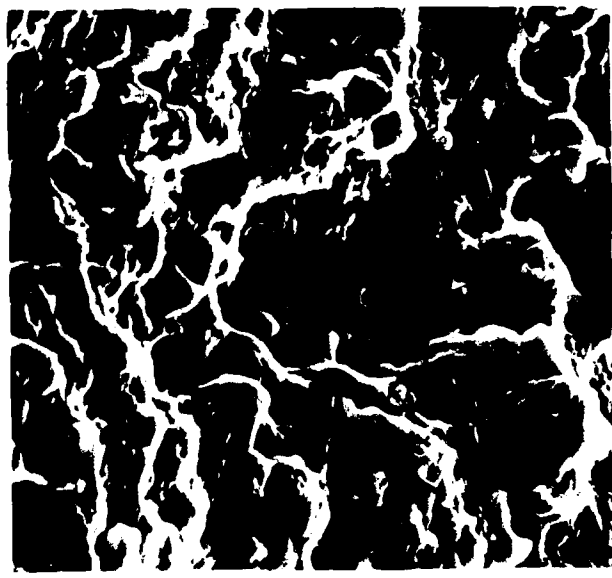


a



b

Figure 36. SEM, fracture surface for $\Delta K = 15 \text{ ksi}\sqrt{\text{in.}}$ ($16.5 \text{ MNm}^{-3/2}$)
 $\epsilon = 0.7$, longitudinal, air, CT specimen: (a) 1000X,
(b) 5000X. Crack growth from left to right.

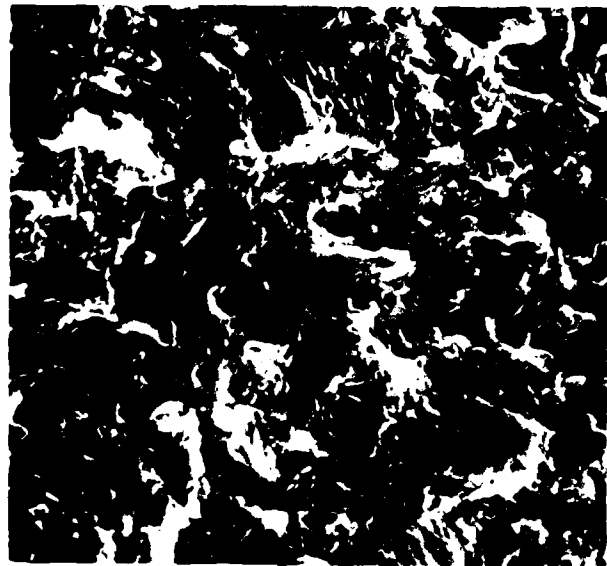


a



b

Figure 37. SEM, fracture surface for $\Delta K = 20 \text{ ksi}\sqrt{\text{in.}}$ ($22 \text{ MNm}^{-3/2}$)
 $\epsilon = 0.7$, longitudinal, air, CT specimen: (a) 1000X,
(b) 5000X. Crack growth from left to right.

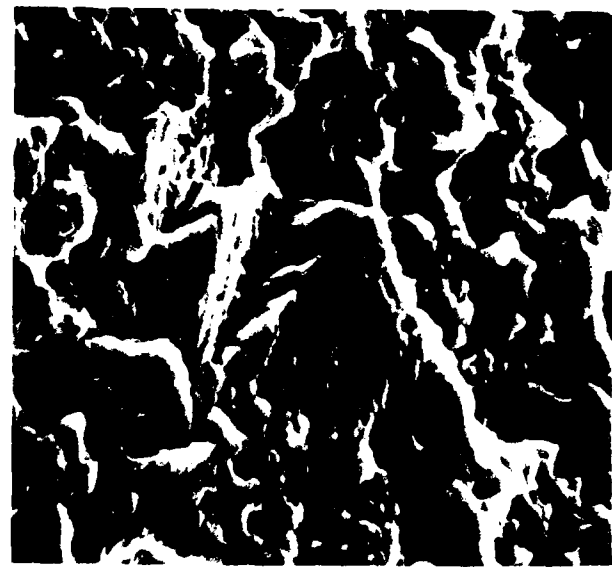


a



b

Figure 38. SEM, "mud cracks" removed, fracture surface for $\Delta K = 7 \text{ ksi}\sqrt{\text{in.}}$ ($7.7 \text{ MNm}^{-3/2}$) $\epsilon=0$, short transverse, salt-fog, CT specimen: (a) 1000X, (b) 5000X.
Crack growth from left to right.



a



b

Figure 39. SEM, fracture surface for $\Delta K = 15 \text{ ksi}\sqrt{\text{in.}}$ ($16.5 \text{ MNm}^{-3/2}$)
 $\epsilon=0$, short transverse, salt-fog, CT specimen: (a) 1000X,
(b) 5000X. Crack growth from left to right.

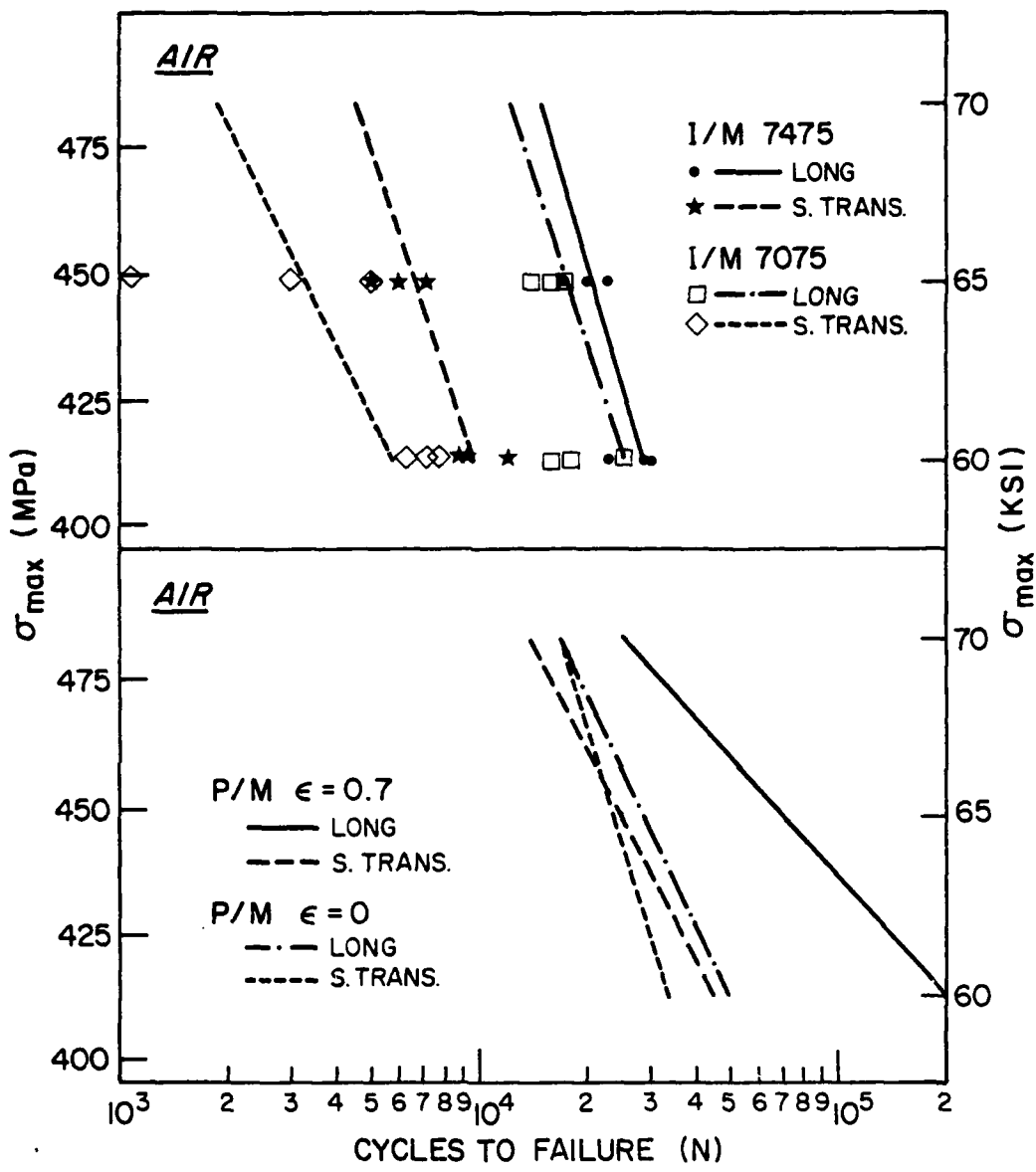


Figure 40. Median fatigue life vs σ_{max} for I/M 7075 and 7475, solution treated and aged material tested in air

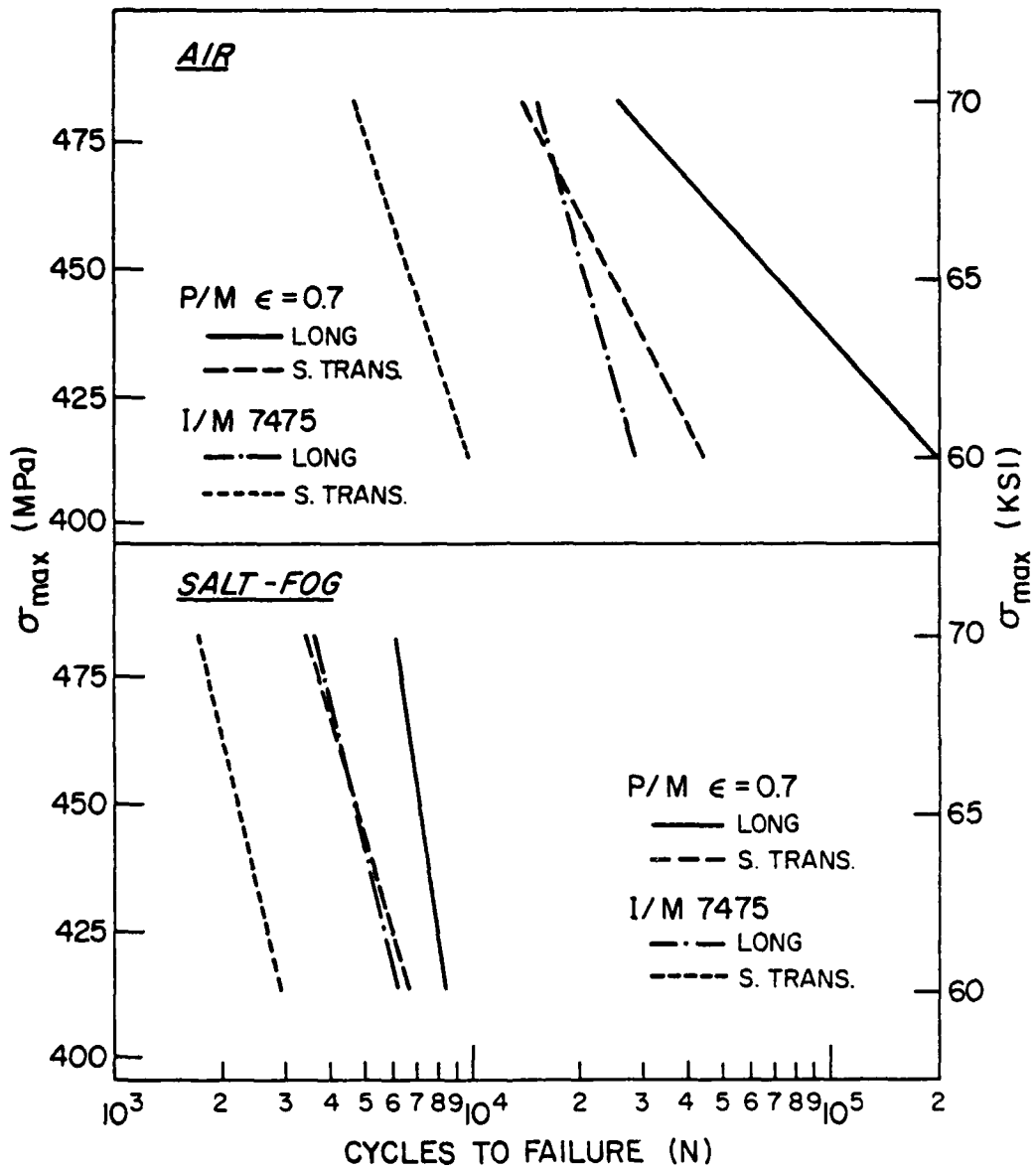


Figure 41. Median fatigue life vs σ_{\max} for P/M forged ($\epsilon = 0.7$) and I/M 7475, solution treated and aged material tested in air and 3 1/2% NaCl solution salt-fog.

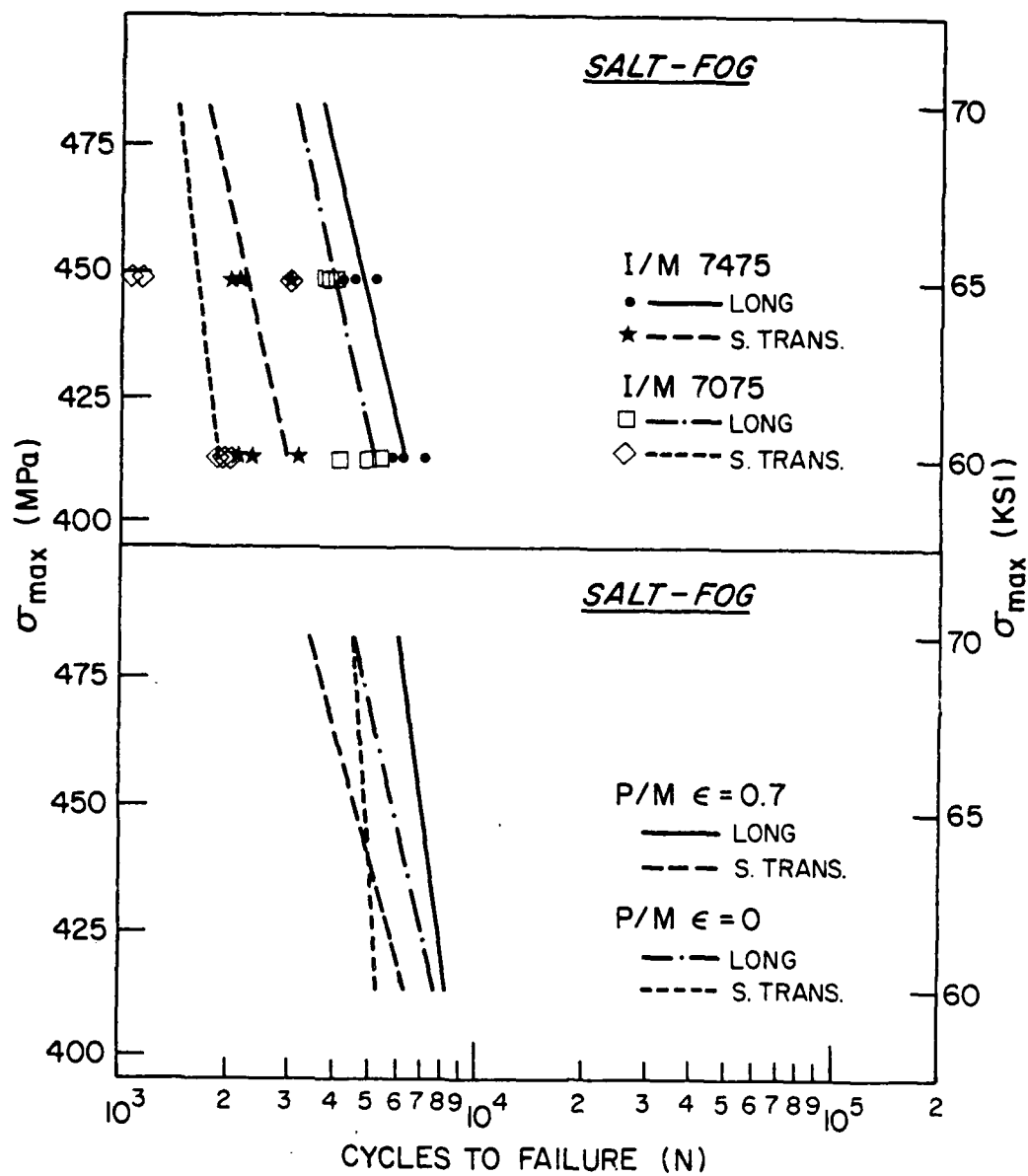
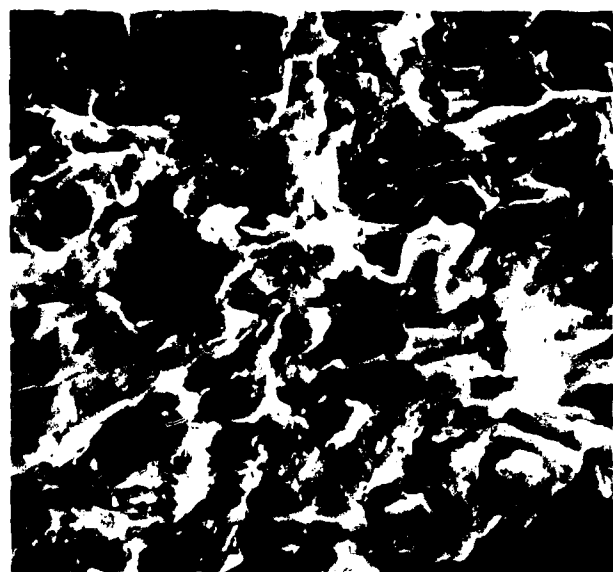


Figure 42. Median fatigue life vs σ_{\max} for I/M 7075 and 7475, solution treated and aged material tested in 3 1/2% NaCl solution salt-fog



a



b

Figure 43. SEM, fracture surface for $\Delta K = 7 \text{ ksi}\sqrt{\text{in.}}$ ($7.7 \text{ MNm}^{-3/2}$)
 $\epsilon=0$, short transverse, air, CT specimen: (a) 1000X,
(b) 5000X. Crack growth from left to right.

PART III

THE LOW-CYCLE FATIGUE OF POWDER-PROCESSED
HIGH STRENGTH ALUMINUM ALLOYS

SUMMARY

The strain-controlled low-cycle fatigue behavior of powder-processed high-strength aluminum alloys has been examined in air. Three cobalt levels (0%, 0.4% and 0.8%) and two processing modes (single upset and die forged (A) or triple upset and die forged (ABC)) were included and a comparison made with ingot metallurgy (I/M) 7475. There is no significant effect of Co level on low-cycle fatigue response. The more complex processing mode (ABC) gives higher values of the fatigue ductility coefficient and longer fatigue life at a given strain amplitude than the A-processing mode. At comparable levels of strain amplitude, the low-cycle fatigue life of the ABC-processed P/M material is superior to that of I/M 7475. At comparable strains, the P/M material exhibits higher stress levels than the I/M alloy. A uniform distribution of η' precipitates in the P/M material results in fine-scale homogeneous deformation. In consequence, fracture surface details are on a finer scale in the P/M material than in the I/M 7475 alloy.

INTRODUCTION

Several high-strength aluminum alloys, based on Al-Zn, Mg, Cu, have become available as the result of extensive processing and alloy development studies (1-3,6-8,37,51). The improvement in static and dynamic mechanical

properties is achieved by careful control of the constituent particles, the size and volume fraction of dispersoids and through grain refinement. Improvement in fatigue life resides in the ability to produce microstructures which resist both crack initiation and propagation.

The development of fully dense aluminum P/M alloys provides for a product with a fine grain size and high degree of homogeneity with attendant improvements in fatigue life in conventional load-controlled (S-N) fatigue (13,17-32). Interest has also been directed to fatigue in which the controlling variable is cyclic strain rather than cyclic load or stress(51-56). This mode of fatigue is referred to as low cycle strain-controlled fatigue. The interest in and importance of strain-controlled fatigue testing stems from the need to develop an understanding of the response of the alloy to a relatively small number of strain cycles by definition <50,000 (57).

In the present program, a limited study has been made of the low-cycle fatigue behavior of three P/M-processed high-strength aluminum alloys. Similar tests were performed on a comparable I/M alloy. The results are evaluated in light of the attendant microstructures and fracture morphologies.

EXPERIMENTAL PROCEDURE

1. Material and Processing

The P/M material used for the strain-controlled fatigue study was the same as that evaluated in Part I. Details of powder preparation, cold and hot compaction, hot working and heat-treatment are contained in Part I of this report. Three cobalt levels (Table I) and two processing modes involving upsetting and forging were included, Figure 1. The P/M billets

were heat-treated to a T6 + overage temper, Table II.

A comparison was made with the strain-controlled fatigue response of I/M 7475. This material was supplied by Alcoa in the T651 condition.

2. Specimens and Fatigue Testing

Cylindrical specimens were machined from the forgings in the longitudinal orientation (Figure 1) with threaded ends and a reduced diameter. Specimen configuration conformed to ASTM E-606-74T with a gage length of 0.5" (12.7 mm) and gage diameter 0.25" (6.35 mm).

Specimens were hand ground down to 600 grit emery paper and electro-polished in Lenoir's solution using a pure aluminum cathode ring. After electropolishing, specimens were washed in distilled water and methanol. Gage diameter was measured along the gage length at points 90° apart, using a toolmakers microscope; the average cross sectional area was calculated from these readings.

Fully-reversed push-pull low cycle fatigue tests were carried out under total strain control on a closed loop servohydraulic MTS machine. For each test, the frequency was adjusted to maintain a constant total strain rate of $5 \times 10^{-3} \text{ s}^{-1}$ using a triangular wave form. Strain was controlled by a 0.5" (12.7 mm) extensometer attached to the specimen. Small strips of tape were placed under the knife edges of the extensometer to prevent cutting of the specimen. A Wood's metal reservoir was used to insure proper alignment of the sample with respect to the loading axis. Load versus deflection data from the specimen were monitored on a X-Y recorder and cycles were recorded at appropriate intervals.

3. Strain-Life Curves

Typical stress-strain behavior in low-cycle fatigue testing is illustrated schematically in Figure 2. The total strain range $\Delta\epsilon$ is controlled by the extensometer output; however, during testing, the plastic ($\Delta\epsilon_p$) and elastic ($\Delta\epsilon_e$) strain ranges and the stress range ($\Delta\sigma$) vary. Accordingly, the strain amplitudes ($\Delta\epsilon_p/2$ and $\Delta\epsilon_e/2$) are usually recorded at their half life value and plotted against the number of load reversals to failure $2N_f$. By varying the total strain range, a complete strain versus load reversals to failure curve can be drawn, Figure 3.

The elastic and plastic strain curves can be described by the following power functions (58).

$$\Delta\epsilon_e/2 = \sigma_a/E = \sigma'_f/E(2N_f)^b \quad (1)$$

where $\Delta\epsilon_e/2$ = elastic strain amplitude

σ_a = stress amplitude

σ'_f = fatigue strength coefficient, defined as the stress intercept at one load reversal ($2N_f = 1$), i.e. true stress required to cause failure in one reversal.

N_f = cycles to failure; $2N_f$ = load reversals to failure

E = modulus of elasticity

b = fatigue strength exponent

$$\Delta\epsilon_p/2 = \epsilon'_f (2N_f)^c \quad (2)$$

where ϵ'_f = fatigue ductility coefficient, defined by the strain intercept at one load reversal ($2N_f = 1$); i.e. true strain required to cause failure in one reversal

c = fatigue ductility exponent, a material property reflecting tolerance to cyclic plastic strain.

4. Metallography

Electron-transparent foils were prepared from the P/M forgings after low-cycle fatigue, using standard twin-jet thinning procedures. Samples were examined in a JEM-120 TEM.

Fracture surfaces were examined directly in a JSM-2 microscope. Crack initiation, propagation and tensile overload regions were identified.

RESULTS AND DISCUSSION

1. Low-Cycle Fatigue Response

Representative data for strain amplitude versus reversals to failure in the P/M forgings for A and ABC processing at the 0.4% Co level are illustrated in Figures 4 and 5. Similar curves were obtained at the 0% and 0.8% Co levels for each processing mode. Coffin-Manson plots of the plastic strain versus reversals to failure as a function of Co level for A-processing are shown in Figure 6. Data for the I/M 7475 alloy are also included. Similarly, the plastic strain response after ABC processing is given in Figure 7.

The Coffin-Manson plots can be considered as an indication of the resistance of the microstructure to crack initiation and failure in the low-cycle fatigue region (57). From Figures 6 and 7 it is seen that there is no significant effect of Co level. Processing mode does influence the low-cycle fatigue response, as illustrated in Figure 8. Thus, ABC-processing gives higher values of ϵ_f' and C than A-processing. The reverse is true for the cyclic strain hardening coefficient n'. At a given strain amplitude, the fatigue life is higher after ABC-processing than A-processing. These improvements are attributed to the small grain size and homogeneous microstructure (50).

The dependence of low-cycle fatigue life on stress amplitude is illustrated for the 0.8% Co alloy (ABC-processing) in Figure 9. A similar form of response was observed at the 0% and 0.4% Co levels and in each processing mode. For comparison, the behavior of the I/M 7475 alloy is shown in Figure 10. At comparable levels of strain, or number of cycles the P/M material exhibited higher stress levels than the I/M alloy. In both the I/M and P/M materials, strain hardening, followed by strain softening, occurs at the higher strain amplitudes. There is a small degree of strain softening in both materials at low strain amplitudes.

At each cobalt level, the P/M material exhibits softening followed by cyclic hardening, as illustrated in Figure 9. This type of behavior has also been reported by Sanders and Starke (6,50) who attributed the effect to the relief of residual stresses present in the samples rather than a precipitate-dislocation interaction. This explanation is supported by the fact that the softening effect varies with strain amplitude from a few cycles at $\epsilon = \pm 0.02$ to approximately 20 cycles at $\epsilon = \pm 0.01$. Residual stress was not measured in this investigation; values of 10-40 MPa have been reported by Sanders and Starke (6).

2. Fractography

Representative fracture morphologies (SEM) of the crack initiation, propagation and tensile overload regions for the 0.4% Co, ABC-processed P/M alloy are illustrated in Figure 11. The crack propagation region in the 0.8% Co alloy after ABC-processing is shown in Figure 12. From the examination of fracture surfaces from each of the three cobalt levels and the two processing modes, it was concluded that as the Co level increased and the processing mode changed from A to ABC, there was a proportionally higher level of secondary (micro-) cracking evident in the crack propagation region.

This is in agreement with Rafalin's observations (41). Rafalin found that at high ΔK levels in the 0.8% Co, ABC-processed alloy, microcracking ahead of the main crack resulted in lower rates of crack propagation. These secondary cracks effectively increase the energy required to propagate the main crack.

Fracture surfaces in the I/M 7475 alloy are shown in Figure 13. Comparison with Figure 11 shows that a comparable strain amplitude, in each of the three regions fracture detail is finer in the P/M material. This is a consequence of the finer grain size ($<10 \mu\text{m}$) and subgrain size ($<2 \mu\text{m}$) in the P/M alloy, compared to a grain size ($\sim 40 \mu\text{m}$) and subgrain size ($\sim 7 \mu\text{m}$) in the I/M 7475. In the crack propagation region, fatigue striations are coarser and more clearly defined in the I/M 7475 alloy. Similarly, the dimples characteristic of tensile overload are coarser in the I/M 7475 alloy.

3. Microstructure

Transmission electron micrographs of the P/M material following low-cycle fatigue are shown in Figure 14. In Figure 14(a), the uniform distribution of η' precipitates is evident; the sample was cycled 4 times. The η' precipitates lead to dislocation looping and homogeneous deformation at high plastic strain amplitudes (50). The uniform distribution of the dislocation substructure after 24 cycles is illustrated in Figure 14(b).

CONCLUSIONS

ABC-processing gives higher fatigue ductility coefficients and longer fatigue lives at a given strain amplitude than A-processing in the P/M material. Low-cycle fatigue life is higher in the ABC-processed P/M material than in the I/M 7475 alloy.

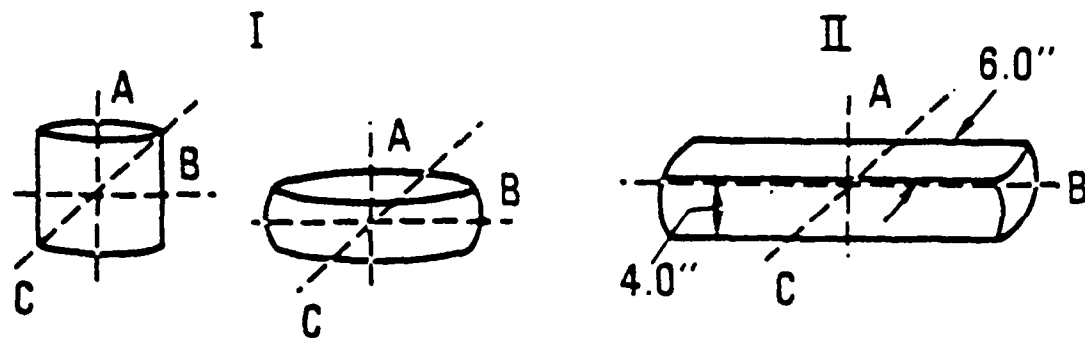
The uniform distribution of η' precipitates in the P/M processed material results in fine-scale homogeneous deformation. Associated fracture surface features are on a finer scale in the P/M material.

Table I: Nominal Composition of Powder Metallurgy (P/M) and Ingot Metallurgy (I/M) Alloys, Wt %.

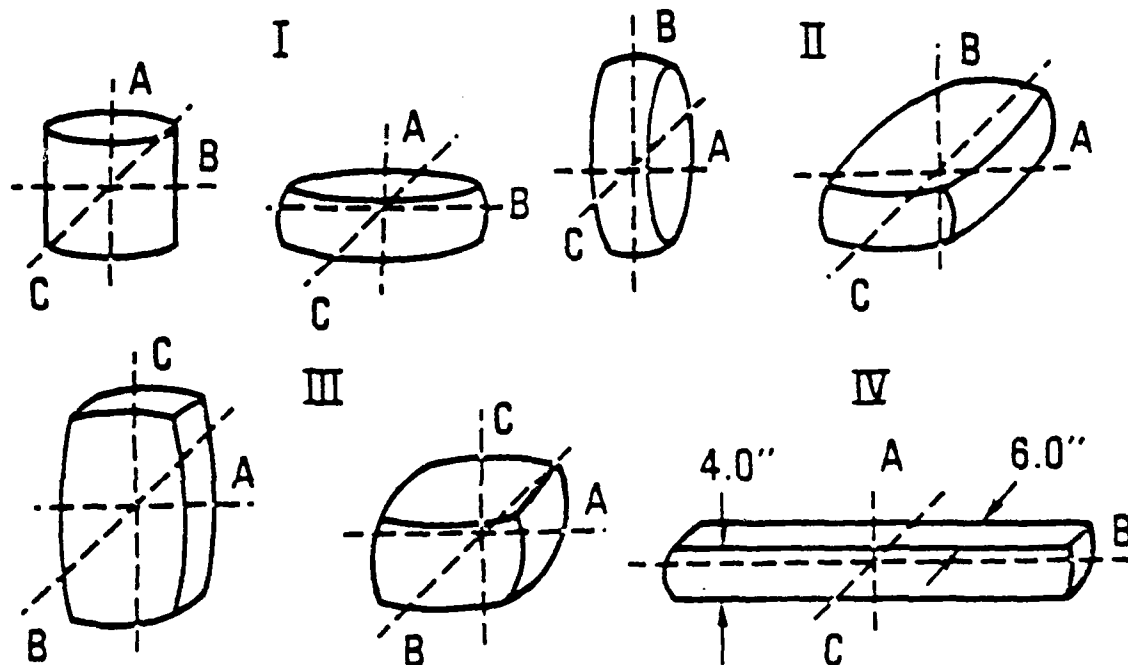
Alloy	Si	Fe	Cu	Mn	Mg	Cr	Zn	Ti	Co	Al
7475 (I/M)	.10	.12	1.2/1.9	.06	1.9/2.6	.18/.25	5.2/6.2	.06	--	Balance
P/M	.05	.09	1.5	--	2.5	--	6.5	--	--	Balance
P/M	.05	.09	1.5	--	2.5	--	6.5	--	0.4	Balance
P/M	.05	.09	1.5	--	2.5	--	6.5	--	0.8	Balance

Table II: Heat Treatment for P/M Forgings.

Solutionize 7200s (2 hours) at 761K (910°F)
 Natural Age 4.3 x 10⁵s (5 days) at 294K (70°F)
 Age 8.6 x 10⁴s (1 day) at 394K (250°F)
 Age 1.4 x 10⁴s (4 hours) at 436K (325°F)



Upset and Forge - A Process



Upset and Forge -

ABC Process

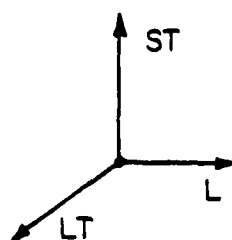


Figure 1: Schematic showing the A and ABC upset and forge modes of deformation (28).

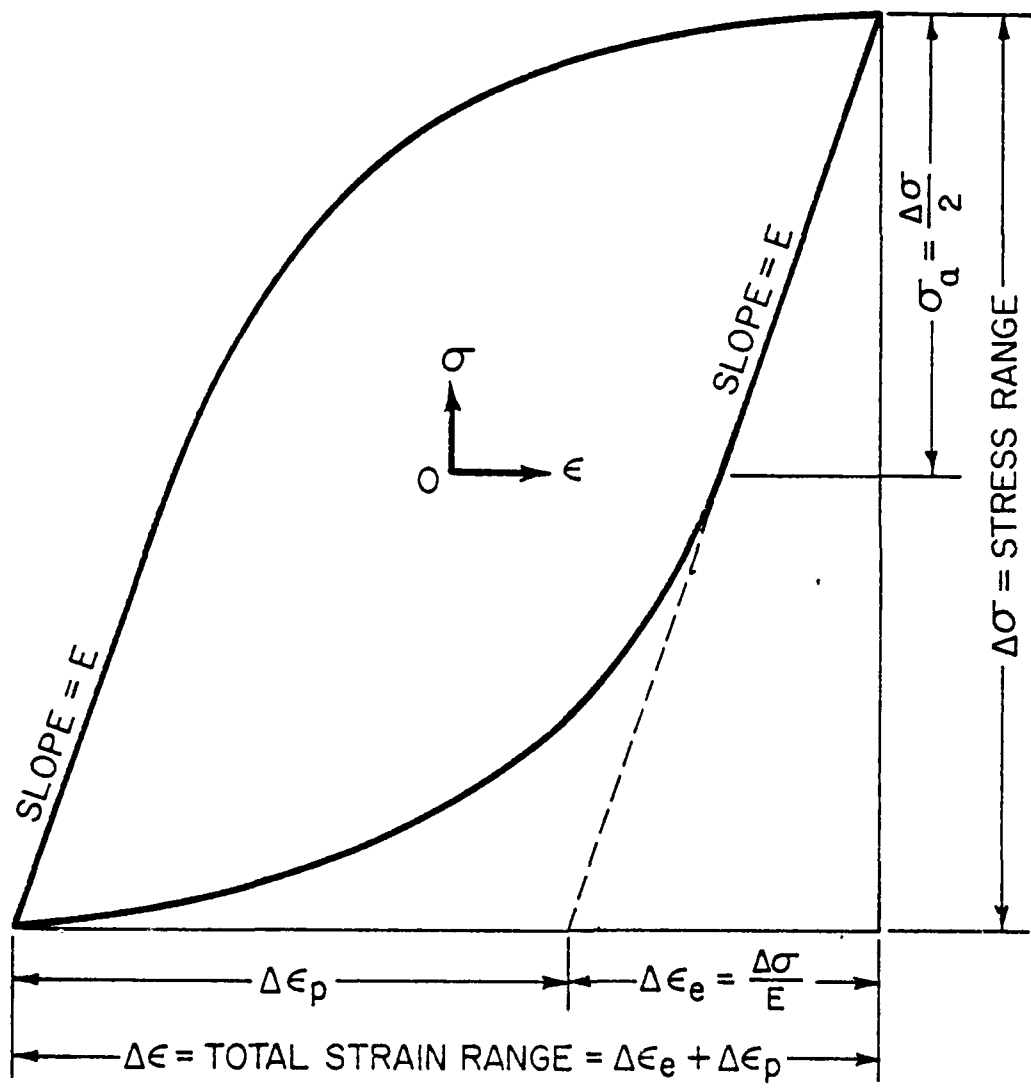


Figure 2: Schematic showing stress-strain behavior in low cycle fatigue.

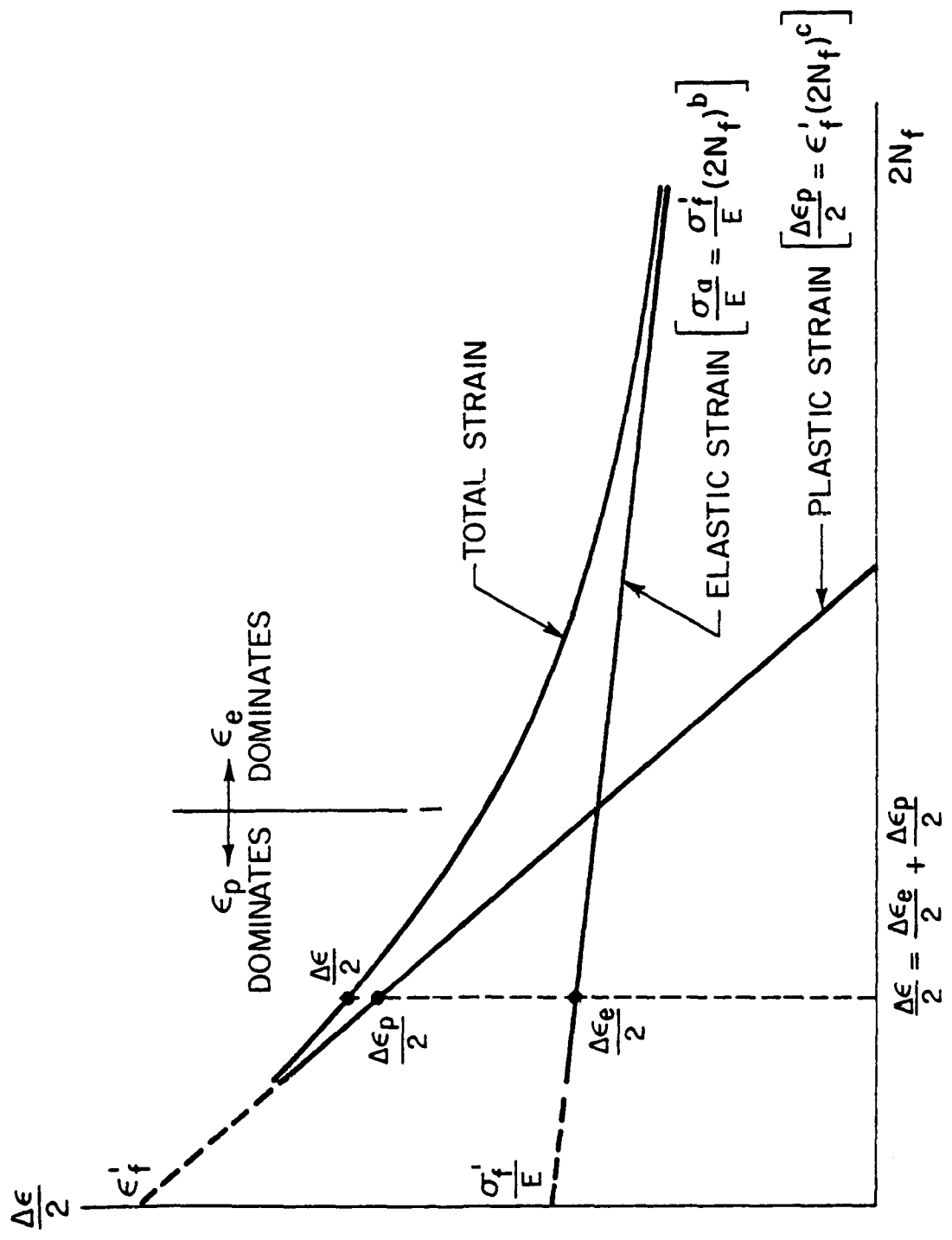


Figure 3: Reversals to failure as a function of elastic, plastic and total strain amplitudes - schematic.

AD-A305 880

DREXEL UNIV PHILADELPHIA PA DEPT OF MATERIALS ENGINEERING F/8 11/6
A FUNDAMENTAL STUDY OF FATIGUE IN POWDER METALLURGY ALUMINUM AL--ETC(U)
AUG 81 A LAWLEY, M J KOCZAK AFOSR-77-3247

UNCLASSIFIED

AFOSR-TR-81-0692

NL

3^a 3
4
400-080

END
DATE
FILED
11-81
NTIC

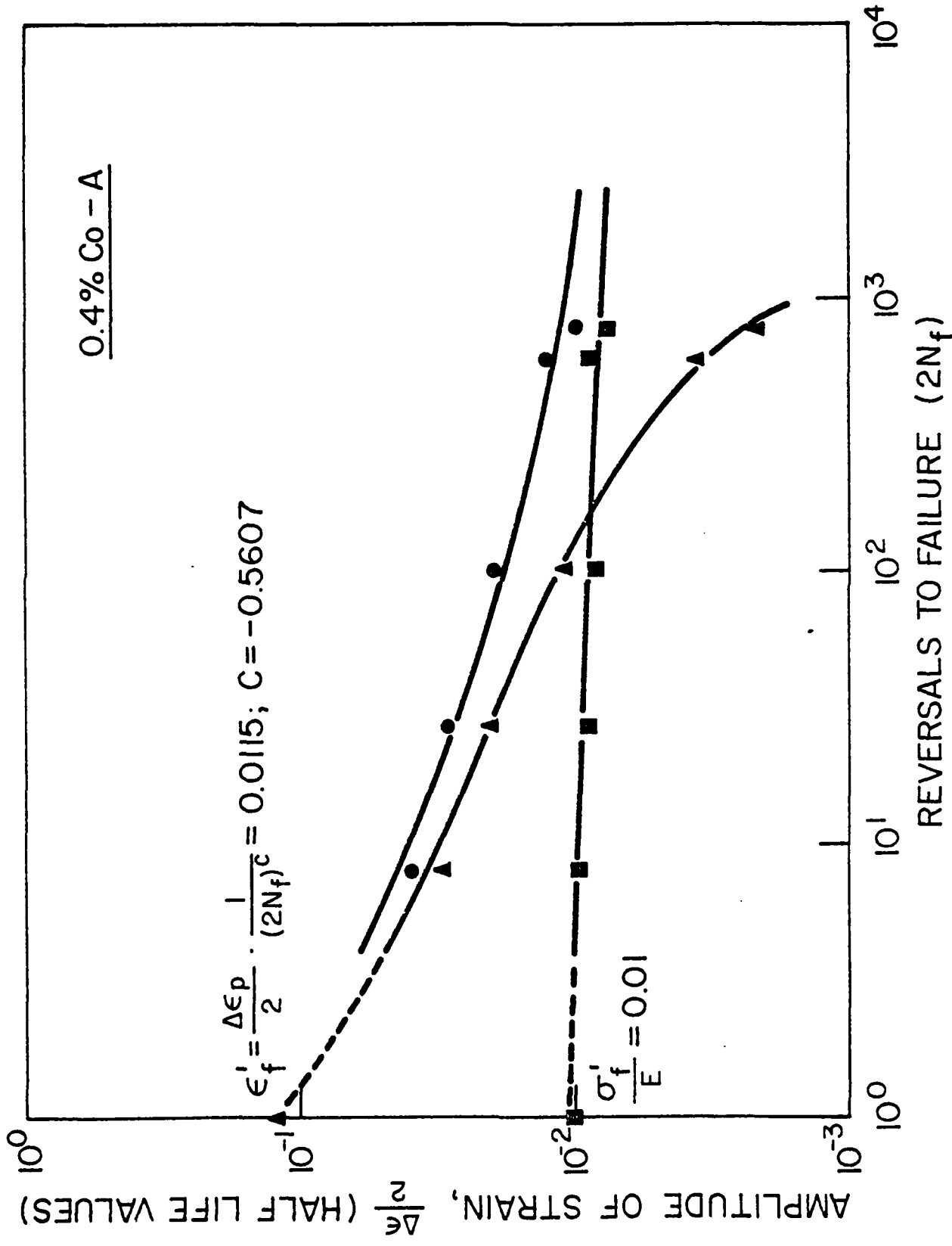


Figure 4: Reversals to failure as a function of elastic, plastic and total strain amplitudes for the A-processed 0.4% P/M forged alloy.

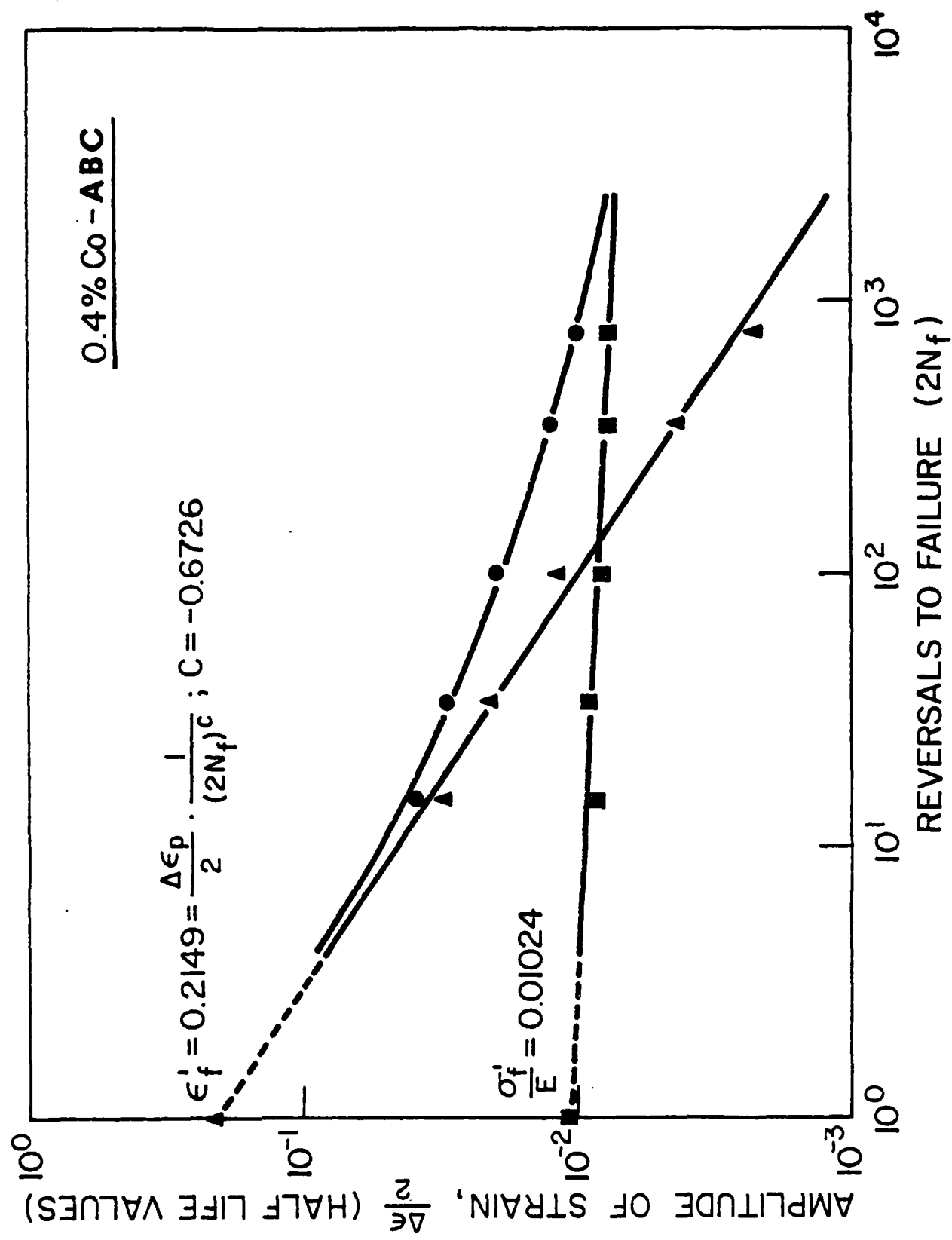


Figure 5: Reversals to failure as a function of elastic, plastic and total strain amplitudes for the ABC-processed 0.4% P/M forged alloy.

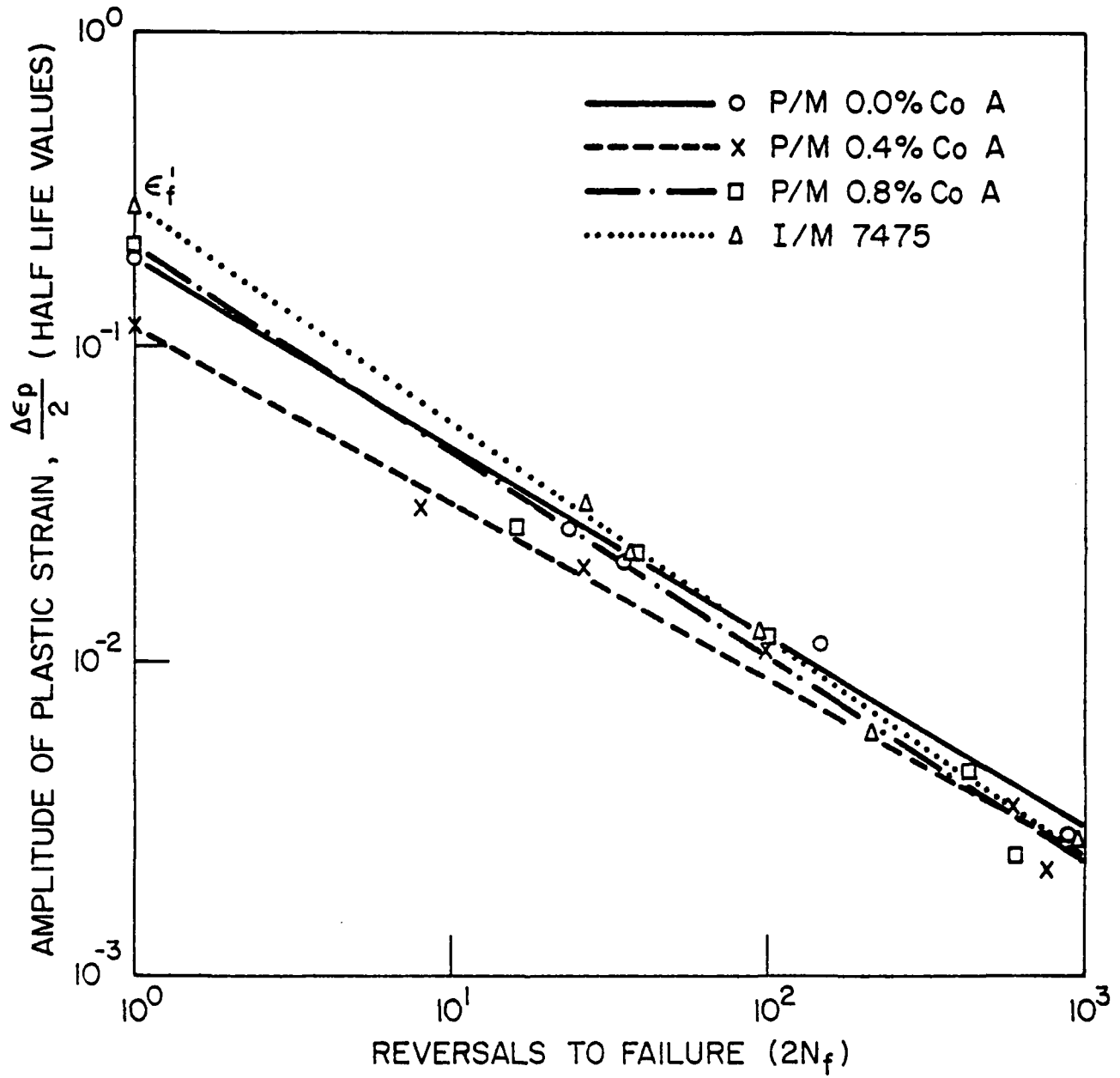


Figure 6: Plastic strain amplitude versus reversals to failure for A-processed P/M and I/M 7475 alloys.

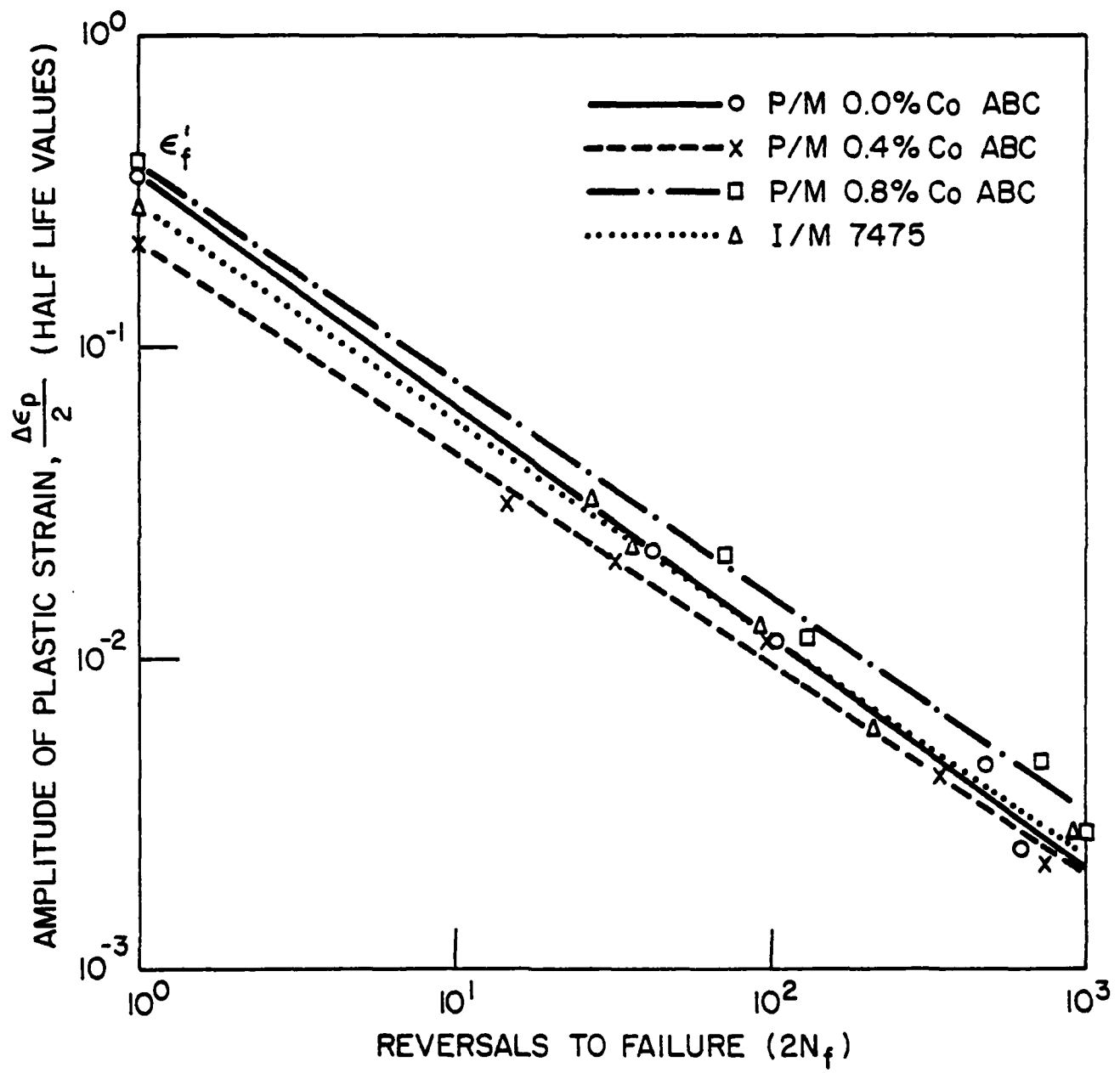


Figure 7: Plastic strain amplitude versus reversals to failure for ABC-processed P/M and I/M 7475 alloys.

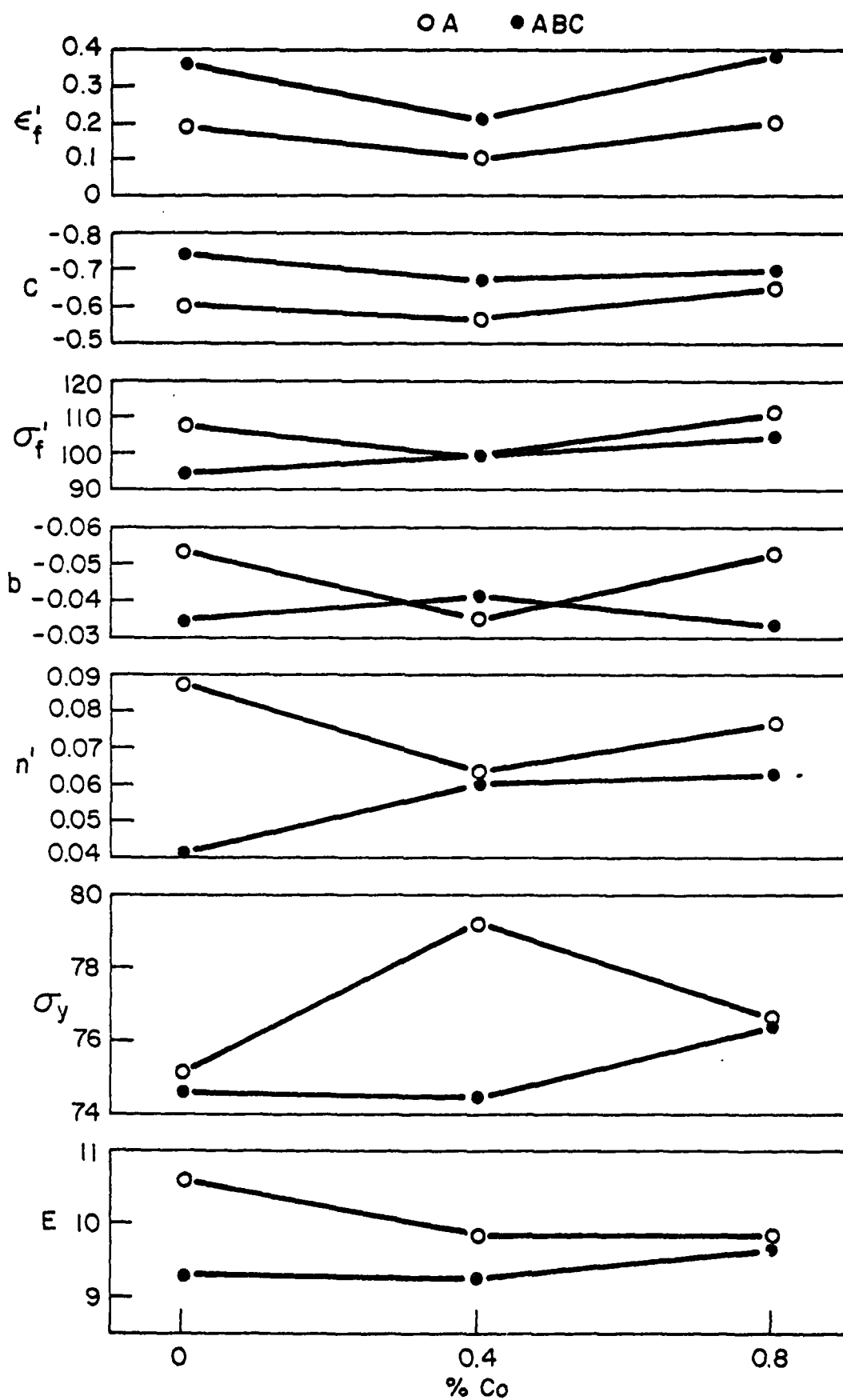


Figure 8: Tensile and fatigue properties and coefficients as a function of cobalt level and processing mode.

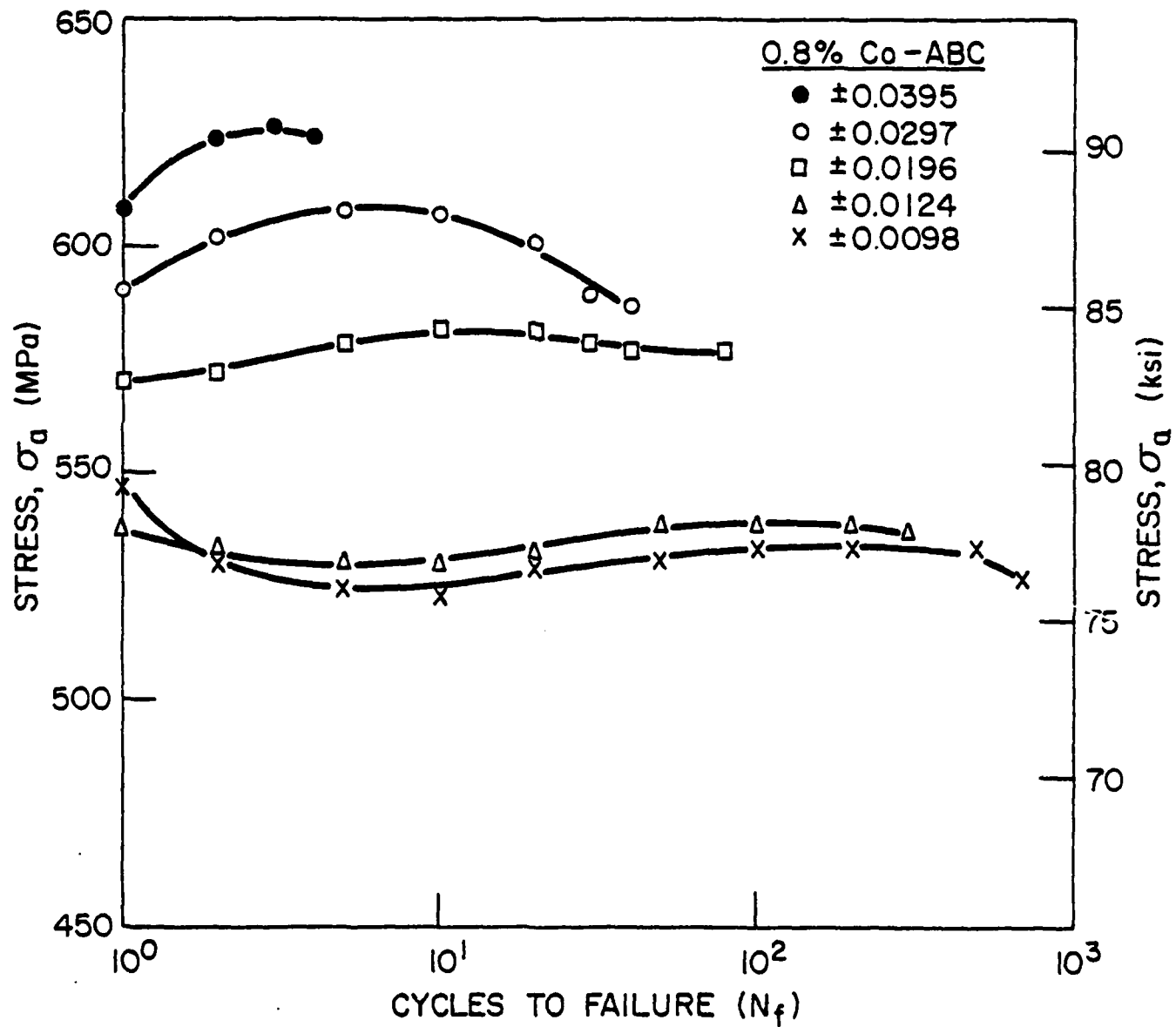


Figure 9: Stress amplitude versus cycles to failure for the ABC-processed 0.8% Co P/M forged alloy.

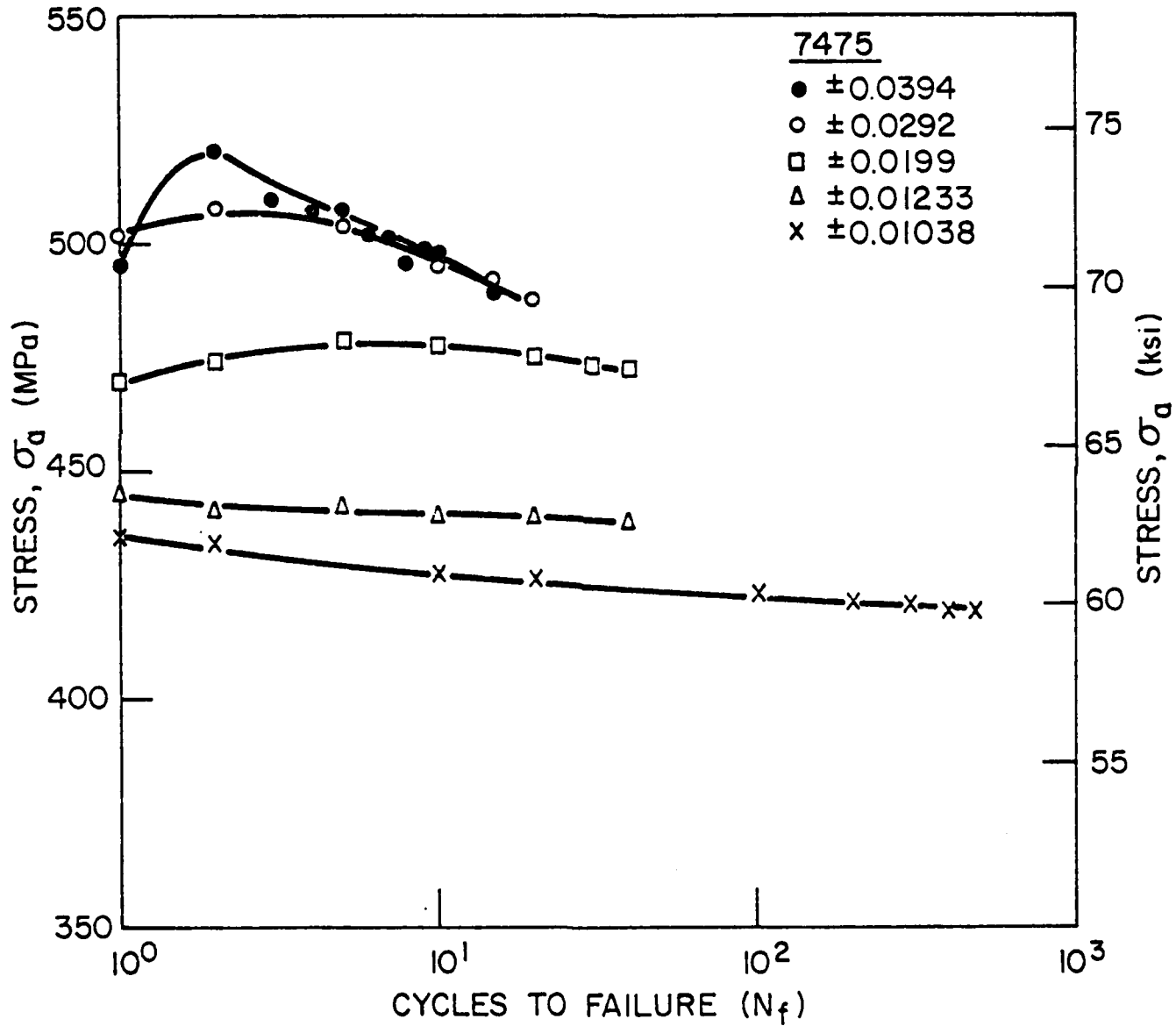
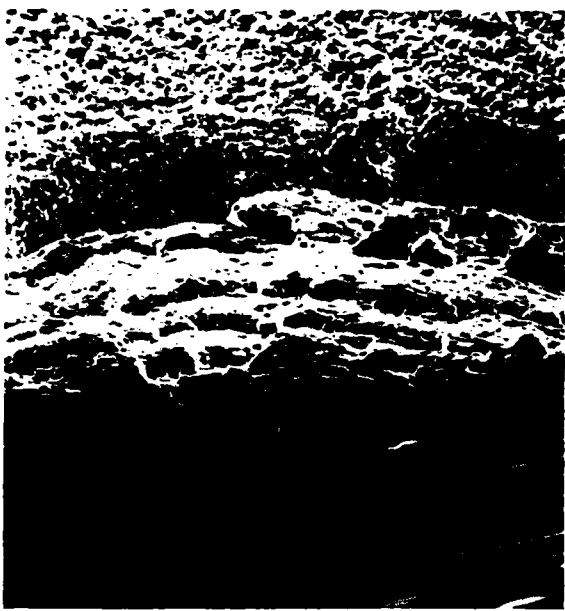
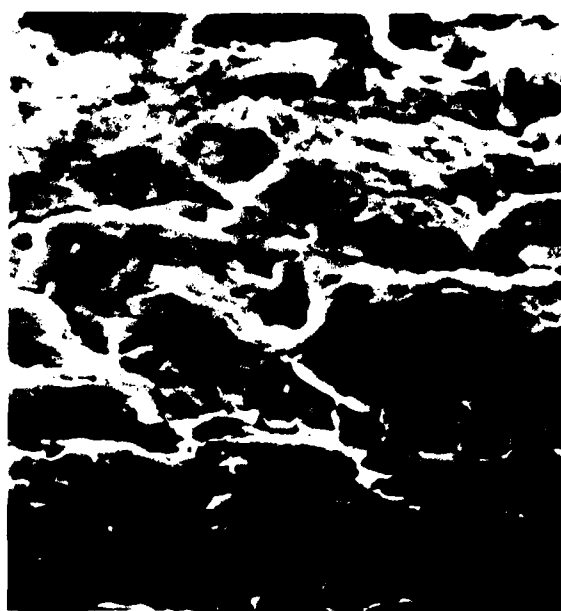


Figure 10: Stress amplitude versus cycles to failure for the I/M 7475 alloy.



(a)



(b)



(c)



(d)

Figure 11: SEM of fracture surfaces in 0.4% Co, ABC-processed P/M forgings; $\epsilon = \pm 0.01$, (a) initiation region, $\times 100$; (b) initiation region $\times 1000$; (c) propagation region, $\times 3000$; (d) tensile overload, $\times 3000$.

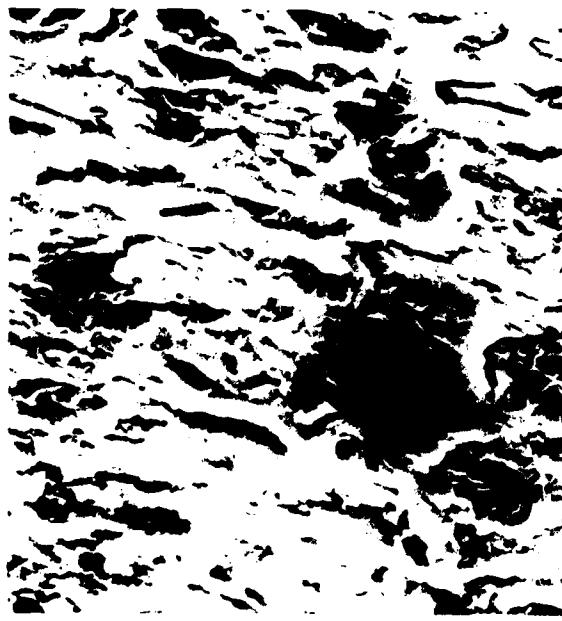


Figure 12: SEM of fracture surface in 0.8% Co, ABC-processed P/M forging; $\epsilon = \pm 0.01$. Fatigue crack propagation region, $\times 1000$.



(a)



(b)



(c)

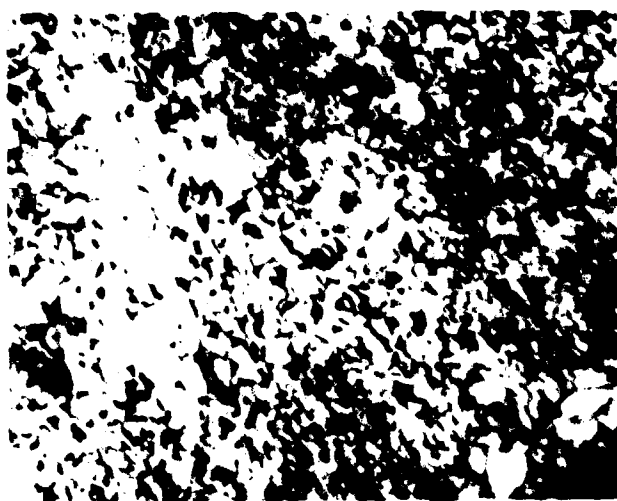


(d)

Figure 13: SEM of fracture surfaces in I/M 7475; $\epsilon = \pm 0.01013$.
(a) initiation region, $\times 100$; (b) propagation region, $\times 300$;
(c) propagation region, $\times 500$; (d) tensile overload, $\times 2000$.



(a)



(b)

Figure 14: TEM of P/M forgings after low cycle fatigue: (a) 0.4% Co, A-processed. $\epsilon = \pm 0.039$, $\times 20,000$; (b) 0% Co, ABC-processed. $\epsilon = \pm 0.029$. $\times 100,000$.

REFERENCES

1. J. T. Staley: "How Microstructure Affects Fatigue and Fracture of Aluminum Alloys", Aluminum Company of America, International Symposium of Fracture Mechanics, George Washington University, Sept. 1978.
2. W. G. Truckner, J. T. Staley, R. J. Bucci and A. B. Thakker: "Effect of Microstructure on Fatigue Crack Growth High-Strength Aluminum Alloys", Technical Report AFML-TR-76-169, Final Report, Aluminum Company of America, October 1976.
3. T. H. Sanders, Jr. and E. A. Starke, Jr., Met. Trans., Vol. 7A, p. 1407, 1976.
4. H. W. Antes and H. Markus: Metals Engineering Quarterly, Vol. 10, No. 4, p. 9, 1970.
5. J. Waldman, H. Sulinski and H. Markus: "New Processing Techniques for Aluminum Alloys", Proceedings of the First Army Materials Technology Conference, Wentworth-by-the-Sea, Portsmouth, New Hampshire, p. 253-271, 1972.
6. R. E. Sanders, Jr., and E. A. Starke, Jr.: Met. Trans., Vol. 9A, p. 1087, 1978.
7. H. W. Antes, S. Lipson and H. Rosenthal: Trans. TMS-AIME, Vol. 239, p. 1634, 1967.
8. E. DiRusso, M. Conserva, F. Gatto and H. Marcus: Met. Trans., Vol. 4, p. 1133, 1144, 1973.
9. J. E. Vruggink: "Study of Improved Aluminum Materials for Vehicular Armor", Technical Report #FA-TR-76-73, Frankford Arsenal, April 1977.
10. F. G. Osterman, Met. Trans., Vol. 2, p. 2877-2902, 1971.
11. F. Mehrpay, D. L. Kudsin and W. L. Horwirth: Met. Trans. A, Vol. 7A, p. 761-762, 1976.
12. Forging of Powder Metallurgy Preforms; New Perspectives in Powder Metallurgy, Editors: H.H. Hausner, K. H. Roll and P. K. Johnson, Vol. 6, Metal Powder Industries Federation, New York, N.Y., 1973.
13. J. P. Lyle and W. S. Cebulak: Met. Trans., Vol. 6A, p. 685-699, 1975.
14. S. G. Roberts: "Research Study for Development of Aluminum Base Alloys by Powder Metallurgy Techniques", Report MSPR61-69, Contract No. DA-04-200-507-ORD-886, Nov. 1961.

15. R. J. Towner: "Development of Aluminum Base Alloys", Annual Progress Report No. 593-32-004, Contract No. DA-36-034-ORD-3559RD, October 1962.
16. A. P. Haarr: "Development of Aluminum Base Alloy, Section III", Final Report, Contract DA-36-04-ORD-3559rd, May 31, 1966.
17. J. P. Lyle and W. S. Cebulak, Metals Eng. Quarterly, Vol. 14, No. 1, p. 52, 1974.
18. W. S. Cebulak: "Rapid Solidification Processing, Principles and Technologies", Claitor's Publishing Division, p. 324, 1978.
19. W. S. Cebulak, E. W. Johnson and H. Markus: The International Journal of Powder Metallurgy and Powder Technology, Vol. 12, No. 4, p. 299, 1976.
20. K. E. Buchovecky and M. R. Rearick: loc. cit. reference #2, p. 319.
21. W. S. Cebulak, E. W. Johnson and H. Markus: Metals Eng. Quarterly, Vol. 16, No. 4, p. 37, 1976.
22. S. C. Park and W. K. Park: Int. J. of Powder Met. and Powder Tech., Vol. 14, No. 4, p. 305, 1978.
23. R. E. Sanders: "Elevated Temperature Al Alloy Development", Alcoa Laboratories, AFML Contract #F33615-77-C-5086, March 1979.
24. R. E. Lewis, D. Webster and I. G. Palmer: "A Feasibility Study for Development of Structural Aluminum Alloys from Rapidly Solidified Powders for Aerospace Structural Applications", Lockheed Palo Alto Res. Lab., AFML Report #TR-78-102; AD A061428, July 1978.
25. D. P. Voss: "Structure and Mechanical Properties of Powder Metallurgy 2024 and 7075 Aluminum Alloys", German Aerospace Res. Est. (DFVLR), Final Report EOARD-TR-80-1, October 1979.
26. V. Anand, A. Kaufman and N. J. Grant: "High Strength Aluminum Alloys by Ultrasonic Atomization", The Metallurgical Society of AIME, Fall Meeting, Milwaukee, Wisconsin, September 1979.
27. R. E. Sanders, Jr. and W. L. Otto: "Microstructure and Fatigue Resistance of 7xxx P/M Aluminum Alloys", ibid, reference #26.
28. W. L. Otto, Jr.: "Metallurgical Factors Controlling Structure in High Strength P/M Products", AFML Report #TR-76-60, Aluminum Company of America, Alcoa Center, PA; Contract #F33615-74-C-5077, May 1976.

29. J. P. Lyle, Jr. and W. S. Cebulak: "Powder Metallurgy for High Performance Applications", Editors: J. J. Burke and V. Weiss, Syracuse University Press, Syracuse, N.Y., p. 321, 1972.
30. P. Ramakrishnan: Powder Met. Assoc. of India, Journal, Vol. 4, No. 3, p. 8, 1978.
31. W. L. Otto, Jr. and R. R. Sawtell: "Fatigue Behavior of High Strength Powder Metallurgy Aluminum Alloys", AIME Annual Meeting, Atlanta, Georgia, March 1977.
32. R. E. Sanders, W. L. Otto, Jr. and R. J. Bucci: "Fatigue Resistant Aluminum P/M Alloy Development", AFML Report #TR-79-4131, Aluminum Company of America, Alcoa Center, PA: Contract #F33615-77-C-5174, September 1979.
33. J. Santner, private communication, AFML; 1978.
34. D. R. Holloway: "Determination of Threshold Stress Intensity Factors for 7175-T651 Aluminum and MA-87 Powdered Aluminum Alloys", M.S. Thesis, Air Force Institute of Technology, September 1977.
35. D. M. Corbly, Jr.: "Fatigue Crack Growth and Retardation in a Powder Aluminum Alloy", AIME Annual Meeting, Atlanta, Georgia, March 1977.
36. T. F. Bower, H. D. Brody and M. C. Flemings: Trans. AIME, Vol. 236, p. 624, 1966.
37. T. H. Sanders, Jr., R. R. Sawtell, J. T. Staley, R. J. Bucci and A. B. Thakker: "Effect of Microstructure on Fatigue Crack Growth of 7xxx Aluminum Alloys Under Constant Amplitude and Spectrum Loading", Final Report: Naval Air System Command, Contract N00019-76-C-0482, April 1978.
38. D. J. Skinner, R. Ker, M. J. Koczak and A. Lawley" "The Aging Response of a High-Strength P/M Aluminum Alloy", in Modern Developments in Powder Metallurgy; Editors: H.H. Hausner, H. W. Antes and G. D. Smith, Metal Powder Industries Federation, Princeton, N.J., Vol. 13, p. 483, 1981.
39. B. I. Sandor: "Fundamentals of Cyclic Stress and Strain", the University of Wisconsin Press, Madison, Wisconsin, 1972.
40. P. C. Paris and F. Erdogan: J. Basic Engr. Trans., ASME Series D. Vol. 85, p. 528, 1963.
41. M. Rafalin: "Fatigue of High-Strength Powder Metallurgy Aluminum Alloys", Ph.D. Thesis, Department of Materials Engineering, Drexel University, Philadelphia, PA, January 1981.

42. E. E. Underwood and E. A. Starke, Jr.: "Quantitative Stereological Methods for Analyzing Important Microstructural Features in Fatigue of Metals and Alloys", in Fatigue Mechanisms, Editor: J. Fong, ASTM STP 675, p. 633-682, 1979.
43. J. Waldman, H. Sulinski and H. Markus: Met. Trans., Vol. 5, p. 573-584, 1979.
44. S. Buzolits and A. Lawley: "A Fundamental Study of Fatigue in High Strength Wrought Aluminum Alloys", Senior Thesis, Drexel University, Philadelphia, Pa., May 1979.
45. J. Goodman: Mechanics Applied to Engineering, Longmans, Green & Co., Ltd., London, 1899.
46. C. Lipson and N. J. Sheth: Statistical Design and Analysis of Engineering Experiments, McGraw-Hill, p. 36-48 and p. 84-87, 1973.
47. H. W. Antes: "Role of Deformation Processing on the Fatigue Behavior of a High Strength Powder Metallurgy Aluminum Alloy", Ph.D. Thesis, Department of Materials Engineering, Drexel University, Philadelphia, Pa., June 1979.
48. Metals Handbook: Fractography and Atlas of Fractographs, Eighth Edition, Vol. 9, American Society for Metals, Metals Park, Ohio, 1974.
49. SEM/TEM Fractography Handbook, Metals and Ceramics Information Center, Battelle Columbus Laboratories, Columbus, Ohio, December 1975.
50. R. E. Sanders, Jr. and E. A. Starke, Jr.: Materials Science and Engineering, Vol. 28, p. 53, 1977.
51. A. Abel and R. K. Ham: Acta Met., Vol. 14, p. 1495, 1966.
52. C. Calabrese and C. Laird: Mats. Sci. Eng., Vol. 13, p. 141, 1974.
53. C. Calabrese and C. Laird: Mats. Sci. Eng., Vol. 13, p. 159, 1974.
54. M. E. Fine and J. S. Santner: Scripta Met., Vol. 9, p. 1239, 1975.
55. T. Endo and J. Morrow: J. Mats., Vol. 4, p. 159, 1969.
56. T. H. Sanders, Jr., J. T. Staley and D. A. Mauney: "Strain Control Fatigue as a Tool to Interpret Fatigue Initiation of Al Alloys", Alcoa Laboratories, Alcoa Center, Pa., 1975.
57. Manual of Low Cycle Fatigue Tests, ASTM STP 465, 1969.
58. B. I. Sandor: Fundamentals of Cyclic Stress and Strain, University of Wisconsin Press, Madison, WI, 1972.

PUBLICATIONS AND DISSERTATIONS

"Fatigue of High-Strength Aluminum Alloy P/M forgings", M. Rafalin, M.J. Koczak and A. Lawley in Thermo-Mechanical Processing of Aluminum Alloys; Editor: J.G. Morris; The Metallurgical Society (AIME), p. 147, 1979.

"Fatigue Properties of a Powder Forged High Strength Aluminum Alloy", H. W. Antes, A. Lawley and M. J. Koczak, in Progress in Powder Metallurgy; Editors: J. Hoffmann, W. Cebulak and E. Klar, vol. 35, p. 311, 1980.

"Fatigue Properties of CT-91 forgings", A. Lawley and M. J. Koczak, Review of Government Sponsored Work on P/M Aluminum - Proceedings; Dayton, Ohio AFML, 1980.

"The Aging Response of a High-Strength P/M Aluminum Alloy", D. J. Skinner, R. Ker, M. J. Koczak and A. Lawley, in Modern Developments in Powder Metallurgy; Editors: H. H. Hausner, H. W. Antes and G. D. Smith, Metal Powder Industries Federation, Princeton, N.J., Vol. 13, p. 483, 1981.

"Role of Deformation Processing on the Fatigue Behavior of a High Strength Powder Metallurgy Aluminum Alloy", H. W. Antes; Ph.D. Thesis, Drexel University, Phila., PA, June 1979.

"Fatigue of High-Strength Powder Metallurgy Aluminum Alloys", M. Rafalin; Ph.D. Thesis, Drexel University, Phila., PA, January 1981.

"A Fundamental Study of Fatigue in High-Strength Wrought Aluminum Alloys", S. R. Buzolits; B.S. Senior Thesis, Drexel University, May 1979.

Papers in preparation:

"Load-Controlled Fatigue of Powder-Processed High-Strength Aluminum Alloys", M. Rafalin, A. Lawley and M. J. Koczak.

"Fatigue Crack Propagation in Powder-Processed High-Strength Aluminum Alloys", M. Rafalin, A. Lawley and M. J. Koczak.

"Crack Propagation in P/M Processed High Strength Aluminum Alloys - Part I: Response in Air", H. W. Antes, M. J. Koczak and A. Lawley.

"Crack Propagation in P/M Processed High Strength Aluminum Alloys - Part II: Response in a Saline Environment", H. W. Antes, M. J. Koczak and A. Lawley.

"Low Cycle Fatigue of Powder-Processed High-Strength Aluminum Alloys", D. J. Skinner, A. Lawley and M. J. Koczak.

"Fatigue of Ingot-Processed 7075 and 7475 Aluminum Alloys", S. R. Buzolits, H. W. Antes and A. Lawley.

PERSONNEL

The program was under the direction of Dr. Alan Lawley, Professor of Materials Engineering and Dr. Michael J. Koczak, Professor of Materials Engineering. Two Ph.D. students (Harry W. Antes and Mario Rafalin) and one Post Doctoral Research Associate (David Skinner) worked on the Program. In addition, Steven R. Buzolits carried out an undergraduate Senior Thesis on ingot metallurgy aluminum alloys as an integral part of the program.

COUPLING ACTIVITIES

This program on fatigue in P/M processed high-strength aluminum alloys complemented several on-going AFOSR and AFML-sponsored studies involving ingot metallurgy and P/M aluminum alloys. Liaison was maintained with T. H. Sanders and E. A. Starke (Georgia Institute of Technology), M. E. Fine (Northwestern University), D. L. Davidson (Southwest Research Institute), W. L. Otto and R. E. Sanders (Alcoa), L. R. Bidwell, W. Griffith (AFML) and D. P. Voss (AFML; formerly with DFLVR, Germany).

Figure 8: Tensile and fatigue properties and coefficients as a function
of cobalt level and processing mode.

END
DATE
FILMED

11/18/81

DTIC